Instytut Fizyki Jądrowej
im. Henryka Niewodniczańskiego
Polskiej Akademii Nauk

The Henryk Niewodniczański
Institute of Nuclear Physics
Polish Academy of Sciences

Rozprawa doktorska

Badanie wpływu domieszek wolframu na dynamikę elektronów w plazmie termojądrowej uwięzionej w tokamaku

Impact of tungsten impurities on electrons dynamics of thermonuclear plasma in tokamaks

Jędrzej Walkowiak

Thesis submitted for the degree of
Doctor of Philosophy in Physics

promotor / supervisor:
dr hab. Jakub Bielecki prof. IFJ

promotor pomocniczy / supporting supervisor:
dr Axel Jardin

Kraków 2024

Podziękowania

Na wstępie chciałbym podziękować osobom, bez których ta praca by nie powstała: mojej rodzinie i przyjaciołom, moim promotorom, współpracownikom z mojego zakładu i IFJ. Szczególne podziękowania kieruję do prof. Jacka Bieronia, bez którego rady i bezinteresownej pomocy trudno mi sobie wyobrazić ukończenie mojego doktoratu. Dziękuję także Marcinowi Wilczyńskiemu za pomoc w implementacji moich modeli do DREAM.

A special thanks to Mathias Hoppe, Tünde Fülöp and the entire Plasma Theory group at Chalmers – for all the help and hospitality.

Acknowledgments

This work has been partially funded by the National Science Centre, Poland (NCN) grant HARMONIA 10 no. 2018/30/M/ST2/00799. We acknowledge the financial support provided by the Polish National Agency for Academic Exchange NAWA under the Programme STER—Internationalisation of doctoral schools, project no. PPI/STE/2020/1/00020". We gratefully acknowledge Polish high-performance computing infrastructure PLGrid (HPC Center: ACK Cyfronet AGH) for providing computer facilities and support within computational grant no. PLG/2022/015994 and PLG/2024/016925. This work has been carried out within the framework of the EUROfusion Consortium, funded by the European Union via the Euratom Research and Training Programme (Grant Agreement No. 633053 and 101052200—EUROfusion). Views and opinions expressed are however those of the author(s) only and do not necessarily reflect those of the European Union or the European Commission. Neither the European Union nor the European Commission can be held responsible for them. This project is co-financed by the Polish Ministry of Education and Science in the framework of the International Co-financed Projects (PMW) programme.

Streszczenie

Wraz z decyzją o zabezpieczeniu wewnętrznej ściany komory próżniowej ITERa za pomocą warstwy wolframu, oddziaływanie elektronów nadtermicznych z domieszkami tego pierwiastka stało się ważną kwestią w modelowaniu plazmy. Mikrofalowe systemy ogrzewania plazmy i generowania w niej prądu, zwłaszcza za pomocą niższej częstotliwości hybrydowej (ang. Lower-Hybrid Current Drive - LHCD), mogą powodować powstawanie znaczącej populacji elektronów nadtermicznych. Ponadto, w przypadku niekontrolowanie rozpędzonych elektronów (ang. runaway electrons - RE) i zapobiegania im poprzez wtrysk dużej ilości gazów do plazmy, zderzenia z domieszkami mogą mieć znaczący wpływ na hamowanie elektronów. Szczegółowy opis zderzeń szybkich elektronów z nie w pełni zjonizowanymi domieszkami wymaga wyznaczenia dwóch parametrów: atomowego współczynnika kształtu dla zderzeń sprężystych i średniej energii wzbudzenia (ang. Mean Excitation Energy - MEE) dla zderzeń niesprężystych. Można to zrobić za pomocą metod *ab initio*, które pozwalają uzyskać dokładne wyniki, jednak ich praktyczne zastosowanie wiąże się z czasochłonnymi obliczeniami. W przypadku MEE, czas obliczeń dla pierwiastków o dużej liczbie atomowej *Z* jest zaporowy.

W niniejszej pracy porównałem istniejące przybliżenia atomowego współczynników kształtu, oparte na modelach Thomasa-Fermiego oraz Pratta-Tsenga. Obliczenia *ab initio* za pomocą teorii funkcjonału gęstości (ang. Density Functional Theory - DFT) są wykorzystywane jako metoda referencyjna do określenia dokładności porównywanych modeli. Na podstawie tej analizy zaproponowałem pewne modyfikacje istniejących modeli, zoptymalizowane za pomocą metod numerycznych, które zapewniają wyższą dokładność przy zachowaniu krótkiego czasu obliczeń. Modyfikacje te obejmują zastosowanie kilku członów eksponencjalnych modelu Pratta-Tsenga i dopasowanie parametrów równania współczynnika kształtu do wyników opartych na DFT. Przedstawiono zastosowania prezentowanych modeli do obliczania częstotliwości zderzeń sprężystych i niesprężystych dla równania Fokkera-Plancka, wykazując dobrą zgodność między wynikami uzyskanymi metodą DFT a proponowanymi modelami.

Prezentowana praca dostarcza wartości MEE dla atomów i ich jonów o liczbach atomowych $1 \leq Z \leq 86$. Aby wypełnić luki w dostępnych danych, zaproponowałem przybliżony model dla jonów pierwiastków o dużej liczbie atomowej *Z*, który wykorzystuje półempiryczny wzór oparty na tzw. lokalnym przybliżeniu plazmy (ang. Local Plasma Approximation - LPA). Pomimo, że LPA w swojej oryginalnej postaci nie przewiduje dokładnie wartości MEE dla silnie zjonizowanych atomów, stosunkowo prosta modyfikacja pozwoliła znacznie poprawić otrzymywane wyniki. W pracy oszacowałem także wpływ efektów relatywistycznych na wyznaczone wartości MEE dla silnie zjonizowanych atomów i porównałem proponowany wzór z innymi przybliżeniami dostępnymi dla pierwiastków o dużej liczbie atomowej Z.

Opracowane modele i uzyskane dane zostały wykorzystane do rozszerzenia możliwości kodu numerycznego służącego do analizy zaburzeń plazmy i niekontrolowanie rozpędzonych elektronów, poprzez uwzględnienie domieszek wolframu w plazmie. Zbadano zależność prądu RE od następujących parametrów plazmy: stężenia wolframu, wielkości zaburzeń pola magnetycznego, modeli populacji elektronów użytych do obliczeń, czasu stygnięcia plazmy oraz geometrii sznura plazmowego – wzorowanej na konfiguracji ITER-a lub ASDEX-a. Przeprowadzona analiza pokazuje, że stężenie wolframu poniżej 10^{-3} nie powoduje znaczącej samoistnej generacji RE. Jednak przy wyższych stężeniach domieszek W możliwe jest osiągnięcie bardzo wysokiego prądu RE. Z dwóch testowanych modeli elektronów w plazmie: płynowego i izotropowego (kinetycznego), wyniki z modelu płynowego są bardziej konserwatywne, co jest przydatne w kontekście analizy bezpieczeństwa. Wyniki te są jednak przeszacowane względem modelu izotropowego, który opiera się na bardziej wiarygodnych założeniach. Wyniki pokazują

również, że mechanizm generowania RE z nadtermicznego ogona (ang. Hot-tail) rozkładu prędkości jest dominującym źródłem RE w zakłóceniach wywołanych wolframem, zwykle zapewniając o rząd wielkości wyższe liczby pierwotnych RE niż mechanizm Dreicera. W przedstawionej pracy zbadano różne podejścia do symulacji plazmy o wysokim stężeniu wolframu i przygotowano na tej podstawie rekomendacje dla przyszłych prac obliczeniowych. Zbadano zależność limitów bezpieczeństwa od zastosowanych modeli oraz ich parametrów i określono największe problemy obecnych technik symulacji. Przeprowadzone prace torują drogę do szerszej analizy wpływu wolframu na dynamikę plazmy, w tym technik zapobiegania RE w ITER w przypadku silnego zanieczyszczenia plazmy wolframem.

Abstract

The selection of tungsten as a plasma-facing material for the ITER tokamak has raised the importance of suprathermal electron interactions with partially ionized impurities in plasma modeling. Heating and current drive methods, particularly electron cyclotron and lower hybrid current drive, can produce a substantial population of such electrons in the plasma. Additionally, during runaway electron generation and mitigation through massive injection of gas, the electron drag force can be significantly affected by collisions with impurity ions. A detailed description of fast electrons collisions with non-fully ionized impurities requires calculation of two parameters: the atomic form factor for elastic collisions and the Mean Excitation Energy (MEE) for inelastic collisions. The *ab initio* models that can be used for this purpose are accurate, but very time consuming in practice. In the case of MEE, the computational time for high-Z elements is prohibitive.

In this thesis, I evaluate existing approximations of the atomic form factor derived from the Pratt–Tseng and Thomas–Fermi models. I consider *ab initio* density functional theory (DFT) calculations as a reference to assess the accuracy of these models. I then propose several changes to the Pratt–Tseng model, optimized with numerical parameter adjustments, which enhance accuracy while keeping computation time short. These modifications involve incorporating several exponents in the Pratt–Tseng model and fitting the parameters of the atomic form factor expression to the results obtained from DFT. I also present applications of the revised models for calculating the elastic and inelastic collision frequencies for the Fokker–Planck solver, demonstrating strong agreement between the proposed models and the DFT approach.

In a second part, I determine values of MEE for each atom and its ions, with the atomic number ranging from 1 to 86. To address gaps in the existing data, I introduce an approximation for ions with high atomic number, employing a semi-empirical formula based on the Local Plasma Approximation (LPA). Although the original LPA is not able to predict MEE accurately for high ionization states, a straightforward modification using a fitting function can correct this limitation. I evaluate the significance of relativistic effects on the MEE for highly ionized atoms and compare the proposed formula with other available approximations for high-Z elements.

The obtained models and data were used to extend the disruption and runaway electron analysis model code DREAM, allowing to include tungsten impurities in disruption simulations, with the aim of studying runaway electron (RE) generation. In this work, I examine the sensitivity of runaway electron (RE) current to various plasma parameters and modeling choices, including magnetic perturbation strength, tungsten concentration, electron modeling approach (fluid vs. kinetic), thermal quench time and tokamak geometry - specifically ITER-like and ASDEX-like configurations. The study reveals that tungsten concentrations below 10^{-3} do not alone cause significant RE generation. Nevertheless, very high RE currents can be achieved at higher tungsten concentrations. Among the two tested models of electrons in plasma - fluid and isotropic (kinetic) - the fluid model yields more conservative results, which is useful for safety assessments. Nonetheless, these findings are more pessimistic than the isotropic model, which relies upon a more reliable approach. The results also indicate that the mechanism of hot-tail RE generation is the dominant source of RE during tungsten-induced disruptions, typically providing a RE seed larger by orders of magnitude with respect to Dreicer generation. I assess best practices for simulating plasma disruption in the presence of tungsten impurities. I discuss how the calculated safety limits depend on modeling choices, and emphasize key shortcomings of current simulation approaches. The findings lay the groundwork for a more comprehensive analysis of tungsten impact on the dynamics of disruptions, including potential mitigation strategies for ITER in cases of significant tungsten influx into the plasma.

TABLE OF CONTENT

LIST OF ABBREVIATIONS

CQ - Current Quench

DFT - Density Functional Theory

DREAM - Disruption and Runaway Electron Analysis Model

D-T - deuterium-tritium

ELM - Edge Localized Modes

FAC -Flexible Atomic Code

GRASP - General-purpose Relativistic Atomic Structure Package

H-mode – High confinement mode

ITER - International Thermonuclear Experimental Reactor

JET - Joint European Torus

LPA - Local Plasma Approximation

MCSCF - Multi-Configurational Self- Consistent Field

MEE - Mean Excitation Energy

MHD - Magnetohydrodynamics

PFC – Plasma Facing Components

RE – Runaway Electrons

TF - Thomas-Fermi

TQ - Thermal Quench

UFO - Unidentified Flying Object / Unidentified Impurity Source

1 MOTIVATION

The main motivation for this work is fusion research. Despite its many benefits, fusion technology is still in its initial stage of development, as fusion reactions require extreme conditions to achieve a reaction rate that would be relevant for energy production. The easiest fusion reaction to conduct in Earth conditions is the reaction of tritium and deuterium, but the temperature required for this process is of the order of hundreds of millions of kelvins.

The main goal of this work was to analyze the impact of tungsten impurities on suprathermal electron dynamics in tokamaks, with a particular focus on runaway electron generation. By suprathermal electrons, we consider the part of the electron population at energies higher than the electron thermal energy, which is in excess with respect to a Maxwellian distribution.

Runaway electrons can be accelerated to relativistic velocities by electric field in plasma, reaching energies of the order of MeV. Fast electrons have lower collision cross-sections in plasma, so the acceleration is stronger for higher velocities, hence the name. This topic is especially important for thermonuclear reactors based on the tokamak concept, as runaway electrons pose a serious threat for the machine components. Tungsten is a specific impurity species, whose influence on plasma can be exceptionally strong. This is related to its high atomic number, resulting in strong Coulomb interactions between tungsten ions and other particles in plasma. It also implies high ionization energy of the innermost electrons. Because of it, tungsten is not fully ionized even at very high temperatures encountered in thermonuclear reactors, which complicates the theoretical description of plasma in such devices. Inclusion of tungsten into simulations of plasma dynamics enables more detailed safety assessment for tokamaks and paves the way for potential analysis of runaway electron termination by heavy element injection. The implementation of tungsten ions into a plasma simulation code required the analysis and development of atomic models, to provide the atomic form factor and mean excitation energy parameters for plasma interactions. Because of this, the presented work is a significant contribution, not only to plasma physics, but also to atomic physics in general. The following problems were investigated in my thesis:

1. Description of the elastic electron-ion collisions in plasma with the partial screening and atomic form factor.
2. Description of the inelastic electron-ion collisions in plasma with high-Z impurities and mean excitation energy of heavy ions.
3. Tungsten impact on the runaway electron generation in numerical simulations of tokamak plasma disruption.

The dissertation consists of three research articles of which I am the main author with leading contribution and one article of which I am a coauthor:

1. J. Walkowiak, A. Jardin, J. Bielecki, Y. Peysson, D. Mazon, D. Dworak, K. Krol and M. Scholz. *Approximate atomic models for fast computation of the Fokker-Planck equation in fusion plasmas with high-Z impurities and suprathermal electrons.*
   Physics of Plasmas **29** (2022) 022501
   https://doi.org/10.1063/5.0075859
2. J. Walkowiak, J. Bielecki, J. Bieroń, A. Jardin, Y. Savoye-Peysson, D. Mazon, K. Król, D. Dworak, M. Scholz. *Mean Excitation Energies of all ionization stages of all atoms with $1 \leq Z \leq 86$.*
   Atomic Data and Nuclear Data Tables (2024) in press
   https://doi.org/10.1016/j.adt.2024.101696

3. J. Walkowiak, M. Hoppe, I. Ekmark, A. Jardin, J. Bielecki, K. Król, Y. Savoye-Peysson, D. Mazon, D. Dworak and M. Scholz. *First numerical analysis of runaway electron generation in tungsten-rich plasmas towards ITER.*
   Nuclear Fusion **64** (2024) 036024
   https://doi.org/10.1088/1741-4326/ad24a0

4. Y. Savoye-Peysson, D. Mazon, J. Bielecki, D. Dworak, K. Król, A. Jardin, M. Scholz, J. Walkowiak and J. Decker. *A unified description of atomic physics for electron Fokker–Planck calculations.*
   Nuclear Fusion **63** (2023) 126041
   https://doi.org/10.1088/1741-4326/acffd9

Those articles follow the main research questions which I tried to answer during my doctoral studies:

1. How can we describe the atomic form factor of heavy ions with the most numerically efficient yet accurate enough approach?
2. How to determine the mean excitation energy of high-Z ions?
3. What is the impact of tungsten on suprathermal electrons in tokamak plasma?

What binds these three topics together is the general aim of my thesis – to describe the interaction of fast electrons with tungsten impurities in fusion plasmas. The first two questions are of very practical nature, as their answers were necessary to investigate the third question. In the following part of the thesis, I give the required background to understand the research presented in this dissertation and summarize the results obtained in the published articles.

2 INTRODUCTION

2.1 NUCLEAR FUSION

Nuclear fusion is a process of merging two nuclei of light elements into a heavier one, accompanied by a release of significant amount of energy. It is the driving force of stars, where hydrogen and other light elements are fused together, producing enormous amounts of energy. The majority of the energy available on Earth comes directly and indirectly from nuclear fusion of hydrogen which takes place in the core of the Sun.

Using controlled nuclear fusion for energy production has a number of significant benefits: hydrogen fuel is abundant, there are no greenhouse gases or long-lived radioactive waste in the products of reaction and the process is inherently safe, since fusion is not a chain reaction. However, the extreme conditions required for fusion make it very challenging to use as an energy source. The least demanding process in terms of temperature is fusion of deuterium and tritium, but the required temperature is still at the level of 150 million degrees Celsius.

There are two approaches for overcoming the difficulty of keeping the hydrogen fuel at such extreme conditions. The first one is inertial confinement, which requires extremely rapid compression and heating of the fuel by nuclear blast or by focused laser light of high intensity. In recent years, the National Ignition Facility at USA proved that inertial fusion implosion can achieve Lawson's criterion for ignition [Zylstra 2022]. Unfortunately, practical application of this method for energy production is still far from being accomplished.

The second approach is based on magnetic confinement, where hydrogen fuel is kept in the state of plasma and confined by a strong magnetic field [Chen 2016]. This approach allows theoretically for a steady production of energy and is investigated intensively by many public institutes and private companies as a possible way for construction of a thermonuclear power plant.

2.2 CONTROLLED FUSION AND TOKAMAK CONCEPT

One of the most advanced concepts of thermonuclear reactors is the tokamak. This device can confine extremely hot hydrogen fuel in a toroidal magnetic field [Wesson 2011]. The hot plasma consists of charged ions and electrons, which follow magnetic field lines. If these field lines are bound in a toroidal shape, it is possible to confine energetic particles inside the tokamak, limiting their flux to the walls. To prevent particle drifts due to magnetic field gradients, it is necessary to introduce some poloidal component to the magnetic field. This combination of field components results in a helical shape of the field lines which is schematically shown in Figure 1. The toroidal

component is created by magnetic coils, while the poloidal component is created mainly by the electric current driven in the plasma.

The magnetic field lines are shaped not to close on themselves after circling the torus, thus they create a magnetic surface. Particles bound to the magnetic surface can travel relatively easily in the toroidal and poloidal direction on the given surface, but their radial transport to another surface is strongly limited. In the macroscopic scale, this results in very low transport coefficient in the radial direction in the tokamak.

The next generation of tokamaks is predicted to achieve breakeven, by producing more energy from fusion reactions than the amount used for external plasma heating. This will require strong magnetic fields, created by superconducting coils and extremely high plasma current, which is expected to reach 15 MA in the International Thermonuclear Experimental Reactor (ITER) [Shimada 2007]. ITER is currently under construction and so far it is one of the most ambitious fusion energy endeavors to create a thermonuclear reactor. Due to its significance to the progress in nuclear fusion, ITER is the reference point for the presented work.

Magnetic confinement is not perfect and some particles leave the plasma with a kinetic energy in the order of tens of eV [Xie 2017, Adamek 2021]. To withstand flux of such energetic particles, plasma-facing components must endure high heat loads and be resistant to sputtering. One of the best materials for such a purpose is tungsten, which is widely used for plasma-facing components in tokamaks. The main alternative for tungsten was carbon, but it was rejected due to high tritium retention [Roth 2009, Merola 2010, Pitts 2013].

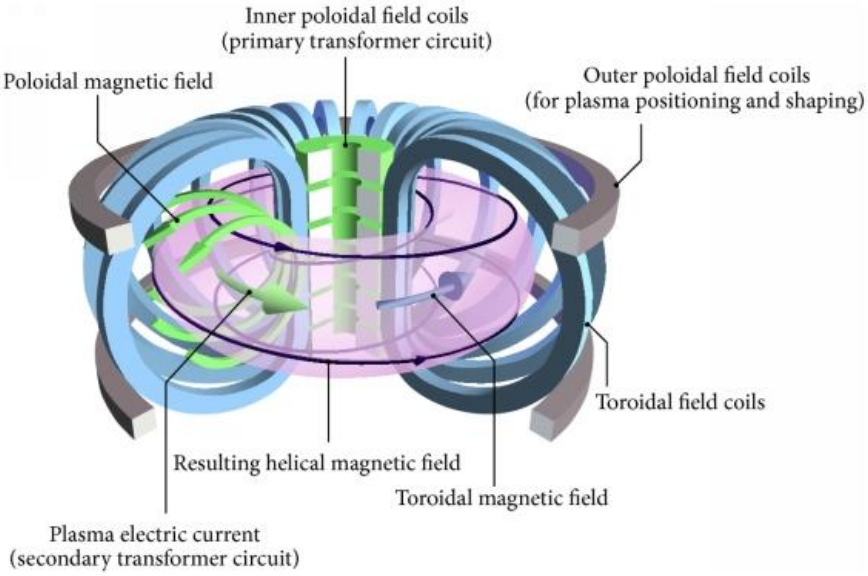

Figure 1. Schematics of a tokamak chamber and magnetic field, reproduced from [Li 2014] on CC BY 3.0 license

2.3 DISRUPTIONS

The tokamak operation requires a fragile balance of plasma in the magnetic field, where current flowing through plasma is an important component of its confinement, but at the same time strongly depends on plasma parameters. Because of this feedback loop, tokamak operation is often ended prematurely by a sudden loss of confinement, which is called a plasma disruption.

During decades of tokamak development, a number of operational stability limits were investigated to ensure stable operation and prevent major disruptions. This includes plasma current, which must be kept in certain limits to avoid magnetohydrodynamic (MHD) instabilities. In this work, disruptions caused by an influx of tungsten impurities are of primary consideration. The direct cause of the loss of confinement are in this case MHD instabilities. They grow due to the current redistribution in plasma caused by resistivity changes, which are in turn the results of plasma cooling effect of impurities [Reinke 2019, Gao 2020].

The process of disruptions can be divided into two distinctive parts: thermal quench (TQ) and current quench (CQ). TQ is the first sign of the disruption, when the plasma temperature drops rapidly. This results in high plasma resistivity, which leads to current dissipation, corresponding to the slower CQ phase. In the considered cases, when TQ is caused by MHD instability, it is usually related to stochastization of the magnetic field lines. When the structure of magnetic field lines becomes stochastic, the magnetic surfaces are broken and radial transport is strongly increased. This leads primarily to fast plasma cooling. Current is less affected, as even if some current carrier particles are lost, the current is induced in charges remaining in the plasma [Lehnen 2015].

Disruptions can cause significant damage to some tokamak components, especially in bigger machines, where the energy stored in plasma during operation is larger. Two main considerations are heat loads and current induction in the machine walls or other components.

Excessive heat loads occur when the energy stored in plasma is deposited locally in a relatively small fragment of the machine wall. Tokamaks should be able to withstand uniform deposition of thermal energy on vacuum chamber walls caused by loss of thermal confinement, but local heat deposition can lead to melting of plasma-facing components. This often happens when runaway electrons (RE) are formed during a disruption. RE generation is the main subject of the presented work, so they are described in detail in section 3.3.

Electromagnetic forces can damage the machine structure if the CQ duration exceeds safety limits. Too fast plasma current quenching leads to strong current induced in conductive components of the machine. Too long CQ usually results in plasma displacement and halo current, which also generates strong forces that can damage the tokamak structures. For ITER, the upper time limit of CQ is 150 ms and the lower limit is set to 50 ms [Lehnen 2015]. If RE electrons are generated during a disruption, they can carry a significant portion of plasma current. Because of this, CQ is based on the current carried by thermal electrons, so-called ohmic current. The RE current decays much more slowly than the ohmic current, due to the low collisionality of RE. Thus, the CQ is followed by a runaway plateau, when current decay is slow, until the plasma displacement results in collision of RE with plasma-facing components and termination of the discharge.

2.4 RUNAWAY ELECTRONS

The main risk created by RE for tokamak operation is localized deposition of energy, which can lead to local melting of machine components or quenching of the superconducting coils due to intense X-ray emission [Lehnen 2015, Torre 2019, Reux 2020]. Such an event can stop the machine operation and it may take months or even years to repair the damage in a reactor-scale tokamak.

Collisions slow down fast electrons, but collision cross-sections are inversely dependent on relative velocity. When a sufficiently strong electric field is applied, some electrons above the critical momentum cannot be slowed down by collisions and accelerate to relativistic velocities, forming a population of RE. For electrons whose kinetic energy reaches values of the order of MeV, synchrotron radiation starts to play a significant role and prevents further acceleration. This

process of RE generation for plasma at stationary temperature was described by Dreicer [Dreicer 1959, Dreicer 1960]. When plasma temperature is decreasing, the electrons from the hot tail of the momentum distribution can more easily accelerate to runaway energy, as they already have higher energy than the electrons in plasma at thermal equilibrium. These two processes are called Dreicer generation and hot-tail generation, respectively. They were analyzed in detail in plasma with tungsten impurities, as described in chapter 4.

The remaining sources of primary RE are Compton scattering and tritium decay. These processes become significant for thermonuclear reactors, where a high amount of tritium is used and gamma radiation from activated machine components can generate a significant number of energetic electrons in plasma [Ekmark 2024]. They were not included in the investigation, as these sources depend mainly on the radioactivity of the fuel and wall and are independent of plasma dynamics.

Once a RE seed is created by the mechanisms mentioned above, so-called secondary RE are produced by the avalanche mechanism. They come from collisions of RE with thermal electrons in plasma. As the RE momentum is usually well above the critical limit to enter the runaway regime, both electrons after such collisions may have a momentum above the runaway threshold. In high-current tokamaks, this mechanism is usually responsible for the majority of the RE generation and is expected to play a dominant role at ITER [Sokolov 1979, Rosenbluth 1997, Hesslow 2019].

2.5 RUNAWAY MITIGATION

To prevent damage from RE, several prediction, prevention and mitigation strategies were developed for tokamaks [Zhang 2023]. One approach is based on injection of a significant amount of material (usually noble gases) into the plasma, just after a potentially harmful plasma disruption is detected by tokamak diagnostics. This enables to increase collisionality and thus the friction force from collisions acting on electrons, preventing their acceleration. Another approach is based on applying magnetic perturbation to the magnetic surfaces, leading to deconfinement of the RE [Izzo 2024].

For ITER, the magnetic perturbation strategy from additional coils is technically not feasible, as extremely strong magnetic perturbation would be required for a tokamak of this size. Instead, material injection techniques were developed. Initially gases were simply injected through valves into tokamak's vacuum vessel. For large tokamaks, the gas penetration into the core plasma was too slow to ensure a reliable mitigation strategy. The current plan for ITER foresees the use of shattered pellet injection, where pellets of frozen gas are accelerated, crushed and injected into the plasma [Luce 2020]. Shards of the pellet can penetrate and rapidly vaporize in the core plasma. This strategy was developed and tested extensively at the largest tokamak operated until the end of 2023 in Europe, namely the Joint European Torus (JET)[Jachmich 2022].

Material injection is an active mitigation strategy, which means that dedicated systems must predict the disruption to react in time. This is not always possible, as some disruptions lack the usual markers of growing plasma instabilities. One example can be rapid introduction of a significant amount of impurities into the plasma, or some machine operator errors [de Vries 2011]. This results in unmitigated disruption. The risk of tokamak damage grows with increasing energy stored in plasma during operation, so for ITER the number of unmitigated disruptions should be limited to not more than few in total [Putvinski 2010, Lehnen 2015].

One way to increase the allowable number of disruptions would be to find a solution for reliable and efficient RE termination. This problem is currently under study and the presented work can be a step to develop such techniques with the use of high-Z elements.

2.6 TUNGSTEN IMPURITIES

Tungsten has many advantages when used as a first wall material: high melting point, low tritium retention, erosion resistance and low neutron activation. Despite being one of the most favored materials for plasma-facing components, tungsten has also a significant drawback - it is a high-Z material which radiates up to 10^5 more energy per atom than hydrogen when it enters plasma as impurity. Because of this, it can easily break the power balance of the plasma and cause radiative collapse. Due to its heavy nucleus, it can also strongly affect electron dynamics, even at low concentrations, by elastic and inelastic collisions. At the same time, tungsten has a very complex electronic configuration, with significant contribution of relativistic effects to the binding energy. This makes it very difficult to obtain necessary atomic data for numerical simulations of plasma with tungsten impurities.

During normal reactor operation, tungsten concentration should be kept at a very low level of 10^{-4} - 10^{-5}. Higher concentrations would cause too strong radiative losses compared to power produced in fusion processes [Putterich 2019]. Another problem is the stability of High-confinement mode (H-mode), which requires a low radiated power fraction from plasma. H-mode is an operating regime in tokamak, which allows to achieve much higher temperatures in the plasma core. It was shown on the WEST tokamak, that in a full tungsten environment H-mode stabilization is a significant challenge during longer discharges [Bucalossi 2022, Ostuni 2022]. This topic is relatively poorly investigated, as JET was able to maintain plasma only for several seconds. In the case of ITER, plasma discharges are expected to last beyond 1000 s [Campbell 2024], which will require much better control over tungsten accumulation.

Small amount of tungsten enters plasma as trace impurity due to erosion of plasma facing components (PFC). Particles in the scrape-off layer are considered cold compared to the core plasma, but they can still hit the wall with energy in the order of tens of eV [Xie 2017, Adamek 2021], which corresponds to temperature of hundreds of thousands of kelvins, leading to tungsten sputtering. If transport in plasma favors tungsten accumulation in the core plasma, this may become an issue for long term operation [Morales 2023]. The topic of controlling transport processes in plasma is however outside the scope of the presented work.

Tungsten can enter plasma at a much faster rate due to PFC melting, which happens mainly due to misalignment of the PFC tiles or uncontrolled edge localized modes (ELM). ELM are periodic relaxations of the edge transport barrier in H-mode, which results in expulsion of particles and energy from the confined plasma into the scrape-off layer. Tile misalignment creates an exposed edge, where heat load can exceed the design limits. Tungsten tiles do not show the ability to 'heal' by aligning the molten surface with the surrounding tile. Instead, the melt layer accumulates at the edge and increases the heat load on the tile, making the situation even worse. With sufficient heat load, tungsten droplets start to spray into plasma, leading to plasma contamination on a much higher rate than due to sputtering [Lipschultz 2012, Gao 2020].

The most dramatic example of plasma contamination are large dust particles or flakes of tungsten, which can enter the core plasma thanks to their large size, as they are too big to become completely vaporized in the edge plasma. Such objects are sometimes referred to as UFO (unidentified flying objects) and their occurrence is usually related to some former damage to the PFC, which produced large particles of tungsten. This can be considered as the most dangerous

form of plasma contamination, as UFOs were recognized as the cause of some unmitigated disruptions in tokamaks [de Vries 2011, de Vries 2012].

Tungsten impurities are mostly problematic because they can break the H-mode and cool down the plasma, but some cases of tungsten-induced disruptions were also observed [de Vries 2011, de Vries 2012]. The challenge for ITER is that even rare cases of unmitigated disruptions must be minimized to ensure sufficient lifetime of the machine. What is only an inconvenience in nowadays machines, can be a serious threat to ITER during its future operation. This is why the impact of tungsten on disruptions is investigated in the presented work [Walkowiak 2024a]. What is characteristic for tungsten impurities is that sometimes the TQ does not lead to a CQ and instead is followed by at least partial temperature recovery and a very slow CQ, or even recovery close to pre-disruptive conditions [de Vries 2012, Flanagan 2015, Reinke 2019]. Similar phenomena were observed in my simulations, as described in detail in chapter 4.

2.7 PLASMA MODELLING

Plasma is an extremely complex state of matter, which is described at many levels of approximations, ranging from MHD models, through gyro-kinetic models to particle-in-cell description. The main interest for this work is the kinetic plasma model described with the Fokker-Planck equation. Plasma evolution is an effect of many Coulomb collisions between electrons and ions, which can be described in a statistical way by the Fokker-Planck equation as an effect of collisions on species distribution in the velocity space [Krall 1973]. In this way, it is possible to describe the time evolution of the probability density function of the particles in the plasma where the dominant type of collisions are small-angle deflections by Coulomb forces.

The effect of collisions on the momentum distribution function is represented by a so-called collision operator. In the specific case of two species, a and b, where the distribution of b is Maxwellian, the collision operator C^{ab} is expressed as follows:

$$C^{ab} = \nu_D^{ab}\mathcal{L}(f_a) + \frac{1}{p^2}\frac{\partial}{\partial p}\left[p^3\left(\nu_s^{ab} f_a + \frac{1}{2}\nu_{||}^{ab} p \frac{\partial f_a}{\partial p}\right)\right] \quad (1)$$

where: ν_D^{ab} – deflection frequency describing elastic collisions, $\mathcal{L}(f_a)$ – Lorentz scattering operator (for electron-ion collisions), ν_s^{ab} – slowing-down frequency describing inelastic collisions, $\nu_{||}^{ab}$ – parallel-diffusion frequency, $p = \gamma v/c$ - normalized momentum, v – velocity, c – speed of light in vacuum, γ – Lorentz factor, f_a – momentum distribution function of species a.

Eq. (1) is applicable to numerous tokamak plasma cases, where the ion momentum distribution can be assumed to be Maxwellian, while the electron momentum distribution is examined in detail. The definition of the deflection frequency and slowing-down frequency for plasma with high-Z impurities is non-trivial, as shown in [Hesslow 2018].

The presented thesis introduces a new practical approach for the calculation of the deflection frequency, which includes the partial screening effect. The detailed description of the work on elastic collisions was published in [Walkowiak 2022] and is presented in Chapter 3. The innovative approach to the calculation of the mean excitation energy needed for the slowing down frequency calculation was published in [Walkowiak 2024b] and is shown in Chapter 4. Chapter 5 is dedicated to the implementation of the models from Chapters 3 and 4 into the runaway electron simulation code DREAM (Disruption and Runaway Electron Analysis Model) [Hoppe 2021], which utilizes the Fokker-Planck operator for the calculation of the fast electron population evolution.

In this last chapter, I present the results of simulations made to assess the impact of tungsten on the runaway electron dynamics, which were published in [Walkowiak 2024a].

3 ELASTIC COLLISIONS

The aim of the first investigation undertaken in the course of this thesis was to study and compare different models which can be used to evaluate the influence of partial screening on fast electron collisions with impurity ions in plasma. This work was published in [J. Walkowiak et al., *Phys. Plasmas 29, 022501 (2022)].*

3.1 COLLISION CROSS-SECTION AND ATOMIC FORM FACTOR

Electron-ion elastic collisions can be described using the Born approximation, by incorporating the atomic form factor for each specific ion into the differential collision cross-section. Considering that ions are infinitely heavy stationary targets initially at rest, the differential cross-section $\frac{d\sigma_e^{coll}}{d\Omega}$ over differential solid angle can be formulated as follows [Mott 1965]:

$$\frac{d\sigma_e^{coll}}{d\Omega} = \frac{{r_0}^2}{4p^4}\left(\frac{cos^2(\theta/2)p^2+1}{sin^4(\theta/2)}\right)[Z-F(q)]^2, \tag{2}$$

where: r_0 – the classical electron radius, θ – the deflection angle, Z – the ion atomic number, F(q) – the atomic form factor.

The atomic form factor is related to the Fourier transform, in the momentum space, of the electron density distribution $\rho(r)$ of bound electrons around the nucleus expressed as:

$$F(q) = \int \rho(r) e^{-iqr/a_0} d^3r, \tag{3}$$

where: $q = 2psin\,(\theta/2)/\alpha$ is the momentum transfer, $\alpha \approx 1/137$ – the fine structure constant, r - atomic radius as a spatial coordinate measured from the centre of the atom, a_0– the Bohr radius.

Eq. (3) implies that $0 \leq F(q) \leq N$, where N is the number of bound electrons. $F(q) = 0$ corresponds to the no screening case, when the interaction between a free electron and the atomic nucleus is unaffected by bound electrons. Conversely, $F(q) = N$ indicates complete screening, when the nucleus is screened by all bound electrons.

3.2 CONSIDERED ATOMIC MODELS

The goal of the undertaken work was to find the most suitable atomic model which can be used to calculate the electron density in order to obtain the atomic form factor and the associated collision parameters.

An *ab initio* model based on Density Functional Theory (DFT) served as the accuracy benchmark for comparing various classical and empirical approximate models. Although this reference model is accurate, it is not typically preferred for numerical integration in a Fokker–Planck solver, due to its high computational cost. The calculations often involve multiple integrations of values derived from the atomic model, with some parameters varying according to plasma conditions. Therefore, it is highly advantageous to utilize a model that can offer an analytical solution for these integrals [Savoye-Peysson 2023]. Consequently, such approximated models can significantly enhance computational speed, albeit at the expense of some accuracy. The objective

was to identify the optimal balance between accuracy and computation time, ultimately providing the best solution for future numerical tools designed for fusion plasma applications.

To address this issue, several models were examined as presented in [Walkowiak 2022]. However, since none of the models reviewed were deemed sufficiently satisfactory, an effort was made to enhance an existing model to better approximate the results based on DFT. The multi-exponential Yukawa potential model was developed and presented in [Walkowiak 2022], which can deliver more accurate results than most of the investigated models while remaining analytically integrable and preserving computational efficiency.

The article discusses the use of the proposed models for evaluation of the plasma collision parameters. The calculated frequency of elastic collisions between free electrons and ions shows that the new approximation yields accurate results while significantly reducing computation time. Notably, incorporating the partial screening effect can lead to collision frequencies that are several times higher than those obtained with the complete screening model, making this effect non-negligible. This is particularly significant for ions with a high number of bound electrons and high energy of colliding free electrons. Although these two conditions might seem contradictory - since higher electron temperatures typically lead to increased ionization - they are common in cases of runaway electrons in relatively cold post-disruptive plasmas, enforcing use of the partial screening for accurate simulations [Ekmark 2024]

4 INELASTIC COLLISIONS

The second step of the research was to evaluate the effects of inelastic collisions on fast electron dynamics in plasma. This was done by using an approximation of the slowing down frequency as initially proposed by Hesslow [Hesslow 2017], which is based on the Bethe theory of stopping power [Bethe 1930, Bethe 1932] and mean excitation energy.

4.1 SLOWING DOWN FREQUENCY AND MEAN EXCITATION ENERGY

In this approach, the slowing-down frequency ν_s^{ee} occurring in the Fokker-Plank collision operator (see eq. 1) can be calculated as follows:

$$\nu_s^{ee} = 4\pi c r_0^2 \frac{\gamma}{p^3}\left[n_e ln\Lambda^{ee} + \sum_j n_j N_j \left(\frac{1}{k}\ln(1+{\mu_j}^k) - \beta^2\right)\right], \tag{4}$$

where n_e – density of free electrons in plasma, n_j – density of ion species j in plasma, N_j – number of bound electrons for the given ion species j, $\beta = v/c$, $\mu_j = \sqrt{\gamma-1}\left(mc^2/MEE_j\right)$ and $ln\Lambda^{ee} = ln\Lambda + 1/k\, ln\left(1+[2\,(\gamma-1)/p_{Te}^2]^{k/2}\right)$,where p_{Te} – thermal momentum, γ - Lorentz factor, k - model parameter and $ln\Lambda = \int \frac{db}{b}$ the so-called Coulomb logarithm with b being the collision impact parameter. This formula is valid for colliding particles with energy much higher than the Mean Excitation Energy (MEE).

In this approach, the MEE is the main parameter of interest, as it characterizes the plasma ions as a stopping medium. MEE represents the potential of an ion to absorb energy during collisions with charged particles through excitation. This quantity can be directly calculated utilizing the

atomic properties of a given ion. For low-Z elements, it was obtained using *ab initio* methods e.g. by Sauer et al. [Sauer 2015, Sauer 2018, Sauer 2020] from its definition:

$$ln(MEE) = \int_{1}^{n} \frac{df}{dE} lnE \, dE / \int_{1}^{n} \frac{df}{dE} dE, \tag{5}$$

where E is the transition energy from the ground state to the n-th excited state and f is the associated dipole oscillator strength (or its density for the continuous case). The sum is performed over the discrete part of the spectrum and integral over its continuous part.

This approach is however computationally highly expensive for high-Z elements and hence mostly impractical or impossible. Not only the number of possible excitations increases with the number of electrons. In the Multi-Configurational Self-Consistent Field (MCSCF) codes like GRASP [Froese Fischer 2018] or Dalton [Aidas 2014], the wave function of the atomic state is described as a combination of configuration wave functions. As the number of electrons increases, the complexity of the atomic state functions is greater as well, implying that more configuration state functions are needed to use for accurate representation. When relativistic effects are considered for higher precision, the computation cost increases even more. I calculated the selected ions with the Flexible Atomic Code (FAC) [Gu 2008], but the computation resources required for most of the tungsten ions made it impossible to calculate all the necessary cases.

4.2 Mean excitation energy approximation

Overcoming the above problem of obtaining MEE values for high-Z elements was tackled during my PhD studies and resulted in an article published in the journal Atomic Data and Nuclear Data Tables [J. Walkowiak et al., *Atomic Data and Nuclear Data Tables*, in press (2024)]. In this work, it was proposed to modify the MEE formula based on the Local Plasma Approximation (LPA) [Lindhard 1953]. This allowed easily obtaining values of MEE for all ions of interest for fusion plasma applications. The original LPA uses electron density as the main quantity to estimate the MEE and thus it was attractive as $\rho(r)$ values obtained from the previous work done within the framework of this PhD thesis could be used. The LPA was derived mainly based on the Thomas-Fermi (TF) atomic model, treating bound electrons as a homogenous electron gas. It does not have a strong theoretical background from the point of view of modern atomic physics, but it provides relatively accurate MEE values for neutral atoms. In the original form of LPA, the estimation of MEE is given by the following formula:

$$ln(MEE) = \frac{1}{N} \int 4\pi r^2 \rho(r) ln(\gamma \hbar \omega_0) dr, \tag{6}$$

where the corresponding local plasma frequency of the electron gas is expressed as:

$$\omega_0 = \sqrt{4\pi e^2 \rho\,(r)/m}, \tag{7}$$

where $\rho(r)$ is the spherically averaged electron density distribution in the ion, N is the number of bound electrons in the ion, $\hbar$ is the reduced Planck constant, e denotes the electron charge, m its mass and r is the radial coordinate. The term $ln(\gamma)$ was treated in some works as a free parameter of the LPA, as its value was only approximately defined by their authors as $\gamma = \sqrt{2}$ [Lindhard 1953].

We propose to replace $\ln(\gamma)$ by a function of Z and N in the form: $f(Z,N) = exp\left(\frac{Z-N}{Z}\right) - 0.84$. The effective equation for the modified LPA of the MEE takes then the following form:

$$ln(MEE) = \frac{4\pi}{N}\int r^2\rho(r)ln\big(\hbar\omega_0(r)\big)dr + exp\left(\frac{Z-N}{Z}\right) - 0.84, \quad (8)$$

The proposed approach was to find a simple analytical function that fits the difference between the original LPA and the results from Sauer et al. [Sauer 2018, Sauer 2020]. The term $exp\left(\frac{Z-N}{Z}\right)$ was proposed based on the observed trend of MEE as a function of the ionization degree (see Fig. 2 in [Walkowiak 2024b]). The factor -0.84 was obtained by finding the best fit to the available results. Two main issues were investigated as a part of this work: (i) impact of relativistic effects on MEE for high-Z ions and (ii) accuracy of the proposed method when compared to other available MEE approximations for tungsten ions. The general conclusion was that relativistic effects should have a minor impact on the results, especially when compared to other sources of uncertainty. The comparison of calculated values of MEE for tungsten ions showed that the proposed approach provides results in agreement with the other approximations, *ab initio* outcomes and available experimental results. The main advantage of the presented solution was the possibility to easily obtain MEE values for all ionization stages of all elements up to radon. In the paper, the calculated MEE values are presented along with other results available in the literature.

5 MODELING OF TUNGSTEN IMPACT ON TOKAMAK PLASMA

As the final part of the presented work, the impact of tungsten impurities on RE generation in tokamak plasma during disruptions was investigated. The results of this work were published in [J. Walkowiak et al, Nucl. Fusion 64 (2024) 036024]. This paper is a part of the collection of thematically related articles that compose my doctoral dissertation.

5.1 SIMULATION TOOL

With plans to equip ITER with tungsten PFCs, it is necessary to estimate the risk posed by the presence of tungsten impurities in plasma to every aspect of machine operation and safety. In terms of RE, tungsten impurities in plasma have not been yet included in the analysis and this is the gap which this work aims to address. It was achieved through a series of numerical experiments conducted with the DREAM code.

The DREAM code enables self-consistent simulations of plasma cooling and the associated dynamics of runaway electrons during plasma disruptions. It can fully-implicitly solve a set of nonlinear coupled equations for the evolution of density, temperature, current density, electric field, along with the complete electron distribution function in arbitrary axisymmetric geometry. The code integrates fluid models for background plasma parameters - such as toroidal electric field, electron and ion temperatures, ion densities, and charge states - with various models for runaway electrons, ranging from fluid to fully kinetic approaches. The most comprehensive model in DREAM is a bounce-averaged kinetic one that utilizes a fully relativistic Fokker-Planck test-particle operator for electron-electron collisions, synchrotron radiation reaction force, an avalanche operator and accounts for bremsstrahlung and screening effects in a partially ionized plasma. While the field-particle component of the collision operator is omitted - potentially leading to an underestimation of conductivity - a conductivity correction is applied to the ohmic

current, ensuring an accurate Spitzer response to the electric field, to address this issue [Hoppe 2021].

For the purpose of this study, the DREAM code has been extended with the necessary atomic data obtained in the previous stages of this PhD thesis, to include W impurities in the simulations. The performed study included hundreds of simulations to investigate the impact of modeling choices and varying plasma parameters on the results. The study took the form of a scan of the RE current as a function of the tungsten concentration in plasma and magnetic perturbation strength. The goal was to determine what level of tungsten concentration can pose an issue during tokamak disruptions. The magnetic perturbation strength is unknown, as it depends on the exact disruption evolution which is a stochastic process sensitive to the initial conditions. For this reason, it was treated as an adjustable scan parameter.

The modeling choices are described in the next subsections.

5.1.1 Electron population model

Two different approaches to model the electron population were studied: a fluid model and an isotropic (kinetic) model. In the fluid model, the bulk of electrons is assumed to have a Maxwellian distribution and the RE population is traced only in terms of its density. Primary RE generation is calculated from models of Dreicer and hot-tail generation. In the isotropic model, a pitch angle-averaged kinetic equation is solved. The name of this approach comes from the fact that in the reduced kinetic equation, the leading order term in the expansion of the distribution function is isotropic. Electrons are divided into 'cold', 'hot' and RE populations. The 'cold' and RE populations are calculated in almost the same way as in the fluid model. The only difference is that the initial temperature of the cold population is set very low – usually 1 eV – and its initial density is a few orders of magnitude smaller than the total plasma density. This way, almost all electrons are initially included in the 'hot' part of the population. The 'cold' population later heats up by receiving electrons from the 'hot' spectrum which cools down below the momentum threshold separating both populations. Electrons coming from the ionization of introduced gases and impurities also enter the 'cold' population. Electrons from the 'hot' part of the distribution are included on the momentum grid - where their normalized momentum is higher than the thermal momentum but still below the runaway threshold. This region is essential for directly simulating the generation rate of RE, which is determined by the flux of electrons passing through the upper boundary of the momentum grid. This approach replaces the hot-tail and Dreicer fluid models.

5.1.2 Thermal Quench (TQ) time definition

TQ refers to the first phase of a plasma disruption, during which the plasma temperature drops abruptly. This drop is associated with increased transport coefficients resulting from strong magnetic perturbations that disrupt the magnetic surfaces. In the simulation, TQ denotes the period when diffusion coefficients are increased, leading to a significantly faster temperature decrease compared to the current quench (CQ). Although, in DREAM simulations, the temperature drop is an effect of TQ rather than a cause, we use it to define the duration of TQ. Generally, disruptions can occur with an incomplete TQ, where the magnetic perturbation ceases before the temperature reaches a very low level [de Vries 2012]. Nevertheless, I concentrate on the pessimistic case characterized by a disruption with one strong TQ.

In the case of mitigation scenarios involving low-Z impurities, like neon or argon, the impurity cooling factor rapidly increases when the plasma temperature falls below 100 eV, due to recombination of nearly stripped impurity ions [Putterich 2019]. This can lead to a rise in radiated power by two orders of magnitude, resulting in very rapid cooling of the plasma below 100 eV. Therefore, the TQ time can be clearly defined as the duration needed to reach

temperatures in the range of a few tens of eV. In contrast, tungsten (W) ions exhibit strong radiation at temperatures up to a few keV due to their higher atomic number. As a result, there is no sharp increase in radiation when the plasma temperature drops below 100 eV, making it more challenging to define the TQ time. In this case, the temperature drop may stop without reaching the specified value, when the radiated power is balanced by ohmic heating.

5.1.3 Tokamak configuration

In order to investigate the impact of tokamak size on our results, simulations were performed for two tokamak configurations: ASDEX-like and ITER-like. The differences in simulation parameters are presented in Table 1.

Table 1. Tokamak geometry and plasma parameters of the ASDEX-like and ITER-like tokamak configurations

Parameter	**ASDEX-like [Hoppe 2021]**	**ITER-like [Pusztai 2022]**
Major radius R_m	1.65 m	6.0 m
Minor radius a	0.5 m	2.0 m
Wall radius b	0.55 m	2.833 m
Elongation at edge $\kappa(a)$	1.15	1.82*
Toroidal magnetic field B_0	2.5 T	5.3 T
Initial plasma current $I_{p,0}$	800 kA	15 MA
Resistive wall time	10 ms	500 ms

* Elongation in the ITER-like example is not homogeneous, but varies in the range 1.5 - 1.82 as the elongation is described with $\kappa = 1.5 + 0.02r^4$, where r is the plasma minor radius coordinate.

5.2 SIMULATION RESULTS

Simulations performed for the ITER-like configuration are moderately concerning. The initial study using the fluid model indicates that a significant generation of RE could occur if W impurity concentration raises to 10^{-3} or higher. This scenario is concerning, since such levels can sometimes be reached in tokamaks [Reinke 2019, Smirnov 2015, Chen 2020]. However, our analysis with the isotropic model suggests that tungsten concentrations of 1% or lower are unlikely to result in significant RE current generation on their own. As explained in section 5.1.1, the isotropic model is considered more reliable than the fluid one. To reach a tungsten concentration of 1%, a 3 mm droplet of tungsten would need to evaporate into the plasma core, which is quite unlikely. It is important to note that if there are additional sources of RE, tungsten may enhance the generation rate. When conditions for an avalanche become favorable, the transition to runaway current can occur rapidly, potentially leading to a catastrophic discharge with runaway currents of several MA. In such scenarios, the current quench (CQ) time could exceed the safety limits projected for ITER, posing a risk of mechanical damage to the vacuum vessel due to the electromagnetic forces from currents induced in the structure.

Assessing how tungsten impurities will affect the planned mitigation system for ITER is an important issue. Mitigation strategies involving the shattered pellets injection require a balance between suppressing RE and preserving ohmic current to prevent an overly rapid CQ [McDevitt 2023]. This balance creates an operational space for the mitigation system concerning the amounts of neon and deuterium that should be injected into the plasma. However, tungsten impurities could narrow or shift this operational space compared to a clean D-T plasma. Further studies are needed to address this issue, which is beyond the scope of this work. Additionally, the estimation of tungsten ablation and evaporation under burning plasma conditions may differ from those in current tokamaks. The high-energy particles present in such plasmas can penetrate the ablated material layer that typically shields the impurities, potentially increasing the evaporation rate. This could pose a significant risk to the integrity of the tokamak, if tungsten concentration reached such unprecedented levels.

The plasma disruption simulations with high tungsten concentration presented in this thesis should be considered as the initial step and highlight the necessity for further investigation in this area. Experimental validation is still missing, as tungsten-induced disruptions have not been intentionally triggered in existing tokamaks, leading to a scarcity of reliable data. Focused research on this topic is essential to assess to which extent mitigation systems of reactor-scale tokamaks can be impacted by the presence of tungsten impurities.

6 SUMMARY AND OUTLOOK

6.1 SUMMARY

In the presented thesis, I performed an interdisciplinary study that connects atomic physics with the field of plasma and nuclear fusion. Although the work was carried out as part of an international cooperation (CEA, Chalmers UT), the following crucial parts are my personal contribution:

1. I investigated different models to describe elastic electron-ion collisions in plasma using the partial screening concept and atomic form factor quantity. Out of them, I selected the most promising ones and extended them further, to obtain a new model which offers high accuracy at very low computational cost. This new approach can be used in Fokker-Planck solvers.
2. I proposed a modification to the LPA of MEE, which extended its usability to highly ionized impurities species. Then, I used it to calculate MEE of all ions and atoms with $Z \leq 86$. To benchmark the obtained values, I calculated MEE of multiple ions with other approximations and using the *ab initio* method implemented in the FAC code.
3. The developed models were implemented in the DREAM code. This allowed me to analyze the impact of tungsten impurities on runaway electron generation in numerical simulations of tokamak plasma disruption. I investigated two tokamak geometries: ITER-like and ASDEX-like. I analyzed the impact of various plasma parameters and simulation settings, to find the best approach for tungsten-rich plasma simulations.

6.2 CONCLUSIONS

The scientific questions raised in the introduction to this thesis can be finally answered in the following manner:

1. **How can we describe the atomic form factor of heavy ions with the most numerically efficient approach?**

The solution to this problem was achieved in this PhD dissertation by using the multi-Yukawa potential model, based on the Pratt-Tseng approach. Free parameters of the model were found by fitting it to the reference values obtained from *ab initio* DFT calculations.

2. **How to determine the mean excitation energy of high-Z ions?**

It was shown in the PhD thesis that MEE can be efficiently calculated using the modified LPA, where the $\ln(\gamma)$ constant was replaced by the function of Z and N in the form: $f(Z,N) = exp\left(\frac{Z-N}{Z}\right) - 0.84$. This approach enabled to evaluate the MEE for all ionization stages of all elements up to radon. Obtaining MEE for high-Z elements is particularly valuable for tokamak plasma physics.

3. **What is the impact of tungsten on suprathermal electrons in tokamak plasma?**

During plasma disruptions, concentrations of tungsten on a level of 1% or lower should not lead to a significant RE current generation on its own. Tungsten impurities tend to increase RE generation due to their strong radiation, which rapidly cools down the plasma. This leads to hot-tail generation, which is the dominant RE generation mechanism is such case. The effects of electron scattering and inelastic electron-ion collisions lead to the RE loss at a much slower rate, so they cannot prevent RE formation, they can however impact the RE plateau phase by faster RE termination.

6.3 PERSPECTIVES

The presented research paves the way for more detailed analysis of runaway electron mitigation and termination strategies, which can now include tungsten impurities in plasma. This is of outmost importance, due to the serious consequences of RE for tokamak operation and especially in light of the recently announced plans to use full tungsten walls for the ITER vacuum chamber [Loarte 2023].

Regarding massive gas injection systems, a specific balance of mass of injected gases is necessary to terminate the discharge without RE generation [Ekmark 2024]. It has been already investigated for the basic ITER discharge, but the impact of heavy impurities, which can accumulate in plasma and trigger the disruption mitigation system, remained unknown. With the tools developed in the course of this thesis, it is now possible to analyze the impact of tungsten and other impurities on the RE generation and its mitigation systems.

Another area of direct applicability and extension of the work presented in this thesis is RE termination systems using heavy impurities. Such systems were proposed already in different forms, mostly using solid tungsten as RE absorbing materials [Nardon 2021, Sergeev 2021, Lively 2024]. With these new developed tools, it will be possible to test termination scenarios in numerical simulations, since hands-on experiments would be expensive, dangerous for machine integrity or simply not possible for machines which are not yet in operation.

Apart from fusion research, the atomic data obtained in the framework of this thesis can be applicable in other areas of plasma research, like laser material ablation, electric discharges and plasma-based techniques in material science. Astrophysics is another discipline, where simulation of ionized matter is very important [Nénon 2018]. Especially in the case of processes in super-heavy objects, like nova stars, neutron stars or kilonovas [Sneppen2023].

7 BIBLIOGRAPHY AND APPENDIXES

7.1 REFERENCES:

[Adamek 2021] J. Adamek, D. Cipciar, A. Devitre, J. Horacek, J. Cavalier, M. Komm, J. Krbec, M. Tichy, D. Trunec and P. Böhm (2021) Nucl. Fusion **61** 036023 https://doi.org/10.1088/1741-4326/abd41d

[Aidas 2014] K. Aidas *et al* (2014) WIREs Comput. Mol. Sci. 4:269–284. https://doi.org/10.1002/wcms.1172

[Bethe 1930] H. A. Bethe, Ann. Phys. (Leipzig) 397 (1930), 325. https://doi.org/10.1002/andp.19303970303

[Bethe 1932] H. A. Bethe, Z. Phys. 76 (1932), 293. https://doi.org/10.1007/BF01342532

[Bucalossi 2022] J. Bucalossi *et al* (2022) Nucl. Fusion **62** 042007 http://dx.doi.org/10.1088/1741-4326/ac2525

[Campbell 2024] D.J. Campbell, A. Loarte, D. Boilson, X. Bonnin, P. de Vries, L. Giancarli, Y. Gribov, S.H. Kim, M. Lehnen, T. Luce, I. Nunes, A.R. Polevoi, S.D. Pinches, R.A. Pitts, R. Reichle, M. Schneider, J. van der Laan, G. Vayakis (2024) *ITER Research Plan within the Staged Approach (Level III — Final Version*, ITR-24-005 https://www.iter.org/technical-reports?id=26

[Chen 2016] F. F. Chen (2016) *Introduction to Plasma Physics and Controlled Fusion*, 3rd Edition, Springer Cham, https://doi.org/10.1007/978-3-319-22309-4

[Chen 2020] Y. Chen, D. Zhang, L. Zhang, L. Hu and EAST team (2020) *Nucl. Mater. Energy* **25** 100833, https://doi.org/10.1016/j.nme.2020.100833

[De Vries 2011] P.C. de Vries, M.F. Johnson, B. Alper, P. Buratti, T.C. Hender, H.R. Koslowski, V. Riccardo and JET-EFDA Contributors (2011) Nucl. Fusion **51** 053018, http://dx.doi.org/10.1088/0029-5515/51/5/053018

[De Vries 2012] P. C. de Vries, G. Arnoux, A. Huber, J. Flanagan, M. Lehnen, V. Riccardo, C. Reux, S. Jachmich, C. Lowry, G. Calabro, D. Frigione, M. Tsalas, N. Hartmann, S. Brezinsek, M. Clever, D. Douai, M. Groth, T. C. Hender, E. Hodille, E. Joffrin, U. Kruezi, G. F. Matthews, J. Morris, R. Neu, V. Philipps, G. Sergienko, M. Sertoli and JET EFDA contributors (2012) *Plasma Phys. Control. Fusion,* **54,** 124032 https://doi.org/10.1088/0741-3335/54/12/124032

[Dreicer 1959] H. Dreicer (1959) Phys. Rev. **115**, 238 https://doi.org/10.1103/PhysRev.115.238

[Dreicer 1960] H. Dreicer (1960) Phys. Rev. **117**, 329 https://doi.org/10.1103/PhysRev.117.329

[Ekmark 2024] I. Ekmark, M. Hoppe, T. Fülöp, P. Jansson, L. Antonsson, O. Vallhagen and I. Pusztai (2024) Journal of Plasma Physics **90**, 3 , 905900306 https://doi.org/10.1017/S0022377824000606

[Flanagan 2015] J. C. Flanagan, M. Sertoli, M. Bacharis, G. F. Matthews, P. C. de Vries, A. Widdowson, I. H. Coffey, G. Arnoux, B. Sieglin, S. Brezinsek, J. W. Coenen, S. Marsen, T. Craciunescu, A. Murari, D. Harting, A. Cackett, E. Hodille and JET-EFDA Contributors (2015) Plasma Phys. Control. Fusion **57** 014037 http://dx.doi.org/10.1088/0741-3335/57/1/014037

[Froese Fischer 2018] C. Froese Fischer, G. Gaigalas, P. Jönsson and J. Bieroń (2018) Comput. Phys. Commun **237** 184-187. https://doi.org/10.1016/j.cpc.2018.10.032

[Gao 2020] B. Gao, R. Ding, H. Xie, L. Zeng, L. Zhang, B. Wang, C. Li, D. Zhu, R. Yan, J. Chen (2020) Fusion Eng. Des. **156** 111616 https://doi.org/10.1016/j.fusengdes.2020.111616

[Gu 2008] M. F. Gu (2008) Can. J. Phys. **86** 675-689. https://doi.org/10.1139/p07-197

[Hesslow 2017] L. Hesslow, O. Embréus, A. Stahl, T. C. DuBois, G. Papp, S. L. Newton, and T. Fülöp, (2017), Phys. Rev. Lett. **118**, 255001. https://doi.org/10.1103/PhysRevLett.118.255001

[Hesslow 2018] L. Hesslow, O. Embréus, G. J. Wilkie, G. Papp and T. Fülöp (2018) Plasma Physics and Controlled Fusion **60**, 074010 https://doi.org/10.1017/S0022377818001113

[Hesslow 2019] L. Hesslow, O. Embréus, O. Vallhagen and T. Fülöp (2019) *Nucl. Fusion* **59** 084004 https://doi.org/10.1088/1741-4326/ab26c2

[Hoppe 2021] M. Hoppe, O. Embréus and T. Fülöp (2021) Comput. Phys. Commun. 268 108098. https://doi.org/10.1016/j.cpc.2021.108098

[Izzo 2024] V.A. Izzo, A. Battey, R.A. Tinguely, R. Sweeney and C. Hansen (2024) Nucl. Fusion **64** 066003 https://doi.org/10.1088/1741-4326/ad3c52

[Jachmich 2022] S. Jachmich, U. Kruezi, M. Lehnen, M. Baruzzo, L.R. Baylor, D. Carnevale, D. Craven, N.W. Eidietis, O. Ficker, T.E. Gebhart, S. Gerasimov, J.L. Herfindal, E. Hollmann, A. Huber, P. Lomas, J. Lovell, A. Manzanares, M. Maslov, J. Mlynar, G. Pautasso, C. Paz-Soldan, A. Peacock, L. Piron, V. Plyusnin, M. Reinke, C. Reux, F. Rimini, U. Sheikh, D. Shiraki, S. Silburn, R. Sweeney, J. Wilson, P. Carvalho and the JET Contributors (2022) *Nucl. Fusion* **62** 026012 https://doi.org/10.1088/1741-4326/ac3c86

[Krall 1973] N.A. Krall and A.W. Trivelpiece (1973) Principles of Plasma Physics. McGraw-Hill, New York

[Lehnen 2015] M. Lehnen, K. Aleynikova, P.B. Aleynikov, D.J. Campbell, P. Drewelow, N.W. Eidietis, Yu. Gasparyan, R.S. Granetz, Y. Gribov, N. Hartmann, E.M. Hollmann, V.A. Izzo, S. Jachmich, S.-H. Kim, M. Kočan, H.R. Koslowski, D. Kovalenko, U. Kruezi, A. Loarte, S. Maruyama, G.F. Matthews, P.B. Parks, G. Pautasso, R.A. Pitts, C. Reux, V. Riccardo, R. Roccella, J.A. Snipes, A.J. Thornton, P.C. de Vries, EFDA JET contributors (2015) Journal of Nuclear Materials, **463**, 39-48 https://doi.org/10.1016/j.jnucmat.2014.10.075

[Li 2014] S. Li, H. Jiang, Z. Ren, C. Xu (2014) *Abstract and Applied Analysis*, 1–8 https://doi.org/10.1155/2014/940965

[Lindhard 1953] J. Lindhard and M. Scharff (1953) Mat. Fys. Medd. - K. Dan. Vidensk. Selsk. **27** 15

[Lipschultz 2012] B. Lipschultz, J.W. Coenen, H.S. Barnard, N.T. Howard, M.L. Reinke, D.G. Whyte and G.M. Wright (2012) *Nucl. Fusion* **52** 123002 https://doi.org/10.1088/0029-5515/52/12/123002

[Lively 2024] M. A. Lively, D. Perez, B. P. Uberuaga, Y. Zhang and X-Z. Tang (2024) *Nucl. Fusion* **64** 056019 https://doi.org/10.1088/1741-4326/ad35d5

[Loarte 2023] A. Loarte (2023), *STAC committee reviews new plans for construction and operation*, ITER Organization, https://www.iter.org/newsline/-/3935

[Luce 2020] T. Luce, U. Kruezi, M. Lehnen, S. Jachmich, M. De Bock, G. Ellwood, A. Loarte, S. Maruyama, R.A. Pitts, V.S. Udintsev, S. Willms (2020) IAEA Fusion Energy Conference, Nice, TECH/1-4Ra. https://nucleus.iaea.org/sites/fusionportal/Shared%20Documents/FEC%202020/fec2020-preprints/preprint1344.pdf

[McDevitt 2023] C. J. McDevitt, X-Z. Tang, C. J. Fontes, P. Sharma and H-K. Chung (2023) *Nucl. Fusion* **63** 024001 https://doi.org/10.1088/1741-4326/acae38

[Merola 2010] M. Merola, D. Loesser, A. Martin, P. Chappuis, R. Mitteau, V. Komarov, R.A. Pitts, S. Gicquel, V. Barabash, L. Giancarli, J. Palmer, M. Nakahira, A. Loarte, D. Campbell, R. Eaton, A. Kukushkin, M. Sugihara, F. Zhang, C.S. Kim, R. Raffray, L. Ferrand, D. Yao, S. Sadakov, A. Furmanek, V. Rozov, T. Hirai, F. Escourbiac, T. Jokinen, B. Calcagno and S. Mori (2010) Fusion Engineering and Design **85**, 10–12, 2312-2322 https://doi.org/10.1016/j.fusengdes.2010.09.013

[Morales 2023] J. Morales, N. Fedorczak, C. Bourdelle, C. Markovitch, V. Ostuni, et al. *WEST tungsten contamination issues and proposed solutions in support to ITER* (2023) 65th Annual Meeting of the APS Plasma Division, Denver (Colorado), United States. https://cea.hal.science/cea-04565576

[Mott 1965] N. F. Mott and H. S. W. Massey, The Theory of Atomic Collisions, 3nd ed. Oxford: The Clarendon Press, 1965

[Nardon 2021] E. Nardon, A. Matsuyama, D. Hu and F. Wieschollek (2021) Nucl. Fusion **62** 026003 https://doi.org/10.1088/1741-4326/ac3ac6

[Nénon 2018] Q. Nénon, A. Sicard, P. Kollmann, H. B. Garrett, S. P. A. Sauer and C. Paranicas (2018). Journal of Geophysical Research: Space Physics, **123**, 3512–3532. https://doi.org/10.1029/2018JA025216

[Ostuni 2022] V. Ostuni, J. Morales, J.-F. Artaud, C. Bourdelle, P. Manas, N. Fedorczak, R. Dumont, M. Goniche, P. Maget, Y. Peysson and the WEST Team (2022) *Nucl. Fusion* **62** 106034 https://doi.org/10.1088/1741-4326/ac8cd6

[Pitts 2013] R. A. Pitts, S. Carpentier, F. Escourbiac, T. Hirai, V. Komaro, S. Lisgo, A.S. Kukushkin, A. Loarte, M. Merola, A. Sashala Naik, R. Mitteau, M. Sugihara, B. Bazylev, P.C. Stangeby (2013) J. Nucl. Mater. **438** S48-S56 http://dx.doi.org/10.1016/j.jnucmat.2013.01.008

[Pusztai 2022] I. Pusztai (2022) *Journal of Plasma Physics, **88***, 4, 905880409. https://doi.org/10.1017/S0022377822000733

[Putvinski 2010] S. Putvinski, L. Baylor, D. Campbell, V. Chuyanov, Yu. Gribov, V. Leonov, A. Loarte, S. Maruyama, R. Pearce, R. A. Pitts, A. Polevoi, R. Mitteau and M. Sugihara (2010) Proc. of the 23rd IAEA Fusion Energy Conference, Daejeon (Republic of Korea), ITR--1-6 IAEA

[Pütterich 2019] T. Pütterich *et al* (2019) *Nucl. Fusion* **59** 056013. https://doi.org/10.1088/1741-4326/ab0384

[Reinke 2019] M.L. Reinke, S. Scott, R. Granetz, J.W. Hughes, S.G. Baek, S. Shiraiwa, R.A. Tinguely, S. Wukitch and The Alcator C-Mod Team (2019) *Nucl. Fusion* **59** 066003 https://doi.org/10.1088/1741-4326/ab0eb2

[Reux 2020] C. Reux, E. Petit, A. Torre, S. Nicollet, F. Saint-Laurent, A. Le Luyer, P. Moreau and the WEST team (2020) 28th IAEA Fusion Energy Conference

[Rosenbluth 1997] M.N. Rosenbluth and S.V. Putvinski (1997) Nucl. Fusion **37** 1355 https://doi.org/10.1088/0029-5515/37/10/I03

[Roth 2009] J. Roth, E. Tsitrone, A. Loarte, Th. Loarer, G. Counsell, R. Neu, V. Philipps, S. Brezinsek, M. Lehnen, P. Coad, Ch. Grisolia, K. Schmid, K. Krieger, A. Kallenbach, B. Lipschultz, R. Doerner, R. Causey, V. Alimov, W. Shu, O. Ogorodnikova, A. Kirschner, G. Federici, A. Kukushkin, EFDA PWI Task Force, ITER PWI Team, Fusion for Energy, ITPA SOL/DIV (2009) *Journal of Nuclear Materials* **390–391**, 1-9 https://doi.org/10.1016/j.jnucmat.2009.01.037

[Savoye-Peysson 2023] Y. Savoye-Peysson, D. Mazon, J. Bielecki, D. Dworak, K. Król, A. Jardin, M. Scholz, J. Walkowiak and J. Decker (2023) Nuclear Fusion **63**, 126041, https://doi.org/10.1088/1741-4326/acffd9

[Sauer 2015] S. P. Sauer, J. Oddershede, and J. R. Sabin (2015) Advances in Quantum Chemistry Vol. **71** (Academic Press, New York), p. 29. https://doi.org/10.1016/bs.aiq.2015.02.001

[Sauer 2018] S.P. Sauer et al, J. R. Sabin and J. Oddershede (2018) J. Chem. Phys. **148** 174307. https://doi.org/10.1063/1.5027708

[Sauer 2020] S.P. Sauer et al, J. R. Sabin and J. Oddershede (2020) Molecular Physics **119**:5 https://doi.org/10.1080/00268976.2020.1823508

[Sergeev 2021] V.Y. Sergeev and B.V. Kuteev (2021) Nucl. Fusion **61** 086021, https://doi.org/10.1088/1741-4326/ac0bfc

[Shimada 2007] M. Shimada, D.J. Campbell, V. Mukhovatov, M. Fujiwara, N. Kirneva, K. Lackner, M. Nagami, V.D. Pustovitov, N. Uckan, J. Wesley, N. Asakura, A.E. Costley, A.J.H. Donné, E.J. Doyle, A. Fasoli, C. Gormezano, Y. Gribov, O. Gruber, T.C. Hender, W. Houlberg, S. Ide, Y. Kamada, A. Leonard, B. Lipschultz, A. Loarte, K. Miyamoto , V. Mukhovatov, T.H. Osborne, A. Polevoi and A.C.C. Sips (2007) *Nucl. Fusion* **47** S1 https://doi.org/10.1088/0029-5515/47/6/S01

[Smirnov 2015] R.D. Smirnov, S. I. Krasheninnikov, A. Yu. Pigarov and T. D. Rognlien (2015) Physics of Plasmas **22,** 012506 https://doi.org/10.1063/1.4905704

[Sneppen2023] A. Sneppen, D. Watson, A. Bauswein, O. Just, R. Kotak, E. Nakar, D. Poznanski and S. Sim (2023) *Nature* **614**, 436–439 https://doi.org/10.1038/s41586-022-05616-x

[Sokolov 1979] Y.A. Sokolov (1979) J. Expl Theor. Phys. **29** (4), 218–221

[Torre 2019] A. Torre, D. Ciazynski, S. Girard, B. Lacroix, S. Nicollet, C. Reux, M. Tena and West Team (2019) IEEE Transactions on Applied Superconductivity, **29**, 5, 4702805 https://doi.org/10.1109/TASC.2019.2911312

[Walkowiak 2022] J. Walkowiak, A. Jardin, J. Bielecki, Y. Peysson, D. Mazon, D. Dworak, K. Król and M. Scholz (2022) Physics of Plasmas **29**, 022501, https://doi.org/10.1063/5.0075859

[Walkowiak 2024a] J. Walkowiak, M. Hoppe, I. Ekmark, A. Jardin, J. Bielecki, K. Król, Y. Savoye-Peysson, D. Mazon, D. Dworak and M. Scholz (2024) Nuclear Fusion **64**, 036024 https://doi.org/10.1088/1741-4326/ad24a0

[Walkowiak 2024b] J. Walkowiak, J. Bielecki, J. Bieroń, A. Jardin, Y. Savoye-Peysson, D. Mazon, K. Król, D. Dworak, M. Scholz (2024) Atomic Data and Nuclear Data Tables, in press https://doi.org/10.1016/j.adt.2024.101696

[Wesson 2011] J. Wesson (2011) *Tokamaks*, 4th Edition, Oxford Science Publications, International Series of Monographs on Physics, Volume 149, ISBN: 9780199592234

[Xie 2017] H. Xie, R. Ding, A. Kirschner, J. L. Chen, F. Ding, H. M. Mao, W. Feng, D. Borodin and L. Wang (2017) Phys. Plasmas **24**, 092512 https://doi.org/10.1063/1.4991457

[Zhang 2023] Y. P. Zhang, R. H. Tong, Z. Y. Yang, Z. Y. Chen, D. Hu, Y. B. Dong, J. Zhang, Y. X. Zhu, H. B. Xu and W. L. Zhong (2023) Rev. Mod. Plasma Phys. **7**, 12 https://doi.org/10.1007/s41614-022-00110-3

[Zylstra 2022] A. B. Zylstra et al. (2022) Phys. Rev. E **106**, 025202 https://doi.org/10.1103/PhysRevE.106.025202

7.2 Articles

The list of all articles of my authorship or co-authorship (including both thematically connected articles which constitute this thesis and other articles):

1. J. Walkowiak, A. Jardin, J. Bielecki, Y. Peysson, D. Mazon, D. Dworak, K. Krol and M. Scholz. *Approximate atomic models for fast computation of the Fokker-Planck equation in fusion plasmas with high-Z impurities and suprathermal electrons.*
   Physics of Plasmas **29** (2022) 022501
   https://doi.org/10.1063/5.0075859

2. J. Walkowiak, J. Bielecki, J. Bieroń, A. Jardin, Y. Savoye-Peysson, D. Mazon, K. Król, D. Dworak, M. Scholz. *Mean Excitation Energies of all ionization stages of all atoms with $1 \leq Z \leq 86$.*
   Atomic Data and Nuclear Data Tables (2024) in press
   https://doi.org/10.1016/j.adt.2024.101696

3. J. Walkowiak, M. Hoppe, I. Ekmark, A. Jardin, J. Bielecki, K. Król, Y. Savoye-Peysson, D. Mazon, D. Dworak and M. Scholz. *First numerical analysis of runaway electron generation in tungsten-rich plasmas towards ITER.*
   Nuclear Fusion **64** (2024) 036024
   https://doi.org/10.1088/1741-4326/ad24a0

4. Y. Savoye-Peysson, D. Mazon, J. Bielecki, D. Dworak, K. Król, A. Jardin, M. Scholz, J. Walkowiak and J. Decker. *A unified description of atomic physics for electron Fokker–Planck calculations.*
   Nuclear Fusion **63** (2023) 126041
   https://doi.org/10.1088/1741-4326/acffd9

5. A. Jardin, J. Bielecki, W. Dąbrowski, K. Drozdowicz, D. Dworak, V. Gerenton, D. Guibert, R. Kantor, K. Król, A. Kulińska, A. Kurowski, B. Łach, D. Mazon, Y. Savoye-Peysson, M. Scholz, J. Walkowiak, U. Wiącek, U. Woźnicka and WEST team. *Energy-resolved x-ray and neutron diagnostics in tokamaks: Prospect for plasma parameters determination*.
   Physics of Plasmas **31** (2024) 082514
   https://doi.org/10.1063/5.0213721

6. A Jardin, D Mazon, J Bielecki, D Dworak, D Guibert, K Król, Y Savoye-Peysson, M Scholz, J Walkowiak and the WEST Team. *Validating and speeding up x-ray tomographic inversions in tokamak plasmas.*
Plasma Physics and Controlled Fusion **66** (2024) 085010
https://doi.org/10.1088/1361-6587/ad5b85

7. J. Bielecki, D. Dworak, A. Jardin, K. Król, D. Mazon,Y. Savoye-Peysson, M. Scholz, J. Walkowiak, (in press) *Atomic models for description of high-Z impurities dynamics in tokamak plasmas – summary of HARMONIA project*. EPJ Web of Conferences

Physics of Plasmas

Approximate atomic models for fast computation of the Fokker–Planck equation in fusion plasmas with high-Z impurities and suprathermal electrons

Cite as: Phys. Plasmas **29**, 022501 (2022); https://doi.org/10.1063/5.0075859
Submitted: 19 October 2021 • Accepted: 08 January 2022 • Published Online: 01 February 2022

J. Walkowiak, A. Jardin, J. Bielecki, et al.

Physics of Plasmas ARTICLE scitation.org/journal/php

Approximate atomic models for fast computation of the Fokker–Planck equation in fusion plasmas with high-Z impurities and suprathermal electrons

Cite as: Phys. Plasmas **29**, 022501 (2022); doi: 10.1063/5.0075859
Submitted: 19 October 2021 · Accepted: 8 January 2022 ·
Published Online: 1 February 2022

J. Walkowiak,[1,a)] A. Jardin,[1] J. Bielecki,[1] Y. Peysson,[2] D. Mazon,[2] D. Dworak,[1] K. Król,[1] and M. Scholz[1]

AFFILIATIONS

[1]Institute of Nuclear Physics Polish Academy of Sciences, PL-31342 Krakow, Poland
[2]CEA, IRFM, F-13108 Saint-Paul-lez-Durance, France

[a)]Author to whom correspondence should be addressed: jedrzej.walkowiak@ifj.edu.pl

ABSTRACT

With the choice of tungsten as a material for the ITER plasma facing components, the suprathermal electron interaction with non-fully ionized impurities emerged as an important issue in plasma modeling. Microwave heating and current drive systems, especially lower hybrid current drive, can generate a significant population of suprathermal electrons in the plasma. Also, in the case of the runaway electron generation and mitigation by massive gas injection, the collisions with impurities can have a significant impact on the electron drag force. A correct description of the fast electrons collisions with non-fully ionized impurities requires calculation of the atomic form factor. This can be done with *ab initio* models that are accurate, though time consuming in practical applications. In this paper, we compare existing approximations of the form factors, based on the Thomas–Fermi or Pratt–Tseng models. *Ab initio* density functional theory (DFT) calculations are used as a reference method to determine the accuracy of the compared models. Based on this analysis, we propose some modifications of the existing models, tuned with numerical parameter optimization, which provide a higher accuracy while maintaining a short computation time. These modifications include multiple exponents in the Pratt–Tseng model and fitting the parameters of the form factor equation to the DFT-based results. Some applications of the presented models to the calculation of the elastic and inelastic collision frequencies for Fokker–Planck equation are presented, showing a good agreement between the results obtained with the DFT method and the proposed models.

I. INTRODUCTION

The progress in theoretical and experimental development of fusion devices brings constant changes in their design, where the combination of different improvements can raise new issues that were previously neglected. An example is the transition of the material of plasma facing components from carbon to tungsten (Pitts *et al.*, 2013). Tungsten is a high-Z element that is not fully ionized in the plasma temperature range of fusion devices. The presence of such impurities, due to their high electric charge, may have a significant impact on the electron dynamics (Hesslow *et al.*, 2017). Their proper description is crucial for the design of current drive systems or for the mitigation of the runaway electrons by massive gas injection in post-disruptive plasmas (Reux *et al.*, 2015). If the plasma contains a large fraction of fast electrons, such as runaway electrons or suprathermal electrons created by Lower Hybrid Current Drive (LHCD), it might be necessary to include effects of partial screening in collision description, in order to obtain accurate results (Hesslow *et al.*, 2018).

The numerical tools created to model the fast electrons dynamics in modern tokamaks (Peysson *et al.*, 2016; Pokol *et al.*, 2019; Król, 2020) should incorporate the corrections necessary to include partial screening to be able to predict plasma behavior, while keeping the additional computational effort at a reasonable level.

The aim of this study is to compare different models which can be used to evaluate the influence of partial screening on electron collisions. An *ab initio* model, based on quantum mechanics, is used as a reference in terms of accuracy when comparing different classical and empirical approximated models. This reference model, despite being accurate, is not preferred in practice for numerical implementation to solve the Fokker–Plank equation, because of the associated computation cost. Since the calculations can require multiple integrations of

the values acquired from the atomic model (integrations over a few parameters, where some of them vary depending on plasma conditions), it is strongly preferable to use a model which can provide an analytic solution of these integrals. Thus, such approximated models can grant a great improvement in computation speed at the cost of a loss of accuracy of the solution. The goal is to find the optimal trade-off between accuracy and computation time and to provide the best solution for future numerical tools designed for the nuclear fusion community.

II. FOKKER–PLANCK EQUATION

When calculating the velocity distribution function with the Fokker–Planck equation, the impact of collisions between a and b species on the distribution f_a is described by the collision operator C^{ab}. In the special case of the two species, a and b, where the distribution of b is Maxwellian, the collision operator takes the following form (Hesslow *et al.*, 2017):

$$C^{ab} = \nu_D^{ab}\mathcal{L}(f_a) + \frac{1}{p^2}\frac{\partial}{\partial p}\left[p^3\left(\nu_s^{ab} f_a + \frac{1}{2}\nu_\parallel^{ab} p \frac{\partial f_a}{\partial p}\right)\right], \quad (1)$$

C^{ab}—collision operator for collisions between particle species a and b, $\mathcal{L}(f_a)$—Lorentz scattering operator, ν_D^{ab}—deflection frequency, ν_s^{ab}—slowing-down frequency, $\nu_\parallel^{ab}$—parallel-diffusion frequency, p— normalized momentum, and f_a—velocity distribution function of species a.

This description can be applied to many cases of tokamak plasmas, where the ion velocity distribution can be assumed as Maxwellian and the electron distribution is analyzed in detail.

If fast electrons with energies in the range of tens of keV and higher are the object of interest, it is necessary to include the effects of the so-called partial screening in the description of the collisions of these electrons with non-fully ionized atoms. Fast electrons are not simply deflected by the Coulomb interaction with the net charge of the ion, but probe its internal electron structure, such that the nuclear charge is not completely screened. This effect modifies the deflection and slowing-down frequencies in the Eq. (1) and must be taken into account for a more accurate description (Hesslow *et al.*, 2018).

A description, within the Born approximation, of the electron-ion elastic collisions can be obtained by including the atomic form factor for the given ion into the differential collision cross section. Assuming that the ions are infinitely heavy stationary targets initially at rest, the cross section can be expressed as follows (Mott and Massey, 1965):

$$\frac{d\sigma_e^{coll}}{d\Omega} = \frac{{r_0}^2}{4\boldsymbol{p}^4}\left(\frac{\cos^2(\theta/2)\boldsymbol{p}^2 + 1}{\sin^4(\theta/2)}\right)\left[Z - F(\boldsymbol{q})\right]^2, \quad (2)$$

where r_0—the classical electron radius, θ—deflection angle, $\boldsymbol{p} = \gamma\boldsymbol{v}/c$—normalized electron momentum, $\boldsymbol{v}$—impacting electron velocity, c—the speed of light in vacuum, γ—Lorentz factor, and Z—atomic number.

$F(\boldsymbol{q})$ denotes the atomic form factor, corresponding to the Fourier transform of the electron density distribution $\rho(\boldsymbol{r})$ in the momentum space, with $0 \le F(\boldsymbol{q}) \le N$. The lower limit $F(\boldsymbol{q}) = 0$ corresponds to the case of no screening, when the interaction between a free electron and the atomic nucleus is not influenced by bound electrons. The upper limit $F(\boldsymbol{q}) = N$, on the other hand, represents complete screening, when the nucleus is screened by all bound electrons. The $F(\boldsymbol{q})$ is expressed as

$$F(\boldsymbol{q}) = \int \rho(\boldsymbol{r}) e^{-i\mathbf{q}\mathbf{r}/a_0}\, d^3r, \quad (3)$$

where: $\boldsymbol{q} = 2\boldsymbol{p}\sin(\theta/2)/\alpha$ is the momentum transfer, $\alpha \approx 1/137$—the fine structure constant, $\boldsymbol{r}$—atomic radius as a spatial coordinate measured from the center of the atom, a_0—in the Bohr radius, and N—the number of bound electrons.

The electron density is normalized such that the number of bound electrons is

$$N = \int \rho(\boldsymbol{r})\, d^3r. \quad (4)$$

Electron densities used in this work are always spherically averaged, so only the radial coordinate r is used in model descriptions, instead of a full 3D representation in $\boldsymbol{r}$. As for $\boldsymbol{q}$ and $\boldsymbol{p}$, only the magnitudes are the values of interest. Hereafter they will be denoted as q and p, respectively, to simplify the notation. In addition, all quantities used in calculations are expressed in atomic units by default unless otherwise noted. In the case of the spherically symmetric electron density (r), the atomic form factor defined by Eq. (3) can be expressed as

$$F(q) = 4\pi\int_0^\infty \rho(r)\frac{ra_0}{q}\sin(qr/a_0)dr, \quad (5)$$

where: $q = |\boldsymbol{q}|$ and $r = |\boldsymbol{r}|$.

III. ELECTRON DENSITY CALCULATION

The atomic form factor is related to the electron density of bound electrons $\rho(r)$ around the atom nucleus. Therefore, the calculation of the atomic form factor strongly depends on the model used to describe the electron density distribution $\rho(r)$ in the atom. The most accurate description requires full quantum relativistic calculations, including the electron exchange and correlation effects. Such calculations are computationally demanding and the obtained solution accuracy is greater than required for applications like solving the Fokker–Planck equation (Peysson *et al.*, 2021; Król *et al.*, 2021). However, there are some semi-classical models, which can provide approximated solutions with far less computational effort. They can provide a significant acceleration of the numerical codes used for solving the Fokker–Planck equation without losing the demanded accuracy.

In the present work, in order to better understand and describe the effects of the used atomic model on the calculation of the atomic form factor, such simple models are compared against ab-inito calculations. In the subsequent part of the article, the Density Functional Theory (DFT) is used as the reference model. Simpler models are based on two approaches and their modifications, namely, Thomas–Fermi (TF) and Pratt–Tseng (PT).

A. Density functional theory

DFT is a method to investigate the electronic structure of matter in a wide range of scales (from atoms to solids and large organic molecules). Its basic principle is that the ground state energy of the system is a unique functional of the electron density $\rho(r)$. DFT is based on two theorems by Hohenberg and Kohn (1964). With Kohn–Sham (KS) equations (Kohn and Sham, 1965), it is possible to calculate

fictitious orbitals of a non-interacting system, which generates the same electron density as the interacting system. Thus DFT is an *ab initio* quantum mechanical model providing results as close to reality as possible and is used here as a reference for models comparison.

In the present work, calculations using DFT were performed with the Gaussian software package (Frisch *et al.*, 2019). The hybrid exchange-correlation functional PBE1PBE (known also as PBE0) (Perdew *et al.*, 1996; Adamo and Barone, 1999), along with the natural orbital-relativistic correlation consistent basic set ANO-RCC, was used. The results from Gaussian were then post-processed in the Multiwfn program (Lu and Chen, 2011), which was used to obtain the spherically averaged electron density $\rho(r)$. An example of the resulting electron density for tungsten ions is presented in Fig. 1. The shell structure of the atom can be clearly seen in the results for different ionization stages.

B. Thomas–Fermi model

The TF model is a well-known semi-empirical approximation for many electron systems in the external potential $V(r)$. It cannot reproduce quantum effects such as the shell structure, but is relatively simple and uses the electron density $\rho(r)$ as a primary quantity—in this way it was a precursor to DFT. In general, the TF model treats bound electrons as an electron gas. This gas, despite being inhomogeneous in atoms or molecules, can be treated locally with relations developed for the homogeneous electron gas. Such approach makes it possible to eliminate the necessity to calculate electron wave functions and allows calculating the electron density directly. The major drawback of this approach is that the used approximations do not hold in the vicinity of the nucleus, at which the electron density becomes singular.

According to the TF model, the electron density $\rho(r)$ can be calculated as (Lundqvist and March, 1983)

$$\rho_{TF}(r < r_{\max}) = \frac{32Z^2}{9\pi^3}\left(\frac{\varphi(x)}{x}\right)^{3/2}, \tag{6}$$

where

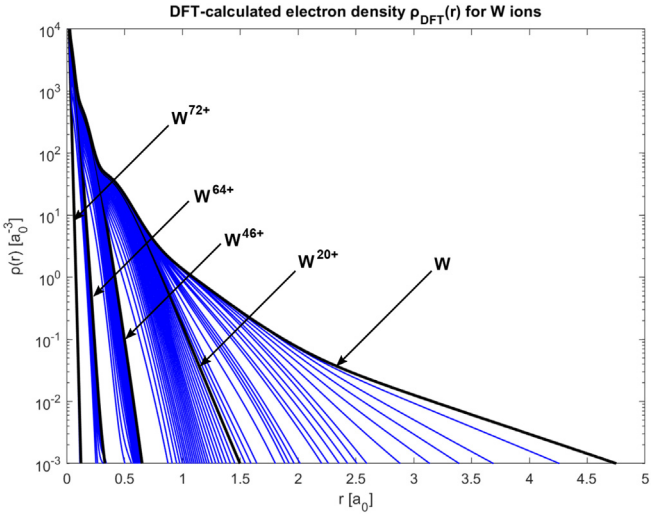

FIG. 1. Spherically averaged electron density $\rho(r)$ calculated with DFT for tungsten ions. Each line represents the electron density of one tungsten ionization stage.

$$x = r/b \quad \text{and} \quad b = \frac{1}{4}\left(\frac{9\pi^2}{2Z}\right)^{\frac{1}{3}} a_0. \tag{7}$$

The electron density vanishes outside of the ion radius $\rho_{TF}(r > r_{\max}) = 0$.

The value of $\varphi(x)$ can be obtained from the Thomas–Fermi equation

$$\frac{d^2\varphi(x)}{d^2x} = \frac{\varphi(x)^{\frac{3}{2}}}{x^{\frac{1}{2}}}, \tag{8}$$

with the following boundary conditions:

$$\varphi(0) = 1, \quad \varphi(x_{\max}) = 0,$$
$$\begin{cases} x_{\max} = \infty & \text{for neutral atom,} \\ -\varphi'(x_{\max})x_{\max} = \dfrac{Z-N}{Z} & \text{for positive ion.} \end{cases} \tag{9}$$

In practice, a solution of the Thomas–Fermi equation was found with an iterative approach, because $x_{\max}$ is not known for ions. The bisection method was used to find the $x_{\max}$ value which satisfied the boundary condition: $\frac{Z-N}{Z} + \varphi'(x_{\max})x_{\max} = 0$ within 0.000 05 margin. The search was made for $x_{\max}$ between 0.001 and 150. This method is very simple and robust, the only drawback was the computational efficiency. However, in this case it was not a major issue since values of the electron density were calculated only once. Moreover, this case is simple enough to be solved on the order of seconds. The boundary condition for neutral atoms must be changed and instead of $\varphi(\infty) = 0$, φ must vanish for some finite value of x, i.e., $\varphi(x_{\max}) = 0$. In this work, calculation with $x_{\max} = 400$ was performed. Influence of the chosen $x_{\max}$ on the solution of the Thomas-Fermi equation was analyzed in other works, e.g., Jardin *et al.* (2020) and based on them, the selected value is considered as a sufficient approximation. An example of the resulting electron density calculated in the framework of the TF model is presented in Fig. 2. One of the most visible differences between DFT and the TF model is the lack of a shell structure in the TF model.

C. Thomas–Fermi–Dirac model

Over time, many modifications to the TF model were developed to improve its accuracy, by including additional electron interactions and relativistic effects. One of the most basic improvements is the Dirac correction, which introduces a term for exchange energy of electrons.

According to the Dirac modification, the modified Thomas–Fermi–Dirac (TFD) equation takes the following form (Csavinszky, 1969):

$$\frac{d^2\varphi}{d^2x} = x\left[\left(\frac{\varphi}{x}\right)^{\frac{1}{2}} + \beta\right]^3, \quad \beta = \left(\frac{3}{32}\pi^2 Z^2\right)^{1/3}, \tag{10}$$

with the following boundary conditions:

$$\varphi(0) = 1, \quad \varphi(x_{\max}) = \frac{1}{16}\beta^2 x_{\max},$$
$$-\varphi'(x_{\max})x_{\max} = \frac{Z-N}{Z} - \varphi(x_{\max}). \tag{11}$$

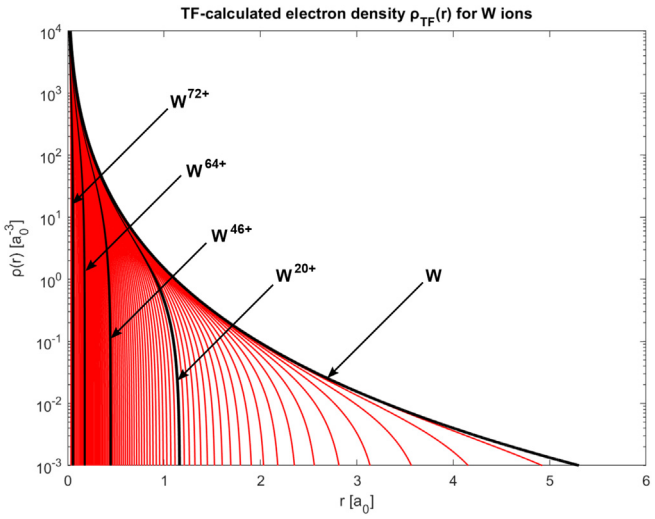

FIG. 2. Spherically averaged electron density $\rho(r)$ calculated with the Thomas–Fermi model for tungsten ions. Each line represents the electron density of one tungsten ionization stage.

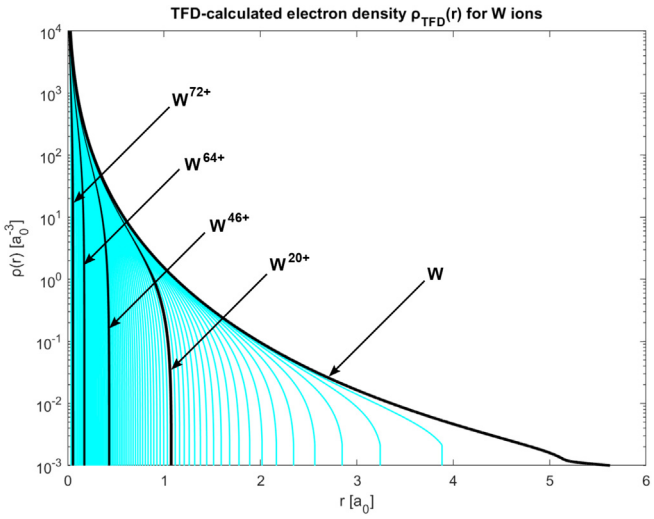

FIG. 3. Spherically averaged electron density $\rho(r)$ calculated with the Thomas–Fermi–Dirac model for tungsten ions. Each line represents the electron density of one tungsten ionization stage.

with the appropriate modification, the final expression of the electron density $\rho(r)$, within the TFD model, takes the following form (Abrahamson, 1961):

$$\rho_{TFD}(r) = \frac{Z}{4\pi b^3}[\varphi(x) + \beta]^3, \tag{12}$$

where $b = r/x$—factor defined in the TF model.

A solution of the TFD equation is found with an iterative approach, in a similar way as in the previous case of the TF equation. The difference is that, due to the change in the boundary conditions, the TFD model no longer requires a solution at $x_{\max} = \infty$ in the case of the neutral atom; thus no approximation for the $x_{\max}$ is needed. An example of the resulting electron density is presented in Fig. 3. The TFD model is very similar to the TF model, but in the TFD the electron density is discontinuous at the ion radius.

D. Pratt–Tseng model

The PT model is an alternative method of deriving an approximated analytical expression for the atomic form factor. It is based on the Yukawa potential, approximating the electrostatic potential around the ion nucleus as the sum of the classical Coulomb term and an exponential term accounting for the screening of bound electrons at short distances from the nucleus. The electron density calculated in this way is a rough approximation of the electron density calculated with DFT, nevertheless its analytical expression allows straightforward calculation of the atomic form factor. The electron density $\rho(r)$ is expressed within the PT model as

$$\rho_{PT}(r) = \frac{N}{4\pi r a^2}\exp\left(-\frac{r}{a}\right). \tag{13}$$

Four versions of this model are investigated with different approaches for calculating the a parameter,

$$a = 1\Big/\sqrt{\lambda^2\frac{(1-x^{n_s+1})}{(1-x)^k}}, \tag{14}$$

where $x = \frac{Z-N}{Z}$.

Other parameters are defined differently in every version of this model, as presented in Table I. The PT_1 model is the modified version of PT_2, where the parameter k was modified to better fit DFT results. PT_2 is the original model proposed by Botto, for which coefficients are based on the fit to the Hermann–Skillman potential. PT_3 is based on the transfer of the analytic results from the Kirillov approximation (Kirillov *et al.*, 1975) of the TF model into the framework of the PT model. The PT4 model was created for the purpose of bremsstrahlung calculation and features modified parameters to better fit the interior of the atom.

The PT models provide closed sets of equations with no need for any iterative process in order to calculate the electron density. In addition, they allow creating an analytical solution for the atomic form factor, as it will be shown later. Thanks to that, it is definitely the most appealing model when considering computation time optimization, granting a few orders of magnitude faster computation than other models. Its computational simplicity takes a price of less accurate results, but still on a satisfactory level. An example of the resulting electron density calculated using PT model 1 (Botto I) is presented in Fig. 4. A significant difference can be seen in comparison not only to DFT results, but also TF and TFD.

The differences between the previously defined electron density models for the tungsten ion W^{10+} are depicted in Fig. 5. It shows that, close to the nucleus, the electron density calculated based on both PT and TF models is in a quite good agreement with the results obtained using DFT. However, when considering values of the electron density in the region further from the nucleus, PT models give rather poor approximation of the DFT results. The results from DFT show the effect of the shell structure of the atom by steep changes of the electron density. Unfortunately, none of the considered simplified models can

TABLE I. PT model variations and their parameters.

Name	Botto I	Botto II	Kirillov TF	Avdonina and Lamoureux
Symbol	PT_1	PT_2	PT_3	PT_4
Reference	Peysson *et al.* (2021)	Botto *et al.* (1978)	Peysson *et al.* (2021)	Lamoureux and Avdonina (1997)
k	2	1	7/3	1
n_s	$Z(1/3-0.002\,Z)$	$Z(1/3–0.002\,Z)$	0	$Z(1/3–0.002\,Z)$
λ	$\lambda = 0.9\,Z^{0.42}$	$\lambda = 0.9\,Z^{0.42}$	$\lambda = 3/4\,Z^{1/3}$	$\lambda = 0.8932\,Z^{0.5}$

reproduce this effect, which is related to the underlying classical assumptions.

IV. ATOMIC FORM FACTOR CALCULATION

For the most accurate electron density distribution obtained from DFT, there is no analytical solution of the form factor. Therefore, the form factor is numerically integrated, which is a time-consuming operation. In this work, the form factor was calculated for 60 001 values of q for each ion, which guaranteed negligible numerical errors. For practical reasons, it would be possible to use a much coarser grid of q with just a few thousand of points, but for this analysis it was important to avoid any influence of numerical error. Even with the detailed representation of the form factor, the most computationally expensive part was the calculation of DFT electron density, which for tungsten ions can take up to a few minutes on 20 CPUs node of a HPC cluster. Integrations, to obtain form factors and later deflection frequency, were made on the order of seconds. For some models, it is possible to derive an analytical solution of the above integral or at least its approximation, granting a significant improvement in computation time. The solution can be later used to create analytical solutions of other integrals needed to calculate collision frequencies. Thank to this, the final result for elastic collisions for a given ion can be obtained on the order of thousandths of a second on a single CPU.

A. Kirillov approximation of the Thomas–Fermi model

The TF model does not have an analytical solution, so to calculate the form factor based on this model, it is necessary to use a similar procedure as in the case of DFT. It means that there is no significant benefit from using this model for calculation of the form factor. It is however possible to obtain an approximated solution of the form factor calculated with the TF model, by using some approximations during the integration, as described by Kirillov *et al.* (1975). This allows to calculate the form factor using the following equation:

$$F_{TFK}(q) = \frac{N}{1 + \left(q\frac{3}{4}N^{\frac{2}{3}}/Z\right)^{3/2}}. \tag{15}$$

Unfortunately, using this approximation provides results which are not so close to DFT calculation as when using the exact TF solution with numerical integration presented in Sec. IV. A comparison of the form factors calculated based on the Kirillov approximation with those calculated by numerical integration of the electron density

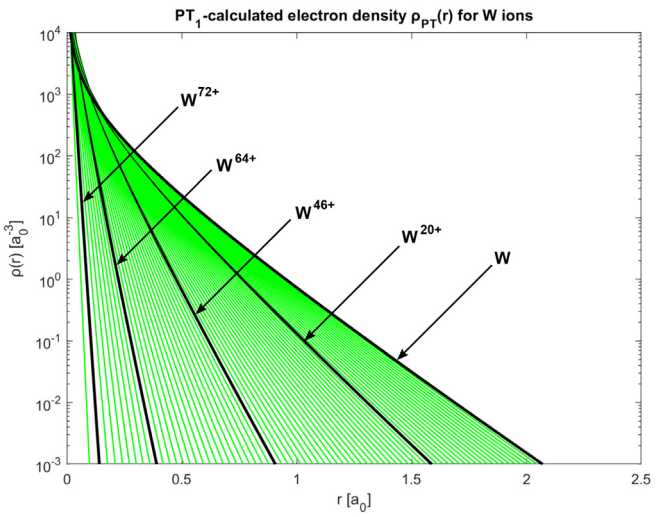

FIG. 4. Spherically averaged electron density $\rho(r)$ calculated with the Pratt–Tseng model in the first presented variant (Botto I) for tungsten ions. Each line represents the electron density of one tungsten ionization stage.

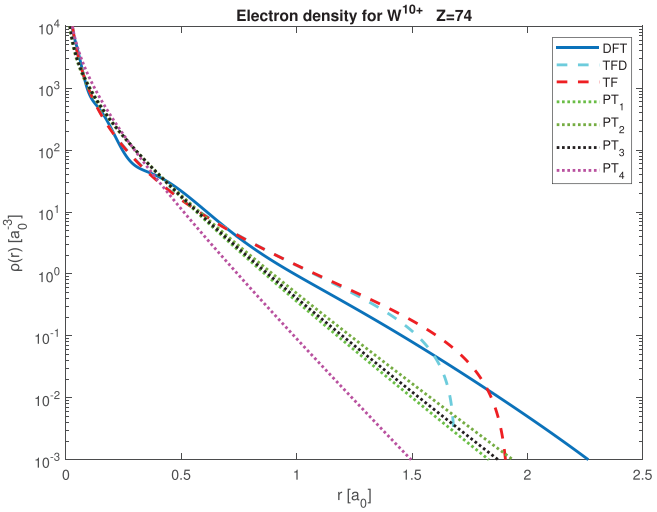

FIG. 5. Spherically averaged electron density $\rho(r)$ calculated for tungsten ion W^{10+} with different models: DFT—Density Functional Theory, TFD—Thomas–Fermi–Dirac, TF—Thomas–Fermi, *and* PT—Pratt–Tseng models with numbers corresponding to different variants in the same order as presented before: (1) Botto I, (2) Botto II, (3) Kirillov, and (4) Avdonina and Lamoureux.

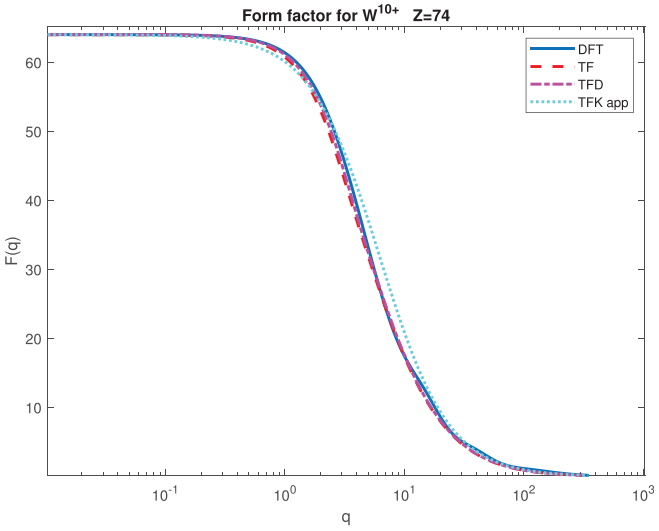

FIG. 6. Atomic form factor $F(q)$ for tungsten ion W^{10+}, as a function of the momentum transfer q, calculated with different models: DFT—Density Functional Theory, TFD—Thomas–Fermi–Dirac, TF—Thomas–Fermi, *and* TFK app—Kirillov approximation of the Thomas–Fermi model. Results from TF and TFD models are calculated with the same integration procedure as in the case of the DFT model.

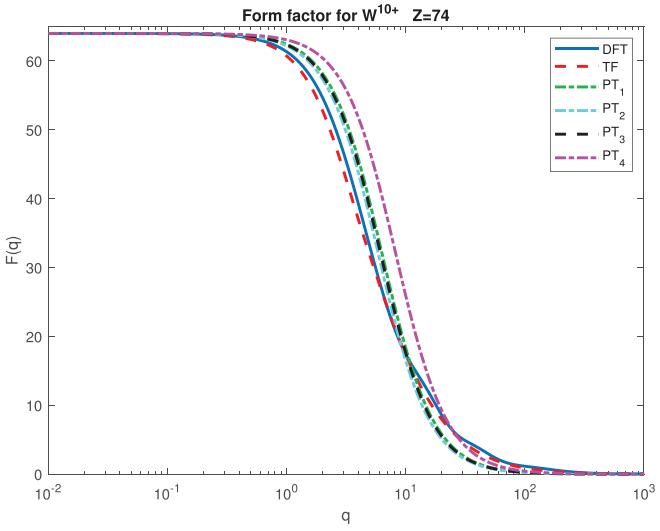

FIG. 7. Atomic form factor $F(q)$ for tungsten ion W^{10+}, as a function of the momentum transfer q, calculated using different models: DFT—Density Functional Theory, TF—Thomas–Fermi, and PT— Pratt–Tseng models with numbers corresponding to different variants in the same order as presented before: (1) Botto I, (2) Botto II, (3) Kirillov, and (4) Avdonina and Lamoureux.

obtained within TF, TFD, and DFT models is presented in Fig. 6. The results show that a simple classical model can give reasonable approximation of the atomic form factors. The TFK approximation is less accurate than the exact TF model, but it is much faster to compute.

B. Pratt–Tseng model

In the case of the PT models, it is possible to give an analytical expression for the form factor, using the electron density in the form defined by Eq. (5),

$$F_{PT}(q) = \frac{N}{1 + (qa)^2}, \tag{16}$$

where a is an individual parameter for every ion as defined in Table I. Its value is common for both the electron density calculation and the form factor calculation. Unfortunately, again the solution obtained with this analytical expression is not close to the form factor obtained with numerical integration of the TF or DFT (but it gives results with similar accuracy to Kirillov approximation). The results of the form factor calculations based on four PT models compared to the form factors calculated within numerical integration scheme of the TF and DFT-calculated electron densities are presented in Fig. 7.

C. Figure of merit

For the presented calculations, the estimates of the atomic form factors $F(q)$ were stored in the computer memory as a table of numerical values with q logarithmically distributed in the range between 10^{-6} and 10^{+6} with 60 001 samples. To create a figure of merit allowing a quantitative comparison of different approaches to the atomic form factor calculations, the root mean square (RMS) of the difference between the normalized form factors calculated within the DFT formalism (reference) and the TF/TP models was calculated for every ion. The difference between form factors was normalized between 0 and 1 by dividing $F(q)$ by the number of electrons bound to the nuclei. This approach allowed to obtain a similar range of values for every ion, while still using all advantages of the RMS error calculation. Sensitivity to outliers is an advantage in this case, because it promotes solutions which have similar accuracy for all values. The equation for the RMS defined above takes the following form:

$$RMS = \frac{1}{N}\sqrt{\frac{1}{n}\sum_{i=1}^{n}\left(F_{DFT}(q_i) - F_2(q_i)\right)^2}, \tag{17}$$

where: n—number of records used for storing the form factor in computer memory, F_{DFT}—value of the first form factor used as a reference for a given q_i value from ith record, F_2—value of the second form factor used in comparison, and N—number of bound electrons in the considered ion.

The calculated values of the RMS mentioned above are presented in Figs. 8 and 9 for tungsten and argon ions, respectively. Tungsten was chosen because of its use as a material for plasma facing components (Brezinsek *et al.*, 2019), and the argon ions are presented due to their importance in experiments for mitigation of runaway electrons (Reux *et al.*, 2015). In the case of tungsten, the results obtained by integration of the electron density obtained from TF models are the closest to the DFT results for most ions. This proves that the classical model can approximate quite well the quantum-mechanical model, but gives no further benefits, as calculating procedure is of the similar level of complexity. The Kirillov approximation of the TF model provides less accurate results than the exact TF solution, comparable to the PT models. From the models which have analytical solutions of the form factor, the first version of the PT models (Botto I) seems to be the best choice for the ionization stages which can be expected in the tokamak

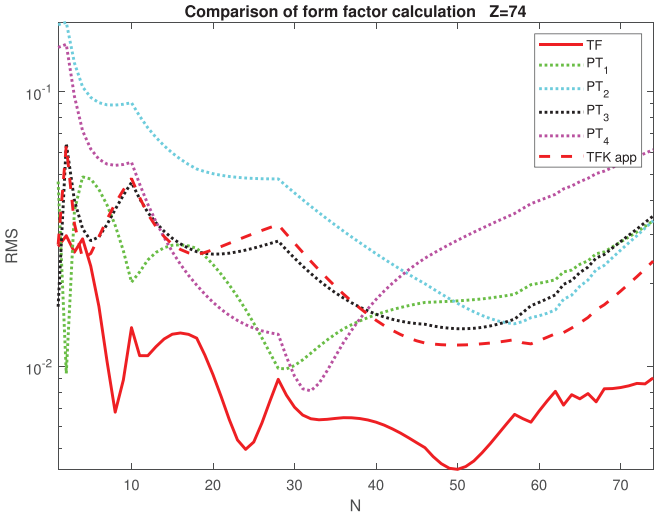

FIG. 8. RMS of the normalized difference between atomic form factors calculated for tungsten ions described by number of bound electrons—*N*, with DFT and TF/PT electron density models: TF—Thomas–Fermi, TFK app—Kirillov approximation of the Thomas–Fermi model, and PT—Pratt–Tseng models with numbers corresponding to different variants in the same order as presented before: (1) Botto I, (2) Botto II, (3) Kirillov, and (4) Avdonina and Lamoureux.

plasma core. The Kirillov approximation, on the other hand, seems to be a better choice for lower ionization stages, which can be found in plasma edge or post-disruptive plasmas. Taking this into consideration, the choice of the most accurate model should be made only after definition of the most important cases, e.g., elastic collisions are most sensitive for partial screening in the case of low ionization stages.

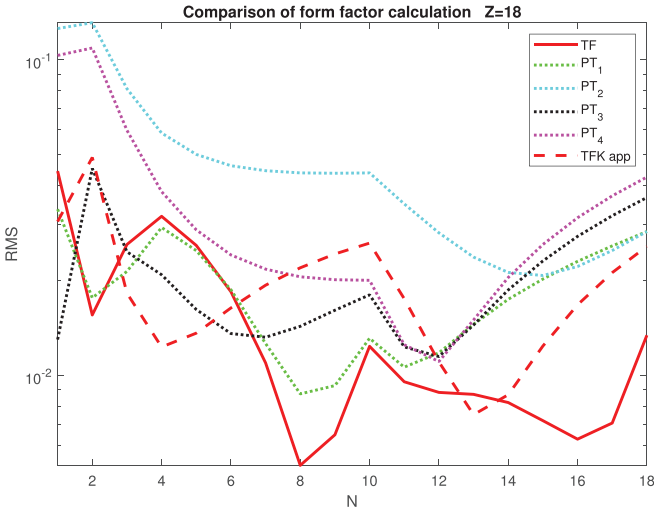

FIG. 9. RMS of the normalized difference between atomic form factors calculated for argon ions described by the number of bound electrons—*N*, with DFT and TF/PT electron density models: TF—Thomas–Fermi, TFK app—Kirillov approximation of the Thomas–Fermi model, and PT—Pratt–Tseng models with numbers corresponding to different variants in the same order as presented before: (1) Botto I, (2) Botto II, (3) Kirillov, and (4) Avdonina and Lamoureux.

In the case of argon, the results are similar—the direct TF model proves to be the most accurate in most cases. Only for a low number of bound electrons the Kirillov approximation is more accurate. The PT_1 model shows the best performance for intermediate ionization states. The conclusion is therefore similar that the choice of the most accurate model depends on the ions of interest.

V. BEYOND THE COMMON MODELS

None of the models investigated in Sec. IV is clearly better than others in all regions of interest. Because it was expected that room for improvement exists, an attempt was made to extend some of these models in order to achieve an increased accuracy while maintaining short computation time. Two modifications of the form factors calculation are presented in Secs. V A and V B.

A. Multi-exponential Yukawa potential

In the case of the PT models, it is possible to give an analytical solution of the form factor using the electron density calculated with more than one exponential. In this way, different parameters for every shell can be used (Peysson *et al.*, 2021). The electron density can then be calculated with the following equation:

$$\rho_{PT_{opt}}(r) = \frac{1}{4\pi r}\left[\sum_{i=1}^{5}\frac{N_i}{a_i^2}\exp\left(-\frac{r}{a_i}\right)\right], \tag{18}$$

with the corresponding analytical solutions of the form factors given as

$$F_{PT_{opt}}(q) = \sum_{i=1}^{5}\frac{N_i}{1+(qa_i)^2}, \tag{19}$$

where $N = \sum_{i=1}^{5} N_i$ and N_i is the number of electrons included in every summation part, a_i are parameters corresponding to each group of electrons.

This means that it is possible to obtain more accurate results of $\rho(r)$ and $F(q)$ by calculating a_i separately for different groups of electrons and then summing up the contributions with different a_i as in Eqs. (18) and (19). In this work, it was decided to use up to five electron groups, each one representing approximation of an electron shell in the atomic structure. The exact number of electrons which can be included in every group is 2, 8, 18, and 26, and the rest are in the 5th group, as presented in Table II. The first two groups represent exactly the electrons on the first and second shell, respectively. The third group includes the third electron shell plus the 4s subshell, because the latter has similar energy to the 3d subshell and the order of filling of these two subshells differs between elements. The choice of the following groups follows similar logic. The fifth shell appears in elements which have as few as 37 electrons, because electrons on the 4f subshell have similar energy as electrons on the 5s and 5p subshells. Because of

TABLE II. Grouping of the electrons in the PT_{opt} model.

Electron group	N_1	N_2	N_3	N_4	N_5
Maximum number of bound electrons in each group	2	8	18	28	Rest
Total bound electrons when group fully occupied	2	10	28	54	Rest

that, filling of the mentioned subshells is quite irregular and the configuration of xenon, which is the last element without the electrons on the sixth shell, is chosen as a limit for the fourth group. The heaviest element considered in the scope of this work is tungsten and only ground states of the ions are taken into account. It means that the sixth shell can be occupied at most by two electrons. Including these two electrons into a separate group would complicate the model while bringing little improvement in terms of accuracy, so it was decided to include them in the group with electrons on the fifth shell. Ions with few electrons have less electron groups, as some electron shells remain unoccupied.

Based on the equation used for calculating a in the different versions of PT models, the following approximation of a_i coefficients was proposed:

$$a_i(Z, N) = 1 \Big/ \sqrt{{\lambda_i}^2 \frac{(1 - x^{n_{s,i}+1})}{1 - x}}, \quad \text{where } x = \frac{Z - N}{Z}, \tag{20a}$$

$$\lambda_i(Z) = c_{1,i} Z^{c_{2,i}}, \tag{20b}$$

$$n_{s,i}(Z) = c_{3,i} Z^{c_{4,i}}, \tag{20c}$$

where $c_{1,i}$, $c_{2,i}$, $c_{3,i}$, $c_{4,i}$ are constants which need to be defined for each electron group. In order to find the optimal values of these parameters, a code was written in Matlab to perform optimization with a *gradient descent with momentum* algorithm (Qian, 1999). The results were fitted to the atomic form factor calculated by integration of the DFT-calculated electron density. As the cost function of the optimization algorithm, a RMS function as presented before was used.

The fitting procedure was as follows: first, the parameters $c_{1,1}$, $c_{2,1}$, $c_{3,1}$, $c_{4,1}$ were optimized for ions of selected elements, with bound electrons only in the first group. With these parameters defined, the parameters $c_{1,2}$, $c_{2,2}$, $c_{3,2}$, $c_{4,2}$ were optimized for ions with a minimum of 3 and a maximum of 10 electrons, i.e., electrons from the second group. With the parameters from the first two groups defined, the next set of parameters for the next group was optimized using ions with the corresponding number of electrons, and so on. This procedure required five optimization runs to define all parameters. Each time, the optimization of the parameters was performed until the RMS function change between iterations was smaller than 10^{-7} and the change of the optimized parameters between iterations was smaller than 10^{-5}. The momentum parameter of the gradient descent algorithm was set to 0.8. The learning rate was in each case manually adjusted by increasing it if the convergence was too slow or decreasing it in the case of divergence or strong oscillations.

As a result, the optimal parameters found for Eqs. (20b) and (20c) are presented in Table III. The values of $c_{3,i}$ and $c_{4,i}$ equal to 1 were rounded to full number, because in these cases the values of $x^{n_{s,i}+1}$ from Eq. (20a) is reaching zero and increasing the values of $c_{3,i}$ and $c_{4,i}$ does not change the result.

TABLE III. Optimized parameters for the PT_{opt} model.

		i = 1	i = 2	i = 3	i = 4	i = 5
$\lambda_i(Z)$	$c_{1,i}$	1.1831	0.1738	0.0913	0.0182	0.7702
	$c_{2,i}$	0.8368	1.0987	0.9642	1.2535	0.2618
$n_{s,i}(Z)$	$c_{3,i}$	0.3841	0.6170	1.0000	1.0000	1.0000
	$c_{4,i}$	0.5883	0.0461	1.0000	1.0000	1.0000

Such approach is in fact a search for minimum of the very complicated function of 20 parameters. It is almost impossible to determine if the minimum found is a global minimum, or just a local one. During investigations performed in the scope of this work, it was observed that obtaining better parameters for some specific ions can reduce the accuracy when calculating the form factor for other ions. The presented set of parameters grants reasonable accuracy for a wide range of elements, though it was created with focus on high-Z elements. In almost all cases, it gives better results than the models presented in Sec. IV. Nevertheless, it would be possible to obtain different sets of parameters if someone would like to focus on the different range of elements or ions.

To check if the a_i values found in this way are close to the best results which can be obtained with the general multi-exponential form of $F(q)$ as in Eq. (19), an additional fitting procedure was performed. The a_i parameters were fitted separately for every tungsten ion, without using Eq. (20a). It means that an optimization process was run 74 times with the a_1, a_2, a_3, a_4, a_5 parameters optimized each time to find the best fit of the resulting form factor to the results obtained with DFT electron density.

The results of the atomic form factor approximation created as described in Eq. (20a) (called PT_{opt} in this work) are presented in Fig. 10. The line described as "Fit" presents the result obtained with fitting the a_i directly, without defining them with universal equations Eqs. (20b) and (20c). The vertical lines mark the electron groups used in multi-exponential Yukawa potential definition.

The obtained results show a significant improvement in terms of RMS. Furthermore, time calculation effort is on the similar level as for

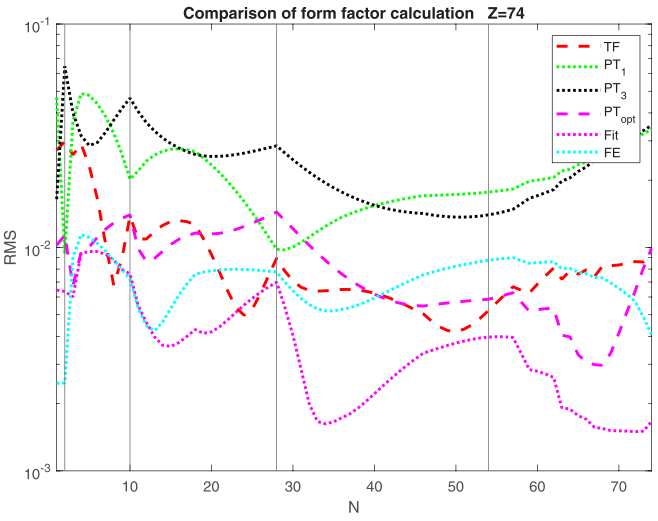

FIG. 10. RMS of the normalized difference between atomic form factors calculated for tungsten ions described by number of bound electrons—*N*, with DFT and TF/PT electron density models: TF—Thomas–Fermi *and* PT—Pratt–Tseng models with numbers corresponding to different variants: (1) Botto I, (3) Kirillov, PT_{opt}—multi-exponential Yukawa potential, Fit—form factor obtained with fitting of the a_i parameters in the multi-exponential Yukawa potential definition separately for every ion, *and* FE—ion specific form factor fitting. The vertical lines on the plot mark the electron groups used in multi-exponential Yukawa potential definition.

other PT models presented before. When comparing the PT_{opt} model with the direct fit of a_i, the equations for a_i used in the PT_{opt} model obviously generate results less accurate than when using directly fitted a_i parameters; however, they provide the ability to calculate the results without storing the fitted parameters for every ion. The resulting form factor can be considered as a relatively good approximation of the DFT model.

B. Ion specific form factor fitting

As shown previously, the form factor formulation in the case of PT and Kirillov approximation has a common form. It is therefore possible to develop a more general definition with two free parameters that will give the same or better accuracy of the form factor. Based on form factor definitions for PT and TFK in Eqs. (15) and (16), a generalized expression of the form factor is proposed as

$$F_{FE}(q) = \frac{N}{1 + (qa)^E}, \tag{21}$$

where a and E were used as free parameters in a fitting procedure to match the resulting form factor with the form factor based on the DFT results.

In this way, a set of two parameters for every ion is enough to calculate the form factor. It is however impossible to derive analytically the electron density from Eq. (21). The other drawback of this method is that it can only be applied to the ions for which the electron density was previously calculated with DFT and the parameters must be found using the fitting procedure. No extrapolation of the model is possible. Despite this, it nevertheless provides a fast way of computing the atomic form factor based on a limited number of parameters. The results of the proposed approaches are compared in Fig. 10 to the other models.

Values of parameters obtained for the FE model for tungsten ions are presented in Figs. 11 and 12. In the case of E, the value of 1.5 is used in the TFK model, and the value of 2 is used in PT models. Values of a obtained from PT_1 and PT_2 are given for comparison.

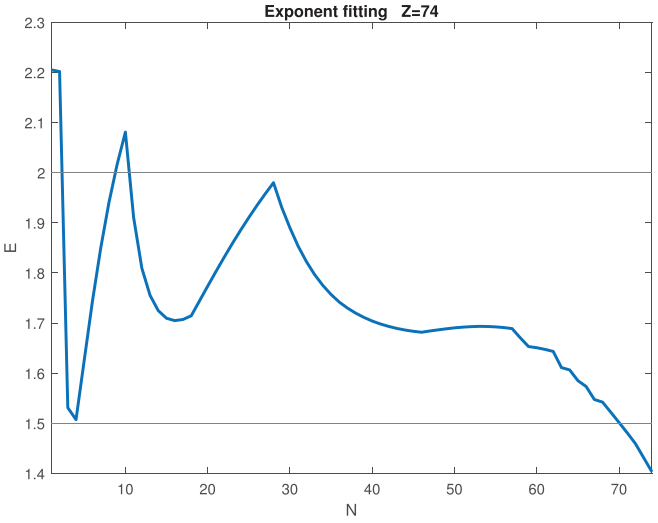

FIG. 11. The parameter E as a function of the number of bound electrons N for tungsten ions defined for the FE model. Value of 2 is used in PT models, 1.5 is used in the TFK model, as indicated by the black horizontal lines.

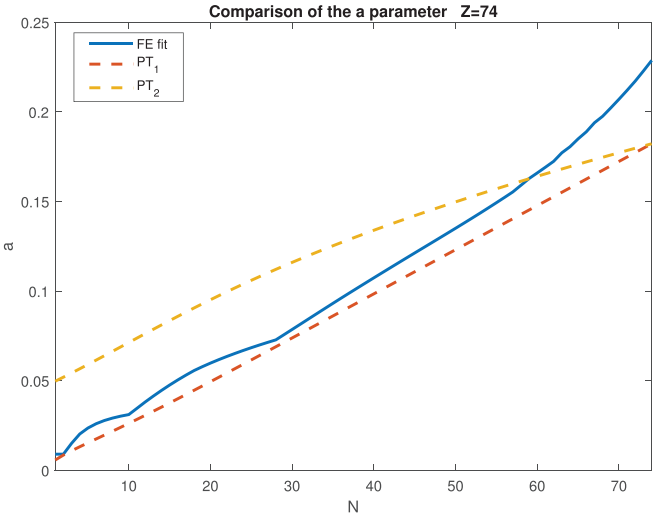

FIG. 12. Parameter a for tungsten ions as a function of the number of bound electrons N, defined with different models: PT_1—Pratt–Tseng Botto I, PT_2—Pratt–Tseng Botto II, *and* FE fit—ion specific form factor fitting.

VI. APPLICATION FOR PLASMA PHYSICS

A. Elastic collisions

The effect of partial screening on the deflection frequency between electrons and ions in Eq. (1) was calculated as in (Hesslow *et al.*, 2017). The goal of these calculations was to show the influence of partial screening on elastic collisions, therefore instead of calculating the absolute values, the ratio between deflection frequency calculated with complete screening and partial screening is used. It is defined with the following equation:

$$\frac{\nu_D^{ei}}{\nu_{D,cs}^{ei}} = 1 + \frac{g(p)}{{Z_0}^2\, ln\Lambda}, \tag{22}$$

where ν_D^{ei} is a deflection frequency calculated with the partial screening, $\nu_{D,cs}^{ei}$ is a deflection frequency calculated with complete screening, $Z_0 = Z - N$, $ln\Lambda$ is the Coulomb logarithm and $g(p)$ is defined as

$$g(p) = \int_0^1 \left(\left| Z - F(q) \right|^2 - {Z_0}^2 \right) \frac{dx}{x}, \tag{23}$$

where $x = q\alpha/2p$.

As the Coulomb logarithm was not the value of interest in this case, it was assumed constant for all tungsten ions $ln\Lambda = 16.3$. It corresponds to conditions in typical tokamak plasma core, with plasma electron density $n_e = 5 \times 10^{19}\ \mathrm{m}^{-3}$ and electron temperature $T_e = 3\,\mathrm{keV}$.

After integration, Eq. (23) takes the following general form for models which can be generalized with Eq. (21):

$$g(p) = \left(\left(Z^2 - {Z_0}^2 \right) ln\left(1 + y^E \right) - N^2 \frac{y^E}{\left(1 + y^E \right)} \right) \Big/ E, \tag{24}$$

where $y = 2a\,p/\alpha$.

In the case of the multi-exponential model described by Eq. (19), the integration gives the following result:

$$g(p) = \sum_{i=1}^{5}\left[\left(\left(Z^2 - Z_{0,i}{}^2\right) ln\left(1+y_i{}^2\right) - N_i{}^2 \frac{y_i{}^2}{\left(1+y_i{}^2\right)}\right)\Big/ 2\right] - \sum_{i=1}^{5}\sum_{k\neq i}^{5} N_i N_k \left(ln\left(1+y_i{}^2\right) + \frac{a_k{}^2}{a_k{}^2 - a_i{}^2} ln\left[\frac{\left(1+y_k{}^2\right)}{\left(1+y_i{}^2\right)}\right]\right). \quad (25)$$

The greatest impact of the partial screening can be observed for weakly ionized atoms and high momentum of the colliding free electron. A comparison of the deflection frequency ratio calculated with different models for tungsten W^{10+} ion is presented in Fig. 13. The DFT model is calculated with numerical integration of $g(p)$ with Eq. (23). The other models are calculated with $g(p)$ as in Eq. (24) or Eq. (25), depending on the model. The thermal and suprathermal ranges of the electron energies are marked in the plot to make the analysis easier. The boundary between these two values was set arbitrarily at 20 keV. The lower limit for the thermal region is set at 10 eV, because at this temperature majority of the electrons will be bound in hydrogen atoms. A vertical line marks the electron momentum for which its kinetic energy is equal to the ionization energy of the tungsten W^{10+} ion which is about 0.2 keV.

To quantify the average performance of different models, the RMS of the difference between DFT based results and different models was calculated for tungsten. The obtained values are presented in Table IV in two versions: the RMS of the absolute and relative difference, respectively, between a given model and the DFT. The resulting quantities for PT_{opt} are about four times smaller than in the case of other models.

B. Inelastic collisions

Most of the approximations of the electron density (r) presented in Secs. III and V A can be used in the calculation of the slowing-down

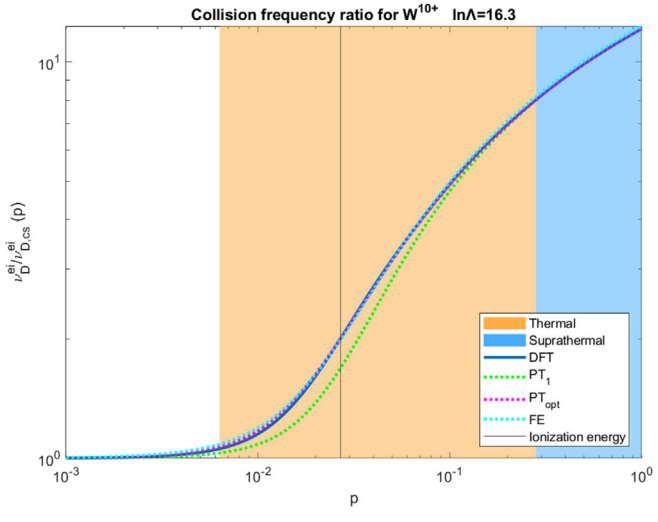

FIG. 13. The deflection frequency ratio calculated for tungsten ion W^{10+} with different models: DFT—Density Functional Theory, PT_1—Pratt–Tseng Botto I, PT_{opt}—multi-exponential Yukawa potential, and FE—ion specified form factor fitting.

TABLE IV. RMS of the deflection frequency ratio difference between DFT and investigated models.

Model	TF	PT_1	PT_2	PT_3	PT_4	PT_{opt}
Absolute error RMS	0.0297	0.0239	0.0239	0.0258	0.1485	0.005 94
Relative error RMS	2.333%	4.661%	4.661%	4.735%	7.989%	1.392%

frequency. It can be done with the Local Plasma Approximation (LPA) proposed by Lindhard and Scharff (1953), which uses the electron density as the main quantity to estimate the mean excitation energy I. This approximation was derived mainly based on the TF atomic model, treating bound electrons as a homogeneous electron gas. It does not have a strong theoretical basis from the point of view of modern atomic physics, but it can still produce some useful results. The mean excitation energy I can be used for the calculation of the inelastic collisions with bound electrons and, in this case, is a primary parameter describing plasma. According to the Bethe stopping-power formula (Hesslow *et al.*, 2017), the slowing-down frequency ν_s^{ee} in Eq. (1) for the Fokker–Plank collision operator is modified as follows:

$$\nu_s^{ee} = 4\pi c r_0^2 \frac{\gamma}{p^3}\left[n_e \ln\Lambda^{ee} + n_i N\left(lnh - \beta^2\right)\right], \quad (26)$$

where n_e—density of free electrons in plasma, n_i—density of ions in plasma, $\beta = v/c$, $h = \sqrt{\gamma - 1}\left(mc^2/I\right)$ and $\ln\Lambda^{ee} = \ln\Lambda + 1/k \ln\left(1 + \left[2(\gamma-1)/p_{Te}^2\right]^{k/2}\right)$, where p_{Te}—thermal momentum, k-model parameter.

The mean excitation energy I can be calculated with the LPA using the following form of lnI for ions:

$$lnI = \frac{1}{N}\int 4\pi r^2 \rho(r)\, ln\left(\sqrt{2}\hbar\omega_0\right) dr, \quad (27)$$

where the corresponding local plasma frequency:

$$\omega_0 = \sqrt{4\pi e^2 \rho(r)/m}, \quad (28)$$

and e—electron charge and m—mass of the electron.

The values of lnI for neutral atoms were calculated using LPA with different models of electron density. To define their accuracy, the results were compared against experimental values from the NIST database (National Institute of Standards and Technology, 1995). The plots of lnI as a function of the atomic number Z for neutral atoms calculated using different models are presented in Fig. 14. To provide more quantitative comparison, the RMS of the difference between LPA models and the NIST database were calculated. Results are presented in Table V in two versions corresponding to the RMS of the absolute and relative difference, respectively, between a given model and the NIST database. For most elements, LPA can be used to obtain approximation of the mean excitation energy. Result obtained based on the PT_{opt} model are similar to results based on the DFT calculation.

The values of lnI for ions of some elements were calculated using different models of electron density and compared to the results

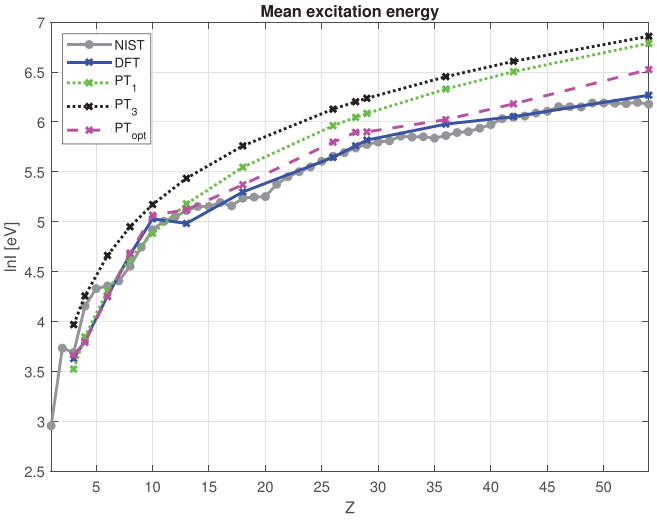

FIG. 14. The logarithm of mean excitation energy for neutral atoms as a function of the atomic number Z, calculated with the LPA using different models of electron density: DFT—Density Functional Theory, PT_1—Pratt–Tseng Botto I, PT_3—Pratt–Tseng Kirillov, *and* PT_{opt}—multi-exponential Yukawa potential. Experimental values from NIST database are used for comparison (National Institute of Standards and Technology, 1995).

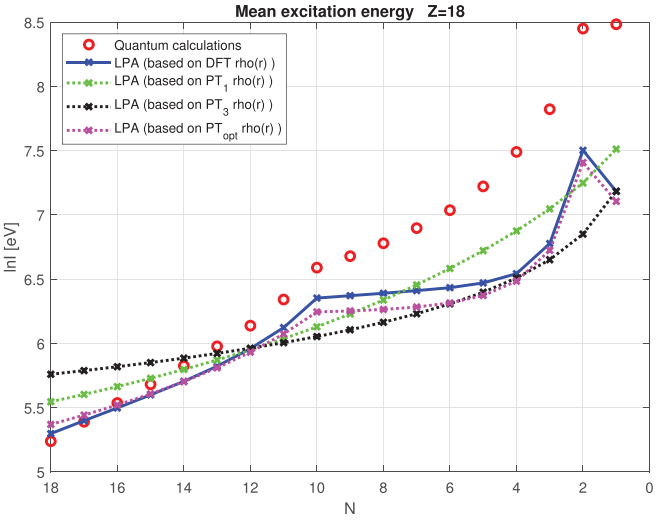

FIG. 15. The logarithm of mean excitation energy for argon ions calculated with the LPA using different models of electron density: DFT—Density Functional Theory, PT_1—Pratt–Tseng Botto I, PT_3—Pratt–Tseng Kirillov, PT_{opt}—multi-exponential Yukawa potential. Quantum calculations - MCSCF results from Sauer *et al.* (2015).

obtained with Multi-Configurational Self-Consistent Field (MCSCF) *ab initio* quantum mechanical calculation by Sauer *et al.* (2015). Results for argon are presented in Fig. 15. Despite the fact that LPA is not well suited for ions, it can be noted that the PT_{opt} model gives very similar results to DFT electron density and is even able to reproduce some features of the atomic shell structure. However, all the models based on LPA underestimate *lnI* for high ionization stages—which is not surprising given the assumptions made in the model.

VII. SUMMARY

Different classical approaches to calculation of the electron density distribution and atomic form factors were compared with the *ab initio* results obtained from the DFT method in order to find a computationally efficient way of calculating the atomic form factors that can be implemented into Fokker–Planck equation solvers. The existence of an analytical solution of the integrals needed to calculate form factor and deflection frequency was an important requirement, because it gives the possibility to achieve a much shorter computation time. As none of the investigated models was considered as satisfactory enough for this purpose, an attempt to extend the existing model was made, in order to achieve better approximation of the DFT-based results. A definition of the multi-exponential Yukawa potential model was presented, which can achieve better accuracy than most of the investigated models, while still providing advantageous computational efficiency. In addition, comparison to some fitting models was presented, as an alternative approach to computing the form factors.

The application of the presented models in calculation of the plasma collision parameters was presented. The calculation of the elastic collisions between free electrons and ions shows that use of the proposed approximation should provide quite accurate results, while significantly reducing computation time. The impact of including partial screening can result in a few times higher collisions frequency than while using the complete screening model, it is thus non-negligible. The effect is more important in the case of ions with high number of bound electrons and high energy of colliding free electrons. These two conditions are *a priori* in contradiction, because higher electron temperatures would result in stronger ionization of atoms. Nevertheless, in the case of runaway electrons in relatively cold post-disruptive plasmas, these conditions are common and the impact of partial screening should be significant. Regarding microwave heating or current drive that can result in the local production of suprathermal electrons, the description of the interaction with non-fully ionized impurities, without the partial screening, could result in an underestimation of the elastic collision frequency and even more significantly of the fast electron Bremsstrahlung (Peysson *et al.*, 2021; Król *et al.*, 2021). The presented models can be implemented into calculation of the fast electron bremsstrahlung in plasma, which also requires atomic form factor integration. In this case, the possibility to find an analytic solution would also be very important, as bremsstrahlung depends on many

TABLE V. RMS of the *lnI* difference between LPA-calculated values for different atomic models and NIST database for neutral atoms.

Model	DFT	TF	PT_1	PT_2	PT_3	PT_4	PT_{opt}
Absolute error RMS	0.1092	0.2403	0.3307	0.3307	0.4667	0.6523	0.1734
Relative error RMS	2.440%	5.104%	5.891%	5.891%	8.507%	11.41%	3.391%

parameters and numerical integration would be a more time consuming solution.

It is planned to include created models into suite of codes used for calculations of plasma dynamics, to verify the influence on plasma properties. Impact of the partial screening on the runaway electron generation, current drive efficiency, and entropy generation in plasma should be investigated.

In the case of inelastic collisions of free electrons with electrons bound to the ion, the proposed models show similar results to the DFT based calculation. Unfortunately, the LPA approach used in this work is a significant source of uncertainty by itself. More reliable methods of calculating mean excitation energy for high-Z element ions will be a subject of further investigation. This is a region so far mostly unexplored, because experimental measurements of the stopping power and related mean excitation energy are usually restricted to neutral atoms. Values for different ionization stages are acquired from *ab initio* models, which meet difficulties in the case of high-Z elements.

The further work is planned to investigate different approaches to obtain mean excitation energy. Application of some ab-initio methods, such as Multi-Configuration Dirac–Hartree–Fock (MCDHF), Coupled Cluster (CC) or Time-Dependent Density Functional Theory (TDDFT) should provide better insight into this topic as well as more accurate results.

The presented calculations should help to better understand and simulate the fast electrons population dynamics in plasma with non-fully ionized impurities. This will allow a precise control of the energy deposition in the case of the LHCD and electron cyclotron resonance heating, as well as more accurate strategies of runaway electron mitigation. The precise description of the electron distribution can also improve understanding of other processes in plasma, like tungsten transport. It should help to enhance the plasma confinement in tokamaks and bring us closer to efficient nuclear fusion.

ACKNOWLEDGMENTS

This work has been partially funded by the National Science Centre, Poland (NCN) Grant HARMONIA 10 No. 2018/30/M/ST2/00799. We thank the PLGrid project for computational resources on the Prometheus cluster. This work has been carried out within the framework of the EUROfusion Consortium and has received funding from the Euratom research and training programme 2014–2018 and 2019–2020 under Grant Agreement No. 633053. The views and opinions expressed herein do not necessarily reflect those of the European Commission.

AUTHOR DECLARATIONS

Conflict of Interest

The authors have no conflicts to disclose.

DATA AVAILABILITY

The data that support the findings of this study are available from the corresponding author upon reasonable request.

REFERENCES

Abrahamson, A. "Statistical electron density distributions and Thomas-Fermi-Dirac screening functions for neutral atoms," Phys. Rev. **123**(2), 538 (1961).

Adamo, C. and Barone, V., "Toward reliable density functional methods without adjustable parameters: The PBE0 model," J. Chem. Phys. **110**(13), 6158–6170 (1999).

Botto, D. J., McEnnan, J., and Pratt, R. H., "Analytic description of photoeffect from atomic ions," Phys. Rev. A **18**(2), 580 (1978).

Brezinsek, S., Kirschner, A., Mayer, M., Baron-Wiechec, A., Borodkina, I., Borodin, D., Coffey, I., Coenen, J., den Harder, N., Eksaeva, A., Guillemaut, C., Heinola, K., Huber, A., Huber, V., Imrisek, M., Jachmich, S., Pawelec, E., Rubel, M., Krat, S., Sergienko, G., Matthews, G. F., Meigs, A. G., Wiesen, S., Widdowson, A., and JET Contributors, "Erosion, screening, and migration of tungsten in the JET divertor," Nucl. Fusion **59**, 096035 (2019).

Csavinszky, P., "Approximate analytical solutions of the Thomas–Fermi–Dirac and Thomas–Fermi–Dirac–Gombás equations," J. Chem. Phys. **50**, 2476 (1969).

Frisch, M. J., Trucks, G. W., Schlegel, H. B., Scuseria, G. E., Robb, M. A., Cheeseman, J. R., Scalmani, G., Barone, V., Petersson, G. A., Nakatsuji, H., Li, X., Caricato, M., Marenich, A. V., Bloino, J., Janesko, B. G., Gomperts, R., Mennucci, B., Hratchian, H. P., Ortiz, J. V., Izmaylov, A. F., Sonnenberg, J. L., Williams-Young, D., Ding, F., Lipparini, F., Egidi, F., Goings, J., Peng, B., Petrone, A., Henderson, T., Ranasinghe, D., Zakrzewski, V. G., Gao, J., Rega, N., Zheng, G., Liang, W., Hada, M., Ehara, M., Toyota, K., Fukuda, R., Hasegawa, J., Ishida, M., Nakajima, T., Honda, Y., Kitao, O., Nakai, H., Vreven, T., Throssell, K., Montgomery, J. A., Jr., Peralta, J. E., Ogliaro, F., Bearpark, M. J., Heyd, J. J., Brothers, E. N., Kudin, K. N., Staroverov, V. N., Keith, T. A., Kobayashi, R., Normand, J., Raghavachari, K., Rendell, A. P., Burant, J. C., Iyengar, S. S., Tomasi, J., Cossi, M., Millam, J. M., Klene, M., Adamo, C., Cammi, R., Ochterski, J. W., Martin, R. L., Morokuma, K., Farkas, O., Foresman, J. B., and Fox, D. J., *Gaussian 16. Revision C.01* (Gaussian, Inc., Wallingford, CT, 2019).

Hesslow, L., Embréus, O., Stahl, A., DuBois, T. C, Papp, G., Newton, S. L., and Fülöp, T., "Effect of partially screened nuclei on fast-electron dynamics," Phys. Rev. Lett. **118**, 255001 (2017).

Hesslow, L., Embréus, O., Wilkie, G. J, Papp, G., and Fülöp, T., "Effect of partially ionized impurities and radiation on the effective critical electric field for runaway generation," Plasma Phys. Controlled Fusion **60**, 074010 (2018).

Hohenberg, P. and Kohn, W., "Inhomogeneous electron gas," Phys. Rev. **136**, B864–B871 (1964).

Jardin, A., Bielecki, J., Krol, K., Peysson, Y., Mazon, D., Dworak, D., and Scholz, M., "Study of the mutual dependence between lower hybrid current drive and heavy impurity transport in tokamak plasmas. Part 1—Preparatory work and theoretical background," Report No. 2105/AP (Institute of Nuclear Physics Polish Academy of Sciences, 2020).

Kirillov, V. D., Trubnikov, B. A., and Trushin, S. A., "Role of impurities in anomalous plasma resistance," Fiz. Plazmy **1**, 218–237 (1975).

Kohn, W. and Sham, J., "Self-consistent equations including exchange and correlation effects," Phys. Rev. **140**, A1133 (1965).

Król, K., "Screening effect of partially ionized high-Z impurities in relativistic electron Fokker-Planck calculations and runaway electron dynamics. Part 1—Preliminary work towards statistical study of partial screening effect in WEST tokamak discharges," Report No. 2103/AP (Institute of Nuclear Physics Polish Academy of Sciences, 2020).

Król, K., Peysson, Y., Mazon, D., Scholz, M., Jardin, A., Bielecki, J., Dworak, D., Artaud, J. F., Hillairet, J., Morales, J., Fleury, L., Decker, J., and Goniche, M., "Impact of partial screening effect on fast electron dynamics in WEST tokamak plasmas with high Z impurities," in 47th EPS Conference on Plasma Physics (2021).

Lamoureux, M. and Avdonina, N., "Bremsstrahlung in hot plasmas with partially ionized atoms," Phys. Rev. E **55**(1), 912–926 (1997).

Lindhard, J. and Scharff, M., "Energy loss in matter by fast particles of low charge," Mat. Fys. Medd. - K. Dan. Vidensk. Selsk. **27**, 15 (1953).

Lu, T. and Chen, F., "Multiwfn: A multifunctional wavefunction analyzer," J. Comput. Chem. **33**, 580 (2011).

Lundqvist, S. and March, N. H., *Theory of the Inhomogeneous Electron Gas* (Springer, 1983).

Mott, N. F. and Massey, H. S. W., *The Theory of Atomic Collisions*, 3nd ed. (The Clarendon Press, Oxford, 1965).

National Institute of Standards and Technology (NIST) Database, see https://physics. nist.gov/PhysRefData/XrayMassCoef/tab1.html for "NIST X-Ray Mass Attenuation Coefficient" (1995).
Perdew, J. P., Ernzerhof, M., and Burke, K., "Rationale for mixing exact exchange with density functional approximations," J. Chem. Phys. **105**(22), 9982–9985 (1996).
Peysson, Y., Decker, J., Nilsson, E., Artaud, J.-F., Ekedahl, A., Goniche, M., Hillairet, J., Ding, B., Li, M., Bonoli, P. T., Shiraiwa, S., and Madi, M., "Advances in modeling of lower hybrid current drive," Plasma Phys. Controlled Fusion **58**, 044008 (2016).
Peysson, Y., Mazon, D., Jardin, A., Król, K., Bielecki, J., Dworak, D., Scholz, M., Embréus, O., Hesslow, L., Fülop, T., Hoppe, M., and Decker, J., "Effect of partially ionized high-Z atoms on fast electron dynamics in tokamak plasmas," in IAEA FEC 2020—The 28th IAEA Fusion Energy Conference (2021).
Pitts, R. A., Carpentier, S., Escourbiac, F., Hirai, T., Komarov, V., Lisgo, S., Kukushkin, A. S., Loarte, A., Merola, M., Naik, A. S., Mitteau, R., Sugihara, M., Bazylev, B., and Stangeby, P. C., "A full tungsten divertor for ITER: Physics issues and design status," J. Nucl. Mater. **438**, S48–S56 (2013).
Pokol, G. I., Olasz, S., Erdos, B., Papp, G., Aradi, M., Hoppe, M., Johnson, T., Ferreira, J., Coster, D., Peysson, Y., Decker, J., Strand, P., Yadikin, D., Kalupin, D., and the EUROfusion-IM Team, "Runaway electron modelling in the self-consistent core European Transport Simulator," Nucl. Fusion **59**, 076024 (2019).
Qian, N., "On the momentum term in gradient descent learning algorithms," Neural Networks **12**, 145–151 (1999).
Reux, C., Plyusnin, V., Alper, B., Alves, D., Bazylev, B., Belonohy, E., Boboc, A., Brezinsek, S., Coffey, I., Decker, J., Drewelow, P., Devaux, S., de Vries, P. C., Fil, A., Gerasimov, S., Giacomelli, L., Jachmich, S., Khilkevitch, E. M., Kiptily, V., Koslowski, R., Kruezi, U., Lehnen, M., Lupelli, I., Lomas, P. J., Manzanares, A., Martin De Aguilera, A., Matthews, G. F., Mlynář, J., Nardon, E., Nilsson, E., Perez von Thun, C., Riccardo, V., Saint-Laurent, F., Shevelev, A. E, Sips, G., Sozzi, C., and JET Contributors, "Runaway electron beam generation and mitigation during disruptions at JET-ILW," Nucl. Fusion **55**, 093013 (2015).
Sauer, S. P., Oddershede, J., and Sabin, J. R., in *Concepts of Mathematical Physics in Chemistry: A Tribute to Frank E. Harris—Part A*, Advances in Quantum Chemistry Vol. 71 (Academic Press, New York, 2015), p. 29.

Atomic Data and Nuclear Data Tables xxx (xxxx) xxx

Contents lists available at ScienceDirect

Atomic Data and Nuclear Data Tables

journal homepage: www.elsevier.com/locate/adt

Mean Excitation Energies of all ionization stages of all atoms with $1 \leq Z \leq 86$

J. Walkowiak [a,b,*], J. Bielecki [a], J. Bieroń [c], A. Jardin [a], Y. Savoye-Peysson [d], D. Mazon [d], K. Król [a], D. Dworak [a], M. Scholz [a]

[a] Institute of Nuclear Physics Polish Academy of Sciences, PL-31342, Krakow, Poland
[b] National Centre for Nuclear Research (NCBJ), 7 Andrzeja Sołtana Str., Otwock 05-400, Poland
[c] Institute of Theoretical Physics, Jagiellonian University, 30-348 Kraków, Poland
[d] CEA, IRFM, F-13108, Saint-Paul-lez-Durance, France

ABSTRACT

The presented work provides values of Mean Excitation Energy (MEE) for all atoms and their ions with atomic numbers $1 \leq Z \leq 86$. To fill in the gaps in the available data, we propose an approximate atomic model for ions of high-Z elements, that uses a semi-empirical formula based on the Local Plasma Approximation (LPA). Despite the fact that the LPA, in its original form, poorly predicts MEE for high ionization states, a relatively simple modification utilizing a fit function can amend this shortcoming. We assess the importance of relativistic effects for the MEE for highly ionized atoms and compare the proposed formula to other approximations available for high-Z elements. We estimate the uncertainty of the presented data to be less than 40% in absolute value for the worst cases and less than 20% for most ions. This corresponds to an uncertainty of the order of few percent for the logarithm of MEE, which is the value of interest in the case of Bethe's theory of stopping power.

* Corresponding author at: Institute of Nuclear Physics Polish Academy of Sciences, PL-31342, Krakow, Poland.
E-mail address: jedrzej.walkowiak@ifj.edu.pl (J. Walkowiak).

https://doi.org/10.1016/j.adt.2024.101696
Received 15 May 2024; Received in revised form 3 September 2024; Accepted 18 September 2024

Contents

1. Introduction

Bethe's theory of stopping power [1,2] was previously implemented in plasma research to describe the effect of inelastic collisions between suprathermal electrons and non-fully ionized atoms [3]. This is an important issue for nuclear fusion in general and tokamak devices in particular, as plasma heating and runaway electrons involve slowing down of electrons which have energies much higher than the thermal background. In particular, inelastic scattering can be included in Fokker–Planck solvers with the use of Bethe's theory of stopping power [4,5]. The detailed theory of collisions of such electrons has been already implemented into simulation software, to assess runaway electrons mitigation scenarios [6] or to improve the efficiency of current drive [7] in tokamaks.

However, using Bethe's stopping power formula requires knowledge of the Mean Excitation Energy (MEE) of ions constituting the plasma, which is still missing for high-Z impurities such as tungsten (W). MEE represents the potential of a given ion to absorb energy during collisions with charged particles through excitation. For low-Z elements, this quantity was calculated by Sauer et al. [8,9] based on the MEE definition:

$$ln(MEE) = \frac{\sum \int \frac{df}{dE} lnE dE}{\sum \int \frac{df}{dE} dE}, \quad (1)$$

where E is the transition energy from the ground state to the nth excited state and f is the associated dipole oscillator strength (or oscillator strength density in the continuous case). The sum is performed over the discrete part of the spectrum and the integral over its continuous part.

Such an approach for high-Z elements is computationally demanding, as the number of possible excitations increases with the number of electrons. Besides, in the Multi-configurational Self-Consistent-Field (MCSCF) calculations implemented in codes such as the General-purpose Relativistic Atomic Structure Package (GRASP) [10] or Dalton [11], the wave function of the atomic state is expressed as a linear combination of configuration state functions. With an increasing number of electrons, the form of an atomic state function becomes more complicated and more configuration state functions are necessary to represent it accurately. When relativistic effects are taken into account for high accuracy, the required computation time grows even further.

The topic of MEE was investigated in numerous publications. Early works are summarized in the report of the International Commission on Radiation Units and Measurements [12]. Data on stopping power of elements was published by Oddershede and Sabin [13], who provided orbital and whole atom stopping power for $Z \leq 36$, or Inokuti et al. [14]. More recent works focus on the stopping power of molecules [15,16] or experimental verification of MEE for different states of matter [17]. Unfortunately, despite a large number of works dedicated to the MEE of neutral atoms and molecules, there is a relatively low number of works which were investigating high ionization states. While the work of Sauer et al. [8,9] is one of the most extensive efforts to provide MEE for ions, there were some other approaches proposed for this problem. One of the most important from the perspective of this work is the Local Plasma Approximation (LPA) proposed by Lindhard and Scharff [18], which is described in more detail in Section 3. Another approach which is used as a reference in this work was proposed by Garbet [19] and is based on the virial theorem. Other interesting works, not used directly in the presented research, were investigation of the aluminium ions by McGuire et al. [20] and the orbital local plasma approximation proposed by Meltzer et al. [21].

In the presented work, we first investigate the impact of relativistic effects on the MEE of H-like ions. Then, we propose a modification of the MEE formula based on the LPA, which allows obtaining easily approximated values of MEE for all investigated ions. We compared the results of the proposed approximation with other available approaches and with calculations done in Flexible Atomic Code (FAC) [22] for selected ions, showing that results are within the expected range. Finally, we present a summary of MEE values which combines results obtained with Eq. (1) (mostly found in the literature) and values which are calculated with the proposed LPA modification. For convenience, in Table 4 we also include the K-shell ionization energies of neutral atoms and H-like ions for all presented elements [23,24]. K-shell ionization energy can be used to estimate the range of validity of the MEE, as the presented values are fully valid when the projectile energy is at least 10–100 times larger than the K-shell ionization energy. At lower projectile energies, a subset of the included transitions is in fact not physically accessible (in particular, the transitions in the continuous spectrum) , thus the MEE is then overestimated.

Table A
Comparison of the MEE calculated by Sauer et al. [8,9] and results obtained with FAC, in eV.

Element	H	He	C	O	Ne	Al	Ar	Ti	Ni	Zn
Z	1	2	6	8	10	13	18	22	28	30
Sauer et al. (NR)	14.99	59.88	539.5	959.0	1498	2534	4857	7256	11 753	13 492
$14.99Z^2$	14.99	59.96	539.6	959.4	1499	2533	4856	7255	11 752	13 491
FAC results (R)	14.95	59.84	539.2	959.3	1501	2540	4887	7323	11 920	13 707
$\frac{FAC}{Sauer\ et\ al.}$ (R/NR)	0.9973	0.9826	0.9994	1.0003	1.0020	1.0023	1.0062	1.0092	1.0142	1.0159

2. Influence of relativistic effects on MEE

2.1. H-like ions

To estimate the impact of relativistic effects, we used FAC to calculate MEE according to Eq. (1) for H-like ions. FAC employs the MCSCF approach with Dirac–Fock-Slater method [25] to represent the Hamiltonian of an ion's electronic system. We calculated oscillator strengths and energies of transitions for the first 40 excited states. Calculations were done in the fully relativistic mode with Babushkin gauge. For the continuous parts of the spectra, we calculated oscillator strength density on an energy grid with a resolution of 30 values up to 15 times the ionization energy.

Given an isonuclear series of ions, direct relativistic effects are the strongest in the H-like ion, because the presence of each additional electron results in partial screening of the inner shells. While the difference between relativistic and non-relativistic description is around 8.5% for tungsten H-like ion, for He-like ion this difference is reduced to 7.9%. In multielectron systems, significant indirect relativistic effects are also observed for electrons occupying valence shells, due to contractions of inner shells [26]. The resulting *relativistic* rearrangements of electronic shells induce *relativistic* changes of binding energies of all electrons. However, valence effects are not important for MEE, since the main contribution to MEE arises from inner electrons. For valence electrons, the relativistic effects result in changes of the energies in the range a few eV, while the MEE values for high-Z elements are in the range of hundreds of eV. Therefore, the isoelectronic series of H-like ions constitute a good starting point for our calculations, because only the direct (strong) relativistic effects are observed (and relatively easily computed), while the indirect (weaker) relativistic effects are absent. It also allows for simple non-relativistic extrapolation from the results obtained for the neutral hydrogen to H-like ions, since the MEE in such a case depends on Z^2. The results obtained in the fully relativistic approach are compared to the results of non-relativistic calculations of Sauer et al. [8,9], and to the approximation described in [27], which is (in eV):

$$MEE_H(Z)\,[\mathrm{eV}] = 14.99\,\mathrm{eV}\,Z^2. \tag{2}$$

Some selected numerical values are presented in Table A, while the complete comparison for all elements from H to Rn is presented in Fig. 1. The accuracy of such calculations can be increased by including higher number of transitions, but it would be at the expense of the calculation time. For hydrogen, our results agree up to three significant digits with the results of Sauer et al. We considered such accuracy completely sufficient for our purpose.

Even for high-Z elements, such as W, the difference between relativistic calculations and non-relativistic approximation for H-like ions is less than 10%. For the highest calculated atomic number $Z = 86$, the difference between our calculations and non-relativistic formula was 13%. This is in line with our expectations, as other investigations of relativistic effects on atomic properties, such as Bethe sum rule, show a similar order of magnitude [28]. The full list of calculated values for H-like ions and deviation from the non-relativistic approximation is presented in Table 2. In Bethe's formula, MEE resides within the argument of a logarithm, thus relativistic effects can have a limited influence on the final results of the stopping power. Even for $Z = 86$, the difference in logarithms is slightly less than 1%. When compared to other sources of uncertainties, the relativistic effects become negligible for the currently available approximations. For this reason, we focused on the extrapolation of non-relativistic results.

2.2. Selected calculations with FAC

For the purpose of comparing of the model presented in the next section, we performed some additional calculations in FAC for the selected ions. Similarly as for H-like ions, calculations were done in the fully relativistic mode with Babushkin gauge. For the continuous parts of the spectra, we calculated oscillator strength density on an energy grid with a resolution of 30 values up to 15 times the ionization energy. The number of excited states was higher, but the principal quantum number of these excited states was limited to avoid excessive computational cost. However, the results obtained from these calculations should not be treated as a very accurate reference for other models — they are included only to show that numerical results are consistent with the proposed model and with the declared code accuracy. As stated in the FAC manual [29]: "*The ions other than H-like, the accuracy of energy levels are usually a few eV [. . .]. For radiative transition rates and cross sections, the accuracies are 10%–20%. Data for near-neutral ions or atoms may have even larger errors.*"

Our attempts showed that for neutral atoms the calculations may have convergence issues, so obtaining reliable results in such cases is very troublesome in FAC. This can be related to some basic assumptions used in FAC, like using mean configuration to calculate central potential for all states. In addition, calculation of excitations from the inner shells creates additional problems, as opening of the inner shell is known to complicate the wavefunction of the atomic state, decreasing the accuracy. Despite these shortcomings, for highly-ionized states we obtained results which are mostly within the declared 10%–20% uncertainty. We selected iso-electronic configurations with closed shells in the ground state, as this allows avoiding some complications which can deteriorate accuracy in other cases. Some selected results are presented in Figs. 4 and 5.

He-like ions are a specific case of multi-electron ions, that include two electrons occupying the same shell which differ only by spin number. Because of that, the results are relatively reliable and for $Z > 30$ we decided to use FAC results for He-like ions instead of the non-relativistic approximation. The full list of calculated values for He-like ions is presented in Table 2. In the same table, we provide the deviation from the non-relativistic approximation as a reference. For this purpose, we use the approximation proposed in [8], which can be written as (in eV):

$$MEE_{He}(Z)\,[\mathrm{eV}] = 14.99\,\mathrm{eV}\,(Z - 0.3)^2. \tag{3}$$

3. Modification of the Local Plasma Approximation (LPA)

3.1. Limitations of the original LPA

One of the early attempts to calculate MEE was the LPA proposed by Lindhard and Scharff [18], which uses electron density as the main quantity. This approximation was derived mainly based on the Thomas–Fermi (TF) atomic model, treating bound electrons as a homogeneous electron gas. It does not have a strong theoretical basis from

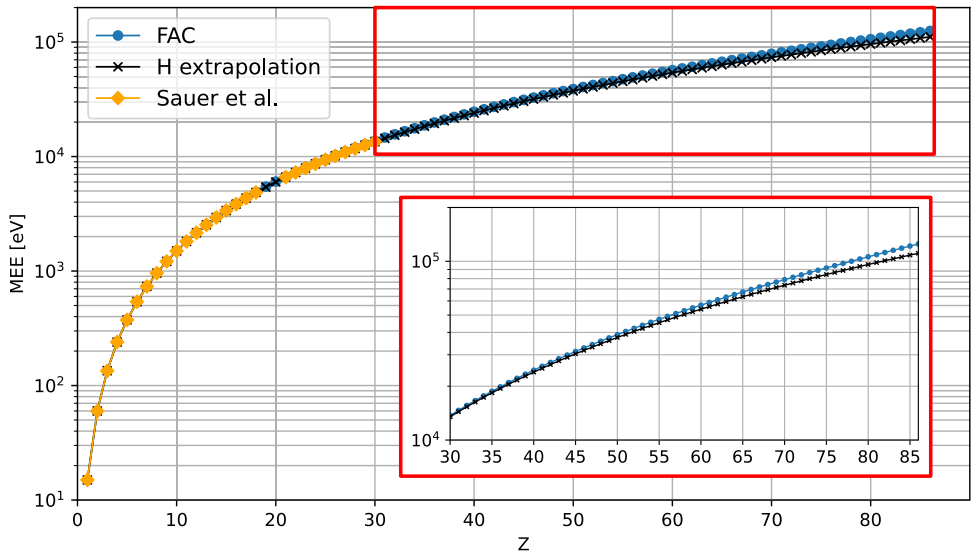

Fig. 1. MEE of H-like ions for elements from H to Rn. Blue dots represent results from FAC, which include relativistic effects. Black dots show extrapolation of the non-relativistic results with Eq. (2). Yellow dots represent results obtained in [8,9]. (For interpretation of the references to colour in this figure legend, the reader is referred to the web version of this article.)

the point of view of modern atomic physics, but it describes relatively well the MEE of neutral atoms. In its original form the LPA yields:

$$ln(MEE) = \frac{1}{N}\int 4\pi r^2 \rho(r) ln(\gamma \hbar\omega_0) dr, \tag{4}$$

where the corresponding local plasma frequency of the electron gas is expressed as:

$$\omega_0 = \sqrt{4\pi e^2 \rho(r)/m}, \tag{5}$$

where $\rho(r)$ is the spherically averaged electron density distribution in the atom, N is the number of bound electrons in the atom, $\hbar$ is the reduced Planck constant, e denotes the electron charge, m its mass and r is the radial coordinate. The γ is correction factor to plasma frequency, which was originally introduced [18] to account for the revolution frequency. The term $ln(\gamma)$ was only approximately defined by their authors as $\gamma \approx 1$ for light atoms and $\gamma \approx \sqrt{2}$ for higher atomic numbers, to account for polarization effects. The accuracy of this assumption was verified in [30], showing that it roughly holds for neutral atoms of higher atomic number, but for light atoms the LPA does not provide correct values. To calculate the electron density required by the LPA, we used the optimized Pratt-Tseng model with multiple Yukawa exponentials, as proposed in [31]. This allowed us to easily calculate the electron density distributions for all investigated ions and use them as input to the LPA. An investigation of the LPA model applied to ions and carried out in [31] showed a significant difference between the LPA model and the results of Sauer et al. [8,9]. The LPA holds well for neutral atoms, but for highly ionized systems it deviates significantly from the expected values. The LPA was derived from the Thomas–Fermi atomic model, which treats electrons as a homogeneous electron gas and is known to poorly describe innermost electrons of the core or highly ionized atoms [19]. This dependency on the Thomas–Fermi model can be one of the reasons of poor performance of the LPA for highly ionized systems. Nevertheless, by analysing the difference between the LPA and results presented by Sauer et al. [8,9], we observed a systematic trend depending on the ionization stage. Further investigations showed that, by introducing a simple correction to the LPA model, it is possible to fit its predictions to the expected results.

The proposed modification to amend this issue occurring at high ionization states is to separate the correction term $ln(\gamma)$ and replace it with some simple function $f(Z, N)$ of the atomic number Z and of the number of bound electrons N. This modification changes the Eq. (4) into the following general form:

$$ln(MEE) = \frac{4\pi}{N}\int r^2 \rho(r) ln(\hbar\omega_0(r)) dr + f(Z, N). \tag{6}$$

Another shortcoming of the LPA is that it cannot reproduce properly MEE differences between H-like and He-like ions. Adding an electron to the K-shell increases electron density approximately twice, so within the LPA model the change is significant. However, the real change of MEE is much smaller, since both electrons occupy the same shell and the rearrangement of energy levels is minor. To overcome this deficiency, for the H-like and He-like ions we used the values obtained from FAC.

3.2. Parametrization of the modified LPA for $Z \leq 30$ elements

The analysis of the difference between results of Sauer et al. [8,9] and the LPA without any correction factor, (i.e. for $f(Z, N) = 0$), as a function of the number of bound electrons N, leads to the conclusion that the difference follows an exponential curve (see Fig. 2). Thus, we propose a function in the following form: $f(Z, N) = exp(\frac{Z-N}{Z}) - 0.84$ to replace $ln(\gamma)$. The effective equation for the modified LPA of the MEE takes then the following form:

$$ln(MEE) = \frac{4\pi}{N}\int r^2 \rho(r) ln(\hbar\omega_0(r)) dr + exp(\frac{Z-N}{Z}) - 0.84. \tag{7}$$

The exponential term was assumed *a priori* and the constant −0.84 was determined from the fit of MEE values to the available results of Sauer et al. [8,9], by minimizing the root mean square of the difference in $ln(MEE)$ values. Fig. 2 shows the difference between results from Sauer et al. and the LPA with $f(Z, N) = 0$. The proposed function $f(Z, N) = exp(\frac{Z-N}{Z}) - 0.84$, which is used to describe this difference, is plotted against it.

To better illustrate how our model compares against results of Sauer et al. [8,9], we present in Fig. 3 the normalized difference calculated as:

$$\delta_{MEE} = \frac{MEE_{Sauer} - MEE_{LPA}}{MEE_{Sauer}}, \tag{8}$$

where MEE_{Sauer} is the result of Sauer et al. [8,9] and MEE_{LPA} is the result from the LPA model. Comparison for both the original and modified LPA is presented.

Fig. 4 presents the comparison of MEE of argon ions obtained by Sauer et al. [8,9] against the results from the proposed modified LPA.

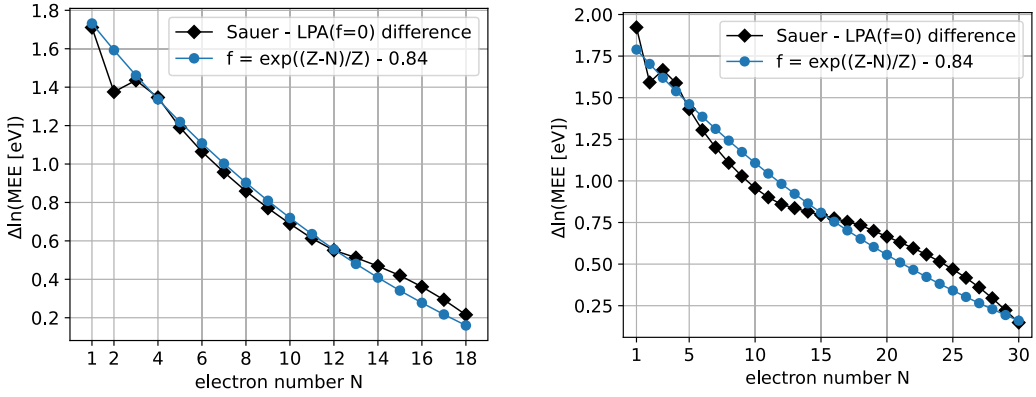

Fig. 2. Difference of ln(MEE) between the original LPA and results presented by Sauer et al. [8,9] for the Ar ions ($Z = 18$) (left) and the Zn ions ($Z = 30$) (right).

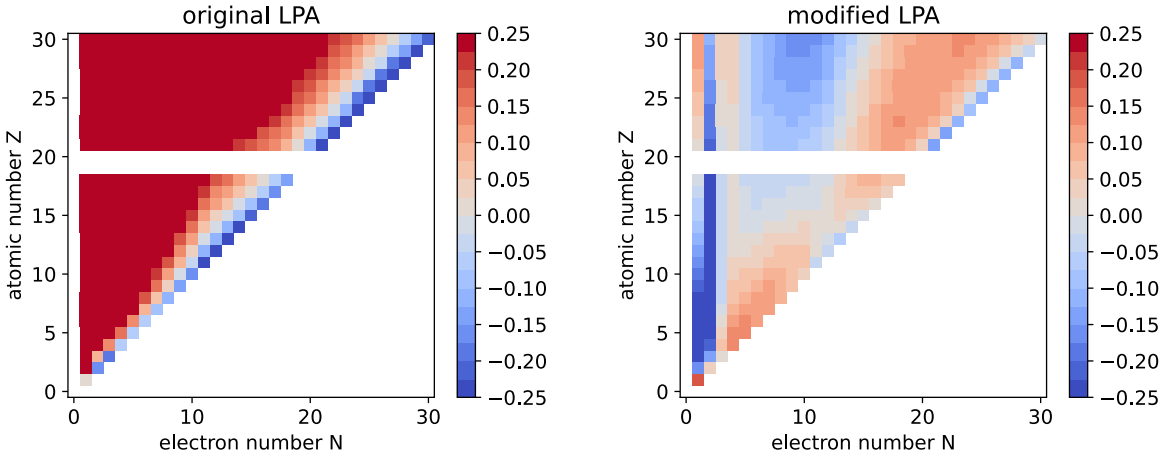

Fig. 3. Normalized difference δ_{MEE} between results from [8,9] and original LPA (left), modified LPA (right) for $1 \leq Z \leq 30$. Data for $Z = 19$, 20 are missing in Sauer et al.

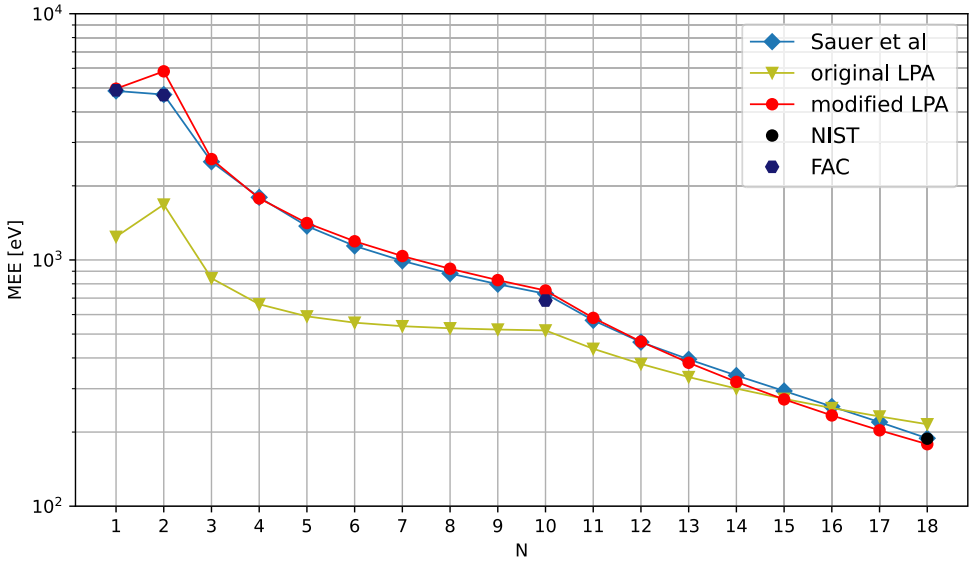

Fig. 4. MEE for Ar ions. Red dots represent the modified LPA model and yellow triangles the original LPA model. Blue squares show the data from [8,9]. The black dot shows the NIST value for the neutral atom [32] and the dark blue hexagon values obtained from FAC calculations for selected ions, as explained in Section 2. (For interpretation of the references to colour in this figure legend, the reader is referred to the web version of this article.)

For the neutral atom, the experimentally measured value, from the NIST database [32], is also presented. The NIST database lists MEE values for substances in normal conditions, so values for the non-noble gases may differ from calculated ones due to molecular bounds.

Excluding H-like and He-like ions, the highest relative difference between the modified LPA and results from Sauer et al. [8,9] is 18%, and is observed for C^{1+} ion. The highest relative difference for the logarithms of the compared values is 5.3% for neutral Be. There seems

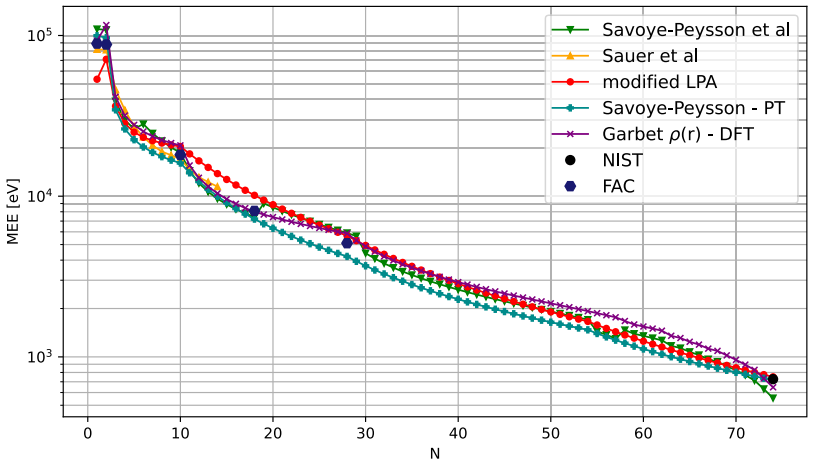

Fig. 5. Comparison of MEE of W ions. The green line represents results based on [3]. The orange line shows the extrapolation proposed in [8,9]. The red line represents the modified LPA model proposed in this work. The dark cyan line presents results obtained with the Savoye-Peysson model using optimized PT parameters. The purple line shows results obtained with the method proposed by Garbet, based on the electron density obtained with DFT. The black dot shows the NIST value for the neutral atom [32] and the dark blue hexagon values obtained from FAC calculations for selected ions. (For interpretation of the references to colour in this figure legend, the reader is referred to the web version of this article.)

to be a systematic pattern in the differences presented in Fig. 3. If additional data for higher Z elements were available, probably it would be possible to introduce a second correction term to amend these differences. Values provided by Sauer et al. [8,9] are preferred over the LPA in the summary of MEE in Table 1. For comparison, results from the modified LPA can be found in Table 3.

3.3. Extrapolation to high-Z elements ($Z > 30$)

Initial tests included elements calculated by Sauer et al. [8,9] The relatively good agreement of the proposed $f(Z,N)$ function in this range raised the question of its applicability at higher atomic numbers. To test it for high-Z elements, heavier than the ones calculated by Sauer et al. ($Z \leq 30$), we compared our model with other approximations available for tungsten. W is an element of special interest for the nuclear fusion community, since it was selected as plasma facing material for the International Thermonuclear Experimental Reactor (ITER) [33,34]. Due to this interest in W, we already had electron densities of tungsten ions calculated using Density Functional Theory (DFT) — an ab-initio method [31]. These DFT calculations were performed with the Gaussian software package [35]. The hybrid exchange–correlation functional PBE1PBE (known also as PBE0) [36,37], along with the atomic natural orbital-relativistic correlation consistent basic set (ANO-RCC) was used. The results from Gaussian were then post-processed in the Multiwfn program [38], which was used to obtain the spherically averaged electron density $\rho(r)$. These results allowed us to compare our results for tungsten with additional methods, with accurate electron density obtained independently of atomic model approximation from [31], thus eliminating this source of uncertainty.

In Fig. 5, we present a comparison of MEE of tungsten ions obtained with different methods. To the best of our knowledge, the results of the ab-initio MEE calculations for tungsten ions have not been published so far, so we compare our proposed model only with other approximations. One of them, proposed by Sauer et al. in [8,9], is based on the structural similarity of the ions with the same number of electrons and basically extrapolates the MEE from the lower-Z elements. The other approximation is the variational quantum description initially proposed by Garbet [19]. The main idea of this approach is that the MEE value is bound by relations between moments of the dipole oscillator strength distribution (DOSD). Taking the average of these bounds, we can estimate the MEE with the following equations (the equations below use atomic units, for the full derivation of this approximation, see [19]):

$$ln(MEE) = \frac{1}{2} ln\left(\frac{S(1)}{S(-1)}\right), \tag{9}$$

where $S(\mu)$ are moments of the DOSD:

$$S(-1) = \frac{2m}{3\hbar^2} a_0^2 \langle (\frac{r}{a_0})^2 \rangle, \tag{10}$$

$$S(1) = 4/3 K_0, \tag{11}$$

where K_0 is the average kinetic energy of the bound electrons, a_0 is the Bohr radius, m denotes the electron mass and r is the radial coordinate. In atomic units, Eq. (9) can be simplified to:

$$MEE = \sqrt{2K_0/\langle r^2 \rangle}. \tag{12}$$

In this work, we use the version of Garbet's method proposed by Savoye-Peysson et al. in [3], where K_0 and $\langle r^2 \rangle$ are calculated with the virial theorem using the multi-Yukawa description of electron density:

$$MEE[eV] = \frac{\alpha^2 mc^2}{\sqrt{6\sum_i a_i \lambda_i^{-2}}} \sqrt{\sum_i (Z-N) a_i \lambda_i + N \sum_i \sum_j a_i a_j \frac{\lambda_i^2}{\lambda_i \lambda_j}}, \tag{13}$$

where $\alpha^2 mc^2 \approx 27.211$ eV represents unit conversion from atomic units to eV, a and λ are parameters of the ions in the multi-Yukawa model, as defined and calculated in [3]. We also calculated MEE using the same methodology, but with a and λ parameters obtained from the optimized PT model [31].

In addition, we also calculated MEE using Garbet's model with the average kinetic energy calculated using the Thomas–Fermi atomic model. For this purpose, we used the following formulas, with the spherically averaged electron density obtained from DFT calculations:

$$K_0 = C_k 4\pi \int r^2 \rho(r)^{5/3} dr, \tag{14}$$

where $C_k = \frac{3}{10}(3\pi^2)^{2/3}$ (in atomic units) and:

$$\langle r^2 \rangle = \frac{4\pi}{N} \int r^4 \rho(r) dr. \tag{15}$$

The highest relative difference between models is for $N = 27$, when the highest value is 36% larger than the lowest one. When comparing $ln(MEE)$, the difference is less than 4.3%. Therefore, the agreement between the compared models is acceptable for the purpose of calculation of the stopping power with Bethe's model, where the logarithm of MEE is used. Estimating an uncertainty of our approach is difficult for elements where no ab-initio results are available as a reference. To provide some figure of merit, we decided to compare the results obtained from these different approaches and to calculate the coefficient of variation (CV, also known as relative standard deviation)

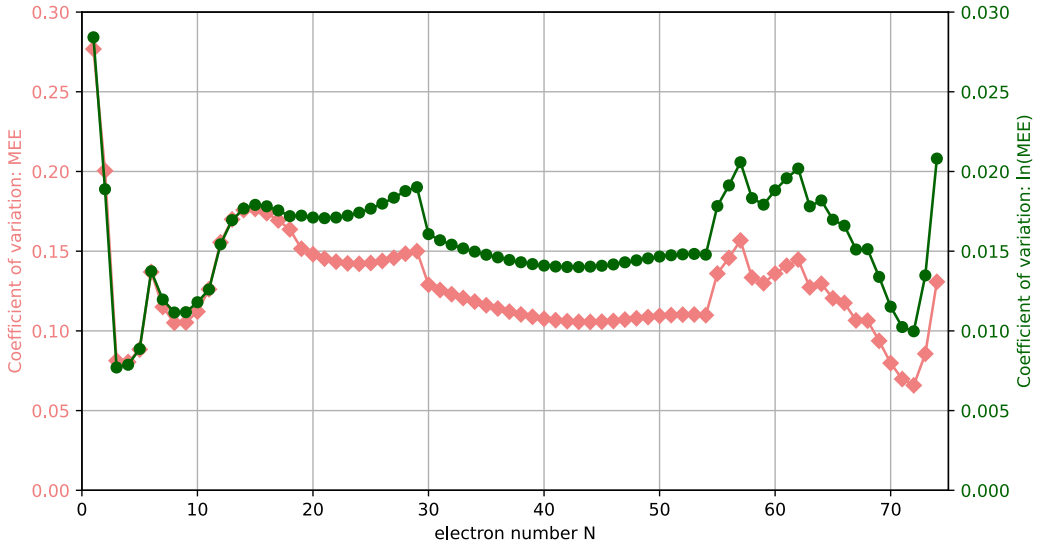

Fig. 6. Coefficient of variation of MEE calculated for tungsten ions, obtained with the models presented in Fig. 5. Light red CV values for MEE, dark green CV values for ln(MEE). (For interpretation of the references to colour in this figure legend, the reader is referred to the web version of this article.)

of results for each W ion. As the logarithm of MEE is the value of interest for practical application, we also present the analogous CV value for $ln(MEE)$, as presented in Fig. 6.

4. Summary

The presented work provides values of MEE for all atoms and ions for $1 \leq Z \leq 86$. An empirical modification of the LPA is proposed, based on the data available in the literature. The proposed modification is to replace the original $ln(\gamma)$ correction term by the function: $exp(\frac{Z-N}{Z}) - 0.84$ of the atomic number Z and the electron number N. It is likely that this simple function compensates some missing terms of the original LPA, though we were not able to find a satisfying physical explanation of the proposed formula, therefore we treat it as an empirical modification. The detailed analysis of the calculation method is presented, along with the comparison of the obtained results with the values from other approximations of MEE available for tungsten. In the worst case, the highest difference between the tested models was 36% in absolute value and 5.3% for the logarithm of MEE. For most ions, the coefficient of variation between the different models is less than 20%. This corresponds to an uncertainty smaller than 5% for the logarithm of MEE, which is the value of interest in the case of Bethe's theory of stopping power.

4.1. Dataset of MEE for all elements and ions for $1 \leq Z \leq 86$

As the final result of this work, we present in Table 1 the MEE values of all ions for all elements up to radon ($Z = 86$). When possible, the values obtained with the definition presented in Eq. (1) and taken from the results of ab-initio calculation of Sauer et al. [8,9] are used. The remaining elements ($Z = 19, 20$ and $Z > 30$) are calculated with the modified version of the LPA given by Eq. (7), except for the H-like and He-like ions — for them the MEE is obtained using FAC. The resulting table is visualized in Fig. 7 and the corresponding values can be accessed in csv format on the GitHub repository of the author 'https://github.com/jjwalkowiak/Mean_excitation_energy'.

4.2. Additional datasets

The MEE values calculated by FAC for H-like and He-like ions can be found in Table 2. Those calculated with the modified LPA, but not presented in Table 1, can be found in Table 3. Table 4 provides K-shell ionization values for neutral atom and H-like ions, which can be used to estimate the range of validity.

CRediT authorship contribution statement

J. Walkowiak: Writing – original draft, Software, Methodology, Conceptualization. **J. Bielecki:** Writing – original draft, Supervision, Methodology, Conceptualization. **J. Bieroń:** Writing – review & editing, Conceptualization. **A. Jardin:** Writing – original draft, Methodology, Conceptualization. **Y. Savoye-Peysson:** Writing – review & editing, Validation. **D. Mazon:** Project administration, Funding acquisition. **K. Król:** Resources. **D. Dworak:** Resources. **M. Scholz:** Project administration, Funding acquisition.

Declaration of competing interest

The authors declare that they have no known competing financial interests or personal relationships that could have appeared to influence the work reported in this paper.

Data availability

Link to the data/code is include in the manuscript.

Acknowledgements

This work has been partially funded by the National Science Centre, Poland (NCN) grant HARMONIA 10 no. 2018/30/M/ST2/00799. We gratefully acknowledge Polish high-performance computing infrastructure PLGrid (HPC Center: ACK Cyfronet AGH) for providing computer facilities and support within computational grant no. PLG/2024/016925. This work has been published in the framework of the international project co-financed by the Polish Ministry of Education and Science, Poland, as program "PMW". This work has been carried out within the framework of the EUROfusion Consortium, funded by the European Union via the Euratom Research and Training Programme (Grant Agreement No 101052200 — EUROfusion). Views and opinions expressed are however those of the authors only and do not necessarily reflect those of the European Union or the European Commission. Neither the European Union nor the European Commission can be held responsible for them.

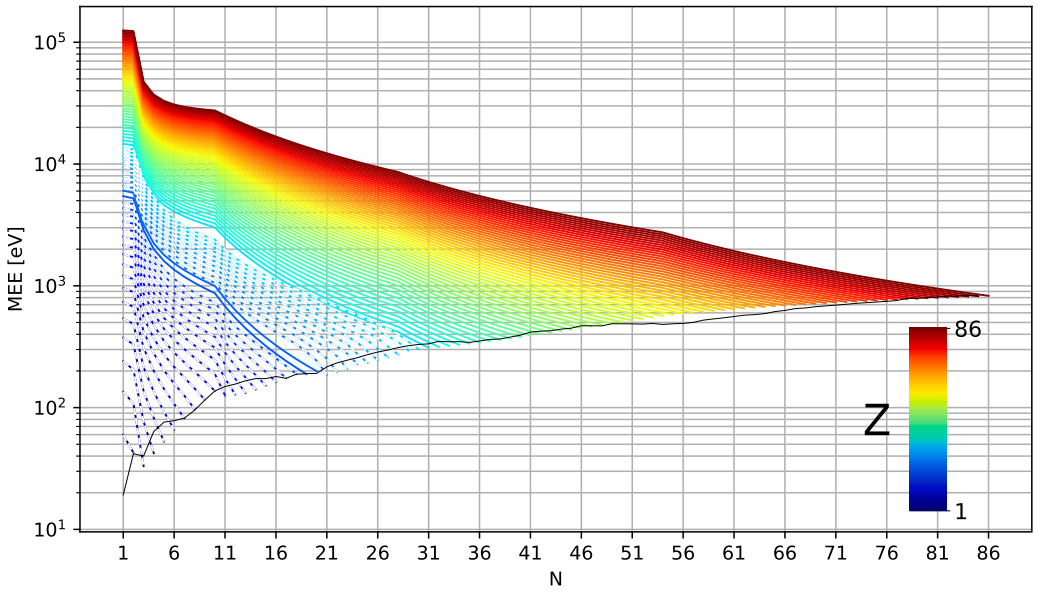

Fig. 7. MEE of all elements and their ions for $1 \leq Z \leq 86$. Each line represents one element and its colour corresponds to the atomic number. The black line represents values from the NIST database for neutral atoms [32]. Dashed lines represent results of Sauer et al. [8,9] for elements included in their work ($Z \leq 30$).

References

[1] H.A. Bethe, Ann. Phys. (Leipzig) 397 (1930) 325, http://dx.doi.org/10.1002/andp.19303970303.
[2] H.A. Bethe, Z. Phys. 76 (1932) 293, http://dx.doi.org/10.1007/BF01342532.
[3] Y. Savoye-Peysson, D. Mazon, J. Bielecki, D. Dworak, K. Król, A. Jardin, M. Scholz, J. Walkowiak, J. Decker, Nucl. Fusion 63 (2023) 126041, http://dx.doi.org/10.1088/1741-4326/acffd9.
[4] L. Hesslow, O. Embréus, A. Stahl, T.C. DuBois, G. Papp, S.L. Newton, T. Fülöp, Phys. Rev. Lett. 118 (2017) 255001, http://dx.doi.org/10.1103/PhysRevLett.118.255001.
[5] L. Hesslow, O. Embréus, G.J. Wilkie, G. Papp, T. Fülöp, Plasma Phys. Control. Fusion 60 (2018) 074010, https://iopscience.iop.org/article/10.1088/1361-6587/aac33e.
[6] M. Hoppe, O. Embréus, T. Fülöp, Comput. Phys. Comm. 268 (2021) 108098, http://dx.doi.org/10.1016/j.cpc.2021.108098.
[7] Y. Peysson, J. Decker, E. Nilsson, J.-F. Artaud, A. Ekedahl, M. Goniche, J. Hillairet, B. Ding, M. Li, P.T. Bonoli, S. Shiraiwa, M. Madi, Plasma Phys. Control. Fusion 58 (2016) 044008, https://iopscience.iop.org/article/10.1088/0741-3335/58/4/044008.
[8] S.P. Sauer, J.R. Sabin, J. Oddershede, J. Chem. Phys. 148 (2018) 174307, http://dx.doi.org/10.1063/1.5027708.
[9] S.P. Sauer, J.R. Sabin, J. Oddershede, Mol. Phys. 119 (5) (2020) http://dx.doi.org/10.1080/00268976.2020.1823508.
[10] C. Froese Fischer, G. Gaigalas, P. Jönsson, J. Bieroń, Comput. Phys. Comm. 237 (2018) 184–187, http://dx.doi.org/10.1016/j.cpc.2018.10.032.
[11] K. Aidas, C. Angeli, K.L. Bak, V. Bakken, R. Bast, L. Boman, O. Christiansen, R. Cimiraglia, S. Coriani, P. Dahle, E.K. Dalskov, U. Ekström, T. Enevoldsen, J.J. Eriksen, P. Ettenhuber, B. Fernández, L. Ferrighi, H. Fliegl, L. Frediani, K. Hald, A. Halkier, C. Hättig, H. Heiberg, T. Helgaker, A.C. Hennum, H. Hettema, E. Hjertenæ s, S. Hø st, I.-M. Hø yvik, M.F. Iozzi, B. Jansík, H.J. Jensen, D. Jonsson, P. Jø rgensen, J. Kauczor, S. Kirpekar, T. Kjæ rgaard, W. Klopper, S. Knecht, R. Kobayashi, H. Koch, J. Kongsted, A. Krapp, K. Kristensen, A. Ligabue, O.B. Lutnæ s, J.I. Melo, K.V. Mikkelsen, R.H. Myhre, C. Neiss, C.B. Nielsen, P. Norman, J. Olsen, J.M. Olsen, A. Osted, J. Packer, F. Pawlowski, T.B. Pedersen, P.F. Provasi, S. Reine, Z. Rinkevicius, T.A. Ruden, K. Ruud, V.V. Rybkin, P. Sał ek, C.C. Samson, A.S. de Merás, T. Saue, S.P. Sauer, B. Schimmelpfennig, K. Sneskov, A.H. Steindal, K.O. Sylvester-Hvid, P.R. Taylor, A.M. Teale, E.I. Tellgren, D.P. Tew, A.J. Thorvaldsen, L. Thø gersen, O. Vahtras, M.A. Watson, D.J. Wilson, M. Ziolkowski, H. Agren, WIREs Comput. Mol. Sci. 4 (2014) 269–284, http://dx.doi.org/10.1002/wcms.1172.
[12] International Commission on Radiation Units and Measurements, Bethesda, MD (United States), 1984, Stopping powers for electrons and positrons (ICRU-37) https://journals.sagepub.com/toc/crub/os-19/2.
[13] J. Oddershede, J.R. Sabin, At. Data Nucl. Data Tables 31 (2) (1984) http://dx.doi.org/10.1016/0092-640X(84)90024-X.
[14] M. Inokuti, J.L. Dehmer, T. Baer, J.D. Hanson, Phys. Rev. A 23 (1981) 95, http://dx.doi.org/10.1103/PhysRevA.23.95.
[15] S. Kamakura, N. Sakamoto, H. Ogawa, Hi. Tsuchida, M. Inokuti, J. Appl. Phys. 100 (2006) 064905, http://dx.doi.org/10.1063/1.2345478.
[16] P.W.K. Jensen, S.P. Sauer, J. Oddershede, J.R. Sabin, Nucl. Instrum. Methods Phys. Res. B. 394 (2017) 73–80, http://dx.doi.org/10.1016/j.nimb.2016.12.034.
[17] M. Strait, JINST 19 (2024) P01009, http://dx.doi.org/10.1088/1748-0221/19/01/P01009.
[18] J. Lindhard, M. Scharff, Mat. Fys. Medd. K. Dan. Vidensk. Selsk. 27 (1953) 15.
[19] X. Garbet, C. Deutsch, G. Maynard, J. Appl. Phys. 61 (1987) 907–916, http://dx.doi.org/10.1063/1.338141.
[20] E.J. McGuire, J.M. Peek, L.C. Pitchford, Phys. Rev. A 26 (1982) 1318, http://dx.doi.org/10.1103/PhysRevA.26.1318.
[21] D.E. Meltzer, J.R. Sabin, S.B. Trickey, Phys. Rev. A 41 (1990) 220, http://dx.doi.org/10.1103/PhysRevA.41.220.
[22] M.F. Gu, Can. J. Phys. 86 (2008) 675–689, http://dx.doi.org/10.1139/p07-197.
[23] A. Kramida, Y. Ralchenko, J. Reader, NIST ASD Team, NIST Atomic Spectra Database (Ver. 5.11), National Institute of Standards and Technology, Gaithersburg, MD, 2024, http://dx.doi.org/10.18434/T4W30F.
[24] A.C. Thompson, D.T. Attwood, E.M. Gullikson, M.R. Howells, J.B. Kortright, A.L. Robinson, J.H. Underwood, K.-J. Kim, J. Kirz, I. Lindau, P. Pianetta, H. Winick, G.P. Williams, J.H. Scofield, D. Vaughan, X-ray Data Booklet, Lawrence Berkeley National Laboratory, University of California, 2009, https://xdb.lbl.gov/.
[25] H. Douglas, Phys. Rev. A 40 (1989) 604, http://dx.doi.org/10.1103/PhysRevA.40.604.
[26] P. Pyykkö, Annu. Rev. Phys. Chem. 63 (2012) 45–64, http://dx.doi.org/10.1146/annurev-physchem-032511-143755.
[27] S. Rosendorff, H.G. Schlaile, Phys. Rev. A 40 (1989) 6892, http://dx.doi.org/10.1103/PhysRevA.40.6892.
[28] S.M. Cohen, Phys. Rev. A 68 (2003) 042704, http://dx.doi.org/10.1103/PhysRevA.68.042704.
[29] M.F. Gu, FAC 1.1.5 manual, 2024, https://github.com/flexible-atomic-code/fac/blob/release-pdf/manual.pdf.
[30] W.K. Chu, D. Powerd, Phys. Rev. A 40 (1972) 23–24, http://dx.doi.org/10.1016/0375-9601(72)90181-8.
[31] J. Walkowiak, A. Jardin, J. Bielecki, Y. Peysson, D. Mazon, D. Dworak, K. Król, M. Scholz, Phys. Plasmas 29 (2022) 022501, http://dx.doi.org/10.1063/5.0075859.
[32] National Institute of Standards, Technology (NIST) Database, https://physics.nist.gov/PhysRefData/XrayMassCoef/tab1.html.
[33] V. Philipps, Ph. Mertens, G.F. Matthews, H. Maier, JET-EFDA contributors, Fusion Eng. Des. 85 (2010) 1581–1586, http://dx.doi.org/10.1016/j.fusengdes.2010.04.048.
[34] R.A. Pitts, X. Bonnin, F. Escourbiac, H. Frerichs, J.P. Gunn, T. Hirai, A.S. Kukushkin, E. Kaveeva, M.A. Miller, D. Moulton, V. Rozhansky, I. Senichenkov, E. Sytova, O. Schmitz, P.C. Stangeby, G. De Temmerman, I. Veselova, S. Wiesen, Nucl. Mater. Energy 20 (2019) 100696, http://dx.doi.org/10.1016/j.nme.2019.100696.
[35] Gaussian 16, Revision C.01, M.J. Frisch, G.W. Trucks, H.B. Schlegel, G.E. Scuseria, M.A. Robb, J.R. Cheeseman, G. Scalmani, V. Barone, G.A. Petersson, H. Nakatsuji, X. Li, M. Caricato, A.V. Marenich, J. Bloino, B.G. Janesko, R. Gomperts, B. Mennucci, H.P. Hratchian, J.V. Ortiz, A.F. Izmaylov, J.L. Sonnenberg, D. Williams-Young, F. Ding, F. Lipparini, F. Egidi, J. Goings, B. Peng, A. Petrone, T. Henderson, D. Ranasinghe, V.G. Zakrzewski, J. Gao, N. Rega, G. Zheng, W. Liang,

M. Hada, M. Ehara, K. Toyota, R. Fukuda, J. Hasegawa, M. Ishida, T. Nakajima, Y. Honda, O. Kitao, H. Nakai, T. Vreven, K. Throssell, Jr. J.A. Montgomery, J.E. Peralta, F. Ogliaro, M.J. Bearpark, J.J. Heyd, E.N. Brothers, K.N. Kudin, V.N. Staroverov, T.A. Keith, R. Kobayashi, J. Normand, K. Raghavachari, A.P. Rendell, J.C. Burant, S.S. Iyengar, J. Tomasi, M. Cossi, J.M. Millam, M. Klene, C. Adamo, R. Cammi, J.W. Ochterski, R.L. Martin, K. Morokuma, O. Farkas, J.B. Foresman, D.J. Fox, 2019, Gaussian, Inc., Wallingford CT, https://gaussian.com/.

[36] J.P. Perdew, M. Ernzerhof, K. Burke, J. Chem. Phys. 105 (22) (1996) 9982–9985, http://dx.doi.org/10.1063/1.472933.

[37] C. Adamo, V. Barone, J. Chem. Phys. 110 (13) (1999) 6158–6170, http://dx.doi.org/10.1063/1.478522.

[38] T. Lu, F. Chen, J. Comput. Chem. 33 (2011) http://dx.doi.org/10.1002/jcc.22885.

Explanation of Tables

Table 1. Mean Excitation Energy for all elements from H to Rn, in eV

Z	Atomic number
N	Number of electrons

Each record represents MEE [eV] for one ion — defined by position in the table as column (Z): element and row (N): number of electrons.

Table 2. Mean Excitation Energy calculated with FAC for H-like and He-like ions

Element	Element symbol
Z	Atomic number
H-like MEE [eV]	Mean excitation energy in eV
H-like R / N-R	presented MEE related to the non-relativistic approximation from Eq. (2)
He-like MEE [eV]	Mean excitation energy in eV
He-like R / N-R	presented MEE related to the non-relativistic approximation from Eq. (3)

Table 3. Mean Excitation Energy from modified LPA for $Z \leq 18$ and $21 \leq Z \leq 30$, in eV

Z	Atomic number
N	Number of electrons

Each record represents MEE [eV] for one ion — defined by position in the table as column (Z): element and row (N): number of electrons.

Table 4. K-shell ionization energy for neutral atoms and H-like ions, retrieved from [23,24]

Element	Element symbol
Z	Atomic number
H-like ion	K-shell ionization energy for H-like ion
neutral	K-shell ionization energy for neutral atom

Table 1
MEE for all elements from H to Rn, in eV

Z	1	2	3	4	5	6	7	8
N	H	He	Li	Be	B	C	N	O
1	1.499E+01	5.988E+01	1.345E+02	2.402E+02	3.746E+02	5.395E+02	7.343E+02	9.590E+02
2		4.268E+01	1.083E+02	2.050E+02	3.304E+02	4.862E+02	6.720E+02	8.878E+02
3			3.310E+01	7.690E+01	1.369E+02	2.142E+02	3.087E+02	4.207E+02
4				4.220E+01	8.230E+01	1.348E+02	2.002E+02	2.786E+02
5					5.260E+01	9.260E+01	1.424E+02	2.022E+02
6						6.590E+01	1.074E+02	1.572E+02
7							8.160E+01	1.252E+02
8								9.790E+01

Z	9	10	11	12	13	14	15	16
N	F	Ne	Na	Mg	Al	Si	P	S
1	1.214E+03	1.498E+03	1.814E+03	2.159E+03	2.534E+03	2.938E+03	3.373E+03	3.838E+03
2	1.134E+03	1.409E+03	1.716E+03	2.052E+03	2.417E+03	2.813E+03	3.239E+03	3.695E+03
3	5.500E+02	6.968E+02	8.612E+02	1.043E+03	1.243E+03	1.460E+03	1.695E+03	1.947E+03
4	3.702E+02	4.750E+02	5.933E+02	7.248E+02	8.696E+02	1.028E+03	1.200E+03	1.385E+03
5	2.723E+02	3.526E+02	4.435E+02	5.448E+02	6.564E+02	7.786E+02	9.112E+02	1.055E+03
6	2.156E+02	2.828E+02	3.587E+02	4.438E+02	5.374E+02	6.401E+02	7.517E+02	8.722E+02
7	1.764E+02	2.352E+02	3.019E+02	3.767E+02	4.592E+02	5.497E+02	6.482E+02	7.546E+02
8	1.440E+02	1.969E+02	2.568E+02	3.243E+02	3.988E+02	4.806E+02	5.697E+02	6.662E+02
9	1.165E+02	1.652E+02	2.204E+02	2.825E+02	3.510E+02	4.265E+02	5.088E+02	5.980E+02
10		1.372E+02	1.892E+02	2.468E+02	3.108E+02	3.814E+02	4.585E+02	5.421E+02
11			1.257E+02	1.737E+02	2.258E+02	2.831E+02	3.459E+02	4.144E+02
12				1.280E+02	1.727E+02	2.212E+02	2.743E+02	3.324E+02
13					1.322E+02	1.772E+02	2.252E+02	2.773E+02
14						1.408E+02	1.853E+02	2.328E+02
15							1.516E+02	1.957E+02
16								1.624E+02

Z	17	18	19	20	21	22	23	24
N	Cl	Ar	K	Ca	Sc	Ti	V	Cr
1	4.333E+03	4.857E+03	5.45E+03	6.04E+03	6.61E+03	7.26E+03	7.93E+03	8.63E+03
2	4.180E+03	4.696E+03	5.22E+03	5.80E+03	6.36E+03	7.06E+03	7.72E+03	8.42E+03
3	2.217E+03	2.505E+03	2.87E+03	3.18E+03	3.47E+03	3.83E+03	4.21E+03	4.60E+03
4	1.584E+03	1.796E+03	2.00E+03	2.23E+03	2.51E+03	2.78E+03	3.06E+03	3.35E+03
5	1.208E+03	1.373E+03	1.60E+03	1.79E+03	1.93E+03	2.14E+03	2.35E+03	2.58E+03
6	1.002E+03	1.140E+03	1.35E+03	1.53E+03	1.61E+03	1.78E+03	1.97E+03	2.16E+03
7	8.691E+02	9.916E+02	1.19E+03	1.34E+03	1.41E+03	1.56E+03	1.72E+03	1.89E+03
8	7.699E+02	8.811E+02	1.06E+03	1.20E+03	1.26E+03	1.40E+03	1.55E+03	1.70E+03
9	6.940E+02	7.970E+02	9.55E+02	1.09E+03	1.15E+03	1.28E+03	1.41E+03	1.56E+03
10	6.321E+02	7.288E+02	8.70E+02	9.98E+02	1.06E+03	1.18E+03	1.31E+03	1.45E+03
11	4.886E+02	5.686E+02	6.77E+02	7.81E+02	8.43E+02	9.46E+02	1.05E+03	1.17E+03
12	3.955E+02	4.639E+02	5.45E+02	6.32E+02	7.00E+02	7.89E+02	8.83E+02	9.83E+02
13	3.338E+02	3.949E+02	4.49E+02	5.22E+02	6.06E+02	6.86E+02	7.71E+02	8.60E+02
14	2.841E+02	3.394E+02	3.77E+02	4.40E+02	5.31E+02	6.03E+02	6.80E+02	7.62E+02
15	2.429E+02	2.937E+02	3.21E+02	3.75E+02	4.69E+02	5.36E+02	6.06E+02	6.81E+02
16	2.068E+02	2.540E+02	2.77E+02	3.25E+02	4.17E+02	4.78E+02	5.43E+02	6.12E+02
17	1.749E+02	2.195E+02	2.41E+02	2.84E+02	3.71E+02	4.29E+02	4.90E+02	5.54E+02
18		1.887E+02	2.13E+02	2.50E+02	3.32E+02	3.86E+02	4.43E+02	5.03E+02
19			1.89E+02	2.23E+02	2.87E+02	3.39E+02	3.93E+02	4.50E+02
20				1.99E+02	2.43E+02	2.95E+02	3.48E+02	4.03E+02
21					1.87E+02	2.53E+02	3.06E+02	3.59E+02
22						1.97E+02	2.64E+02	3.17E+02
23							2.08E+02	2.77E+02
24								2.28E+02

Z	25	26	27	28	29	30	31	32
N	Mn	Fe	Co	Ni	Cu	Zn	Ga	Ge
1	9.37E+03	1.01E+04	1.09E+04	1.18E+04	1.26E+04	1.35E+04	1.46E+04	1.56E+04
2	9.15E+03	9.84E+03	1.07E+04	1.15E+04	1.23E+04	1.32E+04	1.43E+04	1.52E+04
3	5.02E+03	5.45E+03	5.89E+03	6.36E+03	6.84E+03	7.34E+03	7.46E+03	7.92E+03
4	3.66E+03	3.98E+03	4.32E+03	4.67E+03	5.03E+03	5.40E+03	5.49E+03	5.85E+03
5	2.82E+03	3.07E+03	3.33E+03	3.60E+03	3.88E+03	4.17E+03	4.60E+03	4.91E+03
6	2.36E+03	2.57E+03	2.79E+03	3.02E+03	3.26E+03	3.51E+03	4.08E+03	4.36E+03
7	2.07E+03	2.26E+03	2.45E+03	2.66E+03	2.87E+03	3.09E+03	3.71E+03	3.98E+03
8	1.87E+03	2.04E+03	2.21E+03	2.40E+03	2.59E+03	2.79E+03	3.44E+03	3.69E+03
9	1.71E+03	1.87E+03	2.03E+03	2.20E+03	2.38E+03	2.57E+03	3.21E+03	3.46E+03
10	1.59E+03	1.74E+03	1.89E+03	2.05E+03	2.22E+03	2.40E+03	3.02E+03	3.26E+03
11	1.29E+03	1.42E+03	1.55E+03	1.69E+03	1.83E+03	1.98E+03	2.48E+03	2.69E+03
12	1.09E+03	1.20E+03	1.31E+03	1.43E+03	1.56E+03	1.69E+03	2.09E+03	2.27E+03
13	9.54E+02	1.05E+03	1.16E+03	1.27E+03	1.38E+03	1.50E+03	1.78E+03	1.94E+03
14	8.47E+02	9.37E+02	1.03E+03	1.13E+03	1.23E+03	1.34E+03	1.54E+03	1.68E+03

15	7.60E+02	8.42E+02	9.29E+02	1.02E+03	1.12E+03	1.22E+03	1.35E+03	1.48E+03
16	6.85E+02	7.62E+02	8.43E+02	9.27E+02	1.02E+03	1.11E+03	1.19E+03	1.31E+03
17	6.22E+02	6.94E+02	7.69E+02	8.48E+02	9.31E+02	1.02E+03	1.06E+03	1.16E+03
18	5.67E+02	6.35E+02	7.05E+02	7.80E+02	8.58E+02	9.39E+02	9.53E+02	1.05E+03
19	5.11E+02	5.74E+02	6.40E+02	7.10E+02	7.83E+02	8.59E+02	8.60E+02	9.45E+02
20	4.60E+02	5.20E+02	5.83E+02	6.49E+02	7.17E+02	7.89E+02	7.81E+02	8.59E+02
21	4.14E+02	4.72E+02	5.32E+02	5.94E+02	6.59E+02	7.28E+02	7.12E+02	7.84E+02
22	3.71E+02	4.27E+02	4.84E+02	5.44E+02	6.07E+02	6.72E+02	6.53E+02	7.19E+02
23	3.31E+02	3.85E+02	4.41E+02	4.98E+02	5.59E+02	6.21E+02	6.01E+02	6.63E+02
24	2.76E+02	3.43E+02	3.98E+02	4.54E+02	5.12E+02	5.73E+02	5.55E+02	6.13E+02
25	2.33E+02	2.89E+02	3.57E+02	4.12E+02	4.69E+02	5.28E+02	5.15E+02	5.69E+02
26		2.46E+02	3.03E+02	3.71E+02	4.27E+02	4.85E+02	4.79E+02	5.29E+02
27			2.59E+02	3.17E+02	3.86E+02	4.43E+02	4.47E+02	4.94E+02
28				2.73E+02	3.47E+02	4.03E+02	4.18E+02	4.63E+02
29					2.95E+02	3.48E+02	3.76E+02	4.17E+02
30						3.03E+02	3.41E+02	3.78E+02
31							3.10E+02	3.44E+02
32								3.15E+02

Z	33	34	35	36	37	38	39	40
N	As	Se	Br	Kr	Rb	Sr	Y	Zr
1	1.66E+04	1.77E+04	1.87E+04	1.98E+04	2.10E+04	2.22E+04	2.34E+04	2.46E+04
2	1.62E+04	1.73E+04	1.83E+04	1.94E+04	2.05E+04	2.17E+04	2.29E+04	2.41E+04
3	8.39E+03	8.87E+03	9.37E+03	9.87E+03	1.04E+04	1.09E+04	1.15E+04	1.20E+04
4	6.21E+03	6.59E+03	6.97E+03	7.37E+03	7.77E+03	8.18E+03	8.60E+03	9.03E+03
5	5.23E+03	5.56E+03	5.90E+03	6.25E+03	6.60E+03	6.96E+03	7.33E+03	7.71E+03
6	4.66E+03	4.96E+03	5.27E+03	5.59E+03	5.92E+03	6.26E+03	6.60E+03	6.95E+03
7	4.26E+03	4.55E+03	4.84E+03	5.14E+03	5.46E+03	5.77E+03	6.10E+03	6.44E+03
8	3.96E+03	4.23E+03	4.51E+03	4.80E+03	5.10E+03	5.41E+03	5.73E+03	6.05E+03
9	3.71E+03	3.98E+03	4.25E+03	4.53E+03	4.82E+03	5.12E+03	5.42E+03	5.74E+03
10	3.50E+03	3.76E+03	4.02E+03	4.29E+03	4.58E+03	4.86E+03	5.16E+03	5.47E+03
11	2.90E+03	3.12E+03	3.35E+03	3.59E+03	3.84E+03	4.09E+03	4.35E+03	4.62E+03
12	2.45E+03	2.65E+03	2.85E+03	3.06E+03	3.28E+03	3.50E+03	3.74E+03	3.98E+03
13	2.10E+03	2.28E+03	2.46E+03	2.64E+03	2.84E+03	3.04E+03	3.25E+03	3.46E+03
14	1.83E+03	1.98E+03	2.14E+03	2.31E+03	2.49E+03	2.67E+03	2.85E+03	3.05E+03
15	1.61E+03	1.74E+03	1.89E+03	2.04E+03	2.20E+03	2.36E+03	2.53E+03	2.71E+03
16	1.42E+03	1.55E+03	1.68E+03	1.82E+03	1.96E+03	2.11E+03	2.26E+03	2.43E+03
17	1.27E+03	1.39E+03	1.50E+03	1.63E+03	1.76E+03	1.90E+03	2.04E+03	2.19E+03
18	1.14E+03	1.25E+03	1.36E+03	1.47E+03	1.59E+03	1.71E+03	1.85E+03	1.98E+03
19	1.03E+03	1.13E+03	1.23E+03	1.33E+03	1.44E+03	1.56E+03	1.68E+03	1.81E+03
20	9.41E+02	1.03E+03	1.12E+03	1.22E+03	1.32E+03	1.43E+03	1.54E+03	1.65E+03
21	8.60E+02	9.41E+02	1.03E+03	1.12E+03	1.21E+03	1.31E+03	1.41E+03	1.52E+03
22	7.90E+02	8.65E+02	9.44E+02	1.03E+03	1.11E+03	1.21E+03	1.30E+03	1.40E+03
23	7.28E+02	7.98E+02	8.71E+02	9.49E+02	1.03E+03	1.12E+03	1.21E+03	1.30E+03
24	6.74E+02	7.39E+02	8.07E+02	8.80E+02	9.56E+02	1.04E+03	1.12E+03	1.21E+03
25	6.26E+02	6.86E+02	7.51E+02	8.18E+02	8.90E+02	9.66E+02	1.04E+03	1.13E+03
26	5.83E+02	6.40E+02	7.00E+02	7.64E+02	8.31E+02	9.02E+02	9.76E+02	1.05E+03
27	5.44E+02	5.98E+02	6.54E+02	7.14E+02	7.78E+02	8.45E+02	9.15E+02	9.89E+02
28	5.10E+02	5.60E+02	6.14E+02	6.70E+02	7.30E+02	7.93E+02	8.59E+02	9.29E+02
29	4.60E+02	5.06E+02	5.54E+02	6.06E+02	6.61E+02	7.19E+02	7.80E+02	8.44E+02
30	4.17E+02	4.59E+02	5.04E+02	5.52E+02	6.02E+02	6.55E+02	7.11E+02	7.70E+02
31	3.81E+02	4.19E+02	4.61E+02	5.04E+02	5.51E+02	6.00E+02	6.52E+02	7.07E+02
32	3.49E+02	3.85E+02	4.23E+02	4.64E+02	5.07E+02	5.52E+02	6.01E+02	6.52E+02
33	3.21E+02	3.54E+02	3.90E+02	4.28E+02	4.68E+02	5.10E+02	5.55E+02	6.03E+02
34		3.28E+02	3.61E+02	3.96E+02	4.34E+02	4.73E+02	5.15E+02	5.60E+02
35			3.35E+02	3.68E+02	4.03E+02	4.40E+02	4.80E+02	5.21E+02
36				3.43E+02	3.76E+02	4.11E+02	4.48E+02	4.87E+02
37					3.52E+02	3.84E+02	4.19E+02	4.56E+02
38						3.61E+02	3.94E+02	4.28E+02
39							3.70E+02	4.03E+02
40								3.80E+02

Z	41	42	43	44	45	46	47	48
N	Nb	Mo	Tc	Ru	Rh	Pd	Ag	Cd
1	2.59E+04	2.72E+04	2.85E+04	2.99E+04	3.13E+04	3.27E+04	3.42E+04	3.57E+04
2	2.53E+04	2.66E+04	2.80E+04	2.93E+04	3.07E+04	3.21E+04	3.36E+04	3.51E+04
3	1.26E+04	1.31E+04	1.37E+04	1.43E+04	1.49E+04	1.55E+04	1.61E+04	1.68E+04
4	9.47E+03	9.92E+03	1.04E+04	1.08E+04	1.13E+04	1.18E+04	1.23E+04	1.28E+04
5	8.10E+03	8.50E+03	8.90E+03	9.31E+03	9.73E+03	1.02E+04	1.06E+04	1.10E+04
6	7.31E+03	7.68E+03	8.06E+03	8.44E+03	8.83E+03	9.23E+03	9.64E+03	1.01E+04
7	6.78E+03	7.13E+03	7.49E+03	7.86E+03	8.23E+03	8.61E+03	9.00E+03	9.40E+03
8	6.38E+03	6.72E+03	7.07E+03	7.42E+03	7.78E+03	8.15E+03	8.53E+03	8.92E+03
9	6.06E+03	6.39E+03	6.73E+03	7.07E+03	7.43E+03	7.79E+03	8.16E+03	8.53E+03
10	5.78E+03	6.10E+03	6.44E+03	6.77E+03	7.12E+03	7.47E+03	7.84E+03	8.21E+03
11	4.90E+03	5.19E+03	5.48E+03	5.79E+03	6.10E+03	6.41E+03	6.74E+03	7.07E+03
12	4.22E+03	4.48E+03	4.75E+03	5.02E+03	5.30E+03	5.58E+03	5.88E+03	6.18E+03

13	3.69E+03	3.92E+03	4.16E+03	4.40E+03	4.65E+03	4.91E+03	5.18E+03	5.46E+03
14	3.25E+03	3.46E+03	3.68E+03	3.90E+03	4.13E+03	4.37E+03	4.61E+03	4.86E+03
15	2.89E+03	3.08E+03	3.28E+03	3.48E+03	3.69E+03	3.91E+03	4.13E+03	4.36E+03
16	2.59E+03	2.77E+03	2.95E+03	3.13E+03	3.33E+03	3.53E+03	3.73E+03	3.94E+03
17	2.34E+03	2.50E+03	2.67E+03	2.84E+03	3.02E+03	3.20E+03	3.39E+03	3.59E+03
18	2.12E+03	2.27E+03	2.42E+03	2.58E+03	2.75E+03	2.92E+03	3.09E+03	3.28E+03
19	1.94E+03	2.07E+03	2.22E+03	2.36E+03	2.52E+03	2.67E+03	2.84E+03	3.01E+03
20	1.78E+03	1.90E+03	2.03E+03	2.17E+03	2.31E+03	2.46E+03	2.62E+03	2.77E+03
21	1.63E+03	1.75E+03	1.88E+03	2.00E+03	2.14E+03	2.27E+03	2.42E+03	2.57E+03
22	1.51E+03	1.62E+03	1.74E+03	1.86E+03	1.98E+03	2.11E+03	2.24E+03	2.38E+03
23	1.40E+03	1.50E+03	1.61E+03	1.72E+03	1.84E+03	1.96E+03	2.09E+03	2.22E+03
24	1.30E+03	1.40E+03	1.50E+03	1.61E+03	1.72E+03	1.83E+03	1.95E+03	2.07E+03
25	1.22E+03	1.31E+03	1.40E+03	1.50E+03	1.61E+03	1.71E+03	1.83E+03	1.94E+03
26	1.14E+03	1.22E+03	1.31E+03	1.41E+03	1.50E+03	1.61E+03	1.71E+03	1.82E+03
27	1.07E+03	1.15E+03	1.23E+03	1.32E+03	1.41E+03	1.51E+03	1.61E+03	1.72E+03
28	1.00E+03	1.08E+03	1.16E+03	1.24E+03	1.33E+03	1.42E+03	1.52E+03	1.62E+03
29	9.11E+02	9.82E+02	1.06E+03	1.13E+03	1.21E+03	1.30E+03	1.39E+03	1.48E+03
30	8.33E+02	8.98E+02	9.67E+02	1.04E+03	1.11E+03	1.19E+03	1.27E+03	1.36E+03
31	7.65E+02	8.26E+02	8.89E+02	9.56E+02	1.03E+03	1.10E+03	1.18E+03	1.26E+03
32	7.05E+02	7.62E+02	8.21E+02	8.84E+02	9.49E+02	1.02E+03	1.09E+03	1.16E+03
33	6.53E+02	7.06E+02	7.61E+02	8.20E+02	8.81E+02	9.45E+02	1.01E+03	1.08E+03
34	6.07E+02	6.56E+02	7.08E+02	7.63E+02	8.20E+02	8.80E+02	9.43E+02	1.01E+03
35	5.65E+02	6.12E+02	6.61E+02	7.12E+02	7.66E+02	8.22E+02	8.82E+02	9.44E+02
36	5.28E+02	5.72E+02	6.18E+02	6.66E+02	7.17E+02	7.71E+02	8.26E+02	8.85E+02
37	4.95E+02	5.36E+02	5.80E+02	6.25E+02	6.73E+02	7.24E+02	7.77E+02	8.32E+02
38	4.65E+02	5.04E+02	5.45E+02	5.88E+02	6.34E+02	6.81E+02	7.32E+02	7.84E+02
39	4.38E+02	4.75E+02	5.14E+02	5.55E+02	5.98E+02	6.43E+02	6.91E+02	7.40E+02
40	4.13E+02	4.48E+02	4.85E+02	5.24E+02	5.65E+02	6.08E+02	6.53E+02	7.01E+02
41	3.91E+02	4.24E+02	4.59E+02	4.96E+02	5.35E+02	5.76E+02	6.19E+02	6.64E+02
42		4.02E+02	4.35E+02	4.71E+02	5.08E+02	5.47E+02	5.88E+02	6.31E+02
43			4.13E+02	4.47E+02	4.82E+02	5.20E+02	5.59E+02	6.00E+02
44				4.25E+02	4.59E+02	4.95E+02	5.32E+02	5.71E+02
45					4.38E+02	4.72E+02	5.08E+02	5.45E+02
46						4.50E+02	4.85E+02	5.21E+02
47							4.64E+02	4.98E+02
48								4.77E+02

Z	49	50	51	52	53	54	55	56
N	In	Sn	Sb	Te	I	Xe	Cs	Ba
1	3.73E+04	3.89E+04	4.05E+04	4.22E+04	4.39E+04	4.56E+04	4.74E+04	4.92E+04
2	3.66E+04	3.82E+04	3.98E+04	4.15E+04	4.31E+04	4.49E+04	4.66E+04	4.84E+04
3	1.74E+04	1.80E+04	1.87E+04	1.94E+04	2.01E+04	2.07E+04	2.14E+04	2.21E+04
4	1.33E+04	1.38E+04	1.43E+04	1.48E+04	1.54E+04	1.59E+04	1.65E+04	1.70E+04
5	1.15E+04	1.19E+04	1.24E+04	1.29E+04	1.34E+04	1.38E+04	1.43E+04	1.48E+04
6	1.05E+04	1.09E+04	1.13E+04	1.18E+04	1.22E+04	1.27E+04	1.32E+04	1.36E+04
7	9.80E+03	1.02E+04	1.06E+04	1.11E+04	1.15E+04	1.19E+04	1.24E+04	1.28E+04
8	9.31E+03	9.71E+03	1.01E+04	1.05E+04	1.10E+04	1.14E+04	1.18E+04	1.23E+04
9	8.92E+03	9.31E+03	9.71E+03	1.01E+04	1.05E+04	1.09E+04	1.14E+04	1.18E+04
10	8.58E+03	8.97E+03	9.36E+03	9.76E+03	1.02E+04	1.06E+04	1.10E+04	1.14E+04
11	7.41E+03	7.76E+03	8.12E+03	8.48E+03	8.85E+03	9.23E+03	9.62E+03	1.00E+04
12	6.49E+03	6.81E+03	7.13E+03	7.46E+03	7.80E+03	8.15E+03	8.50E+03	8.86E+03
13	5.74E+03	6.03E+03	6.32E+03	6.63E+03	6.94E+03	7.26E+03	7.58E+03	7.91E+03
14	5.12E+03	5.38E+03	5.66E+03	5.94E+03	6.22E+03	6.51E+03	6.81E+03	7.12E+03
15	4.60E+03	4.85E+03	5.10E+03	5.35E+03	5.62E+03	5.89E+03	6.17E+03	6.45E+03
16	4.16E+03	4.39E+03	4.62E+03	4.86E+03	5.10E+03	5.35E+03	5.61E+03	5.88E+03
17	3.79E+03	4.00E+03	4.21E+03	4.43E+03	4.66E+03	4.89E+03	5.13E+03	5.38E+03
18	3.47E+03	3.66E+03	3.86E+03	4.07E+03	4.28E+03	4.50E+03	4.72E+03	4.95E+03
19	3.18E+03	3.36E+03	3.55E+03	3.74E+03	3.94E+03	4.15E+03	4.36E+03	4.57E+03
20	2.94E+03	3.11E+03	3.28E+03	3.46E+03	3.65E+03	3.84E+03	4.04E+03	4.24E+03
21	2.72E+03	2.88E+03	3.04E+03	3.21E+03	3.39E+03	3.57E+03	3.75E+03	3.94E+03
22	2.53E+03	2.68E+03	2.83E+03	2.99E+03	3.15E+03	3.32E+03	3.50E+03	3.68E+03
23	2.36E+03	2.50E+03	2.64E+03	2.79E+03	2.95E+03	3.11E+03	3.27E+03	3.44E+03
24	2.20E+03	2.33E+03	2.47E+03	2.61E+03	2.76E+03	2.91E+03	3.07E+03	3.23E+03
25	2.06E+03	2.19E+03	2.32E+03	2.45E+03	2.59E+03	2.73E+03	2.88E+03	3.04E+03
26	1.94E+03	2.06E+03	2.18E+03	2.31E+03	2.44E+03	2.58E+03	2.72E+03	2.86E+03
27	1.82E+03	1.94E+03	2.05E+03	2.17E+03	2.30E+03	2.43E+03	2.56E+03	2.70E+03
28	1.72E+03	1.83E+03	1.94E+03	2.05E+03	2.17E+03	2.30E+03	2.42E+03	2.56E+03
29	1.58E+03	1.67E+03	1.78E+03	1.89E+03	2.00E+03	2.11E+03	2.23E+03	2.35E+03
30	1.45E+03	1.54E+03	1.64E+03	1.74E+03	1.84E+03	1.95E+03	2.06E+03	2.17E+03
31	1.34E+03	1.43E+03	1.52E+03	1.61E+03	1.71E+03	1.81E+03	1.91E+03	2.02E+03
32	1.24E+03	1.32E+03	1.41E+03	1.49E+03	1.59E+03	1.68E+03	1.78E+03	1.88E+03
33	1.15E+03	1.23E+03	1.31E+03	1.39E+03	1.48E+03	1.57E+03	1.66E+03	1.75E+03
34	1.08E+03	1.15E+03	1.22E+03	1.30E+03	1.38E+03	1.47E+03	1.55E+03	1.64E+03
35	1.01E+03	1.08E+03	1.15E+03	1.22E+03	1.30E+03	1.38E+03	1.46E+03	1.54E+03
36	9.46E+02	1.01E+03	1.08E+03	1.15E+03	1.22E+03	1.29E+03	1.37E+03	1.45E+03
37	8.90E+02	9.50E+02	1.01E+03	1.08E+03	1.15E+03	1.22E+03	1.29E+03	1.37E+03
38	8.39E+02	8.96E+02	9.56E+02	1.02E+03	1.08E+03	1.15E+03	1.22E+03	1.30E+03
39	7.92E+02	8.47E+02	9.04E+02	9.63E+02	1.03E+03	1.09E+03	1.16E+03	1.23E+03

40	7.50E+02	8.02E+02	8.56E+02	9.13E+02	9.72E+02	1.03E+03	1.10E+03	1.16E+03
41	7.11E+02	7.61E+02	8.13E+02	8.67E+02	9.23E+02	9.82E+02	1.04E+03	1.11E+03
42	6.76E+02	7.23E+02	7.72E+02	8.24E+02	8.78E+02	9.34E+02	9.93E+02	1.05E+03
43	6.43E+02	6.88E+02	7.35E+02	7.85E+02	8.36E+02	8.90E+02	9.46E+02	1.00E+03
44	6.13E+02	6.56E+02	7.01E+02	7.48E+02	7.98E+02	8.49E+02	9.03E+02	9.59E+02
45	5.85E+02	6.26E+02	6.69E+02	7.15E+02	7.62E+02	8.11E+02	8.63E+02	9.17E+02
46	5.59E+02	5.98E+02	6.40E+02	6.83E+02	7.29E+02	7.76E+02	8.26E+02	8.77E+02
47	5.35E+02	5.73E+02	6.13E+02	6.54E+02	6.98E+02	7.44E+02	7.91E+02	8.41E+02
48	5.12E+02	5.49E+02	5.87E+02	6.27E+02	6.69E+02	7.13E+02	7.59E+02	8.07E+02
49	4.91E+02	5.26E+02	5.63E+02	6.02E+02	6.43E+02	6.85E+02	7.29E+02	7.75E+02
50		5.06E+02	5.41E+02	5.78E+02	6.17E+02	6.58E+02	7.01E+02	7.45E+02
51			5.20E+02	5.56E+02	5.94E+02	6.33E+02	6.74E+02	7.17E+02
52				5.36E+02	5.72E+02	6.10E+02	6.49E+02	6.91E+02
53					5.51E+02	5.88E+02	6.26E+02	6.66E+02
54						5.67E+02	6.04E+02	6.43E+02
55							5.79E+02	6.16E+02
56								5.91E+02

Z	57	58	59	60	61	62	63	64
N	La	Ce	Pr	Nd	Pm	Sm	Eu	Gd
1	5.10E+04	5.29E+04	5.48E+04	5.68E+04	5.88E+04	6.09E+04	6.30E+04	6.51E+04
2	5.02E+04	5.21E+04	5.40E+04	5.60E+04	5.80E+04	6.00E+04	6.21E+04	6.42E+04
3	2.29E+04	2.36E+04	2.43E+04	2.51E+04	2.58E+04	2.66E+04	2.73E+04	2.81E+04
4	1.76E+04	1.82E+04	1.88E+04	1.93E+04	1.99E+04	2.05E+04	2.12E+04	2.18E+04
5	1.53E+04	1.59E+04	1.64E+04	1.69E+04	1.74E+04	1.80E+04	1.85E+04	1.91E+04
6	1.41E+04	1.46E+04	1.51E+04	1.56E+04	1.61E+04	1.66E+04	1.71E+04	1.76E+04
7	1.33E+04	1.38E+04	1.42E+04	1.47E+04	1.52E+04	1.57E+04	1.62E+04	1.67E+04
8	1.27E+04	1.32E+04	1.36E+04	1.41E+04	1.46E+04	1.51E+04	1.56E+04	1.61E+04
9	1.23E+04	1.27E+04	1.32E+04	1.36E+04	1.41E+04	1.46E+04	1.51E+04	1.56E+04
10	1.19E+04	1.23E+04	1.28E+04	1.32E+04	1.37E+04	1.42E+04	1.47E+04	1.51E+04
11	1.04E+04	1.08E+04	1.12E+04	1.17E+04	1.21E+04	1.25E+04	1.30E+04	1.34E+04
12	9.23E+03	9.61E+03	9.99E+03	1.04E+04	1.08E+04	1.12E+04	1.16E+04	1.20E+04
13	8.25E+03	8.60E+03	8.95E+03	9.32E+03	9.68E+03	1.01E+04	1.04E+04	1.08E+04
14	7.43E+03	7.76E+03	8.08E+03	8.42E+03	8.76E+03	9.11E+03	9.46E+03	9.82E+03
15	6.74E+03	7.04E+03	7.34E+03	7.65E+03	7.97E+03	8.30E+03	8.63E+03	8.96E+03
16	6.15E+03	6.42E+03	6.71E+03	7.00E+03	7.29E+03	7.60E+03	7.91E+03	8.22E+03
17	5.63E+03	5.89E+03	6.16E+03	6.43E+03	6.70E+03	6.99E+03	7.28E+03	7.57E+03
18	5.18E+03	5.43E+03	5.68E+03	5.93E+03	6.19E+03	6.46E+03	6.73E+03	7.01E+03
19	4.79E+03	5.02E+03	5.25E+03	5.49E+03	5.74E+03	5.99E+03	6.24E+03	6.51E+03
20	4.45E+03	4.66E+03	4.88E+03	5.10E+03	5.33E+03	5.57E+03	5.81E+03	6.06E+03
21	4.14E+03	4.34E+03	4.55E+03	4.76E+03	4.98E+03	5.20E+03	5.43E+03	5.66E+03
22	3.86E+03	4.05E+03	4.25E+03	4.45E+03	4.66E+03	4.87E+03	5.08E+03	5.31E+03
23	3.62E+03	3.80E+03	3.98E+03	4.17E+03	4.37E+03	4.57E+03	4.77E+03	4.98E+03
24	3.39E+03	3.57E+03	3.74E+03	3.92E+03	4.11E+03	4.30E+03	4.49E+03	4.69E+03
25	3.19E+03	3.36E+03	3.52E+03	3.69E+03	3.87E+03	4.05E+03	4.24E+03	4.43E+03
26	3.01E+03	3.16E+03	3.32E+03	3.49E+03	3.66E+03	3.83E+03	4.01E+03	4.19E+03
27	2.84E+03	2.99E+03	3.14E+03	3.30E+03	3.46E+03	3.62E+03	3.79E+03	3.97E+03
28	2.69E+03	2.83E+03	2.98E+03	3.13E+03	3.28E+03	3.44E+03	3.60E+03	3.76E+03
29	2.48E+03	2.61E+03	2.75E+03	2.88E+03	3.03E+03	3.18E+03	3.33E+03	3.48E+03
30	2.29E+03	2.42E+03	2.54E+03	2.67E+03	2.81E+03	2.95E+03	3.09E+03	3.24E+03
31	2.13E+03	2.24E+03	2.36E+03	2.49E+03	2.61E+03	2.74E+03	2.88E+03	3.02E+03
32	1.98E+03	2.09E+03	2.20E+03	2.32E+03	2.44E+03	2.56E+03	2.69E+03	2.82E+03
33	1.85E+03	1.96E+03	2.06E+03	2.17E+03	2.29E+03	2.40E+03	2.52E+03	2.65E+03
34	1.74E+03	1.83E+03	1.93E+03	2.04E+03	2.15E+03	2.26E+03	2.37E+03	2.49E+03
35	1.63E+03	1.72E+03	1.82E+03	1.92E+03	2.02E+03	2.12E+03	2.23E+03	2.35E+03
36	1.54E+03	1.62E+03	1.71E+03	1.81E+03	1.90E+03	2.00E+03	2.11E+03	2.21E+03
37	1.45E+03	1.53E+03	1.62E+03	1.71E+03	1.80E+03	1.90E+03	1.99E+03	2.10E+03
38	1.37E+03	1.45E+03	1.53E+03	1.62E+03	1.71E+03	1.80E+03	1.89E+03	1.99E+03
39	1.30E+03	1.38E+03	1.45E+03	1.53E+03	1.62E+03	1.70E+03	1.79E+03	1.89E+03
40	1.23E+03	1.31E+03	1.38E+03	1.46E+03	1.54E+03	1.62E+03	1.71E+03	1.80E+03
41	1.17E+03	1.24E+03	1.31E+03	1.39E+03	1.46E+03	1.54E+03	1.63E+03	1.71E+03
42	1.12E+03	1.18E+03	1.25E+03	1.32E+03	1.40E+03	1.47E+03	1.55E+03	1.63E+03
43	1.07E+03	1.13E+03	1.19E+03	1.26E+03	1.33E+03	1.41E+03	1.48E+03	1.56E+03
44	1.02E+03	1.08E+03	1.14E+03	1.21E+03	1.27E+03	1.34E+03	1.42E+03	1.49E+03
45	9.73E+02	1.03E+03	1.09E+03	1.15E+03	1.22E+03	1.29E+03	1.36E+03	1.43E+03
46	9.31E+02	9.87E+02	1.05E+03	1.11E+03	1.17E+03	1.23E+03	1.30E+03	1.37E+03
47	8.93E+02	9.46E+02	1.00E+03	1.06E+03	1.12E+03	1.18E+03	1.25E+03	1.32E+03
48	8.57E+02	9.08E+02	9.62E+02	1.02E+03	1.08E+03	1.14E+03	1.20E+03	1.26E+03
49	8.23E+02	8.73E+02	9.25E+02	9.79E+02	1.04E+03	1.09E+03	1.15E+03	1.22E+03
50	7.91E+02	8.40E+02	8.90E+02	9.42E+02	9.96E+02	1.05E+03	1.11E+03	1.17E+03
51	7.62E+02	8.08E+02	8.57E+02	9.07E+02	9.60E+02	1.01E+03	1.07E+03	1.13E+03
52	7.34E+02	7.79E+02	8.26E+02	8.75E+02	9.25E+02	9.78E+02	1.03E+03	1.09E+03
53	7.08E+02	7.51E+02	7.97E+02	8.44E+02	8.93E+02	9.44E+02	9.97E+02	1.05E+03
54	6.83E+02	7.25E+02	7.69E+02	8.15E+02	8.62E+02	9.12E+02	9.63E+02	1.02E+03
55	6.54E+02	6.94E+02	7.36E+02	7.79E+02	8.24E+02	8.71E+02	9.19E+02	9.70E+02
56	6.27E+02	6.65E+02	7.05E+02	7.46E+02	7.88E+02	8.33E+02	8.79E+02	9.27E+02
57	6.02E+02	6.38E+02	6.76E+02	7.15E+02	7.55E+02	7.98E+02	8.41E+02	8.87E+02
58		6.13E+02	6.49E+02	6.86E+02	7.25E+02	7.65E+02	8.06E+02	8.49E+02

59			6.23E+02	6.59E+02	6.96E+02	7.34E+02	7.74E+02	8.15E+02
60				6.33E+02	6.69E+02	7.05E+02	7.43E+02	7.82E+02
61					6.43E+02	6.78E+02	7.14E+02	7.52E+02
62						6.53E+02	6.88E+02	7.23E+02
63							6.62E+02	6.97E+02
64								6.72E+02

Z	65	66	67	68	69	70	71	72
N	Tb	Dy	Ho	Er	Tm	Yb	Lu	Hf
1	6.73E+04	6.95E+04	7.18E+04	7.41E+04	7.65E+04	7.89E+04	8.14E+04	8.39E+04
2	6.63E+04	6.86E+04	7.08E+04	7.31E+04	7.54E+04	7.78E+04	8.03E+04	8.28E+04
3	2.89E+04	2.97E+04	3.05E+04	3.13E+04	3.21E+04	3.30E+04	3.38E+04	3.46E+04
4	2.24E+04	2.30E+04	2.37E+04	2.43E+04	2.50E+04	2.56E+04	2.63E+04	2.70E+04
5	1.97E+04	2.02E+04	2.08E+04	2.14E+04	2.20E+04	2.26E+04	2.32E+04	2.38E+04
6	1.82E+04	1.87E+04	1.93E+04	1.98E+04	2.04E+04	2.09E+04	2.15E+04	2.21E+04
7	1.72E+04	1.78E+04	1.83E+04	1.88E+04	1.94E+04	1.99E+04	2.05E+04	2.10E+04
8	1.66E+04	1.71E+04	1.76E+04	1.81E+04	1.87E+04	1.92E+04	1.97E+04	2.03E+04
9	1.61E+04	1.66E+04	1.71E+04	1.76E+04	1.81E+04	1.86E+04	1.92E+04	1.97E+04
10	1.56E+04	1.61E+04	1.66E+04	1.72E+04	1.77E+04	1.82E+04	1.87E+04	1.93E+04
11	1.39E+04	1.44E+04	1.48E+04	1.53E+04	1.58E+04	1.63E+04	1.68E+04	1.73E+04
12	1.24E+04	1.29E+04	1.33E+04	1.38E+04	1.42E+04	1.47E+04	1.51E+04	1.56E+04
13	1.12E+04	1.16E+04	1.20E+04	1.25E+04	1.29E+04	1.33E+04	1.37E+04	1.42E+04
14	1.02E+04	1.06E+04	1.10E+04	1.13E+04	1.17E+04	1.21E+04	1.26E+04	1.30E+04
15	9.31E+03	9.66E+03	1.00E+04	1.04E+04	1.08E+04	1.11E+04	1.15E+04	1.19E+04
16	8.54E+03	8.87E+03	9.21E+03	9.55E+03	9.90E+03	1.03E+04	1.06E+04	1.10E+04
17	7.88E+03	8.19E+03	8.50E+03	8.82E+03	9.15E+03	9.48E+03	9.83E+03	1.02E+04
18	7.29E+03	7.58E+03	7.88E+03	8.18E+03	8.49E+03	8.81E+03	9.13E+03	9.46E+03
19	6.77E+03	7.05E+03	7.33E+03	7.61E+03	7.91E+03	8.20E+03	8.51E+03	8.82E+03
20	6.31E+03	6.57E+03	6.84E+03	7.11E+03	7.39E+03	7.67E+03	7.96E+03	8.25E+03
21	5.90E+03	6.15E+03	6.40E+03	6.66E+03	6.92E+03	7.19E+03	7.46E+03	7.74E+03
22	5.53E+03	5.77E+03	6.00E+03	6.25E+03	6.50E+03	6.75E+03	7.01E+03	7.28E+03
23	5.20E+03	5.42E+03	5.65E+03	5.88E+03	6.12E+03	6.36E+03	6.61E+03	6.86E+03
24	4.90E+03	5.11E+03	5.33E+03	5.55E+03	5.77E+03	6.00E+03	6.24E+03	6.48E+03
25	4.62E+03	4.83E+03	5.03E+03	5.24E+03	5.46E+03	5.68E+03	5.90E+03	6.13E+03
26	4.37E+03	4.57E+03	4.76E+03	4.96E+03	5.17E+03	5.38E+03	5.60E+03	5.82E+03
27	4.15E+03	4.33E+03	4.52E+03	4.71E+03	4.91E+03	5.11E+03	5.31E+03	5.53E+03
28	3.93E+03	4.11E+03	4.29E+03	4.47E+03	4.66E+03	4.86E+03	5.05E+03	5.26E+03
29	3.64E+03	3.81E+03	3.98E+03	4.15E+03	4.33E+03	4.51E+03	4.70E+03	4.89E+03
30	3.39E+03	3.54E+03	3.70E+03	3.87E+03	4.03E+03	4.21E+03	4.38E+03	4.56E+03
31	3.16E+03	3.31E+03	3.46E+03	3.61E+03	3.77E+03	3.93E+03	4.10E+03	4.27E+03
32	2.96E+03	3.10E+03	3.24E+03	3.39E+03	3.54E+03	3.69E+03	3.85E+03	4.01E+03
33	2.77E+03	2.91E+03	3.04E+03	3.18E+03	3.32E+03	3.47E+03	3.62E+03	3.78E+03
34	2.61E+03	2.73E+03	2.86E+03	3.00E+03	3.13E+03	3.27E+03	3.42E+03	3.56E+03
35	2.46E+03	2.58E+03	2.70E+03	2.83E+03	2.96E+03	3.09E+03	3.23E+03	3.37E+03
36	2.32E+03	2.44E+03	2.55E+03	2.68E+03	2.80E+03	2.93E+03	3.06E+03	3.19E+03
37	2.20E+03	2.31E+03	2.42E+03	2.54E+03	2.65E+03	2.78E+03	2.90E+03	3.03E+03
38	2.09E+03	2.19E+03	2.30E+03	2.41E+03	2.52E+03	2.64E+03	2.76E+03	2.88E+03
39	1.98E+03	2.08E+03	2.18E+03	2.29E+03	2.40E+03	2.51E+03	2.62E+03	2.74E+03
40	1.89E+03	1.98E+03	2.08E+03	2.18E+03	2.28E+03	2.39E+03	2.50E+03	2.62E+03
41	1.80E+03	1.89E+03	1.98E+03	2.08E+03	2.18E+03	2.28E+03	2.39E+03	2.50E+03
42	1.72E+03	1.80E+03	1.89E+03	1.99E+03	2.08E+03	2.18E+03	2.28E+03	2.39E+03
43	1.64E+03	1.72E+03	1.81E+03	1.90E+03	1.99E+03	2.09E+03	2.19E+03	2.29E+03
44	1.57E+03	1.65E+03	1.73E+03	1.82E+03	1.91E+03	2.00E+03	2.10E+03	2.19E+03
45	1.50E+03	1.58E+03	1.66E+03	1.75E+03	1.83E+03	1.92E+03	2.01E+03	2.10E+03
46	1.44E+03	1.52E+03	1.60E+03	1.68E+03	1.76E+03	1.84E+03	1.93E+03	2.02E+03
47	1.39E+03	1.46E+03	1.53E+03	1.61E+03	1.69E+03	1.77E+03	1.86E+03	1.94E+03
48	1.33E+03	1.40E+03	1.47E+03	1.55E+03	1.63E+03	1.70E+03	1.79E+03	1.87E+03
49	1.28E+03	1.35E+03	1.42E+03	1.49E+03	1.56E+03	1.64E+03	1.72E+03	1.80E+03
50	1.23E+03	1.30E+03	1.37E+03	1.44E+03	1.51E+03	1.58E+03	1.66E+03	1.74E+03
51	1.19E+03	1.25E+03	1.32E+03	1.39E+03	1.45E+03	1.53E+03	1.60E+03	1.68E+03
52	1.15E+03	1.21E+03	1.27E+03	1.34E+03	1.40E+03	1.47E+03	1.55E+03	1.62E+03
53	1.11E+03	1.17E+03	1.23E+03	1.29E+03	1.36E+03	1.42E+03	1.49E+03	1.57E+03
54	1.07E+03	1.13E+03	1.19E+03	1.25E+03	1.31E+03	1.38E+03	1.45E+03	1.52E+03
55	1.02E+03	1.08E+03	1.13E+03	1.19E+03	1.25E+03	1.31E+03	1.38E+03	1.44E+03
56	9.76E+02	1.03E+03	1.08E+03	1.13E+03	1.19E+03	1.25E+03	1.31E+03	1.37E+03
57	9.34E+02	9.82E+02	1.03E+03	1.08E+03	1.14E+03	1.19E+03	1.25E+03	1.31E+03
58	8.94E+02	9.40E+02	9.88E+02	1.04E+03	1.09E+03	1.14E+03	1.20E+03	1.25E+03
59	8.57E+02	9.01E+02	9.47E+02	9.94E+02	1.04E+03	1.09E+03	1.14E+03	1.20E+03
60	8.23E+02	8.65E+02	9.08E+02	9.53E+02	9.99E+02	1.05E+03	1.10E+03	1.15E+03
61	7.91E+02	8.31E+02	8.72E+02	9.15E+02	9.59E+02	1.00E+03	1.05E+03	1.10E+03
62	7.60E+02	7.99E+02	8.38E+02	8.79E+02	9.21E+02	9.64E+02	1.01E+03	1.06E+03
63	7.32E+02	7.69E+02	8.07E+02	8.46E+02	8.86E+02	9.27E+02	9.70E+02	1.01E+03
64	7.06E+02	7.41E+02	7.77E+02	8.14E+02	8.53E+02	8.92E+02	9.33E+02	9.75E+02
65	6.80E+02	7.14E+02	7.49E+02	7.85E+02	8.22E+02	8.60E+02	8.99E+02	9.39E+02
66		6.89E+02	7.22E+02	7.57E+02	7.92E+02	8.29E+02	8.66E+02	9.05E+02
67			6.98E+02	7.31E+02	7.65E+02	8.00E+02	8.36E+02	8.73E+02
68				7.06E+02	7.39E+02	7.72E+02	8.07E+02	8.42E+02
69					7.14E+02	7.46E+02	7.80E+02	8.14E+02

70						7.22E+02	7.54E+02	7.87E+02
71							7.29E+02	7.61E+02
72								7.37E+02

Z	73	74	75	76	77	78	79	80
N	Ta	W	Re	Os	Ir	Pt	Au	Hg
1	8.65E+04	8.91E+04	9.17E+04	9.45E+04	9.73E+04	1.00E+05	1.03E+05	1.06E+05
2	8.53E+04	8.79E+04	9.05E+04	9.32E+04	9.60E+04	9.88E+04	1.02E+05	1.05E+05
3	3.55E+04	3.64E+04	3.72E+04	3.81E+04	3.90E+04	3.99E+04	4.08E+04	4.17E+04
4	2.77E+04	2.84E+04	2.91E+04	2.98E+04	3.05E+04	3.12E+04	3.19E+04	3.26E+04
5	2.44E+04	2.50E+04	2.57E+04	2.63E+04	2.69E+04	2.76E+04	2.82E+04	2.89E+04
6	2.27E+04	2.33E+04	2.38E+04	2.44E+04	2.51E+04	2.57E+04	2.63E+04	2.69E+04
7	2.16E+04	2.22E+04	2.27E+04	2.33E+04	2.39E+04	2.45E+04	2.51E+04	2.57E+04
8	2.08E+04	2.14E+04	2.20E+04	2.26E+04	2.31E+04	2.37E+04	2.43E+04	2.49E+04
9	2.03E+04	2.08E+04	2.14E+04	2.20E+04	2.26E+04	2.31E+04	2.37E+04	2.43E+04
10	1.98E+04	2.04E+04	2.09E+04	2.15E+04	2.21E+04	2.27E+04	2.33E+04	2.38E+04
11	1.78E+04	1.83E+04	1.89E+04	1.94E+04	1.99E+04	2.05E+04	2.10E+04	2.16E+04
12	1.61E+04	1.66E+04	1.71E+04	1.76E+04	1.81E+04	1.86E+04	1.91E+04	1.97E+04
13	1.46E+04	1.51E+04	1.56E+04	1.60E+04	1.65E+04	1.70E+04	1.75E+04	1.80E+04
14	1.34E+04	1.38E+04	1.43E+04	1.47E+04	1.52E+04	1.56E+04	1.61E+04	1.65E+04
15	1.23E+04	1.27E+04	1.31E+04	1.35E+04	1.40E+04	1.44E+04	1.48E+04	1.53E+04
16	1.14E+04	1.17E+04	1.21E+04	1.25E+04	1.29E+04	1.33E+04	1.37E+04	1.42E+04
17	1.05E+04	1.09E+04	1.13E+04	1.16E+04	1.20E+04	1.24E+04	1.28E+04	1.32E+04
18	9.79E+03	1.01E+04	1.05E+04	1.08E+04	1.12E+04	1.16E+04	1.19E+04	1.23E+04
19	9.14E+03	9.46E+03	9.79E+03	1.01E+04	1.05E+04	1.08E+04	1.12E+04	1.15E+04
20	8.55E+03	8.86E+03	9.17E+03	9.48E+03	9.81E+03	1.01E+04	1.05E+04	1.08E+04
21	8.02E+03	8.31E+03	8.61E+03	8.91E+03	9.22E+03	9.53E+03	9.85E+03	1.02E+04
22	7.55E+03	7.83E+03	8.11E+03	8.40E+03	8.69E+03	8.99E+03	9.29E+03	9.60E+03
23	7.12E+03	7.38E+03	7.65E+03	7.93E+03	8.21E+03	8.49E+03	8.78E+03	9.08E+03
24	6.73E+03	6.98E+03	7.24E+03	7.50E+03	7.77E+03	8.04E+03	8.32E+03	8.60E+03
25	6.37E+03	6.61E+03	6.86E+03	7.11E+03	7.37E+03	7.63E+03	7.89E+03	8.16E+03
26	6.04E+03	6.27E+03	6.51E+03	6.75E+03	7.00E+03	7.25E+03	7.50E+03	7.76E+03
27	5.74E+03	5.96E+03	6.19E+03	6.42E+03	6.66E+03	6.90E+03	7.14E+03	7.39E+03
28	5.46E+03	5.68E+03	5.89E+03	6.12E+03	6.34E+03	6.57E+03	6.81E+03	7.05E+03
29	5.09E+03	5.29E+03	5.49E+03	5.70E+03	5.92E+03	6.13E+03	6.36E+03	6.59E+03
30	4.75E+03	4.94E+03	5.13E+03	5.33E+03	5.54E+03	5.74E+03	5.96E+03	6.17E+03
31	4.45E+03	4.63E+03	4.81E+03	5.00E+03	5.19E+03	5.39E+03	5.59E+03	5.80E+03
32	4.18E+03	4.35E+03	4.53E+03	4.70E+03	4.89E+03	5.08E+03	5.27E+03	5.47E+03
33	3.94E+03	4.10E+03	4.27E+03	4.44E+03	4.61E+03	4.79E+03	4.97E+03	5.16E+03
34	3.71E+03	3.87E+03	4.03E+03	4.19E+03	4.36E+03	4.53E+03	4.71E+03	4.88E+03
35	3.51E+03	3.66E+03	3.81E+03	3.97E+03	4.13E+03	4.29E+03	4.46E+03	4.63E+03
36	3.33E+03	3.47E+03	3.62E+03	3.77E+03	3.92E+03	4.08E+03	4.24E+03	4.40E+03
37	3.16E+03	3.30E+03	3.44E+03	3.58E+03	3.73E+03	3.88E+03	4.03E+03	4.19E+03
38	3.01E+03	3.14E+03	3.27E+03	3.41E+03	3.55E+03	3.69E+03	3.84E+03	3.99E+03
39	2.86E+03	2.99E+03	3.12E+03	3.25E+03	3.38E+03	3.52E+03	3.66E+03	3.81E+03
40	2.73E+03	2.85E+03	2.98E+03	3.10E+03	3.23E+03	3.37E+03	3.50E+03	3.64E+03
41	2.61E+03	2.73E+03	2.84E+03	2.97E+03	3.09E+03	3.22E+03	3.35E+03	3.49E+03
42	2.50E+03	2.61E+03	2.72E+03	2.84E+03	2.96E+03	3.08E+03	3.21E+03	3.34E+03
43	2.39E+03	2.50E+03	2.61E+03	2.72E+03	2.84E+03	2.96E+03	3.08E+03	3.20E+03
44	2.29E+03	2.40E+03	2.50E+03	2.61E+03	2.72E+03	2.84E+03	2.96E+03	3.08E+03
45	2.20E+03	2.30E+03	2.40E+03	2.51E+03	2.62E+03	2.73E+03	2.84E+03	2.96E+03
46	2.11E+03	2.21E+03	2.31E+03	2.41E+03	2.52E+03	2.62E+03	2.73E+03	2.85E+03
47	2.03E+03	2.13E+03	2.22E+03	2.32E+03	2.42E+03	2.53E+03	2.63E+03	2.74E+03
48	1.96E+03	2.05E+03	2.14E+03	2.24E+03	2.33E+03	2.43E+03	2.54E+03	2.64E+03
49	1.89E+03	1.97E+03	2.06E+03	2.16E+03	2.25E+03	2.35E+03	2.45E+03	2.55E+03
50	1.82E+03	1.90E+03	1.99E+03	2.08E+03	2.17E+03	2.27E+03	2.36E+03	2.46E+03
51	1.76E+03	1.84E+03	1.92E+03	2.01E+03	2.10E+03	2.19E+03	2.28E+03	2.38E+03
52	1.70E+03	1.78E+03	1.86E+03	1.94E+03	2.03E+03	2.12E+03	2.21E+03	2.30E+03
53	1.64E+03	1.72E+03	1.80E+03	1.88E+03	1.96E+03	2.05E+03	2.14E+03	2.23E+03
54	1.59E+03	1.66E+03	1.74E+03	1.82E+03	1.90E+03	1.98E+03	2.07E+03	2.16E+03
55	1.51E+03	1.58E+03	1.65E+03	1.73E+03	1.80E+03	1.88E+03	1.96E+03	2.05E+03
56	1.44E+03	1.50E+03	1.57E+03	1.64E+03	1.71E+03	1.79E+03	1.87E+03	1.94E+03
57	1.37E+03	1.43E+03	1.50E+03	1.56E+03	1.63E+03	1.70E+03	1.78E+03	1.85E+03
58	1.31E+03	1.37E+03	1.43E+03	1.49E+03	1.56E+03	1.62E+03	1.69E+03	1.76E+03
59	1.25E+03	1.31E+03	1.37E+03	1.43E+03	1.49E+03	1.55E+03	1.62E+03	1.68E+03
60	1.20E+03	1.25E+03	1.31E+03	1.36E+03	1.42E+03	1.48E+03	1.54E+03	1.61E+03
61	1.15E+03	1.20E+03	1.25E+03	1.31E+03	1.36E+03	1.42E+03	1.48E+03	1.54E+03
62	1.10E+03	1.15E+03	1.20E+03	1.25E+03	1.31E+03	1.36E+03	1.42E+03	1.47E+03
63	1.06E+03	1.11E+03	1.15E+03	1.20E+03	1.25E+03	1.31E+03	1.36E+03	1.41E+03
64	1.02E+03	1.06E+03	1.11E+03	1.16E+03	1.20E+03	1.25E+03	1.30E+03	1.36E+03
65	9.80E+02	1.02E+03	1.07E+03	1.11E+03	1.16E+03	1.21E+03	1.25E+03	1.30E+03
66	9.45E+02	9.85E+02	1.03E+03	1.07E+03	1.11E+03	1.16E+03	1.21E+03	1.25E+03
67	9.11E+02	9.50E+02	9.90E+02	1.03E+03	1.07E+03	1.12E+03	1.16E+03	1.21E+03
68	8.79E+02	9.17E+02	9.55E+02	9.95E+02	1.04E+03	1.08E+03	1.12E+03	1.16E+03
69	8.49E+02	8.85E+02	9.22E+02	9.60E+02	1.00E+03	1.04E+03	1.08E+03	1.12E+03
70	8.21E+02	8.55E+02	8.91E+02	9.28E+02	9.65E+02	1.00E+03	1.04E+03	1.08E+03
71	7.94E+02	8.27E+02	8.62E+02	8.97E+02	9.33E+02	9.70E+02	1.01E+03	1.05E+03
72	7.68E+02	8.01E+02	8.34E+02	8.68E+02	9.03E+02	9.38E+02	9.75E+02	1.01E+03

73	7.44E+02	7.75E+02	8.07E+02	8.40E+02	8.74E+02	9.08E+02	9.44E+02	9.80E+02
74		7.51E+02	7.82E+02	8.14E+02	8.46E+02	8.80E+02	9.14E+02	9.49E+02
75			7.58E+02	7.89E+02	8.20E+02	8.52E+02	8.85E+02	9.19E+02
76				7.65E+02	7.96E+02	8.27E+02	8.58E+02	8.91E+02
77					7.72E+02	8.02E+02	8.33E+02	8.64E+02
78						7.79E+02	8.08E+02	8.39E+02
79							7.85E+02	8.15E+02
80								7.92E+02

Z	81	82	83	84	85	86
N	Tl	Pb	Bi	Po	At	Rn
1	1.09E+05	1.12E+05	1.15E+05	1.18E+05	1.22E+05	1.25E+05
2	1.08E+05	1.11E+05	1.14E+05	1.17E+05	1.20E+05	1.23E+05
3	4.26E+04	4.36E+04	4.45E+04	4.55E+04	4.64E+04	4.74E+04
4	3.34E+04	3.41E+04	3.49E+04	3.56E+04	3.64E+04	3.72E+04
5	2.96E+04	3.02E+04	3.09E+04	3.16E+04	3.23E+04	3.30E+04
6	2.76E+04	2.82E+04	2.88E+04	2.95E+04	3.01E+04	3.08E+04
7	2.63E+04	2.70E+04	2.76E+04	2.82E+04	2.89E+04	2.95E+04
8	2.55E+04	2.61E+04	2.68E+04	2.74E+04	2.80E+04	2.87E+04
9	2.49E+04	2.55E+04	2.61E+04	2.68E+04	2.74E+04	2.80E+04
10	2.44E+04	2.51E+04	2.57E+04	2.63E+04	2.69E+04	2.75E+04
11	2.22E+04	2.27E+04	2.33E+04	2.39E+04	2.45E+04	2.51E+04
12	2.02E+04	2.07E+04	2.13E+04	2.19E+04	2.24E+04	2.30E+04
13	1.85E+04	1.90E+04	1.95E+04	2.01E+04	2.06E+04	2.11E+04
14	1.70E+04	1.75E+04	1.80E+04	1.85E+04	1.90E+04	1.95E+04
15	1.57E+04	1.62E+04	1.66E+04	1.71E+04	1.76E+04	1.81E+04
16	1.46E+04	1.50E+04	1.55E+04	1.59E+04	1.64E+04	1.68E+04
17	1.36E+04	1.40E+04	1.44E+04	1.48E+04	1.53E+04	1.57E+04
18	1.27E+04	1.31E+04	1.35E+04	1.39E+04	1.43E+04	1.47E+04
19	1.19E+04	1.23E+04	1.26E+04	1.30E+04	1.34E+04	1.38E+04
20	1.12E+04	1.15E+04	1.19E+04	1.22E+04	1.26E+04	1.30E+04
21	1.05E+04	1.08E+04	1.12E+04	1.15E+04	1.19E+04	1.22E+04
22	9.92E+03	1.02E+04	1.06E+04	1.09E+04	1.12E+04	1.16E+04
23	9.38E+03	9.69E+03	1.00E+04	1.03E+04	1.06E+04	1.10E+04
24	8.89E+03	9.19E+03	9.49E+03	9.79E+03	1.01E+04	1.04E+04
25	8.44E+03	8.72E+03	9.01E+03	9.30E+03	9.60E+03	9.91E+03
26	8.03E+03	8.30E+03	8.58E+03	8.86E+03	9.14E+03	9.43E+03
27	7.65E+03	7.91E+03	8.17E+03	8.44E+03	8.72E+03	9.00E+03
28	7.29E+03	7.55E+03	7.80E+03	8.06E+03	8.33E+03	8.60E+03
29	6.82E+03	7.06E+03	7.30E+03	7.55E+03	7.80E+03	8.05E+03
30	6.39E+03	6.62E+03	6.85E+03	7.08E+03	7.32E+03	7.57E+03
31	6.01E+03	6.23E+03	6.45E+03	6.67E+03	6.90E+03	7.13E+03
32	5.67E+03	5.87E+03	6.08E+03	6.29E+03	6.51E+03	6.74E+03
33	5.35E+03	5.55E+03	5.75E+03	5.95E+03	6.16E+03	6.38E+03
34	5.07E+03	5.26E+03	5.45E+03	5.64E+03	5.84E+03	6.05E+03
35	4.81E+03	4.99E+03	5.17E+03	5.36E+03	5.55E+03	5.75E+03
36	4.57E+03	4.74E+03	4.92E+03	5.10E+03	5.28E+03	5.47E+03
37	4.35E+03	4.52E+03	4.68E+03	4.86E+03	5.03E+03	5.22E+03
38	4.15E+03	4.31E+03	4.47E+03	4.64E+03	4.81E+03	4.98E+03
39	3.96E+03	4.11E+03	4.27E+03	4.43E+03	4.59E+03	4.76E+03
40	3.79E+03	3.93E+03	4.08E+03	4.24E+03	4.40E+03	4.56E+03
41	3.62E+03	3.77E+03	3.91E+03	4.06E+03	4.21E+03	4.37E+03
42	3.47E+03	3.61E+03	3.75E+03	3.90E+03	4.04E+03	4.19E+03
43	3.33E+03	3.47E+03	3.60E+03	3.74E+03	3.88E+03	4.03E+03
44	3.20E+03	3.33E+03	3.46E+03	3.60E+03	3.73E+03	3.87E+03
45	3.08E+03	3.20E+03	3.33E+03	3.46E+03	3.59E+03	3.73E+03
46	2.96E+03	3.08E+03	3.21E+03	3.33E+03	3.46E+03	3.59E+03
47	2.86E+03	2.97E+03	3.09E+03	3.21E+03	3.34E+03	3.47E+03
48	2.75E+03	2.87E+03	2.98E+03	3.10E+03	3.22E+03	3.34E+03
49	2.66E+03	2.77E+03	2.88E+03	2.99E+03	3.11E+03	3.23E+03
50	2.57E+03	2.67E+03	2.78E+03	2.89E+03	3.01E+03	3.12E+03
51	2.48E+03	2.58E+03	2.69E+03	2.80E+03	2.91E+03	3.02E+03
52	2.40E+03	2.50E+03	2.60E+03	2.71E+03	2.81E+03	2.92E+03
53	2.32E+03	2.42E+03	2.52E+03	2.62E+03	2.73E+03	2.83E+03
54	2.25E+03	2.34E+03	2.44E+03	2.54E+03	2.64E+03	2.75E+03
55	2.13E+03	2.22E+03	2.31E+03	2.40E+03	2.50E+03	2.60E+03
56	2.02E+03	2.11E+03	2.19E+03	2.28E+03	2.37E+03	2.46E+03
57	1.93E+03	2.00E+03	2.08E+03	2.17E+03	2.25E+03	2.34E+03
58	1.83E+03	1.91E+03	1.99E+03	2.06E+03	2.14E+03	2.23E+03
59	1.75E+03	1.82E+03	1.89E+03	1.97E+03	2.04E+03	2.12E+03
60	1.67E+03	1.74E+03	1.81E+03	1.88E+03	1.95E+03	2.02E+03
61	1.60E+03	1.66E+03	1.73E+03	1.80E+03	1.86E+03	1.93E+03
62	1.53E+03	1.59E+03	1.65E+03	1.72E+03	1.78E+03	1.85E+03
63	1.47E+03	1.53E+03	1.59E+03	1.65E+03	1.71E+03	1.77E+03
64	1.41E+03	1.47E+03	1.52E+03	1.58E+03	1.64E+03	1.70E+03
65	1.36E+03	1.41E+03	1.46E+03	1.52E+03	1.57E+03	1.63E+03
66	1.30E+03	1.35E+03	1.41E+03	1.46E+03	1.51E+03	1.57E+03
67	1.26E+03	1.30E+03	1.35E+03	1.40E+03	1.45E+03	1.51E+03

68	1.21E+03	1.26E+03	1.30E+03	1.35E+03	1.40E+03	1.45E+03
69	1.17E+03	1.21E+03	1.26E+03	1.30E+03	1.35E+03	1.40E+03
70	1.13E+03	1.17E+03	1.21E+03	1.26E+03	1.30E+03	1.35E+03
71	1.09E+03	1.13E+03	1.17E+03	1.21E+03	1.26E+03	1.30E+03
72	1.05E+03	1.09E+03	1.13E+03	1.17E+03	1.21E+03	1.26E+03
73	1.02E+03	1.05E+03	1.09E+03	1.13E+03	1.17E+03	1.22E+03
74	9.84E+02	1.02E+03	1.06E+03	1.10E+03	1.14E+03	1.18E+03
75	9.54E+02	9.89E+02	1.02E+03	1.06E+03	1.10E+03	1.14E+03
76	9.24E+02	9.58E+02	9.93E+02	1.03E+03	1.07E+03	1.10E+03
77	8.96E+02	9.29E+02	9.63E+02	9.98E+02	1.03E+03	1.07E+03
78	8.70E+02	9.02E+02	9.34E+02	9.68E+02	1.00E+03	1.04E+03
79	8.45E+02	8.76E+02	9.07E+02	9.39E+02	9.72E+02	1.01E+03
80	8.21E+02	8.51E+02	8.81E+02	9.12E+02	9.44E+02	9.77E+02
81	7.98E+02	8.27E+02	8.56E+02	8.86E+02	9.17E+02	9.49E+02
82		8.04E+02	8.33E+02	8.62E+02	8.92E+02	9.22E+02
83			8.10E+02	8.38E+02	8.67E+02	8.97E+02
84				8.16E+02	8.44E+02	8.73E+02
85					8.22E+02	8.50E+02
86						8.28E+02

Table 2
MEE calculated with FAC for H-like and He-like ions

Element	Z	H-like MEE [eV]	R/N-R	He-like[a] MEE [eV]	R/N-R
H	1	1.4951E+01	1.00	–	–
He	2	5.9842E+01	1.00	–	–
Li	3	1.3468E+02	1.00	–	–
Be	4	2.3948E+02	1.00	–	–
B	5	3.7430E+02	1.00	–	–
C	6	5.3917E+02	1.00	–	–
N	7	7.3417E+02	1.00	–	–
O	8	9.5934E+02	1.00	–	–
F	9	1.2148E+03	1.00	–	–
Ne	10	1.5005E+03	1.00	1.3800E+03	0.98
Na	11	1.8167E+03	1.00	1.6843E+03	0.98
Mg	12	2.1633E+03	1.00	2.0191E+03	0.98
Al	13	2.5404E+03	1.01	2.3845E+03	0.99
Si	14	2.9483E+03	1.01	2.7805E+03	0.99
P	15	3.3868E+03	1.01	3.2072E+03	0.99
S	16	3.8561E+03	1.01	3.6647E+03	0.99
Cl	17	4.3563E+03	1.01	4.1296E+03	0.99
Ar	18	4.8874E+03	1.01	4.6723E+03	0.99
K	19	5.4496E+03	1.01	5.2223E+03	1.00
Ca	20	6.0429E+03	1.01	5.8037E+03	1.00
Sc	21	6.6674E+03	1.01	6.4161E+03	1.00
Ti	22	7.3232E+03	1.01	7.0597E+03	1.00
V	23	8.0104E+03	1.01	7.7346E+03	1.00
Cr	24	8.7291E+03	1.01	8.4407E+03	1.00
Mn	25	9.4793E+03	1.01	9.1786E+03	1.00
Fe	26	1.0261E+04	1.02	9.9478E+03	1.00
Co	27	1.1075E+04	1.02	1.0749E+04	1.01
Ni	28	1.1920E+04	1.02	1.1581E+04	1.01
Cu	29	1.2798E+04	1.02	1.2446E+04	1.01
Zn	30	1.3707E+04	1.02	1.3342E+04	1.01
Ga	31	1.4649E+04	1.02	1.4271E+04	1.01
Ge	32	1.5623E+04	1.02	1.5231E+04	1.01
As	33	1.6629E+04	1.02	1.6224E+04	1.01
Se	34	1.7668E+04	1.02	1.7250E+04	1.01
Br	35	1.8740E+04	1.02	1.8307E+04	1.01
Kr	36	1.9844E+04	1.02	1.9397E+04	1.02
Rb	37	2.0982E+04	1.03	2.0521E+04	1.02
Sr	38	2.2153E+04	1.03	2.1678E+04	1.02
Y	39	2.3357E+04	1.03	2.2868E+04	1.02
Zr	40	2.4595E+04	1.03	2.4091E+04	1.02
Nb	41	2.5867E+04	1.03	2.5347E+04	1.02
Mo	42	2.7172E+04	1.03	2.6638E+04	1.02
Tc	43	2.8512E+04	1.03	2.7962E+04	1.02
Ru	44	2.9886E+04	1.03	2.9321E+04	1.02
Rh	45	3.1295E+04	1.03	3.0714E+04	1.03
Pd	46	3.2739E+04	1.03	3.2142E+04	1.03
Ag	47	3.4218E+04	1.04	3.3605E+04	1.03
Cd	48	3.5733E+04	1.04	3.5103E+04	1.03
In	49	3.7283E+04	1.04	3.6637E+04	1.03
Sn	50	3.8870E+04	1.04	3.8207E+04	1.03
Sb	51	4.0494E+04	1.04	3.9813E+04	1.03
Te	52	4.2154E+04	1.04	4.1455E+04	1.03
I	53	4.3852E+04	1.04	4.3135E+04	1.04
Xe	54	4.5587E+04	1.05	4.4852E+04	1.04
Cs	55	4.7360E+04	1.05	4.6607E+04	1.04
Ba	56	4.9172E+04	1.05	4.8401E+04	1.04
La	57	5.1024E+04	1.05	5.0232E+04	1.04
Ce	58	5.2915E+04	1.05	5.2100E+04	1.04
Pr	59	5.4845E+04	1.05	5.4014E+04	1.05
Nd	60	5.6817E+04	1.06	5.5965E+04	1.05
Pm	61	5.8829E+04	1.06	5.7957E+04	1.05
Sm	62	6.0884E+04	1.06	5.9990E+04	1.05
Eu	63	6.2981E+04	1.06	6.2065E+04	1.05
Gd	64	6.5121E+04	1.06	6.4183E+04	1.06
Tb	65	6.7306E+04	1.07	6.6346E+04	1.06
Dy	66	6.9534E+04	1.07	6.8550E+04	1.06
Ho	67	7.1809E+04	1.07	7.0801E+04	1.06
Er	68	7.4129E+04	1.07	7.3097E+04	1.06
Tm	69	7.6497E+04	1.07	7.5440E+04	1.07
Yb	70	7.8912E+04	1.08	7.7829E+04	1.07
Lu	71	8.1376E+04	1.08	8.0267E+04	1.07
Hf	72	8.3891E+04	1.08	8.2755E+04	1.07
Ta	73	8.6457E+04	1.09	8.5294E+04	1.08
W	74	8.9074E+04	1.09	8.7884E+04	1.08
Re	75	9.1745E+04	1.09	9.0526E+04	1.08
Os	76	9.4470E+04	1.09	9.3221E+04	1.09
Ir	77	9.7252E+04	1.10	9.5973E+04	1.09
Pt	78	1.0009E+05	1.10	9.8779E+04	1.09

Au	79	1.0299E+05	1.10	1.0164E+05	1.09
Hg	80	1.0594E+05	1.11	1.0457E+05	1.10
Tl	81	1.0896E+05	1.11	1.0755E+05	1.10
Pb	82	1.1204E+05	1.11	1.1058E+05	1.11
Bi	83	1.1519E+05	1.12	1.1371E+05	1.11
Po	84	1.1840E+05	1.12	1.1688E+05	1.11
At	85	1.2168E+05	1.13	1.2013E+05	1.12
Rn	86	1.2502E+05	1.13	1.2343E+05	1.12

[a] For He-like ions we omit the near-neutral ions. This is due to the degraded accuracy of the FAC calculations in such case, as described in Section 2.2.

Table 3
MEE from the modified LPA for $Z \leq 18$ and $21 \leq Z \leq 30$, in eV

Z	1	2	3	4	5	6	7	8
N	H	He	Li	Be	B	C	N	O
1	1.22E+01	6.92E+01	1.71E+02	3.12E+02	4.87E+02	6.92E+02	9.25E+02	1.18E+03
2		4.13E+01	1.23E+02	2.50E+02	4.21E+02	6.36E+02	8.90E+02	1.18E+03
3			3.24E+01	7.27E+01	1.33E+02	2.13E+02	3.13E+02	4.32E+02
4				3.68E+01	7.18E+01	1.20E+02	1.83E+02	2.60E+02
5					4.59E+01	8.06E+01	1.26E+02	1.84E+02
6						5.81E+01	9.41E+01	1.40E+02
7							7.28E+01	1.11E+02
8								9.00E+01

Z	9	10	11	12	13	14	15	16
N	A	Ne	Na	Mg	Al	Si	P	S
1	1.47E+03	1.77E+03	2.10E+03	2.45E+03	2.82E+03	3.21E+03	3.62E+03	4.05E+03
2	1.51E+03	1.87E+03	2.26E+03	2.69E+03	3.14E+03	3.63E+03	4.14E+03	4.68E+03
3	5.70E+02	7.26E+02	9.00E+02	1.09E+03	1.30E+03	1.52E+03	1.76E+03	2.02E+03
4	3.51E+02	4.57E+02	5.76E+02	7.09E+02	8.56E+02	1.02E+03	1.19E+03	1.37E+03
5	2.53E+02	3.35E+02	4.28E+02	5.34E+02	6.52E+02	7.81E+02	9.22E+02	1.07E+03
6	1.96E+02	2.63E+02	3.41E+02	4.30E+02	5.30E+02	6.41E+02	7.62E+02	8.94E+02
7	1.58E+02	2.15E+02	2.82E+02	3.59E+02	4.47E+02	5.44E+02	6.52E+02	7.70E+02
8	1.31E+02	1.81E+02	2.39E+02	3.07E+02	3.85E+02	4.72E+02	5.70E+02	6.77E+02
9	1.10E+02	1.54E+02	2.06E+02	2.67E+02	3.37E+02	4.16E+02	5.05E+02	6.03E+02
10		1.32E+02	1.79E+02	2.34E+02	2.98E+02	3.70E+02	4.52E+02	5.42E+02
11			1.31E+02	1.74E+02	2.23E+02	2.79E+02	3.43E+02	4.15E+02
12				1.34E+02	1.74E+02	2.19E+02	2.71E+02	3.29E+02
13					1.39E+02	1.76E+02	2.19E+02	2.68E+02
14						1.45E+02	1.81E+02	2.22E+02
15							1.52E+02	1.87E+02
16								1.60E+02

Z	17	18	21	22	23	24
N	Cl	Ar	Sc	Ti	V	Cr
1	4.50E+03	4.96E+03	6.45E+03	6.99E+03	7.53E+03	8.10E+03
2	5.24E+03	5.83E+03	7.76E+03	8.45E+03	9.16E+03	9.90E+03
3	2.28E+03	2.57E+03	3.50E+03	3.84E+03	4.19E+03	4.56E+03
4	1.57E+03	1.78E+03	2.48E+03	2.73E+03	3.00E+03	3.27E+03
5	1.24E+03	1.41E+03	2.00E+03	2.22E+03	2.44E+03	2.68E+03
6	1.04E+03	1.19E+03	1.71E+03	1.91E+03	2.11E+03	2.32E+03
7	8.99E+02	1.04E+03	1.51E+03	1.69E+03	1.88E+03	2.08E+03
8	7.94E+02	9.21E+02	1.36E+03	1.53E+03	1.70E+03	1.89E+03
9	7.11E+02	8.28E+02	1.24E+03	1.39E+03	1.56E+03	1.73E+03
10	6.42E+02	7.51E+02	1.14E+03	1.28E+03	1.44E+03	1.60E+03
11	4.94E+02	5.82E+02	8.94E+02	1.01E+03	1.14E+03	1.28E+03
12	3.94E+02	4.66E+02	7.26E+02	8.27E+02	9.36E+02	1.05E+03
13	3.22E+02	3.82E+02	6.02E+02	6.89E+02	7.82E+02	8.82E+02
14	2.68E+02	3.20E+02	5.08E+02	5.83E+02	6.64E+02	7.51E+02
15	2.27E+02	2.72E+02	4.35E+02	5.00E+02	5.71E+02	6.48E+02
16	1.95E+02	2.34E+02	3.77E+02	4.35E+02	4.97E+02	5.65E+02
17	1.69E+02	2.03E+02	3.30E+02	3.81E+02	4.37E+02	4.97E+02
18		1.79E+02	2.92E+02	3.38E+02	3.87E+02	4.42E+02
19			2.60E+02	3.01E+02	3.46E+02	3.95E+02
20			2.33E+02	2.70E+02	3.11E+02	3.56E+02
21			2.10E+02	2.44E+02	2.82E+02	3.22E+02
22				2.22E+02	2.56E+02	2.94E+02
23					2.34E+02	2.69E+02
24						2.47E+02

Z	25	26	27	28	29	30
N	Mn	Fe	Co	Ni	Cu	Zn
1	8.68E+03	9.27E+03	9.88E+03	1.05E+04	1.12E+04	1.18E+04
2	1.07E+04	1.14E+04	1.22E+04	1.31E+04	1.39E+04	1.48E+04
3	4.94E+03	5.33E+03	5.73E+03	6.14E+03	6.57E+03	7.01E+03
4	3.56E+03	3.86E+03	4.16E+03	4.48E+03	4.81E+03	5.15E+03
5	2.93E+03	3.18E+03	3.45E+03	3.72E+03	4.01E+03	4.30E+03
6	2.55E+03	2.78E+03	3.02E+03	3.27E+03	3.53E+03	3.80E+03
7	2.28E+03	2.50E+03	2.72E+03	2.96E+03	3.20E+03	3.45E+03
8	2.08E+03	2.28E+03	2.50E+03	2.72E+03	2.95E+03	3.19E+03
9	1.92E+03	2.11E+03	2.31E+03	2.52E+03	2.74E+03	2.97E+03
10	1.78E+03	1.96E+03	2.16E+03	2.36E+03	2.57E+03	2.79E+03
11	1.43E+03	1.58E+03	1.75E+03	1.92E+03	2.10E+03	2.28E+03
12	1.18E+03	1.31E+03	1.45E+03	1.60E+03	1.75E+03	1.92E+03
13	9.90E+02	1.10E+03	1.23E+03	1.35E+03	1.49E+03	1.63E+03
14	8.45E+02	9.44E+02	1.05E+03	1.16E+03	1.28E+03	1.41E+03
15	7.30E+02	8.18E+02	9.12E+02	1.01E+03	1.12E+03	1.23E+03
16	6.38E+02	7.16E+02	8.00E+02	8.90E+02	9.85E+02	1.09E+03
17	5.63E+02	6.33E+02	7.08E+02	7.89E+02	8.75E+02	9.66E+02
18	5.00E+02	5.64E+02	6.32E+02	7.05E+02	7.82E+02	8.65E+02
19	4.48E+02	5.06E+02	5.67E+02	6.34E+02	7.04E+02	7.80E+02
20	4.04E+02	4.56E+02	5.13E+02	5.73E+02	6.38E+02	7.07E+02
21	3.67E+02	4.14E+02	4.66E+02	5.22E+02	5.81E+02	6.45E+02
22	3.34E+02	3.78E+02	4.26E+02	4.77E+02	5.32E+02	5.90E+02
23	3.06E+02	3.47E+02	3.91E+02	4.38E+02	4.89E+02	5.43E+02
24	2.82E+02	3.19E+02	3.60E+02	4.04E+02	4.51E+02	5.01E+02
25	2.60E+02	2.95E+02	3.33E+02	3.74E+02	4.18E+02	4.65E+02
26		2.74E+02	3.09E+02	3.47E+02	3.88E+02	4.32E+02

27	2.88E+02	3.23E+02	3.62E+02	4.03E+02
28		3.02E+02	3.38E+02	3.77E+02
29			3.03E+02	3.39E+02
30				3.06E+02

Table 4
K-shell ionization energy for neutral atoms and H-like ions, retrieved from [23,24]

Element	Z	H-like [eV]	neutral [eV]	Element	Z	H-like [eV]	neutral [eV]
H	1	1.36E+01	1.36E+01	Ru	44	2.70E+04	2.21E+04
He	2	5.44E+01	2.46E+01	Rh	45	2.83E+04	2.32E+04
Li	3	1.23E+02	5.47E+01	Pd	46	2.96E+04	2.44E+04
Be	4	2.18E+02	1.12E+02	Ag	47	3.10E+04	2.55E+04
B	5	3.40E+02	1.88E+02	Cd	48	3.23E+04	2.67E+04
C	6	4.90E+02	2.84E+02	In	49	3.38E+04	2.79E+04
N	7	6.67E+02	4.10E+02	Sn	50	3.52E+04	2.92E+04
O	8	8.71E+02	5.43E+02	Sb	51	3.67E+04	3.05E+04
F	9	1.10E+03	6.97E+02	Te	52	3.82E+04	3.18E+04
Ne	10	1.36E+03	8.70E+02	I	53	3.97E+04	3.32E+04
Na	11	1.65E+03	1.07E+03	Xe	54	4.13E+04	3.46E+04
Mg	12	1.96E+03	1.30E+03	Cs	55	4.29E+04	3.60E+04
Al	13	2.30E+03	1.56E+03	Ba	56	4.46E+04	3.74E+04
Si	14	2.67E+03	1.84E+03	La	57	4.62E+04	3.89E+04
P	15	3.07E+03	2.15E+03	Ce	58	4.80E+04	4.04E+04
S	16	3.49E+03	2.47E+03	Pr	59	4.97E+04	4.20E+04
Cl	17	3.95E+03	2.82E+03	Nd	60	5.15E+04	4.36E+04
Ar	18	4.43E+03	3.21E+03	Pm	61	5.33E+04	4.52E+04
K	19	4.93E+03	3.61E+03	Sm	62	5.52E+04	4.68E+04
Ca	20	5.47E+03	4.04E+03	Eu	63	5.71E+04	4.85E+04
Sc	21	6.03E+03	4.49E+03	Gd	64	5.91E+04	5.02E+04
Ti	22	6.63E+03	4.97E+03	Tb	65	6.11E+04	5.20E+04
V	23	7.25E+03	5.47E+03	Dy	66	6.31E+04	5.38E+04
Cr	24	7.90E+03	5.99E+03	Ho	67	6.51E+04	5.56E+04
Mn	25	8.57E+03	6.54E+03	Er	68	6.72E+04	5.75E+04
Fe	26	9.28E+03	7.11E+03	Tm	69	6.94E+04	5.94E+04
Co	27	1.00E+04	7.71E+03	Yb	70	7.16E+04	6.13E+04
Ni	28	1.08E+04	8.33E+03	Lu	71	7.38E+04	6.33E+04
Cu	29	1.16E+04	8.98E+03	Hf	72	7.61E+04	6.54E+04
Zn	30	1.24E+04	9.66E+03	Ta	73	7.84E+04	6.74E+04
Ga	31	1.32E+04	1.04E+04	W	74	8.08E+04	6.95E+04
Ge	32	1.41E+04	1.11E+04	Re	75	8.32E+04	7.17E+04
As	33	1.50E+04	1.19E+04	Os	76	8.56E+04	7.39E+04
Se	34	1.60E+04	1.27E+04	Ir	77	8.81E+04	7.61E+04
Br	35	1.69E+04	1.35E+04	Pt	78	9.07E+04	7.84E+04
Kr	36	1.79E+04	1.43E+04	Au	79	9.33E+04	8.07E+04
Rb	37	1.90E+04	1.52E+04	Hg	80	9.59E+04	8.31E+04
Sr	38	2.00E+04	1.61E+04	Tl	81	9.86E+04	8.55E+04
Y	39	2.11E+04	1.70E+04	Pb	82	1.01E+05	8.80E+04
Zr	40	2.22E+04	1.80E+04	Bi	83	1.04E+05	9.05E+04
Nb	41	2.34E+04	1.90E+04	Po	84	1.07E+05	9.31E+04
Mo	42	2.46E+04	2.00E+04	At	85	1.10E+05	9.57E+04
Tc	43	2.58E+04	2.10E+04	Rn	86	1.13E+05	9.84E+04

OPEN ACCESS
IOP Publishing | International Atomic Energy Agency
Nuclear Fusion
Nucl. Fusion **64** (2024) 036024 (15pp)
https://doi.org/10.1088/1741-4326/ad24a0

First numerical analysis of runaway electron generation in tungsten-rich plasmas towards ITER

J. Walkowiak[1,2,*], M. Hoppe[3], I. Ekmark[4], A. Jardin[1], J. Bielecki[1], K. Król[1], Y. Savoye-Peysson[5], D. Mazon[5], D. Dworak[1] and M. Scholz[1]

[1] Institute of Nuclear Physics Polish Academy of Sciences, PL-31342 Krakow, Poland
[2] National Centre for Nuclear Research (NCBJ), 7 Andrzeja Sołtana Str., Otwock 05-400, Poland
[3] Fusion Plasma Physics, Department of Electric Energy Engineering, KTH, 10044 Stockholm, Sweden
[4] Department of Physics, Chalmers University of Technology, Gothenburg SE-41296, Sweden
[5] CEA, IRFM, F-13108 Saint-Paul-lez-Durance, France

E-mail: jedrzej.walkowiak@ifj.edu.pl

Received 14 November 2023, revised 22 January 2024
Accepted for publication 31 January 2024
Published 13 February 2024

Abstract

The disruption and runaway electron analysis model code was extended to include tungsten impurities in disruption simulations with the aim of studying the runaway electron (RE) generation. This study investigates RE current sensitivity on the following plasma parameters and modelling choices: tungsten concentration, magnetic perturbation strength, electron modelling, thermal quench time and tokamak geometry—ITER-like or ASDEX-like. Our investigation shows that a tungsten concentration below 10^{-3} does not cause significant RE generation on its own. However, at higher concentrations it is possible to reach a very high RE current. Out of the two tested models of electrons in plasma: fluid and isotropic (kinetic), results from the fluid model are more conservative, which is useful when it comes to safety analysis. However, these results are overly pessimistic when compared to the isotropic model, which is based on a more reliable approach. Our results also show that the hot-tail RE generation mechanism is dominant as a primary source of RE in tungsten induced disruptions, usually providing orders of magnitude higher RE seed than Dreicer generation. We discuss best practices for simulations with tungsten-rich plasma, present the dependence of the safety limits on modelling choices and highlight the biggest shortcoming of the current simulation techniques. The obtained results pave the way for a wider analysis of tungsten impact on the disruption dynamics, including the mitigation techniques for ITER in the case of strong contamination of the plasma with tungsten.

Keywords: runaway electrons, tungsten impurities, ITER, computational plasma physics

(Some figures may appear in colour only in the online journal)

* Author to whom any correspondence should be addressed.

1. Motivation

Runaway electrons (RE) are one of the major issues for tokamak safety. When unmitigated, they can cause local melting of the plasma-facing components (PFC) and sometimes even damage the underlying components of the machine [1, 2]. Extensive work has been done to develop techniques for suppressing RE generation during the disruption, e.g. by massive material injection [3]. Unfortunately, active methods of mitigation require the disruption to be predicted in time and a finely tuned material injection, to avoid a too fast current quench (CQ), which can lead to mechanical failure of the machine components.

Some disruptions occur very suddenly, without the usual signals of growing plasma instability that allow the triggering of the mitigation system. One such scenario is the impurity influx resulting from large sources such as flakes or dust, which is often labelled as UFO (as such particles were described as unidentified flying objects), or unidentified impurity influx [4–6]. These events are responsible for up to a few percent of the disruptions in present-day tokamaks, but their occurrence is strongly related to the PFC condition. In some campaigns, UFOs are practically not occurring, while if the machine experienced some significant damage such as PFC melting, they sometimes become a significant issue [7]. In reactor-scale tokamaks, with discharge times extended into minutes, PFC degradation can occur even as a result of normal operation conditions [8]. The impact of PFC degradation on the impurity influx into the plasma in the long-term operation is still an open question.

The effects of UFOs can vary depending on the PFC composition. Operation at JET showed that carbon wall tokamaks cannot serve as thermonuclear reactors due to their tritium retention [9]. This resulted in increased use of tungsten (W) as plasma-facing material [8, 10, 11]. Unfortunately, W is a heavy element with $Z = 74$, which creates significant problems when entering the plasma as an impurity. Complete ionisation of *W* requires an energy of $\sim$80 keV [12], much higher than plasma temperatures foreseen even in the largest tokamaks such as ITER or DEMO [13]. This results in strong line radiation of partially ionised W impurities, orders of magnitude higher than for low-*Z* elements of similar concentration. Therefore, the *W* impurity concentration in the plasma must be kept at a much lower level than in the case of carbon impurities. Concentrations limited to a relatively small fraction 10^{-5}–10^{-4} are required for a positive energy balance in a fusion reactor [14].

When the *W* concentration rises in the plasma core, it can break the H-mode or lead to a disruption. It is worth mentioning that *W* influx can lead both to slow accumulation in the plasma core, which at some point causes an MHD instability, or to much faster impurity influx observed as a radiation spike [15]. In the former case, it is usually possible to mitigate a disruption, but the latter case can be much more problematic. A characteristic for high-*Z* impurities is that sometimes the thermal quench (TQ) does not lead to a CQ and is instead followed by at least partial temperature recovery and a very slow CQ, or even recovery close to pre-disruptive conditions [5, 15]. This can be the case when tungsten impurities are expelled from the plasma by a MHD instability [16, 17]. However, it seems that producing such disruptions on purpose in a reliable way is beyond control capabilities.

With plans to start ITER with tungsten PFCs, it is necessary to estimate the risk posed by tungsten impurities to every aspect of machine operation and safety. For REs, tungsten was not yet included in the analysis and this is the gap which this work aims to address. It was done in a series of numerical experiments conducted with the disruption and runaway electron analysis model (DREAM) code [18], collecting results from a few hundreds of plasma simulations in total. DREAM, for the purpose of this work, has been extended with the necessary atomic data, to include *W* impurities in the simulations. The basic assumptions of the simulations and their limitations are introduced in section 2. Section 3 describes the investigated simulation approaches and their consequences. It is divided into the following parts:

- Comparison of two models of the electron distribution: fluid and kinetic.
- Impact of magnetic perturbation strength during TQ and CQ on the RE generation. In DREAM, stochastization of the magnetic field lines during disruptions is modelled by an effective radial diffusion, because calculation of the magnetic flux surfaces would be very expensive and sensitive to initial conditions [19, 20].
- The contribution of the Dreicer mechanism to overall RE generation and different approaches to the Dreicer generation modelling with a fluid plasma model (Connor–Hastie and neural network).
- Various approaches to the TQ time definition and effects of varying the TQ period in simulations, when radial transport is enhanced.
- Influence of the device parameters on the RE generation in a W induced disruption.

Section 4 describes the results in an ITER-like disruption scenario, which is followed by a discussion of the consequences for the ITER disruption mitigation system analysis.

2. Methods

Results presented in the following sections were obtained with the DREAM code, which allows for self-consistent simulation of plasma cooling and associated RE dynamics during disruptions. The code can fully-implicitly solve a set of nonlinear coupled equations describing the evolution of temperature, density, current density and electric field, as well as the full electron distribution function in arbitrary axisymmetric geometry. It employs a combination of fluid models for background plasma parameters, including the toroidal electric field, electron and ion temperatures, ion densities and charge states, as well as various models for REs, ranging from fluid to fully kinetic. The most complete model included in

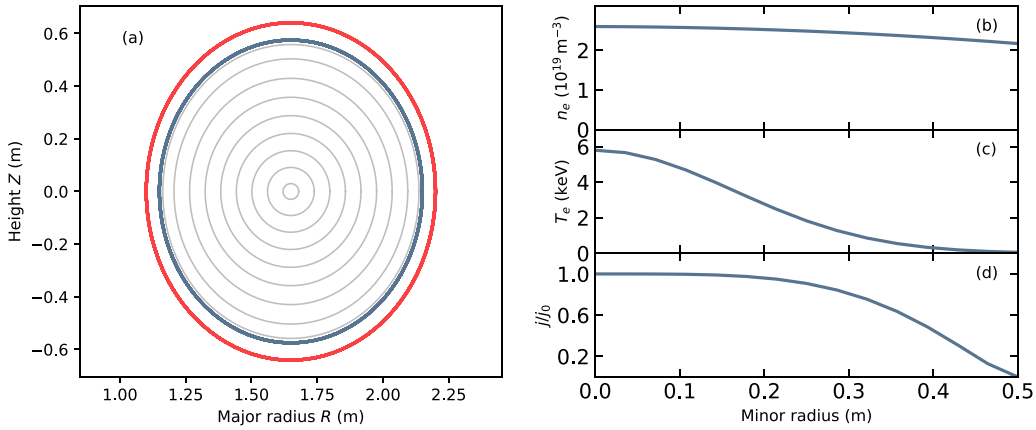

Figure 1. Parameters for the baseline ASDEX-like scenario: (*a*) magnetic field flux surfaces (gray), with the plasma boundary shown in blue and vessel wall in red. Profiles of: (*b*) initial electron density n_e, (*c*) initial electron temperature T_e, and (*d*) initial plasma current density $j/j_0, j_0 = 1.62MA\,\mathrm{m}^{-2}$ [18]. Reproduced from [18]. CC BY 4.0.

DREAM is drift-kinetic model with a fully relativistic Fokker–Planck test-particle operator for electron-electron collisions, synchrotron radiation reaction force, an avalanche operator, bremsstrahlung and screening effects in a partially ionised plasma. The field-particle part of the collision operator is neglected, which would result in underestimated conductivity. To amend that, the ohmic current is corrected with a conductivity correction, to capture the correct Spitzer response to an electric field [18]. In the presented work, we used a feature of DREAM which allows parts of the electron phase space to be modelled kinetically, and the remainder to be described by fluid equations. The two approaches were compared, one with a fully fluid representation of plasma, and the other one with a reduced kinetic model, where suprathermal electrons are modelled with kinetic equations and the bulk of electrons is modelled with a fluid approach. A detailed description of differences between these two models is presented in section 3.3.

Each disruption simulation was divided into two phases: TQ and CQ. The first phase is a short period at the beginning of the disruption, when the temperature drops rapidly. During the TQ, the magnetic flux surfaces are usually destroyed by intense MHD activity in a process called stochastization of the magnetic flux surfaces [19]. However, this is a very complex process, a detailed simulation of which would be time consuming and possibly too sensitive to initial conditions to make it useful in our study. Instead, elevated transport coming from destruction of magnetic flux surfaces is modelled as increased diffusion of heat [21] and RE current [22]. While newer transport models have been developed, they are either not applicable in this scenario, or would require input from 3D MHD simulations. Furthermore, due to the way how these operators are implemented, using a more recent transport model would effectively correspond to using a slightly different $\delta B/B_0$ value. Since $\delta B/B_0$ is not determined self-consistently, but is one of the input parameters whose impact is investigated in this work, the choice of exact transport model should not change the final conclusion. During the CQ, RE diffusion is set to zero while a weak magnetic perturbation is prescribed for the heat diffusion in order to maintain a small amount of heat transport and avoid unphysical effects [23]. For numerical stability, change of the transport parameters is not instantaneous, but takes place over the last 1% of the TQ time. Otherwise, the CQ simulation would be prone to diverge at the first time step. The moment at which the disruption transfers from the TQ to the CQ phase is difficult to define, so this point is investigated in detail in section 3.1.

2.1. Tokamak geometry and plasma parameters

Simulations were conducted with two scenarios: the baseline discharge presented in the DREAM reference paper [18], which was created to resemble experimental results from ASDEX-U, and the ITER-like scenario modelling a disruption during the ITER H-mode flattop phase. Radial profiles of plasma electron density n_e, electron temperature T_e and normalised plasma current density j are presented in figures 1 and 2 for ASDEX-like and ITER-like cases, respectively. Geometry and plasma parameters are listed in table 1. The two sources of primary RE are Dreicer and hot-tail generation. RE generation by tritium decay and Compton scattering are neglected as they do not originate from the presence of impurities in the plasma and are relevant mainly for burning plasma scenarios. Avalanche RE generation is included.

In theory it is possible for gamma radiation to be present due to bremsstrahlung interaction between REs and tungsten impurities, but at the given plasma density the total fraction of bremsstrahlung reactions leading to the creation of another RE is negligible. Because of very small scattering cross-section, plasma can be in this matter treaded as optically thin, meaning that almost all photons created in the plasma will leave its volume without interactions with other particles. Compton scattering is important source when gamma radiation comes from external sources like walls, because it generates primary RE. When radiation is created by interaction

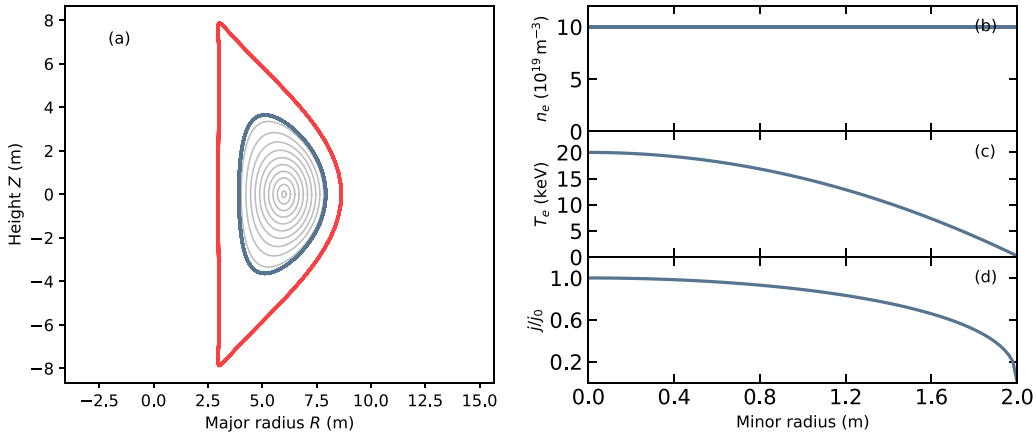

Figure 2. Parameters for the baseline ITER-like scenario: (*a*) magnetic field flux surfaces (gray), with the plasma boundary shown in blue and vessel wall in red. Profiles of: (*b*) initial electron density n_e, (*c*) initial electron temperature T_e, and (*d*) initial plasma current density $j/j_0, j_0 = 1.12\ MA\,\mathrm{m}^{-2}$ [24]. Reproduced from [23]. CC BY 4.0.

Table 1. Tokamak geometry and plasma parameters of the ASDEX-like and ITER-like scenarios Adapted from [18]. CC BY 4.0.

Parameter	ASDEX-like [18]	ITER-like [24]
Major radius R_m	1.65 m	6.0 m
Minor radius a	0.5 m	2.0 m
Wall radius b	0.55 m	2.833 m
Elongation at edge $\kappa(a)$	1.15	1.82[a]
Toroidal magnetic field B_0	2.5 T	5.3 T
Initial plasma current $I_{\mathrm{p},0}$	800 kA	15 MA
Resistive wall time	10 ms	500 ms

[a] Elongation in the ITER-like example is not homogeneous, but varies in the range 1.5–1.82 as the elongation is described with $\kappa = 1.5 + 0.02r^4$, where r is the plasma minor radius coordinate.

of RE, it would be only small correction to the avalanche term.

During a disruption, part of the current is induced in the tokamak wall. The effective wall conductivity is included by prescribing the resistive wall time ($\tau_W = L_W/R_W$), whose exact value can be obtained from detailed simulation of the vacuum vessel inductance L_W and resistance R_W or measurements on existing devices. Neglecting the wall conductivity can lead to unphysical results, as it affects the disruption dynamics and current distribution.

2.2. Tungsten impurities

Tungsten impurities are introduced at the beginning of the simulation, as neutral atoms with an initial temperature of 1 eV. The W concentration is defined as $n_W/n_{e,0}$, where n_W is W density and $n_{e,0}$ is the initial density of free electrons. In order to identify the main factors which influence RE generation in tungsten-rich plasmas, n_W is assumed to be spatially uniform and constant during the whole simulation. Assuming a strongly peaked impurity profile in the simulation would result in local plasma cooling and subsequent current redistribution. In reality, this results in an MHD instability, followed by magnetic field line stochastization and elevated transport. When magnetic surfaces are destroyed, the impurities should be diffused across plasma which would result in a mostly flat W concentration profile. Reproducing such effects in detail would require significant computational effort and is outside the scope of this work. When a constant, strongly inhomogeneous W profile is prescribed in the simulation, there is no CQ, as part of the plasma is not sufficiently cooled and some current can be maintained by redistribution to the hot region. The assumption of a flat tungsten concentration profile simplifies the interpretation of the results and should not be far from reality shortly after the TQ.

Performing simulations with W impurities in DREAM required some additional atomic data, which has not been included earlier in the code. Most of the necessary quantities were obtained from the ADAS database [25]. To calculate inelastic collisions in the Fokker–Planck collision operator, the Bethe stopping power theory is used [26]. This requires the mean excitation energy (MEE) for tungsten ions, which is not available neither from measurements nor from present ab-initio theoretical calculations. MEE was calculated with an approach based on the local plasma approximation (LPA) corrected to fit the results from Sauer *et al* [27–29]. More detailed comments on the selection of ADAS coefficients and MEE calculation can be found in appendices A and B.

2.3. Magnetic perturbation

One of the main parameters which have a strong influence on the disruption dynamics is the magnetic perturbation due to magnetic flux surface stochastization during the TQ. Nevertheless, the exact simulation of the disruption with magnetic surfaces is usually not feasible due to the large number of unknowns in the plasma initial state and exact disruption evolution, which would require much more detailed simulations at extremely high computational costs. Therefore, averaged magnetic perturbation strengths were provided instead, which were given with respect to the magnetic field strength on

the magnetic axis and denoted as $\delta B/B_0$. Based on the numerical simulations of MHD instabilities, it is expected to be in the range of 10^{-3}–10^{-2} [23, 30]. As diffusion coefficients in the simulation depend on this parameter, it has a direct effect on the temperature evolution and RE confinement in the initial phase of the disruption. As long as the W concentration is not extremely high, it will have an effect on the proportion of the energy lost by radiation to the energy lost through the diffusion to the walls.

We conducted a parameter scan with different tungsten concentrations and $\delta B/B_0$ values for the TQ. The W concentration was varied from 10^{-3} to 3.16×10^{-1}. At lower concentrations, tungsten has a very weak effect on plasma dynamics. The upper limit was selected arbitrarily, as reaching such high concentrations is rather improbable in tokamaks, nevertheless it is useful to show the trends with rising W concentration. $\delta B/B_0$ was varied between 10^{-3} and 10^{-2}. Values for both the W concentration and magnetic perturbation were distributed logarithmically with two values per order of magnitude, giving 6 values of W concentration and 3 values of $\delta B/B_0$. During the CQ, the heat diffusion was set with $\delta B/B_0 = 4 \cdot 10^{-4}$, to avoid unphysical concentration of current into hot channels. This value was used before in other works [24, 31] and we confirmed in test simulations that also in our case lower values can lead to such unphysical effects. The transition between TQ and CQ, when the transport coefficients are changed according to decreasing $\delta B/B_0$, takes place during the last 1% of the TQ time. As the real duration of this transition is impossible to accurately predict within the presented approach, we used a transition time which was as short as possible from the numerical stability point of view.

The scan was repeated for different simulation approaches and the results are presented in the following section. Unfortunately, for some simulations the solver failed to find a convergent solution. The failure to converge is usually related to the Newton solver and not to the given set of physical equations. This is a common numerical issue in many computational tools, usually related to the too large time step, which leads to overshoots of predictions when the time derivative is large. In some cases the reason is different and usually difficult to identify. In our analysis the convergence was usually ensured by a change of the time step. In cases where we could not obtain convergence in any known way, we do not present the results.

3. Investigated simulation approaches

3.1. TQ time

TQ is the initial period during the disruption, when plasma temperature decreases rapidly. It is related to increased transport coefficients due to strong magnetic perturbation when the magnetic surfaces are broken. In the simulation TQ refers to the period when diffusion coefficients are increased, which results in much faster temperature decrease than in the CQ. Despite the fact that in simulation the temperature decrease is just the result of the TQ, not the cause, we use it to define the TQ duration. In general, there can be disruptions with incomplete TQ, where the magnetic perturbation stops before a very low temperature is reached [15]. However, we focus on the most pessimistic scenario of a disruption with a single strong TQ. In mitigation scenarios with low-Z impurities like neon or argon, there is a rapid increase of the impurity cooling factor when the plasma temperature drops below 100 eV as nearly stripped impurity ions recombine [14]. The radiated power can then rise by two orders of magnitude. This makes the cooling of the plasma very rapid below 100 eV, so the TQ time can be straightforwardly defined as the time needed to reach temperatures of a few tens eV.

However, W impurities radiate strongly in temperatures up to few keV—this is an effect of much higher atomic number of tungsten ions. Because of that, there is no steep radiation increase at low temperatures. Defining a TQ time is then more difficult, because the temperature drop will stop when the radiated power is balanced by ohmic heating without necessarily reaching the prescribed temperature. As a first approach, we used a definition of the TQ time (τ_{TQ}) similar to the definition of the CQ time [23]. It is formulated as follows:

$$\tau_{\mathrm{TQ}} = \frac{t(T = 0.2T_0) - t(T = 0.8T_0)}{0.6} \tag{1}$$

where T_0 is the initial temperature before the disruption.

In this approach, hereafter referred to as 80–20, the TQ time is defined as the time it would take for the temperature to drop from its initial value T_0 to 0, assuming the temperature drops at the same rate as from 80% to 20% of T_0.

In general, many other definitions can be used, for example by changing time measurement points to 90% and 10% of the initial temperature. We decided to investigate the effects of our TQ time definition by comparing it with a different approach, which provided a longer TQ time and was based on the measurement of the temperature time derivative, $\mathrm{d}T/\mathrm{d}t$. This definition is based on the assumption that the time derivative becomes very small at the end of the TQ. The problem is that the magnitude of the time derivative of the temperature can be very different depending on the magnetic perturbation strength and amount of impurities, which define the energy losses. To solve this problem, we calculate $\mathrm{d}T/\mathrm{d}t$ and normalise it to its maximum value, which is reached in the first time steps of the simulation. We assumed that when normalised $\mathrm{d}T/\mathrm{d}t < 10^{-4}$, then the TQ is over. While the exact number is selected arbitrarily, it is in the order of magnitude which provides a TQ time a few times longer than the 80–20 definition, while still being robust enough to be useful in most of the simulated cases.

As shown in figure 3, the TQ time can have an impact on the initial seed of REs for the avalanche occurring during the CQ. The increased radial diffusion accelerates the temperature drop, which is a driving force for hot-tail generation. But at the same time, REs are deconfined, so the overall RE population will peak and then decline if the TQ is long enough. This is in line with our expectations, as intentionally applied magnetics

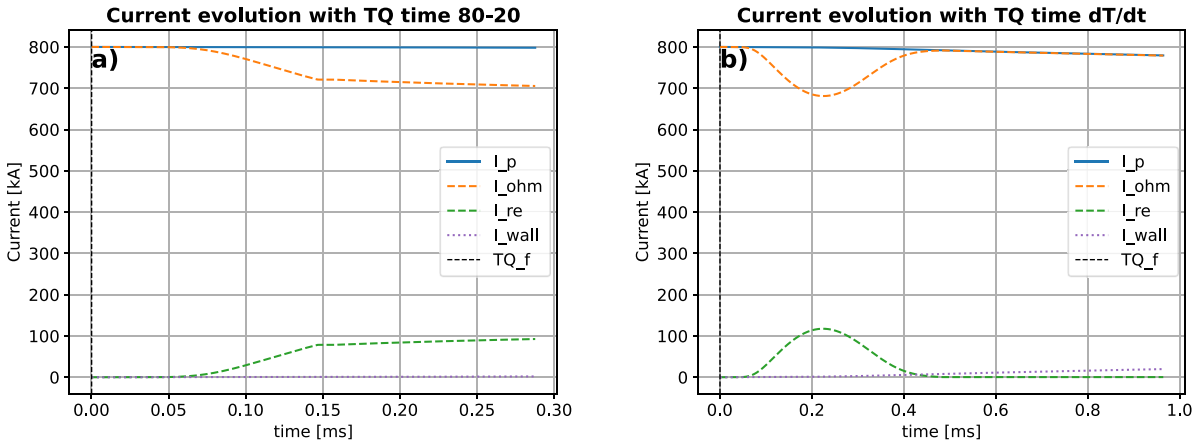

Figure 3. Time evolution of total plasma current (I_p), ohmic current (I_ohm), RE current (I_re), wall current (I_wall). Transition from TQ to CQ is marked with a dashed black line (TQ_f). Simulation was performed with ASDEX-like parameters and fluid model. W concentration was 1×10^{-2}, $\delta B/B_0$ in TQ was 3.16×10^{-3}, $\delta B/B_0$ in CQ was 4×10^{-4}. (*a*) Results from the simulation with TQ time obtained from the 80–20 definition. (*b*) Results from simulation with the TQ time obtained from the dT/dt definition.

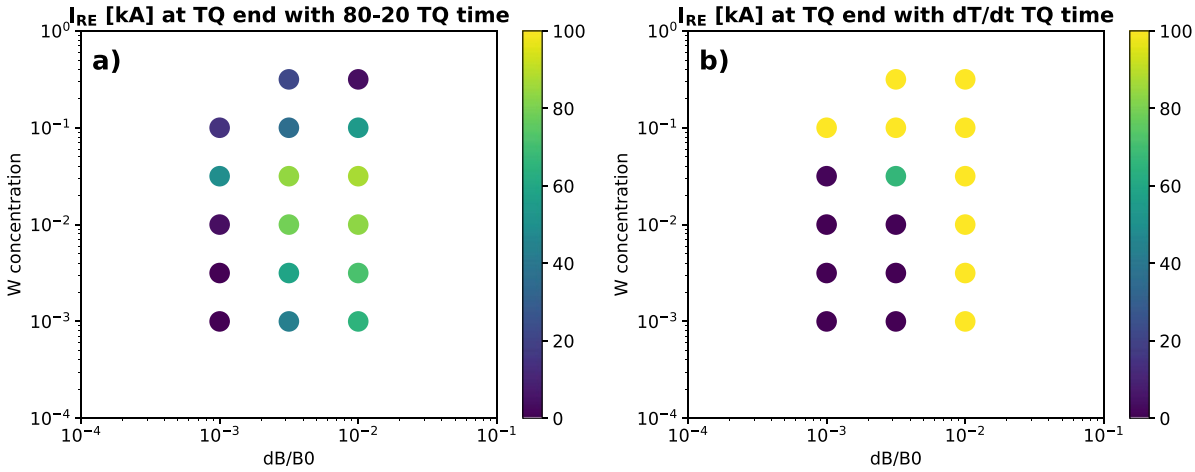

Figure 4. RE current at the moment of transition from TQ to CQ for fluid model simulations with different W concentrations and $\delta B/B_0$ during TQ in the ASDEX-like disruption scenario. (*a*) Results with TQ time obtained from 80–20 definition. (*b*) Results from simulation with TQ time obtained from dT/dt definition.

perturbations of sufficient strength were already recognized as one of the possible ways to mitigate RE [32]. The exact TQ time will be decisive for the initial RE population for the CQ and thus will influence the final RE current during the plateau phase. The dependence of the RE current at the moment of transition from TQ to CQ is presented on figure 4. The 80–20 definition seems to be a safe choice for the TQ time definition. Indeed, it is fast enough to break the TQ before REs are almost fully deconfined, so there is no risk that the initial RE population of the CQ will be strongly underestimated. It seems there is no need to catch the maximum of the RE population during the TQ. From the point of view of breaching the safety limits, it can be important only for cases at the border of allowed RE current, but in such cases the RE generation is very weak even during the TQ and will be negligible, if any during the CQ. The difference in the RE current generated in both approaches is presented in figure 5.

3.2. Dreicer generation

In the investigated cases for the ASDEX-like scenario, the dominant source of primary REs in the fluid model is the hot-tail mechanism. Dreicer generation can be modelled with either the Connor–Hastie formula [33], or with a neural network (NN) which was trained on results from kinetic simulations [34]. Unfortunately, the NN used currently in DREAM was trained on a number of cases which included different amounts of impurities much lighter than W. Despite the fact that it was proven that this NN can extrapolate to impurities not given during training, uncertainties remained about its robustness with W impurities. The general rule for a NN is that extreme care must be taken when using it outside of its training bounds. For this reason, we compared the NN with the Connor–Hastie model, which is known to overestimate the RE generation, so it provides an upper bound for RE generation

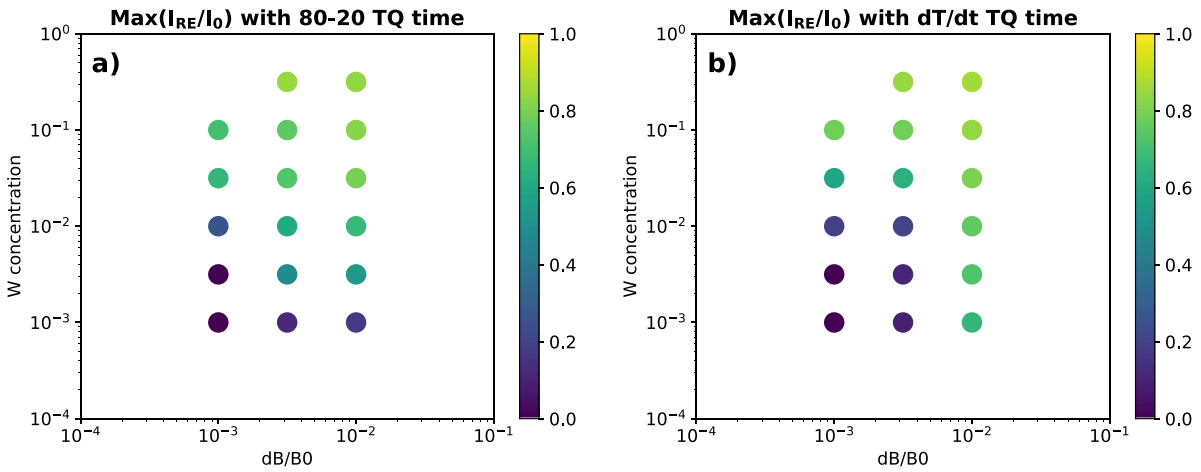

Figure 5. Maximum RE current compared to initial plasma current for fluid model simulations with different W concentrations and $\delta B/B_0$ during TQ in the ASDEX-like disruption scenario. $\delta B/B_0$ during CQ was always set to 4×10^{-4}. (*a*) Results with TQ time obtained from 80–20 definition. (*b*) Results from simulation with TQ time obtained from dT/dt definition.

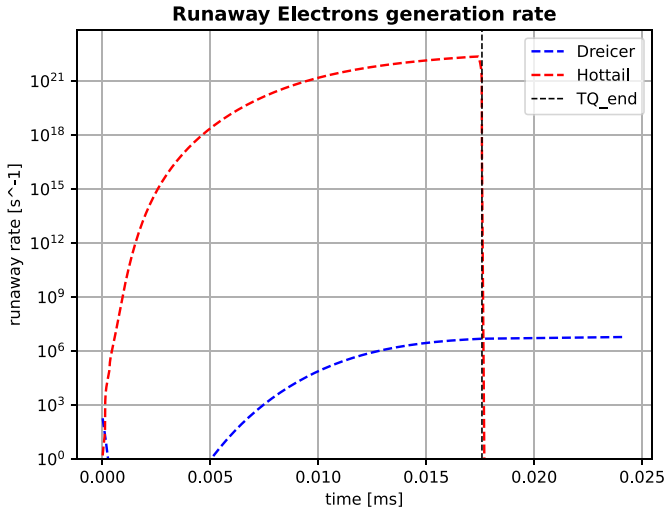

Figure 6. RE generation rate from Dreicer (Connor–Hastie) and hot-tail (Svenningsson) mechanisms in the ASDEX-like disruption simulation with a fluid model. Transition from TQ to CQ is marked with a dashed black line (TQ_f). W concentration was 1×10^{-3}, $\delta B/B_0$ in TQ was 1×10^{-2}, $\delta B/B_0$ in CQ was 4×10^{-4}.

from the Dreicer mechanism. In the isotropic simulation, the RE generation is calculated by resolving the flux of electrons through the upper boundary of the momentum grid calculated with the Fokker–Planck equation. Therefore, distinguishing between hot-tail and Dreicer RE is not possible in the isotropic case.

The obtained results for the ASDEX-like disruption scenario show that even with the Connor–Hastie model, the Dreicer generation is several orders of magnitude smaller than hot-tail generation in every investigated case. As shown in figure 6, the strongest primary RE generation occurs during the TQ, when the enhanced transport, due to magnetic perturbations, accelerates the temperature drop and fuels the hot-tail generation mechanism.

In some cases for the ITER-like discharge, Dreicer generation was significant, as shown in figure 7. The results from some of the simulations show that the NN can give Dreicer generation values even higher than the Connor–Hastie model. It proves that in the investigated cases the NN cannot be trusted, as it can overestimate the RE generation by many orders of magnitude. For now no good solution for the fluid model exists, as Connor–Hastie is known to overestimate the Dreicer generation and the NN is unreliable with W impurities. Due to the unpredictable nature of errors from the machine learning algorithms, it is not recommended to use this NN in the presence of W impurities. The Connor–Hastie model can be used only if a high accuracy of the Dreicer generation rate is not needed. For an accurate prediction, a kinetic simulation is necessary. Retraining the NN using dedicated cases with W impurities is planned in the future, but it lies outside the scope of this work.

3.3. *Fluid and Isotropic models*

DREAM can be used with different levels of complexity, starting from the kinetic representation of the electron population on the momentum-space grid, through various averages and approximations up to the simple fluid-like representation. In this work, two approaches were tested. The first is the fluid model, where the bulk of electrons is assumed to have a Maxwellian distribution and the RE population is traced only in terms of its density. Primary RE generation is calculated from models of Dreicer and hot-tail generation, as described in section 3.2. The second approach is referred to as the isotropic model, where a pitch angle-averaged kinetic equation is solved. The electrons are divided into ‘cold’, ‘hot’ and RE populations. The ‘cold’ and RE population are calculated in almost the same way as in the fluid model. The only difference is that cold population temperature is set to very low temperature (usually 1 eV) and very low density. It later heats up by receiving electrons from the ‘hot’ spectrum

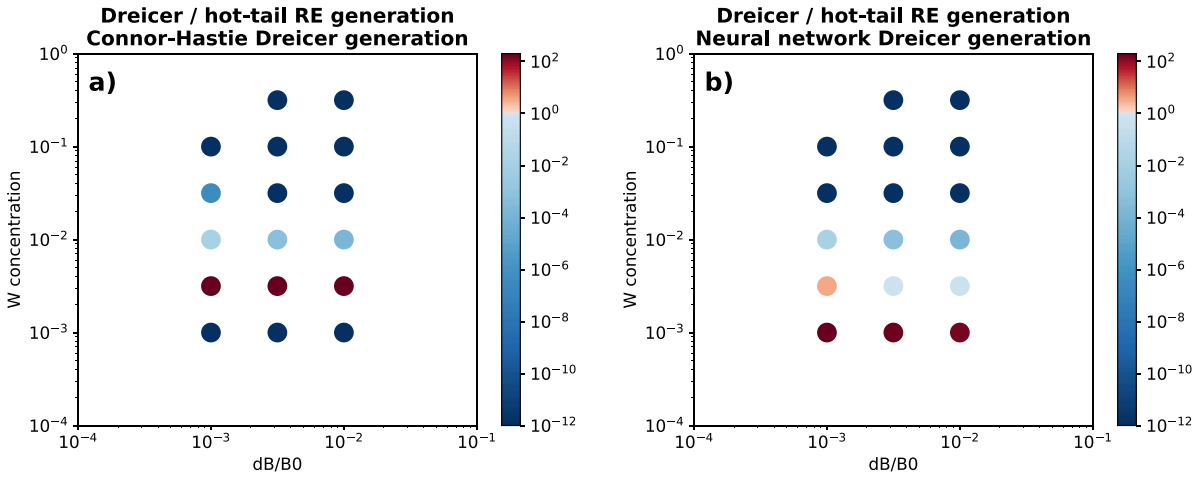

Figure 7. Maximum Dreicer RE generation rate compared to maximum hot-tail generation rate for simulations with different W concentrations and $\delta B/B_0$ during TQ. Disruption conditions were based on the ITER-like scenario, $\delta B/B_0$ during CQ was always set to 4×10^{-4}. (*a*) Results from simulation with a Connor–Hastie model of Dreicer generation. (*b*) Results from simulation with NN modeling of the Dreicer generation.

which cool down below the momentum threshold separating both populations. The momentum grid includes electrons from the so-called 'hot' part of the momentum spectrum—their normalised momentum is well above the thermal momentum and below the specified runaway threshold, as described in [18]. This region is critical to directly simulate the RE generation rate—it is obtained from the flux of electrons through the upper boundary of the momentum grid, which replaces the fluid Dreicer and hot-tail models. The name of this approach comes from the fact that in the reduced kinetic equation, the leading order term in the expansion of the distribution function is isotropic [18]. The isotropic model is the simplest kinetic model available in DREAM. Its computation cost is roughly 3–4 times larger than that of the fluid model, which we consider a reasonable trade-off between computation time and additional insight obtained by using a more complex model.

The first difference between both approaches can be noticed during the TQ, after W impurities are ionised. In the fluid model, all non- REs are treated as one fluid, so new electrons coming from ionisation are instantly thermalized with the bulk electron population. This causes faster cooling of the initial electron population. In the isotropic model, new electrons are introduced into the 'cold' population, but the bulk population of electrons in the plasma is in the 'hot' population for the first microseconds, so the thermalization is not instantaneous. After the ionisation, the electrons from the 'hot' population will either cool down and join the 'cold' population, or accelerate and become REs—depending on their momentum. Generation of the REs is not based on the models of Dreicer and hot-tail generation, but is instead a result of kinetic equations on the momentum grid. The main results are lower RE generation and longer CQ in the isotropic model. Similar effects, but at much smaller scale, were observed in other work [31].

Results from the fluid model are more conservative than the results from the isotropic model. Fluid simulations use the Svenningsson model for hot-tail generation [35], which is not fully valid for plasma with weakly ionised impurities. It probably overestimates the RE generation, which can be the main reason for the noticeable discrepancies between both approaches, as visible in figure 8. The isotropic model, on the other hand is not well suited for the cases with low amounts of impurities, when there is a small population of 'cold' electrons compared to 'hot' electrons, as one of the assumptions of the model is that collisions amongst the 'hot' electrons are negligible. These collisions would probably decrease the RE generation and make current decay longer. Bearing in mind the differences between fluid and isotropic models, it is possible to use just the fluid model for testing RE mitigation strategies or in the initial scans of the parameter space. It can also be useful for comparison with experiments, as diagnostics for temperature and current can be used to prescribe part of the plasma evolution. The isotropic model should probably give more accurate predictions, despite the fact that collisions between hot electrons are neglected. Still, the experimental validation of these models with W impurities should be made to give a definite statement on their accuracy.

3.4. *Impact of tokamak size*

The last investigated parameter in simulations of RE generation was the tokamak size. At the same W concentration, the number of radiating W atoms scales with volume, while the heat diffused to walls comes only through the plasma surface. The radiated power should thus dominate over the transport effects in a bigger tokamak, keeping the same transport coefficients. To investigate how different ratios of these two factors will influence the disruption dynamics, we compared simulations made in two different geometries: one based on the ASDEX-like characteristics and one based on the ITER-like ones. The minor and major plasma radii are approximately 4 times bigger in the ITER-like case, see table 1. Figure 9 presents results from these simulations, which were performed with the isotropic model.

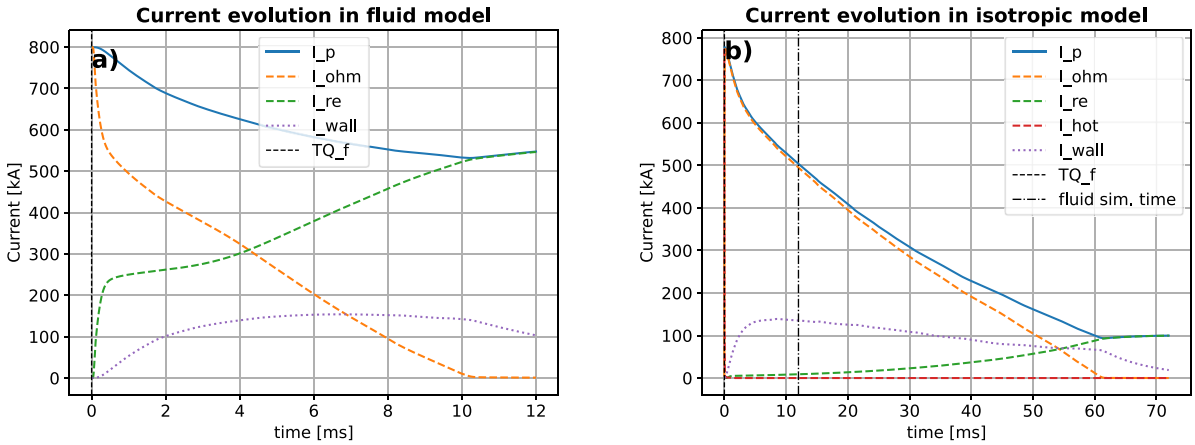

Figure 8. Time evolution of total plasma current (I_p), ohmic current (I_ohm), RE current (I_re), hot electrons current (I_hot), wall current (I_wall) in the ASDEX-like disruption simulation with (*a*) the fluid model and (*b*) the isotropic model of plasma. Transition from TQ to CQ is marked with a dashed black line (TQ_f). Simulation time from the fluid model case is marked in the plot (*b*) with a dash-dot line. *W* concentration was 3.16×10^{-2}, $\delta B/B_0$ in TQ was 3.16×10^{-3}, $\delta B/B_0$ in CQ was 4×10^{-4}.

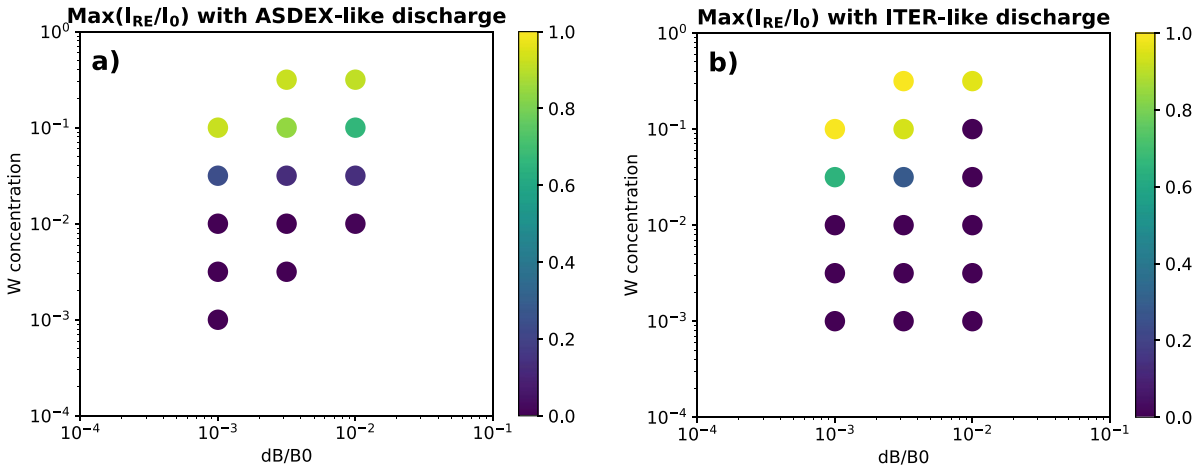

Figure 9. Maximum RE current compared to initial plasma current for simulations using the isotropic model with different *W* concentrations and $\delta B/B_0$ during TQ in (*a*) ASDEX-like disruption scenario (*b*) ITER-like disruption scenario. TQ time obtained from 80–20 definition, $\delta B/B_0$ during CQ was always set to 4×10^{-4}.

In neither machine do plasmas with *W* concentration up to 10^{-2} disrupt through a radiative collapse. Radiated power is balanced by ohmic heating, so the temperature is kept at the level of hundreds of eV for more than 0.15 s. This is a limit after which we can expect plasma disruption by vertical displacement event and excess halo current in the surrounding structures [3]. With higher tungsten concentrations, there is a negative dependence of the maximum RE current on the magnetic perturbation strength. This can be partially explained by the increased transport of the RE during TQ, which leads not only to loss of the RE, but also to their redistribution to the regions where electric field is lower and cannot sustain the avalanche growth.

There is a visible difference in maximum current conversion to RE current between both geometries. This shows that RE current on larger tokamaks could be higher than a simple scaling by maximum current would suggest. The RE current can also reach significant values at lower tungsten concentration in larger tokamaks. This is in line with the general expectations that RE generation can become more problematic when reactor-scale tokamaks are considered. Many of these issues are however related to the plasma current, so in case of compact tokamaks with high magnetic field a similar issue can occur as in ITER-size devices.

4. Simulation results in the ITER-like scenario

As the last step of the presented work, a series of simulations for the ITER-like disruption scenario was conducted in four different configurations. Two simulations were done with the 80–20 TQ time definition and two with the dT/dt TQ time definition. In each case, one simulation was performed with the fluid model and one with the isotropic model of the electrons in the plasma. The resulting RE current is presented in figures 10 and 11. For ITER, the safety limit of RE current, set

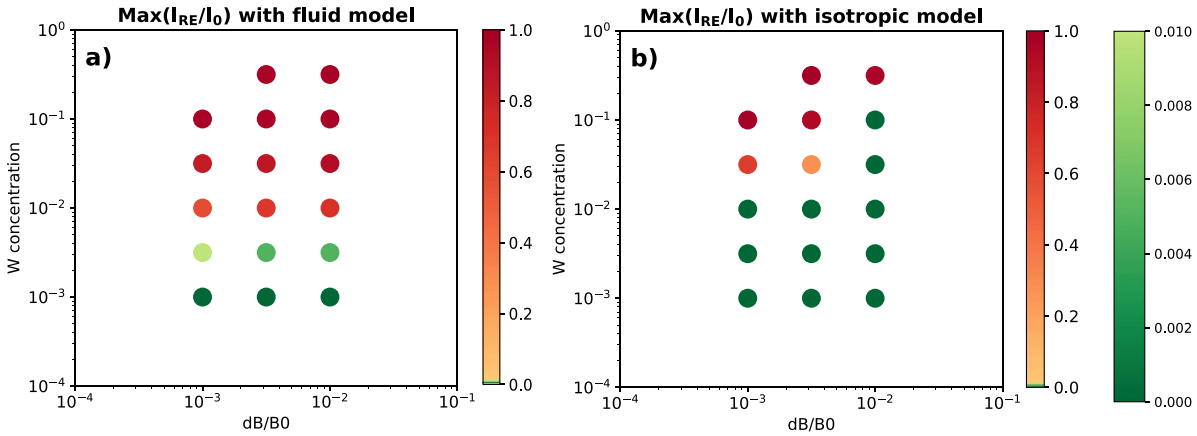

Figure 10. Maximum RE current compared to initial plasma current for simulations with different W concentrations and $\delta B/B_0$ during TQ in the ITER-like disruption scenario. TQ time obtained from the 80–20 definition. $\delta B/B_0$ during CQ was always set to 4×10^{-4}. (*a*) Results from simulations with the fluid model. (*b*) Results from simulations with the isotropic model.

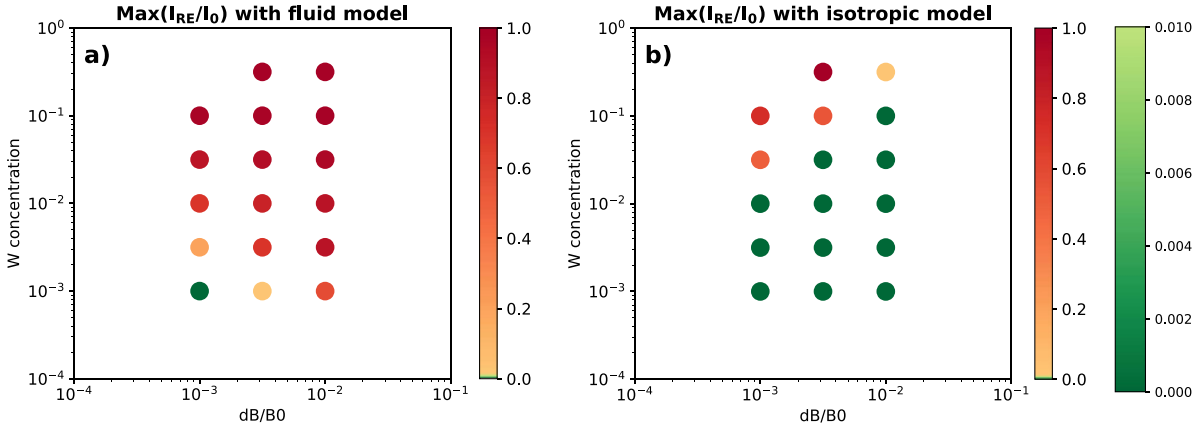

Figure 11. Maximum RE current compared to initial plasma current for simulations with different W concentrations and $\delta B/B_0$ during TQ in the ITER-like disruption scenario. TQ time obtained from the dT/dt definition. $\delta B/B_0$ during CQ was always set to 4×10^{-4}. (*a*) Results from simulations with the fluid model. (*b*) Results from simulations with the isotropic model.

to prevent PFC damage, is 150 kA [23], which corresponds to 1% of the initial plasma current. In the plots, RE current which was within this limit is marked in a green colour scale and cases where the limit was breached are presented in a red colour scale.

The general result is that RE generation increases with higher W concentration. This seems to be a consequence of the faster plasma cooling, which enhances the hot-tail generation. In theory, an increased electron density in the plasma can increase the chance of secondary generation through avalanching. However, in our simulations, high RE currents are in some cases reached even when the W concentration is not high enough to significantly increase the electron density.

There is a clear discrepancy between fluid and isotropic models in terms of RE generation. The fluid model in a qualitative sense was always overpredicting the RE generation—so for safety analysis it should not give false negative answers about the risk of RE current. It is however not reliable in quantitative terms, as the exact value of RE current is, in many cases, strongly overpredicted when compared to an isotropic model. We expect the isotropic model to be more accurate than the fluid model due to more accurate calculation of the electrons dynamics in the 'hot' population, which is crucial for the detailed simulation of the RE generation. However both are just numerical models which should be verified by comparison with dedicated experiments before making any conclusive statements.

In the case of the fluid model, the magnetic perturbation usually increases the RE generation rate (the exceptions from this rule can be mostly observed when RE current is very small compared to the total plasma current). This is contrary to the results of the isotropic model. The difference is most likely due to the overestimated plasma cooling rate and resulting increased hot-tail generation in the fluid model. In general, the isotropic model should be able to describe the same physical phenomena as the fluid model, so there is no reason to assume that this is some physical phenomena not captured by one of the models. The most likely explanation is a different balance of two factors which depend on magnetic perturbation: hot-tail generation, which is increased by faster cooling,

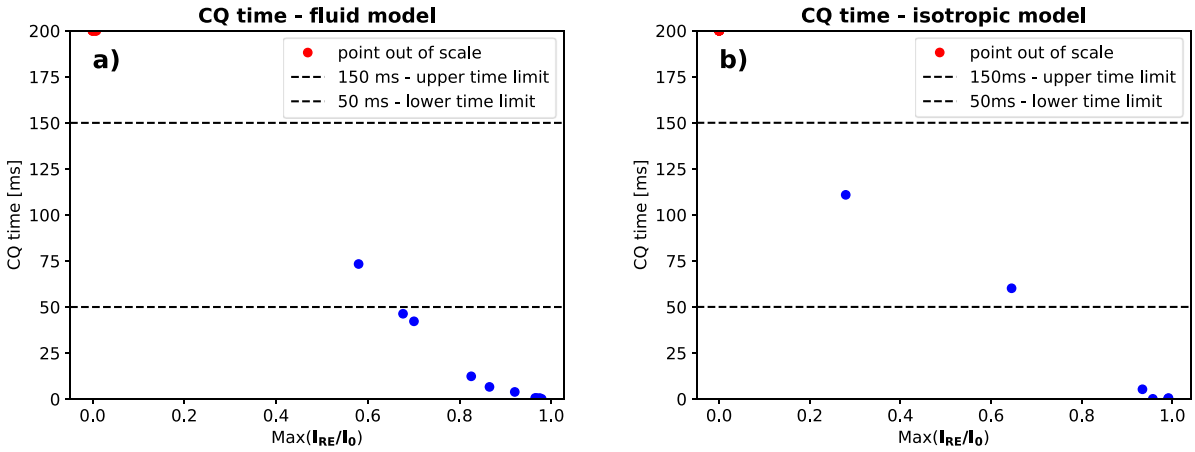

Figure 12. CQ time as a function of maximum ratio of RE current in the ITER-like disruption scenario. TQ time obtained from the 20–80 definition. $\delta B/B_0$ during CQ was always set to 4×10^{-4}. (*a*) Results from simulations with the fluid model. (*b*) Results from simulations with the isotropic model. Blue points represents CQ time for given value of max ($\boldsymbol{I_{RE}}/\boldsymbol{I}_0$), red points marks simulations where CQ time was out of scale for given max ($\boldsymbol{I_{RE}}/\boldsymbol{I}_0$). Horizontal lines represent minimum and maximum of allowed CQ time for ITER [3].

and deconfinement of RE. RE transport is the same in both models, but the isotropic model calculates the hot-tail generation with a more detailed approach, which should lead to more accurate results.

Figure 11 shows results of simulations with a longer TQ time, obtained from the dT/dt definition. It shows that the presented models also provide different trends related to the TQ time, as fluid simulations show in this case an extremely high RE generation risk, while isotropic simulations result in even lower RE levels than in the 80–20 TQ.

The observation of the CQ times in the simulated ITER-like disruption scenario shows that in the cases without RE generation, the CQ exceeds 0.15 s. The situation changes dramatically when a large fraction of RE current is generated, as shown on figure 12. When ohmic heating decreases, the current is transformed on the timescale of milliseconds mostly into RE current and partially into currents in the tokamak structure. Strong currents flowing in the machine structure can lead to mechanical failure due to electromagnetic forces. In the presented work, wall currents were included to account for important effects in the plasma dynamics. Analysis of the machine safety from the related forces would require separate investigations.

The CQ time is defined as:

$$\tau_{\mathrm{CQ}} = \frac{t(I_{\mathrm{ohm}} = 0.2I_0) - t(I_{\mathrm{ohm}} = 0.8I_0)}{0.6} \qquad (2)$$

where I_{ohm} is the ohmic component of the plasma current and I_0 is the plasma current at the beginning of the simulation (pre-disruption current).

5. Outlook and summary

Our results show that RE generation caused by tungsten impurities may become a significant problem only at tungsten concentrations above 10^{-3}, which is unlikely to occur during normal tokamak operation. As long as an abnormal event does not introduce large amounts of tungsten dust or flakes into the plasma, W-induced RE should not pose a direct threat to the tokamak operation.

The RE current depends on the TQ dynamics, which is different than in the case of intentional disruption mitigation by massive material injection. The exact TQ time and magnetic perturbation are difficult to predict due to uncertainties in the initial conditions and high computational cost, though a worst case scenario can be defined for safety analysis. For such application, the fluid model can be sufficient, but a number of limitations connected to this approach should be kept in mind. The isotropic model, which is the simplest kinetic model available in DREAM, can be used at a computation cost roughly 3–4 times larger than the fluid model [18], providing additional insight into electron dynamics. To create a truly self-consistent simulation, it would be necessary to include the magnetic surface evolution, especially magnetic surface stochastization and healing. This however was outside the scope of the presented work, as it would require a different modelling approach and significantly more computational resources.

Results from the fluid model are more conservative than the results from the isotropic model. This comes from higher RE generation rates, which are probably overestimated. The isotropic model, on the other hand, is not well suited for the cases with low amounts of impurities, where electrons coming from introduced impurities do not dominate over the electrons already present in plasma. However, the aspects neglected in the isotropic model should only overestimate the results, so there is a solid basis to assume that the results are still conservative. Bearing in mind the differences between fluid and isotropic models, it is possible to use only the fluid model for testing RE mitigation strategies or in the initial scans of the parameter space, while the isotropic model should be used to assess the accuracy of the solution. A more definitive statement about accuracy would require dedicated experiments for validation of the models.

The TQ time cannot be accurately predicted without MHD simulations. When using approximated TQ time definitions, a conservative approach should be used which, on the one hand, ensures a significant temperature drop (so the radiation is stronger, or at least balances the ohmic heating) and on the other hand the initial RE seed should not be deconfined by the magnetic perturbation. Magnetic perturbation strength can have a significant effect on the RE generation in medium size tokamaks, but for ITER the exact value is less important for RE generating scenarios, as radiation losses are dominant in these cases.

In the analysed cases, the hot-tail RE generation mechanism was dominant as a primary source of RE. The Dreicer generation mechanism cannot be reliably estimated using the NN proposed by Hesslow *et al* [34]. When verification with kinetic simulation is not available, it is recommended to use the Connor–Hastie model, as it sets an upper bound of the Dreicer generation providing conservative, but not necessarily accurate, estimations of the RE generation. The NN should be retrained on the cases which include tungsten impurities before it can be used in simulation tools.

Simulations performed for the ITER-like scenario are moderately concerning. The first analysis with the fluid model suggests that RE generation is possible if tungsten intrusion causes a rise of impurity concentration to a value of 10^{-3} or higher. This would be concerning if left alone, as such levels can be reached in tokamaks [17, 36, 37]. However, our analysis made with the isotropic model shows that concentrations of tungsten on a level of 1% or lower should not lead to a significant RE current generation on its own. As mentioned before, the isotropic model should be more trustworthy. A 3 mm droplet of tungsten evaporated into the core plasma would be required to reach a tungsten concentration of 1%, which is unlikely. It should be kept in mind that in the case of additional RE sources, tungsten will probably increase the generation rate. When the conditions for avalanche become favourable, the transition to runaway current is fast and can lead to a catastrophic discharge with a few MA runaway current. In such cases, the CQ time would probably exceed the safety limits predicted for ITER, causing a risk of mechanical damage of the vacuum vessel due to electromagnetic forces from currents induced in the structure.

An open question is the impact of tungsten impurities on the planned mitigation system for ITER. Mitigation with shattered pellet injection requires balance between RE suppression and ohmic current preservation (to avoid a too fast CQ) [38]. This creates an operational space for the mitigation system in terms of the neon and deuterium quantities that should be injected into the plasma. With the presence of tungsten impurities, this operational space can become narrower or shifted in relation to pure D-T plasma without impurities. This requires further investigations which are outside the scope of this work. Furthermore, estimation of tungsten ablation and evaporation in the burning plasma conditions can be different than in present-day tokamaks, as the high-energy particles present in such plasmas will be able to penetrate the ablated sheet of material that normally shields the impurities and reduce the evaporation rate. This can lead to an unprecedented rate of tungsten concentration, which would be detrimental for the tokamak integrity.

We believe that the presented results of disruption simulations with high tungsten content are just a first step and emphasise the need for further studies on this topic. The current simulations require validation efforts, as tungsten-induced disruptions were not initiated on purpose in current tokamaks, so existing data is scarce and fragmented. Dedicated research on this topic should help to evaluate the risk posed by tungsten impurities and its effects on the mitigation systems of reactor-scale tokamaks.

Acknowledgments

The authors would like to thank T. Fülöp and I. Pusztai for the fruitful discussions and support. Also they would like to thank Martin O'Mullane and Thomas Pütterich for their advice on the selection of ADAS datasets and their comments about tungsten specific issues.

J. Walkowiak acknowledges financial support provided by the Polish National Agency for Academic Exchange NAWA under the Programme STER—Internationalisation of doctoral schools, Project no. PPI/STE/2020/1/00020". We gratefully acknowledge Poland's high-performance computing infrastructure PLGrid (HPC Centers: ACK Cyfronet AGH) for providing computer facilities and support within computational Grant No. PLG/2022/015994. This work has been carried out within the framework of the EUROfusion Consortium, funded by the European Union via the Euratom Research and Training Programme (Grant Agreement No. 101052200—EUROfusion). Views and opinions expressed are however those of the author(s) only and do not necessarily reflect those of the European Union or the European Commission. Neither the European Union nor the European Commission can be held responsible for them. This project is co-financed by the Polish Ministry of Education and Science in the framework of the International Co-financed Projects (PMW) programme Contract No. 5450/HEU—EURATOM/2023/2.

Appendix A. ADAS data selection

Most of the atomic data in DREAM is retrieved from the ADAS database [25] through the OPEN-ADAS system from the ADF11 class. The datasets used in the code are: data for ionisation (SCD), recombination (ACD), line power (PLT) and recombination/bremsstrahlung power (PRB). Charge-exchange cross-coupling coefficients (CCD) are not used in DREAM, but were implemented to maintain compatibility with the rest of the data, because the same datasets are used also by the related code STREAM [39]. For CCD there is only one dataset available for every element, so the selection is straightforward. For the remaining parameters, there are few datasets to choose from. These datasets are marked by numbers which are sometimes referred to as years, although in the case of tungsten this is just a jargon, as these numbers do not

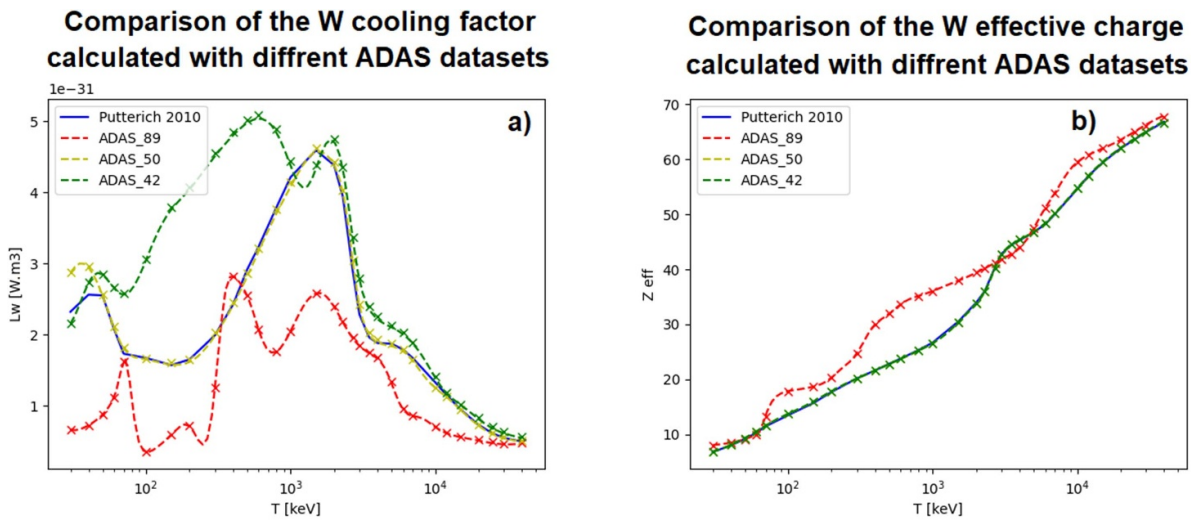

Figure 13. Comparison of (*a*) the *W* cooling factor and (*b*) the effective charge of *W* ions as a function of the electron temperature, obtained with different versions of the ADAS datasets. For ADAS_89 and ADAS_50, all datasets were from the year 89 and 50, respectively. In case of ADAS_42, the PLT file is from year 42 and SCD, ACD, PRB files are taken from the year 50.

correspond to the years of creation of the dataset in any way. The selection of the most suitable dataset is usually done by referring to the ADAS recommendation (https://open.adas.ac.uk/man/appxa-11.pdf), which unfortunately does not include tungsten. The selection of the most advanced datasets for tungsten was therefore done after consultation with the authors of the ADAS database. The datasets were obtained from a spectrum of raw atomic data of different quality. Selected databases were created with a larger number of atomic states included and more detailed approximations of wave functions representing atomic states, so they are the most accurate estimations currently available. For SCD, ACD and PRB files, the year 50 was chosen while for the PLT file, the year 42 was selected.

It was found during the validation of the code that for low temperatures, the cooling factor calculated with the PLT year 50 dataset was different from the corresponding data published in Putterich [40]. The difference is smaller than the uncertainty in the atomic data for this temperature range, so it is not considered to be problematic, but the exact source of the difference could not be concluded. For completeness, we present in figure 13 the comparison of the results from different datasets.

Appendix B. MEE

The MEE of *W* ions was calculated using the modified LPA as described in [27, 41]:

$$\mathrm{MEE} = \exp\left[\frac{4\pi}{N}\int {r_i}^2 \rho(r_i)\ln\left(\hbar\omega_0(r_i)\right)\mathrm{d}r_i + F\right] \tag{3}$$

where N is the number of electrons bound to the considered ion, r_i is the radial coordinate of the ion, $\rho(r_i)$ is the electron density distribution, which is assumed to be spherically symmetric around the nucleus, $\omega_0(r_i)$ is the local plasma frequency of the electron gas in the ion [42] and F is a correction factor derived by fitting the LPA to the results from Sauer *et al* [28, 29]:

$$F = \exp\left(\frac{Z-N}{Z}\right) - 0.9 \tag{4}$$

where Z is the atomic number of the ion.

The electron density distribution $\rho(r_i)$ was calculated with the so-called optimised Pratt–Tseng ($\mathrm{PT_{opt}}$) model as described in [41] The expression for $\rho(r_i)$ is:

$$\rho(r_i) = \frac{1}{4\pi\, r_i}\left[\sum_{s=1}^{5}\frac{N_s}{{a_s}^2}\exp\left(-\frac{r_i}{a_s}\right)\right] \tag{5}$$

where $N = \sum_{s=1}^{5} N_s$ is the number of electrons bound to the ion, N_s is the number of electrons included in each summation part and a_s are parameters corresponding to each group of electrons.

The grouping of electrons is given in table 2.

The a_s coefficients can be approximated with the following equations:

$$_s(Z,\,N) = 1\Big/\sqrt{{\lambda_s}^2\frac{(1-x^{n_s+1})}{1-x}} \tag{6}$$

$$\lambda_s(Z) = c_{1,s}Z^{c_{2,s}} \tag{6.1}$$

$$n_s(Z) = c_{3,s}Z^{c_{4,s}} \tag{6.2}$$

where $x = \frac{Z-N}{Z}$ and Z is the atomic number of the considered ion. The optimised $c_{n,s}$ parameters are presented in table 3.

Table 2. Grouping of electrons in the PT_{opt} model Adapted from [41]. CC BY 4.0.

Electron group	N_1	N_2	N_3	N_4	N_5
Max. number of bound electrons in each group	2	8	18	28	Rest
Total bound electrons when group fully occupied	2	10	28	54	Rest

Table 3. Optimised parameters for PT_{opt} model Adapted from [41]. CC BY 4.0.

		$i=1$	$i=2$	$i=3$	$i=4$	$i=5$
$\lambda_i(Z)$	$c_{1,s}$	1.1831	0.1738	0.0913	0.0182	0.7702
	$c_{2,s}$	0.8368	1.0987	0.9642	1.2535	0.2618
$n_{s,i}(Z)$	$c_{3,s}$	0.3841	0.6170	1.0000	1.0000	1.0000
	$c_{4,s}$	0.5883	0.0461	1.0000	1.0000	1.0000

ORCID iDs

J. Walkowiak https://orcid.org/0000-0002-9787-1691
M. Hoppe https://orcid.org/0000-0003-3994-8977
I. Ekmark https://orcid.org/0000-0001-8065-4650
A. Jardin https://orcid.org/0000-0003-4910-1470
J. Bielecki https://orcid.org/0000-0002-3460-8677
Y. Savoye-Peysson https://orcid.org/0000-0001-8594-9474
D. Mazon https://orcid.org/0000-0001-5560-2277
D. Dworak https://orcid.org/0000-0002-0768-1748
M. Scholz https://orcid.org/0000-0002-7330-1782

References

[1] Reux C. *et al* 2020 *28th IAEA Fusion Energy Conf. Link (virtual event, 10–15 May 2021)* (available at: www.iaea.org/events/fec-2020)
[2] Torre A., Ciazynski D., Girard S., Lacroix B., Nicollet S., Reux C. and Tena M. 2019 *IEEE Trans. Appl. Supercond.* **29** 4702805
[3] Lehnen M. *et al* 2015 *J. Nucl. Mater.* **463** 39–48
[4] de Vries P.C., Johnson M.F., Alper B., Buratti P., Hender T.C., Koslowski H.R. and Riccardo V. 2011 *Nucl. Fusion* **51** 053018
[5] Flanagan J.C. *et al* 2015 *Plasma Phys. Control. Fusion* **57** 014037
[6] Zhu J.X., Rea C., Granetz R.S., Marmar E.S., Sweeney R., Montes K. and Tinguely R.A. 2023 *Nucl. Fusion* **63** 046009
[7] Lipschultz B., Coenen J.W., Barnard H.S., Howard N.T., Reinke M.L., Whyte D.G. and Wright G.M. 2012 *Nucl. Fusion* **52** 123002
[8] Bucalossi J. *et al* 2022 *Nucl. Fusion* **62** 042007
[9] Pitts R.A. *et al* 2013 *J. Nucl. Mater.* **438** S48–S56
[10] Neu R. *et al* 2013 *J. Nucl. Mater.* **438** S34–S41
[11] Ruset C., Grigore E., Maier H., Neu R., Li X., Dong H., Mitteau R. and Courtois X. 2007 *Phys. Scr.* **2007** 171
[12] Kramida A., Ralchenko Y. and Reader J. and NIST ASD Team 2022 NIST atomic spectra database (ver. 5.10) (National Institute of Standards and Technology) (available at: https://physics.nist.gov/asd) (Accessed 12 April 2023)
[13] Siccinio M. 2020 *Fusion Eng. Des.* **156** 111603
[14] Pütterich T., Fable E., Dux R., O'Mullane M., Neu R. and Siccinio M. 2019 *Nucl. Fusion* **59** 056013
[15] de Vries P.C. *et al* 2012 *Plasma Phys. Control. Fusion* **54** 124032
[16] Gao B., Ding R., Xie H., Zeng L., Zhang L., Wang B., Li C., Zhu D., Yan R. and Chen J. 2020 *Fusion Eng. Des.* **156** 111616
[17] Reinke M.L., Scott S., Granetz R., Hughes J.W., Baek S.G., Shiraiwa S., Tinguely R.A. and Wukitch S. 2019 *Nucl. Fusion* **59** 066003
[18] Hoppe M., Embreus O. and Fülöp T. 2021 *Comput. Phys. Commun.* **268** 108098
[19] Sommariva C., Nardon E., Beyer P., Hoelzl M., Huijsmans G.T.A. and van Vugt D. 2018 *Nucl. Fusion* **58** 016043
[20] Sommariva C., Nardon E., Beyer P., Hoelzl M. and Huijsmans G.T.A. 2018 *Nucl. Fusion* **58** 106022
[21] Rechester A.B. and Rosenbluth M.N. 1978 *Phys. Rev. Lett.* **40** 38
[22] Rosenbluth M.N. and Putvinski S.V. 1997 *Nucl. Fusion* **37** 1355
[23] Pusztai I., Ekmark I., Bergström H., Halldestam P., Jansson P., Hoppe M., Vallhagen O. and Fülöp T. 2023 *J. Plasma Phys.* **89** 905890204
[24] Pusztai I. 2022 *J. Plasma Phys.* **88** 905880409
[25] Summers H.P. 2004 The ADAS user manual version 2.6 (available at: www.adas.ac.uk)
[26] Hesslow L., Embréus O., Wilkie G.J., Papp G. and Fülöp T. 2018 *Plasma Phys. Control. Fusion* **60** 074010
[27] Walkowiak J. *et al* 2022 *48th EPS Conf. on Plasma Physics (virtual event, 27 June–1 July 2022)* (available at: https://epsplasma2022.eu/)
[28] Sauer S.P., Sabin J.R. and Oddershede J. 2018 *J. Chem. Phys.* **148** 174307
[29] Sauer S.P. *et al* 2020 *Mol. Phys.* **119** e1823508
[30] Hu D., Nardon E., Hoelzl M., Wieschollek F., Lehnen M., Huijsmans G.T.A., van Vugt D.C., Kim S.-H., Contributors J. and team J. 2021 *Nucl. Fusion* **61** 026015
[31] Ekmark I. 2023 Chalmers university of technology *MSc Thesis* (available at: https://ft.nephy.chalmers.se/files/publications/642aaa80e21df.pdf)
[32] Izzo V.A., Pusztai I., Särkimäki K., Sundström A., Garnier D.T., Weisberg D., Tinguely R.A., Paz-Soldan C., Granetz R.S. and Sweeney R. 2022 *Nucl. Fusion* **62** 096029
[33] Connor J.W. and Hastie R.J. 1975 *Nucl. Fusion* **15** 415
[34] Hesslow L., Unnerfelt L., Vallhagen O., Embreus O., Hoppe M., Papp G. and Fülöp T. 2019 *J. Plasma Phys.* **85** 475850601
[35] Svenningsson I. 2020 Chalmers university of technology *MSc Thesis* (available at: https://odr.chalmers.se/bitstreams/606f8fe6-bb70-4472-a229-a64605368803/download)
[36] Chen Y., Zhang D., Zhang L., Hu L. and team E. 2020 *Nucl. Mater. Energy* **25** 100833

[37] Smirnov R.D., Krasheninnikov S.I., Pigarov A.Y. and Rognlien T.D. 2015 *Phys. Plasmas* **22** 012506
[38] McDevitt C.J., Tang X.-Z., Fontes C.J., Sharma P. and Chung H.-K. 2023 *Nucl. Fusion* **63** 024001
[39] Hoppe M., Ekmark I., Berger E. and Fülöp T. 2022 *J. Plasma Phys.* **88** 905880317
[40] Pütterich T. *et al* 2010 *Nucl. Fusion.* **50** 025012
[41] Walkowiak J., Jardin A., Bielecki J., Peysson Y., Mazon D., Dworak D., Król K. and Scholz M. 2022 *Phys. Plasmas* **29** 022501
[42] Lindhard J. and Scharff M. 1953 *Mat. Fys. Medd.—K. Dan. Vidensk. Selsk.* **27** 15

OPEN ACCESS
IOP Publishing | International Atomic Energy Agency
Nuclear Fusion
Nucl. Fusion **63** (2023) 126041 (23pp)
https://doi.org/10.1088/1741-4326/acffd9

A unified description of atomic physics for electron Fokker–Planck calculations

Y. Savoye-Peysson[1,*], D. Mazon[1], J. Bielecki[2], D. Dworak[2], K. Król[2], A. Jardin[2], M. Scholz[2], J. Walkowiak[2] and J. Decker[3]

[1] CEA, IRFM, F-13108 Saint-Paul-lez-Durance, France
[2] Institute of Nuclear Physics, Polish Academy of Sciences, PL-31342 Krakow, Poland
[3] Ecole Polytechnique Fédérale de Lausanne (EPFL), Swiss Plasma Center (SCP), CH-1015 Lausanne, Switzerland

E-mail: yves.savoye-peysson@cea.fr

Received 5 May 2023, revised 7 August 2023
Accepted for publication 4 October 2023
Published 25 October 2023

Abstract

Most realistic kinetic calculations for tokamak plasmas are now required to incorporate the effect of partially ionized high-Z elements arising either from uncontrolled influxes of metallic impurities, such as tungsten in high input power regimes or from mitigation of runaway electrons generated after possible major disruptions by massive gas injection. The usual electron–ion Fokker–Planck collision operator must therefore be modified, because all plasma atoms are not entirely ionized, as is the case for light elements. This represents a challenge, in order to perform fast but also accurate calculations, regardless of the type of element present in the plasma, but also their local levels of ionization while covering a wide range of electron energies in a consistent way, from a few keV to tens of MeV in plasmas whose electron temperature may itself vary from 10 eV to several keV. In this context, a unified description of the atomic models is proposed, based on a multi-Yukawa representation of the electrostatic potential calibrated against results obtained by advanced quantum calculations. Besides the possibility to improve the description of inner and outer atomic shells in the determination of the atomic form factor, this model allows one to derive analytical formulations for both elastic and inelastic scattering, which can then be easily incorporated in kinetic calculations. The impact of the number of exponentials in the description of the atomic potential is discussed, and a comparison with simple and advanced atomic models is also performed.

Keywords: atomic physics, Fokker–Planck equation, elastic and inelastic scattering

(Some figures may appear in colour only in the online journal)

1. Introduction

The use of tungsten (W) as the plasma-facing material in present-day experimental fusion devices, such as WEST [1], EAST [2] and the International Thermonuclear Experimental Reactor (ITER) that is currently being constructed [3], has raised the question of the impact of partially ionized high-Z impurities on the performance of hot plasmas. For example, the ability to efficiently drive the toroidal plasma current by radio-frequency (RF) electromagnetic waves may be reduced by an enhanced electron pitch-angle scattering and electron-ion slowing-down due to tungsten, thus limiting the capability of control for improved plasma performance [4]. In standard tokamak fusion plasmas, the usual electron temperature T_e is supposed to be in the range between 1 and 10 keV, so

* Author to whom any correspondence should be addressed.

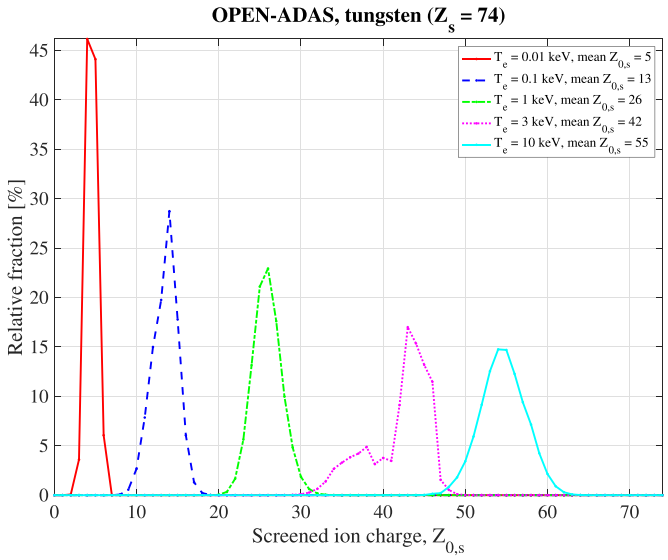

Figure 1. Relative fraction of different screened ion charges for tungsten at different plasma electron temperatures using the *OPEN-ADAS* database [5].

that most of the low-Z impurities are fully ionized over a large volume, except possibly in the outermost regions near the separatrix. Conversely, high-Z elements remain partially ionized everywhere, even in the core of the plasma, and the nucleus charge Z_s of the species s may still be partially screened by many bound electrons. For the tungsten element whose atomic number is $Z_s = 74$, the mean screened ion charge is $\overline{Z}_{0,s} \simeq 42$ in a plasma whose electron temperature is $T_\mathrm{e} = 3\,\mathrm{keV}$ according to the OPEN-ADAS database, as shown in figure 1, so that $\overline{N}_s \simeq 32$ electrons are still bound [5]. Even at $T_\mathrm{e} = 10\,\mathrm{keV}$, as expected in ITER plasmas, $\overline{N}_s$ is still large for the tungsten element, in the order of twenty[4].

The role played by the screening of partially ionized high-Z elements has first been considered in order to accurately describe the dynamics of runaway electrons in very cold post-disruptive plasmas, and also to investigate the possibility to mitigate them by massive gas injection of high-Z elements up to argon. It is shown that the dynamics in momentum space of the non-thermal electrons can be notably modified compared to the traditional picture because of the partial screening, with a significant impact on the critical electric field (Hastie–Connor) beyond which electrons may run away [6–8]. This original work, implemented in the *CODE* code dedicated to runaway electron physics in almost zero-temperature post-disruptive plasmas [9], was later extended to standard tokamak regimes in the *LUKE* solver of the 3D linearized bounce-averaged relativistic electron Fokker–Planck equation [10]. This allows us to describe the consequences of uncontrolled impurity influxes of high-Z metallic elements, such as tungsten on RF current drive, for example [4]. More recently, kinetic calculations have been carried out, showing that RF current driven by the lower hybrid wave is moderately lowered despite a strong thermal collapse ascribed to an uncontrolled accumulation of tungsten in the plasma core of WEST tokamak [11]. In both studies, a standard Yukawa potential (single exponential) was used in the *LUKE* code.

Even if the atomic processes that must be described in the *CODE* and *LUKE* kinetics codes are rather similar, some differences specific to hot plasmas must be investigated. Indeed, while the atomic physics of argon and elements with lower Z_s values has been thoroughly studied by quantum non-relativistic codes describing the ground-state and mean excitation energies for different ionization states [12–15], the knowledge of atomic properties for metallic elements with higher Z_s values, and in particular for tungsten, is much more sparse. This is a consequence of the relativistic effects and the resulting complex orbital coupling, which must be fully incorporated in quantum calculations, making them considerably more difficult. Indeed, by combining the virial theorem with the quantum uncertainty principle, relativistic effects become significant when the relativistic Lorentz factor γ_s significantly exceeds unity, where $\gamma_s^2 = (\alpha Z_s)^2 + 1$, and α is the usual fine structure constant. While for argon, relativistic corrections are negligible since $\gamma_s^{\mathrm{Ar}} \simeq 1.0086$, they become more significant for tungsten, as $\gamma_s^{W} \simeq 1.136$. If the ground state may be obtained for the field-free tungsten element using the density functional theory (DFT) or the multi-configuration Dirac–Hartree–Fock (MCDHF) approaches[5] implemented in the *GAUSSIAN* and *GRASP* codes, respectively [12, 13],[6] the mean excitation energies for all ionization states that play an important role in the inelastic electron–ion scattering processes are still not available. In much the same way, while screening effects on bremsstrahlung by runaway electrons may be reasonably described using a standard angular-averaged formula in the first Born approximation [18], such an approximation cannot be considered for less energetic electrons resonantly accelerated by RF waves, for example, since the angular cone of emission is much larger [19]. Therefore, in order to continuously cover the range of kinetic energies from a few keV to several tens of MeV photons, a fully numerical integration over the electron emission angle of the cross-section differential in photon energy and in photon and electron emission angles must be carried out, which represents a considerable numerical task.

In this context, the accurate incorporation of atomic physics in kinetic codes, while keeping computational effort at a

[4] The mean screened ion charge is defined as $\overline{Z}_{0,s} = \sum_i f_{0,s,i} Z_{0,s,i}$ where $f_{0,s,i}$ is the local fraction of all ionization states $Z_{0,s,i}$. By definition, $\sum_i f_{0,s,i} = 1$, $Z_{0,s,i} \in \{0, Z_s\}$. The number of bound electrons is $N_{s,i} = Z_s - Z_{0,s,i}$ and the mean value is $\overline{N}_s = \sum_i f_{0,s,i} N_{s,i}$.

[5] In tokamak plasmas, the mean distance $\overline{d} = n^{-1/3}$ between particles, where n is the plasma density, is always much greater than the atomic radius in the approximate range between Bohr radius a_0 and $4 \times a_0$ for neutral atoms and less for corresponding ions. Therefore, for all elements and regardless of their states, they can always be considered as in vacuum or field-free, which considerably simplifies ground-state calculations. This is not the case in inertial fusion plasmas [16].

[6] The FAC code based on the modified multiconfigurational Dirac–Hartree–Fock–Slater (MC-DHFS) procedure may also be an interesting alternative tool [17].

reasonable level, is a serious challenge, especially for describing inelastic scattering. A similar effort should concern the screening effects on bremsstrahlung, a major moment of the non-thermal distribution function for diagnosing fast electron dynamics. The use of analytical formulas based on simple parameterized models is consequently a more suitable approach, with absolute calibration against results obtained by advanced numerical quantum codes. However, simple atomic models usually have limited applicability, which prevents the systematic and consistent use of all quantities that must be modified to take into account the atomic physics. While the well-known Thomas–Fermi model [20] and its approximate formulations [21, 22] are well suited for neutral or weakly ionized atoms, they usually give less accurate results when the number N_s of bound electrons is small compared to Z_s. The charge density of the inner shell is usually better described by a Yukawa electrostatic potential [23], which itself is not relevant for neutral or weakly ionized atoms. This is because the charge density fall-off is generally too sharp at large distances from the nucleus compared to DFT or MCDHF calculations. However, the Yukawa atomic model is widely used for bremsstrahlung studies even if the target atom is neutral or weakly ionized, since this physics process usually involves deep electronic shells to calculate the radiation emission [24–28]. Consequently, a unified and accurate description of the atomic electrostatic potential that can be used either for kinetic calculations or for bremsstrahlung without a significant degradation of the numerical performance of the kinetic code, whatever the plasma conditions (cold or hot) and the type of element, is of great interest.

The purpose of this paper is therefore to propose a general and global approach for incorporating atomic physics in Fokker–Planck electron solvers, allowing existing codes to be easily and robustly updated for realistic simulations, whatever the consequences on fast electron dynamics, which will be the object of a separate study.

This objective is addressed by expressing the atomic electrostatic potential as a series of Yukawa potentials. There is a consequent trade-off between keeping codes fast and accurate over a wide range of electron kinetic energies, regardless of the ionization state of the elements, and with a reasonably correct description of the physics involving both outer and inner electron shells. This approach has already been successfully considered for modeling results of Hartree–Fock–Slater calculations for neutral elements only, from hydrogen to uranium, using up to three exponentials [29]. In addition, it was successfully applied for deriving an analytical formula for the bremsstrahlung with screening effects, valid from the classical to the fully relativistic limits [30, 31]. The modeling here considered, the so-called multi-Yukawa (MY), is basically an extension of Moliere's approach initially used to describe the Thomas–Fermi potential of neutral elements as a linear combination of three exponentials [32]. The great advantage of this method is the possibility to obtain easily analytical derivations for many physical quantities of interest in the first Born approximation due to the simple analytical expression of the Fourier transform of an exponential function in the calculation of the atomic form factor, assuming a spherical symmetry for the density of bound electrons in the ground state [29].

In section 2, the MY atomic model is introduced, and the calibration procedure is explained in detail for an arbitrary number of exponentials. Comparison with DFT and MCDHF calculations is presented. In Fokker–Planck calculations, the electron-ion collision operator is described by a friction vector and a diffusion tensor resulting from elastic and inelastic collisions. In the presence of partially ionized high-Z elements, inelastic electron-ion collisions must also be taken into account, since free electrons in the plasma may lose part of their kinetic energy by either atomic excitation or ionization. The latter process may have a critical impact on the early build-up of electron avalanches, which play a major role in the dynamics of the runaway electron population in post-disruptive plasmas [33]. The incorporation of atomic physics in the Fokker–Planck collision operator is first detailed in section 3, for both elastic and inelastic processes. The screening function describing the impact of partially ionized atoms on elastic Coulomb collisions is derived in section 4, using the MY atomic model. The inelastic electron–ion collisions are then considered in section 5, with the approximate approach based on Bethe's formula for electron energy losses per unit length [34, 35]. In this case, the atomic physics is described by the mean excitation energy of the ground state, which can be calculated by several methods. This quantity can be derived from a non-relativistic variational quantum approach, but also with the classical local plasma approximation (LPA), both using the MY atomic model [36, 37]. Conclusions are given in section 6.

Although the impact of the screening on bremsstrahlung can be described with the same atomic form factor as that used for the Mott relativistic cross-section, this problem will be addressed in a separate paper.

2. Atomic model

2.1. Radial distribution of charge in the ground state and form factor

Kinetic calculations with partially ionized high-Z atoms require an atomic model that accurately describes the spatial distribution of bound electrons $\rho_{Z_{0,s}}(\mathbf{r})$ in the ground state, regardless of the type of atom and its level of ionization, where $\mathbf{r}$ is the distance to the nucleus. Indeed, excited states are transient and their lifetimes are generally much shorter than the mean time between two collisions in standard tokamak plasmas[7]. By definition, $\int_V \rho_{Z_{0,s}} \mathrm{d}\mathbf{r} = N_s = Z_s - Z_{0,s}$ where V is the volume of reference characterizing the ion size, N_s is the number of bound electrons, $Z_{0,s}$ is the screened ion charge and Z_s is the atomic number. The screening effects are determined by evaluating the form factor $F_{Z_{0,s}}(\mathbf{q}) \equiv \int_V \exp(-i\mathbf{q}\cdot\mathbf{r}/\hbar)\,\rho_{Z_{0,s}} \mathrm{d}\mathbf{r}$, where $\mathbf{q}$ is

[7] This condition may be marginally fulfilled in very cold post-disruptive plasmas.

the usual recoil momentum in Coulomb collisions. Since the kinetic energy is conserved in the elastic scattering process and assuming that small-angle scattering predominates, $|\mathbf{q}| \simeq 2|\mathbf{p}|\sin(\theta/2)$, with $\mathbf{p}$ being the incoming electron momentum and θ the deflection angle. Here, $\mathbf{q} = \mathbf{p}_f - \mathbf{p}_i$, where $\mathbf{p}_{i[f]} = \hbar\mathbf{k}_{i[f]}$, while $\mathbf{k}_{i[f]}$ are the wave vectors associated with the spinless wavefunctions $|i[f]\rangle = \exp\left(i\mathbf{k}_{i[f]}\cdot\mathbf{r}\right)/\sqrt{V}$ of the incoming $|i\rangle$ and outgoing electron $|f\rangle$, respectively, both being considered as plane waves (first Born approximation)[8]. Based on Fermi's golden rule, the relativistic Mott cross-section that describes Coulomb collisions in kinetic calculations must be modified according to the simple rule $Z_s \to Z_s - F_{Z_{0,s}}(\mathbf{q})$ in order to account for the partial atomic screening. For low-energy electrons, since $\lim_{\|\mathbf{q}\|\to 0} F_{Z_{0,s}}(\mathbf{q}) = N_s$, the ion is fully screened, i.e. $Z_s \to Z_{0,s} = Z_s - N_s$, while conversely, for very energetic electrons, it is fully stripped, since $\lim_{\|\mathbf{q}\|\to\infty} F_{Z_{0,s}}(\mathbf{q}) = 0$.[9] Within this framework, the form factor $F_{Z_{0,s}}(\mathbf{q})$ is simply the Fourier transform of the spatial distribution of the bound electrons, whose determination is the starting point for investigating the effect of atomic screening in Fokker–Planck calculations.

2.2. Description of the MY electrostatic potential description

For the approximate formulation of the Thomas–Fermi atomic model, as derived by Kirillov *et al* [22], but also for a Yukawa electrostatic potential (single exponential), the form factor may be expressed analytically in the same way according to the formula $F_{Z_{0,s}}(\bar{q}) = N_s/\left(1 + \left(\bar{q}\,\bar{a}_{Z_{0,s}}/2\right)^m\right)$, where $\bar{a}_{Z_{0,s}} \equiv 2a_{Z_{0,s}}/\alpha$ following the notation used in [7], and $\bar{q} = q/(m_e c)$ with $q = \|\mathbf{q}\|$. Here, $a_{Z_{0,s}}$ may be considered as an effective radius of the ion of charge $Z_{0,s}$ which depends on the chosen atomic model, α is the fine structure constant, c is the speed of light and m_e is the electron rest mass. While $m = 3/2$ with $a_{Z_{0,s}} = 3N_s^{2/3}/(4Z_s)$ for the approximate Thomas–Fermi model [22], $m = 2$ and $a_{Z_{0,s}} = \lambda_{Z_{0,s}}^{-1}$ for the Yukawa electrostatic potential, where $\lambda_{Z_{0,s}}^{-1}$ is a characteristic screening length, its value being usually determined by a best fit of results obtained with advanced atomic calculations using DHFS (Dirac–Hartree–Fock–Slater) codes [24–28].[10]

The cloud of bound electrons is assumed to be spherically symmetric around the nucleus, an approximation which turns out to be reasonably well satisfied for most ground states here considered. Indeed, the level of spherical symmetry can be evaluated from the matrix elements of the quadrupole moment of the rank-two tensor, directly obtained from DFT calculations [39], which essentially measures the deviation of the charge distribution $\rho_{Z_{0,s}}(\mathbf{r})$ from spherical symmetry. It is evaluated by a global parameter, $\Delta\Theta = |(\max(XX,YY,ZZ) - \min(XX,YY,ZZ))/\max(XX,YY,ZZ)|$, where the diagonal elements of the tensor are XX, YY and ZZ. According to this simple definition, $\Delta\Theta = 0$ corresponds to a perfect spherical symmetry for which all diagonal elements are identical. It turns out that this parameter progressively increases with the ionization level, as shown in figure 2. It is always much lower than 0.15 for $Z_{0,s} \leqslant 40$, and very small for all noble gas-like electronic configurations, regardless of the $Z_{0,s}$ value. Above $Z_{0,s} = 40$, some electronic configurations exhibit larger departure from spherical symmetry, but they concern primarily a few values for $Z_{0,s} \geqslant 56$, which will hardly ever be found in tokamak plasmas.

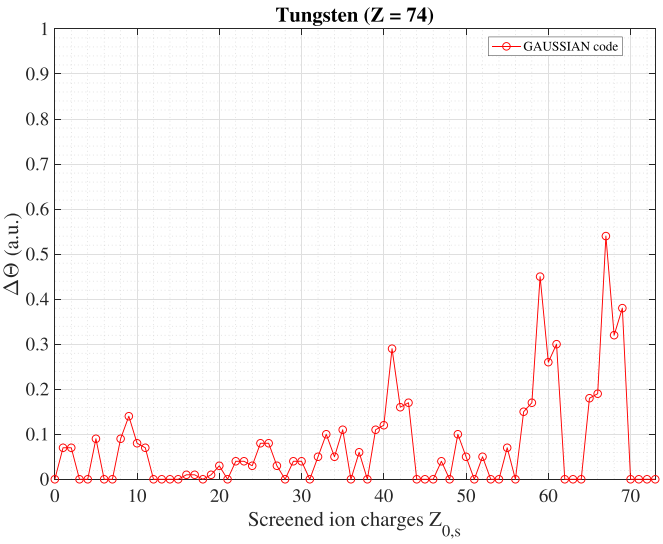

Figure 2. Deviation of the bound electron density of from spherical symmetry as estimated by the parameter $\Delta\Theta$ for all the screened charges of tungsten, from DFT calculations using the GAUSSIAN code [12]. When $\Delta\Theta = 0$, the cloud of bound electrons is spherically symmetric around the nucleus. $\Delta\Theta$ is very small for all nobel gas-like electronic configurations.

For both approximate atomic models, calculations of the screening effects on elastic scattering in kinetic calculations can be fully performed analytically [7]. However, the derivation of the bremsstrahlung cross-section differential in photon energy and angle with partial screening effects, which requires an angular integration over the deflection angle of the scattered electron [18], cannot be carried out fully analytically with $m = 3/2$. An explicit analytical formulation can only be obtained with $m = 2$, as demonstrated for the case of a neutral atom [30, 40]. Therefore, with the constraint of performing fast and accurate kinetics, but also bremsstrahlung calculations, based on analytical formulas within a unified atomic model, the use of the Yukawa electrostatic potential is unambiguously more appropriate. In order to keep its technical advantages without the intrinsic limitations of neutral or weakly ionized atoms, the simplest approach is to consider, instead, a generalized Yukawa potential, here named MY, which can be expressed as a series of exponentials:

[8] The volume V is chosen so that $\langle i \mid i\rangle = \langle f \mid f\rangle = 1$, a condition necessary to have a probabilistic interpretation of the wave functions.

[9] The procedure is general and may be applied to all cross-sections derived within the first Born approximation as for bremsstrahlung.

[10] For a neutral atom of atomic number Z_s and if the Thomas–Fermi model is used, $\lambda_{0,s} \equiv \lambda_{Z_{0,s}=0} = b_s^{-1} = 4\left[9\pi^2/2\right]^{-1/3} Z_s^{1/3} a_0^{-1} \simeq 1.13 Z_s^{1/3} a_0^{-1}$, a value frequently found in the literature [38]. Here, b_s is the atomic radius in the Thomas–Fermi model.

$$4\pi\epsilon_0 r U_{Z_{0,s}}(r) = -Z_{0,s} - \sum_i A_{Z_{0,s,i}} \exp\left(-\lambda_{Z_{0,s,i}} r\right), \quad (1)$$

each of which accurately describes the charge distribution around the nucleus, either close to or far from it. From the Poisson's equation $\triangle U_{Z_{0,s}} = \nabla^2 U_{Z_{0,s}} = -\rho_{Z_{0,s}}/\epsilon_0$, the radial normalized distribution of bound electrons is,

$$\overline{\rho}_{Z_{0,s}}(\overline{r}) = \frac{Z_s - Z_{0,s}}{4\pi\overline{r}} \sum_i \overline{\lambda}^2_{Z_{0,s,i}} \overline{A}_{Z_{0,s,i}} \exp\left(-\overline{\lambda}_{Z_{0,s,i}}\overline{r}\right), \quad (2)$$

where the density $\overline{\rho}_{Z_{0,s}}(\overline{r}) = \rho_{Z_{0,s}}(\overline{r})\, a_0^3$ is in atomic units, $\overline{\lambda}_{Z_{0,s,i}} \equiv \lambda_{Z_{0,s,i}} a_0$ and $\overline{A}_{Z_{0,s,i}} = A_{Z_{0,s,i}}/(Z_s - Z_{0,s})$, $\overline{\lambda}_{Z_{0,s,i}}$ being the inverse of the normalized characteristic length and $\overline{A}_{Z_{0,s,i}}$ the weight of the i^{th} Yukawa exponential, respectively. Here, $\overline{r} \equiv r/a_0$, where a_0 is the classical Bohr radius. The corresponding form factor is therefore,

$$F_{Z_{0,s}}(\overline{q}) = (Z_s - Z_{0,s}) \sum_i \frac{\overline{A}_{Z_{0,s,i}}}{1 + \left(\overline{q}\,\overline{a}_{Z_{0,s,i}}/2\right)^2}, \quad (3)$$

where $\overline{a}_{Z_{0,s,i}} \equiv 2\overline{\lambda}^{-1}_{Z_{0,s,i}}/\alpha$. By definition $\sum_i \overline{A}_{Z_{0,s,i}} = 1$, which guarantees that $F_{Z_{0,s}}(0) = Z_s - Z_{0,s} = N_s$.

This approach has long been considered appropriate to describe the Thomas–Fermi atomic potential by Moliere using three exponentials [32]. The correspondence between coefficients (B_i, β_i) found in the literature and $\left(\overline{A}_{Z_{0,s,i}}, \overline{\lambda}_{Z_{0,s,i}}\right)$ is given in appendix A. This method has also been used to fit the density of bound electrons calculated by a DHFS code for neutral atoms only, whose Z_s value ranges from 1 (hydrogen) to 92 (uranium) [29]. For most elements above argon, approximately three exponentials are necessary to accurately reproduce the radial distribution of charges when ionization is weak. Naturally, the analytical density given by equation (2) can only partially reproduce the oscillations of the DHFS linear density $4\pi\overline{r}^2\overline{\rho}_{Z_{0,s}}(\overline{r})$ associated with different inner shell contributions. However, the approximate form factor $F_{Z_{0,s}}(\overline{q})$ given by equation (3) remains very close to the numerical value determined from DHFS calculations, as core oscillations of the linear density have a small spatial weight, which validates the overall procedure.

2.3. Absolute model calibration

In the present study, the method used in [29] is generalized to all ionization states of any type of element. In this case, the effective number of exponentials used in (2) and (3) is determined by the possibility of finding a full set of positive $\overline{\lambda}_{Z_{0,s,i}}$ values. For some elements with an atomic number larger than tungsten, such as gold ($Z_s = 79$), up to four exponentials can be found using the calibration procedure, but for lower Z_s values, the number of exponentials usually never exceeds three, as found for tungsten. The determination of $\overline{A}_{Z_{0,s,i}}$ and $\overline{\lambda}_{Z_{0,s,i}}$ cannot be performed using a conventional least-squares fit method because of the non-linearity of the problem and the existence of many local minima in the function to be minimized [29].

The method is consequently based on a technique of moments, which guarantees the uniqueness of the solution under strict conditions, if it exists. However, the solution may not correspond to the best adjustment of the numerical atomic density. Nevertheless, as shown by the rather good agreement with quantum calculations, it is likely very close to it, by construction. The approach considered here ensures that the elastic Born cross-sections practically coincide with those derived from DFT or MCDHF calculations because the error on the form factor is rather small, as this term is an integral of the bound electron density.

The coefficients $\left(\overline{A}_{Z_{0,s,i}}, \overline{\lambda}_{Z_{0,s,i}}\right)$ of the MY description are determined from the condition $\langle \overline{r}^l \rangle = \langle \overline{r}^l \rangle^{\text{num}}$, with $\langle \overline{r}^l \rangle^{\text{num}}$ being the moment of order l calculated numerically from the density of bound electrons $\rho^{\text{num}}_{Z_{0,s}}(\overline{r})$ obtained using advanced atomic quantum codes. Here, from the MY density given by equation (2),

$$\langle \overline{r}^l \rangle = \sum_i \overline{\lambda}^{-l}_{Z_{0,s,i}} \overline{A}_{Z_{0,s,i}} \Gamma(l+2) = (l+1)! \sum_i \overline{\lambda}^{-l}_{Z_{0,s,i}} \overline{A}_{Z_{0,s,i}} \quad (4)$$

where $\Gamma(z)$ is the Gamma function. Defining $\mathcal{R}_l \equiv \langle \overline{r}^l \rangle/(l+1)!$, a set of $2l$ equations depending upon the number of parameters $\left(\overline{A}_{Z_{0,s,i}}, \overline{\lambda}_{Z_{0,s,i}}\right)$ to be determined is obtained,

$$\mathcal{R}_l = \sum_i \overline{A}_{Z_{0,s,i}} \overline{\lambda}^{-l}_{Z_{0,s,i}} \quad (5)$$

and $\left(\overline{A}_{Z_{0,s,i}}, \overline{\lambda}_{Z_{0,s,i}}\right)$ are calculated by solving the equation $\mathcal{R}_l = \mathcal{R}^{\text{num}}_l$, where

$$\mathcal{R}^{\text{num}}_l = \frac{\langle \overline{r}^l \rangle^{\text{num}}}{(l+1)!} = \frac{1}{(l+1)!} \frac{4\pi}{(Z_s - Z_{0,s})} \int_0^\infty \overline{r}^{l+2} \overline{\rho}^N_{Z_{0,s}}(\overline{r})\, \mathrm{d}\overline{r} \quad (6)$$

the number l being an integer greater than -1.

For a fit with a single Yukawa potential, only two terms remain, and since $\sum_i \overline{A}_{Z_{0,s,i}} = 1$, it can be deduced that $\overline{A}_{Z_{0,s,1}} = 1$ and $\overline{\lambda}_{Z_{0,s,1}} = \mathcal{R}^N_{-1}$. For two exponentials, four equations with four unknowns must be considered. By grouping the equations,

$$\overline{\lambda}_{Z_{0,s,1}} + \overline{\lambda}_{Z_{0,s,2}} = \frac{\mathcal{R}^{\text{num}}_1 - \mathcal{R}^{\text{num}}_{-1}\mathcal{R}^{\text{num}}_2}{\left(\mathcal{R}^{\text{num}}_1\right)^2 - \mathcal{R}^{\text{num}}_2}, \quad (7)$$

$$\overline{\lambda}_{Z_{0,s,1}} \overline{\lambda}_{Z_{0,s,2}} = \frac{1 - \mathcal{R}^{\text{num}}_{-1}\mathcal{R}^{\text{num}}_1}{\left(\mathcal{R}^{\text{num}}_1\right)^2 - \mathcal{R}^{\text{num}}_2}, \quad (8)$$

and the values $\overline{\lambda}$ are therefore solutions of the quadratic equation,

$$\left(\left(\mathcal{R}^{\text{num}}_1\right)^2 - \mathcal{R}^{\text{num}}_2\right)\overline{\lambda}^2 - \left(\mathcal{R}^{\text{num}}_1 - \mathcal{R}^{\text{num}}_{-1}\mathcal{R}^{\text{num}}_2\right)\overline{\lambda} + \left(1 - \mathcal{R}^{\text{num}}_{-1}\mathcal{R}^{\text{num}}_1\right) = 0. \quad (9)$$

If both roots are real and positive, they correspond to $\left(\overline{\lambda}_{Z_{0,s,1}}, \overline{\lambda}_{Z_{0,s,2}}\right)$, respectively, so that

$$\overline{A}_{Z_{0,s,1}} = \frac{\mathcal{R}^{\text{num}}_{-1} - \overline{\lambda}_{Z_{0,s,2}}}{\overline{\lambda}_{Z_{0,s,1}} - \overline{\lambda}_{Z_{0,s,2}}}, \quad (10)$$

and $\overline{A}_{Z_{0,s,2}} = 1 - \overline{A}_{Z_{0,s,1}}$, otherwise, a single exponential must be considered for the modelization. In this case, there is some loss of accuracy in the modeling of the bound electron density, but it has a moderate impact on the form factor, regarding its definition given by equation (3). This is an intrinsic limitation of this method, despite its robustness, highlighting that not all bound electron density profiles may be described by a series of multiple exponentials. This arises principally for highly ionized atoms because the highest moments $\mathcal{R}_l^{\text{num}}$ are too small compared to the lowest ones. The weight of $\overline{\rho}^N_{Z_{0,s}}(\overline{r})$ at large $\overline{r}$ is therefore unable to identify a single exponential from this method. In this case, it is worth noting that standard non-linear techniques usually do not converge.

The procedure may be extended to three exponentials, and all $\overline{\lambda}$ values must be real and positive solutions of the polynomial equation $\overline{\lambda}^3 - X_1\overline{\lambda}^2 + X_2\overline{\lambda} - X_3 = 0$ to ensure that the atomic potential may be well described by a MY potential with the use of three exponentials. Otherwise, two exponentials must be considered in the modeling procedure, thus removing useless moments associated with three exponentials. Defining the vector $\mathbf{X}$ from coefficients $\{X_1, X_2, X_3\}$ of the polynomial equation in $\overline{\lambda}$,

$$\mathbf{X} = \begin{bmatrix} X_1 \\ X_2 \\ X_3 \end{bmatrix} = \begin{bmatrix} \overline{\lambda}_{Z_{0,s,1}} + \overline{\lambda}_{Z_{0,s,2}} + \overline{\lambda}_{Z_{0,s,3}} \\ \overline{\lambda}_{Z_{0,s,1}}\overline{\lambda}_{Z_{0,s,2}} + \overline{\lambda}_{Z_{0,s,2}}\overline{\lambda}_{Z_{0,s,3}} + \overline{\lambda}_{Z_{0,s,1}}\overline{\lambda}_{Z_{0,s,3}} \\ \overline{\lambda}_{Z_{0,s,1}}\overline{\lambda}_{Z_{0,s,2}}\overline{\lambda}_{Z_{0,s,3}} \end{bmatrix}, \tag{11}$$

the coefficients $\overline{A}_{Z_{0,s,i}}$ are determined from the matrix relation $\mathbf{A} = \mathbb{N}^{-1}\mathbb{M}\mathbf{X}$, where parameters $\overline{A}_{Z_{0,s,i}}$ are components of the vector,

$$\mathbf{A} = \begin{bmatrix} \overline{A}_{Z_{0,s,1}} \\ \overline{A}_{Z_{0,s,2}} \\ \overline{A}_{Z_{0,s,3}} \end{bmatrix}, \tag{12}$$

with

$$\mathbb{M} = \begin{bmatrix} 1 & -\mathcal{R}_1^{\text{num}} & \mathcal{R}_2^{\text{num}} \\ \mathcal{R}_1^{\text{num}} & -\mathcal{R}_2^{\text{num}} & \mathcal{R}_3^{\text{num}} \\ \mathcal{R}_2^{\text{num}} & -\mathcal{R}_3^{\text{num}} & \mathcal{R}_4^{\text{num}} \end{bmatrix}, \tag{13}$$

and

$$\mathbb{N} = \begin{bmatrix} \overline{\lambda}_{Z_{0,s,1}} & \overline{\lambda}_{Z_{0,s,2}} & \overline{\lambda}_{Z_{0,s,3}} \\ 1 & 1 & 1 \\ \overline{\lambda}^{-1}_{Z_{0,s,1}} & \overline{\lambda}^{-1}_{Z_{0,s,2}} & \overline{\lambda}^{-1}_{Z_{0,s,3}} \end{bmatrix}. \tag{14}$$

Formally, it is possible to easily extend this method by recurrence to any number of exponentials. The dimensions of $\mathbf{X}$, $\mathbb{N}$ and $\mathbb{M}$ must be adjusted according to the number of exponentials, as well as the degree of the polynomial equation in $\overline{\lambda}$ to be solved, its coefficients being determined by expanding the product $\prod_i \left(\overline{\lambda} - \overline{\lambda}_{Z_{0,s,i}}\right)$. In the numerical implementation of the method of moments, the possibility of finding up to four exponentials has been considered. However, a larger number of exponentials is rarely found, only for a few low ionization states of elements heavier than tungsten, such as gold. For tungsten, the maximum number of exponentials never exceeds three, regardless of its ionization state. As discussed previously, if no solution is found for a given set of multiple exponentials, a solution is sought for a number of exponentials decremented by one unity, and the procedure is repeated until a set of positive and real $\overline{\lambda}$ values is found. The case with a single exponential corresponding to the standard Yukawa potential is the ultimate solution if a MY potential cannot be found numerically.

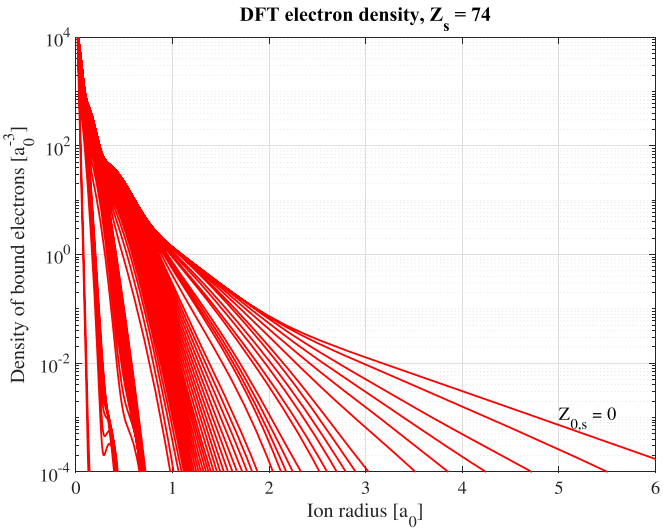

Figure 3. Density of bound electrons for all ionization states of tungsten calculated by the DFT method using the *GAUSSIAN* code [12]. Upper red line corresponds to neutral atoms. Details of the simulations are given in appendix B.

2.4. Comparisons between MY model and quantum relativistic calculations

Numerical calculations of the radial profiles of the bound electrons have been performed for most of the elements that can be found in a plasma, regardless of their ionization states, using *GAUSSIAN* and *GRASP* codes, respectively [12, 13]. They are all implemented in the *LUKE* suite of codes for studies of the atomic physics of fast electron dynamics in magnetized plasmas [10]. Details about the parameters used for the simulations with *GAUSSIAN* and *GRASP* codes are given in appendix B. In figure 3, the radial profiles of the density of bound electrons for all ionization states of tungsten calculated using the *GAUSSIAN* code are displayed. For low ionization states, the density clearly exhibits several bumps, which correspond approximately to the principal quantum numbers n of the atomic orbitals. Excellent agreement is found between the results of the two codes for all ionization states, as shown for the neutral tungsten atoms and the ions W^{10+}, W^{42+} and W^{56+} in figure 4. Consequently, numerical densities of reference $\rho^N_{Z_{0,s}}(\overline{r})$ given by one or the other of the two codes can be used indifferently for determining the coefficients $\left(\overline{A}_{Z_{0,s,i}}, \overline{\lambda}_{Z_{0,s,i}}\right)$ of the MY description.

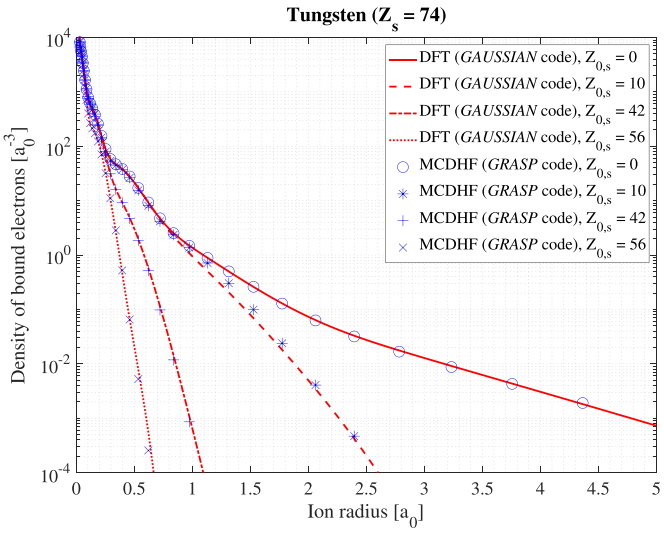

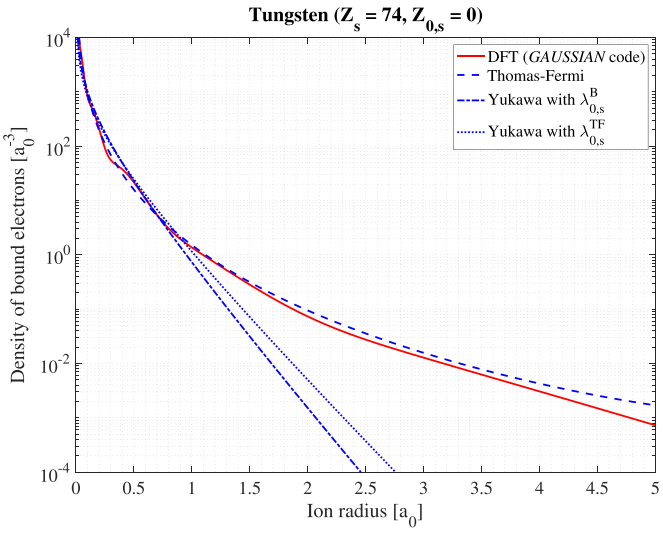

Figure 4. Comparison between radial densities of bound electrons for neutral tungsten W^0 and ionized states W^{+10}, W^{+42} and W^{+56}, as calculated by the *GAUSSIAN* (DFT method, red lines) and *GRASP* (MCDHF method, blue symbols) codes. Excellent agreement in found between the two quantum relativistic codes. Details of the simulations are given in appendix B.

In the literature, a comparison between DFT and the simple atomic models frequently used in publications has been carried out. Here, the radial dependencies of the density of bound electrons are evaluated for neutral tungsten and the ion W^{42+} using the Thomas–Fermi model as well as the standard Yukawa one (single exponential). For the latter, two inverse screening lengths have been considered: $\lambda^B_{0,s} \simeq 0.9 Z_s^{0.42} a_0^{-1}$ from a fit of the Herman–Skillman potentials determined by solving the DHFS equations [38] and $\lambda^{TF}_{0,s} = b_s^{-1} \simeq 1.13 Z_s^{1/3} a_0^{-1}$, where b_s is the reference length in the Thomas–Fermi model. As shown in figure 5, a good quantitative agreement is observed between DFT and the Thomas–Fermi model for neutral tungsten, as expected from the theory, while the agreement is poor with the standard Yukawa model, regardless of the inverse screening length. Conversely, the agreement for W^{42+} between DFT and the standard Yukawa model is better than with the Thomas–Fermi model. This highlights the fact that none of the simple models have a wide range of applications for accurately describing the atomic physics in kinetic and radiation calculations since the types of elements in the plasma may change with operating conditions, while their ionization states can also vary considerably with the temperature of the plasma.

Using results obtained with the DFT model, the set of coefficients $\left(\overline{A}_{Z_{0,s,i}}, \overline{\lambda}_{Z_{0,s,i}}\right)$ has been determined for up to four exponentials, but for elements lighter than gold, the maximum number of exponentials never exceeds three, as for tungsten. The full list of all ionization states of tungsten is given as a reference in table 1. For very weakly ionized states, $Z_{0,s} \leqslant 5$, three exponentials are found by the numerical procedure, because of the different slopes in the radial density, as shown in figure 3, while the number of exponentials is usually

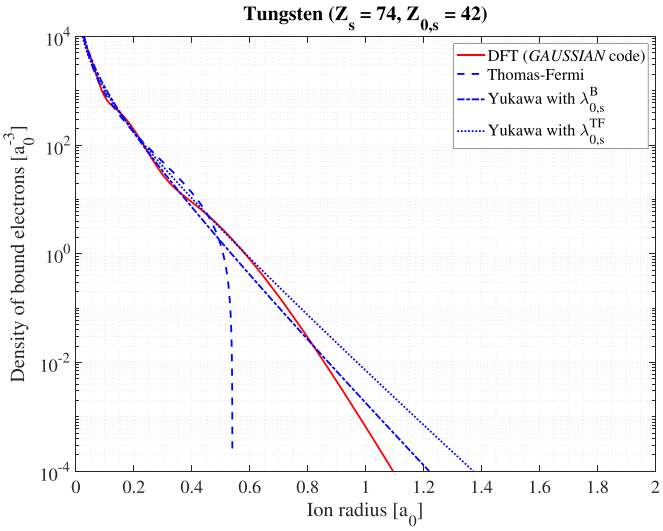

Figure 5. Comparison between densities of bound electrons for neutral tungsten W^0 (upper plot) and the ionized state W^{+42} (lower plot) as calculated by *GAUSSIAN* (DFT method, red line) and simple atomic models: Thomas–Fermi (blue dotted line), Yukawa with the inverse screening length $\lambda^B_{0,s} \simeq 0.9 Z_s^{0.42} a_0^{-1}$ [38] (blue dotted-dashed line) and Yukawa with the inverse screening length $\lambda^{TF}_{0,s} \simeq 1.13 Z_s^{1/3} a_0^{-1}$ [24, 27, 38, 41, 42] (blue dashed line). Details of the simulation for the DFT calculation are given in appendix B.

lower for larger $Z_{0,s}$ values since the decrease in the radial density from the nucleus becomes more regular and generally steeper. A comparison of the impact of the number of exponentials on the density profile for neutral tungsten is shown in figure 6.

With the use of three exponentials, an excellent quantitative agreement is found between $\overline{\rho}^N_{Z_{0,s}}(\overline{r})$ determined by DFT and the approximate MY description $\overline{\rho}_{Z_{0,s}}(\overline{r})$ at almost all radii. With a reduced number of exponentials, the agreement tends to deteriorate and is poor for a single exponential corresponding to the standard Yukawa description. It is interesting to note that Molière's description of the Thomas–Fermi model

Table 1. MY coefficients (3 exponentials) for the different ionization states of tungsten, based on DFT calculations done with the *GAUSSIAN* code for the density of [12]. Note that $\overline{A}_{W,3} = 1 - \overline{A}_{W,2} - \overline{A}_{W,1}$ by definition and in the case of two exponentials, $\overline{A}_{W,1} + \overline{A}_{W,2} = 1$.

Z_0	$\overline{A}_{W,1}$	$\overline{A}_{W,2}$	$\overline{\lambda}_{W,1}$	$\overline{\lambda}_{W,2}$	$\overline{\lambda}_{W,3}$
0	0.0964	0.7058	40.7776	4.7464	1.2612
1	0.1129	0.6490	36.2792	4.8617	1.5970
2	0.1134	0.5416	35.9580	5.4016	2.1100
3	0.0872	0.4628	42.7872	6.4409	2.4903
4	0.0447	0.3844	66.8955	8.5866	2.8794
5	0.2404	0.7595	22.7136	3.4038	—
6	0.2001	0.7998	25.9976	3.6903	—
7	0.1916	0.8084	27.0553	3.8056	—
8	0.1691	0.8309	29.603 11	4.0558	—
9	0.1540	0.8460	31.8430	4.2397	—
10	0.1336	0.8673	35.4275	4.4711	1.8417
11	0.1321	0.8786	36.0567	4.5467	2.7534
12	0.0781	0.9219	53.8146	5.0492	—
13	0.0735	0.9265	56.8908	5.1789	—
14	0.0703	0.9297	59.4299	5.3019	—
15	0.0683	0.9317	61.3319	5.4187	—
16	0.0464	0.9536	84.5389	5.7162	—
17	0.0217	0.9783	65.8142	6.0570	—
18	0.0195	0.9805	84.0652	6.1945	—
19	0.0181	0.9819	98.7309	6.3284	—
20	0.0173	0.9827	208.1839	6.4596	—
21	0.0172	0.9828	211.7881	6.5890	—
22	0.0179	0.9821	205.6840	6.7123	—
23	0.0191	0.9809	195.1947	6.8342	—
24	0.0208	0.9791	181.9760	6.9551	—
25	0.0232	0.9768	166.6728	7.0732	—
26	0.0260	0.9740	152.0133	7.1919	—
27	0.0293	0.9707	138.2625	7.3109	—
28	0.033 30	0.9667	125.1738	7.4282	—
29	0.0371	0.9629	115.1210	7.5611	—
30	0.0409	0.9591	106.6938	7.7017	—
31	0.0449	0.9551	99.6147	7.8511	—
32	0.0488	0.9511	93.6306	8.0104	—
33	0.0529	0.9471	88.4122	8.1797	—
34	0.0569	0.9431	84.1192	8.3633	—
35	0.0603	0.9397	80.8589	8.5669	—
36	0.0634	0.9366	78.2547	8.7894	—
37	0.0657	0.9342	76.5450	9.0381	—
38	0.0668	0.9332	75.9433	9.3208	—
39	0.067 23	0.9328	75.6537	9.6390	—
40	0.097 35	1.0166	58.6355	9.3206	6.8896
41	0.078 58	0.9464	67.6093	10.1206	6.1217
42	0.058 95	0.9532	82.4553	10.8159	6.0350
43	0.040 67	1.0524	108.3990	11.2870	8.6963
44	0.072 09	−0.3479	83.3834	21.2223	13.5253
45	1	—	16.3046	—	—
46	1	—	16.7547	—	—
47	1	—	17.1551	—	—
48	1	—	17.5828	—	—
49	1	—	18.0408	—	—
50	1	—	18.5337	—	—
51	1	—	19.0654	—	—
52	1	—	19.6402	—	—
53	1	—	20.2658	—	—
54	1	—	20.9494	—	—

(Continued.)

Table 1. (Continued.)

Z_0	$\overline{A}_{W,1}$	$\overline{A}_{W,2}$	$\overline{\lambda}_{W,1}$	$\overline{\lambda}_{W,2}$	$\overline{\lambda}_{W,3}$
55	1	—	21.7004	—	—
56	0.014 99	0.9850	383.7327	17.0332	—
57	0.032 14	0.9679	203.7360	17.4369	—
58	0.053 57	0.9464	139.5996	17.9070	—
59	0.080 41	0.9196	106.6274	18.4671	—
60	0.1128	0.8872	87.0463	19.1924	—
61	0.1501	0.8499	74.3800	20.1958	—
62	0.1813	0.8187	67.0734	21.8502	0.0069
63	0.05 328	0.9327	113.6346	27.6518	12.2918
64	1	—	34.3729	—	—
65	1	—	36.1418	—	—
66	1	—	38.3347	—	—
67	1	—	41.1288	—	—
68	1	—	44.8359	—	—
69	0.03 841	0.9616	333.5709	38.6642	—
70	0.1713	0.8287	152.9629	38.0016	—
71	0.5829	0.4171	94.1997	34.8665	—
72	−0.1893	1.1893	311.7230	127.7285	—
73	−0.2028	1.2028	305.1938	128.8713	—

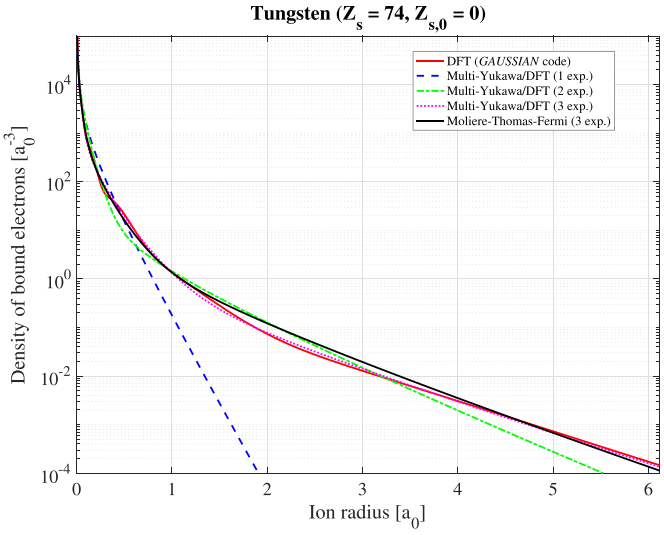

Figure 6. Atomic density for neutral tungsten element, $Z_{0,s} = 0$, calculated from DFT (red full line) using the *GAUSSIAN* code [12] and approximated using the method of moments with a single exponential (blue dashed line), two exponentials (green dotted dashed line) and three exponentials (pink dashed line) [29]. Moliere's solution, as given in appendix A is also displayed (black full line) [32].

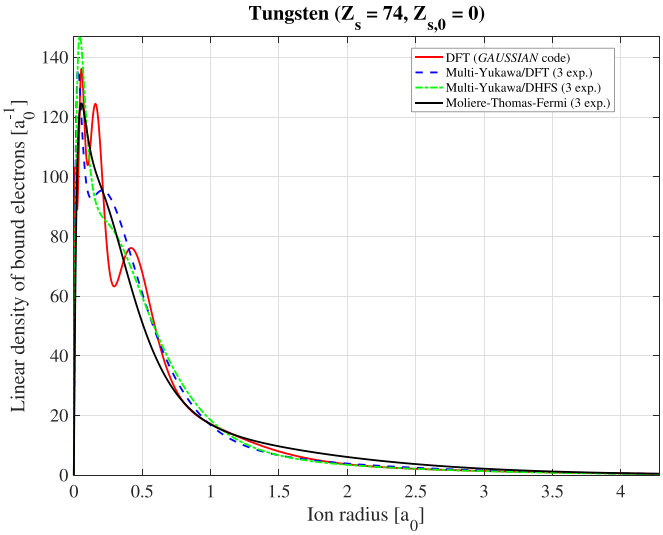

Figure 7. Atomic linear density $4\pi\bar{r}^2\overline{\rho}_{Z_{0,s}}(\bar{r})$ for neutral tungsten element, $Z_{0,s} = 0$, calculated from DFT (red full line) using the *GAUSSIAN* code [12] and approximated using the method of moments with a single exponential (blue dashed line), two exponentials (green dotted dashed line) and three exponentials (pink dashed line) [29]. Moliere's solution, as given in appendix A is also displayed (black full line) [32].

is also in very good agreement with the DFT results, which is consistent with the results shown in figure 5. Even if the radial dependence of the density of the nucleus is well reproduced, in the core of the atom, oscillations of the linear density $4\pi\bar{r}^2\overline{\rho}^{\text{num}}_{Z_{0,s}}(\bar{r})$ cannot be well reproduced by a series of exponentials, as shown in figure 7. This intrinsic limitation has already been observed in [29], where the same approach is considered but with another reference atomic model (DHFS). However, since the discrepancy occurs for $\bar{r} < 0.5$, its impact on the form factor remains small, as displayed in figure 8, when the normalized recoil momentum $\bar{q}$ is less than 0.1. Knowing that most of the Coulomb collisions occur principally for very low $\bar{q}$ values corresponding to the first Born approximation, the MY description is therefore remarkably robust for very weakly ionized atoms.

For higher ionization states, the advantage of the MY description is that it remains accurate for describing both the density and the form factor. An example is given in figure 9 for

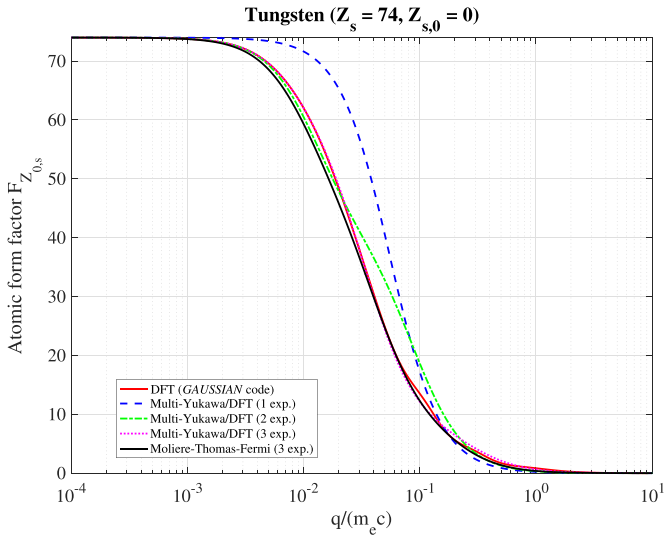

Figure 8. Atomic form factor for neutral tungsten element, $Z_{0,s} = 0$, calculated from DFT (red full line) using the *GAUSSIAN* code [12] and approximated using the method of moments with a single exponential (blue dashed line), two exponentials (green dotted dashed line) and three exponentials (pink dashed line) [29]. Moliere's solution, as given in appendix A is also displayed (black full line) [32]. Only the three exponentials case is very close to the DFT solution when $\bar{q} \geqslant 0.08$.

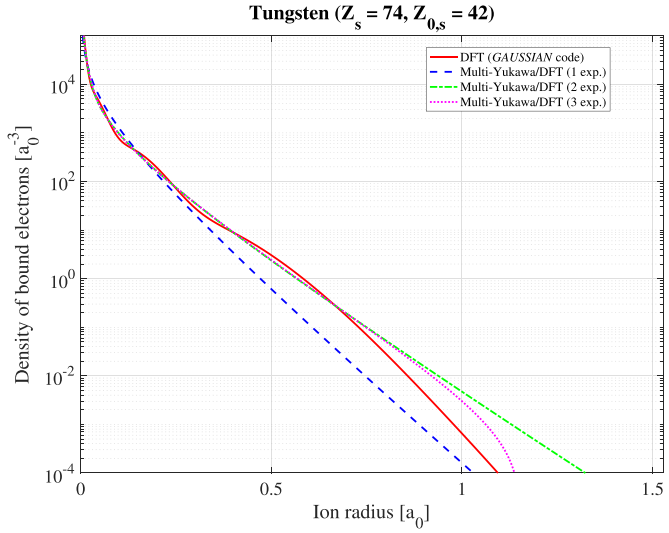

Figure 9. Atomic density for charged tungsten element, $Z_{0,s} = 42$, calculated from DFT (red full line) using the *GAUSSIAN* code [12] and approximated using the method of moments with a single exponential (blue dashed line), two exponentials (green dotted dashed line) and three exponentials (pink dashed line) [29].

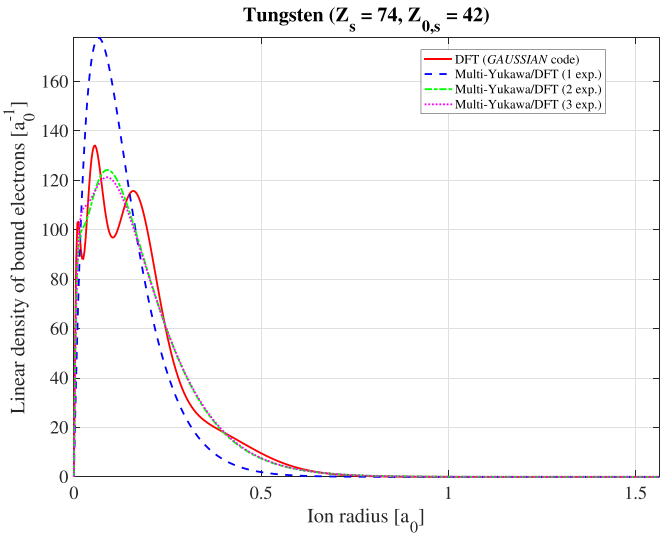

Figure 10. Atomic linear density $4\pi\bar{r}^2\bar{\rho}_{Z_{0,s}}(\bar{r})$ for charged tungsten element, $Z_{0,s} = 42$, calculated from DFT (red full line) using the *GAUSSIAN* code [12] and approximated using the method of moments with a single exponential (blue dashed line), two exponentials (green dotted dashed line) and three exponentials (pink dashed line) [29].

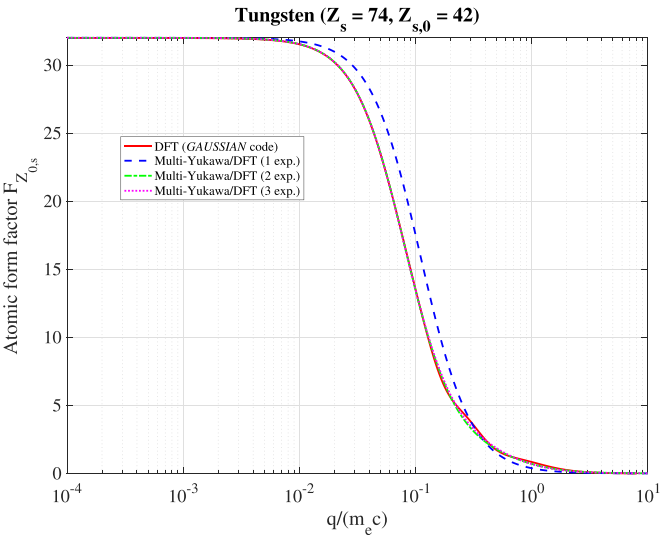

Figure 11. Atomic form factor for charged tungsten element, $Z_{0,s} = 42$, calculated from DFT (red full line) using the *GAUSSIAN* code [12] and approximated using the method of moments with a single exponential (blue dashed line), two exponentials (green dotted dashed line) and three exponentials (pink dashed line) [29]. Only the three exponentials case is very close to the DFT solution when $\bar{q} \geqslant 0.08$.

W^{42+}. In this case, the agreement is very good for both two and three exponentials, while the standard Yukawa description with a single exponential has rather poor agreement with the radial dependence of the density determined by DFT. However, as expected, the discrepancy is less pronounced compared to the case of neutral atoms due to the small remaining bumps in the radial density. For the neutral atom case, the small oscillations of the numerical linear density $4\pi\bar{r}^2\bar{\rho}^{\text{num}}_{Z_{0,s}}(\bar{r})$ are not well reproduced by the series of exponentials, as shown in figure 10, but the departure from $\bar{\rho}^{\text{num}}_{Z_{0,s}}(\bar{r})$ has again a very small impact on the form factor (see figure 11).

In table 2, the set of values $\left(\bar{A}_{Z_{0,s,i}}, \bar{\lambda}_{Z_{0,s,i}}\right)$ obtained for the neutral tungsten from the DFT and DHFS methods are given for comparison [29]. The coefficients of Moliére's method are also reported [32]. Even if the methodology is similar to the one detailed in [29], the coefficients for the three exponentials case exhibit a quite significant difference. Nevertheless,

Table 2. The coefficients $\left(\overline{\lambda}_{Z_{0,s},i}, \overline{A}_{Z_{0,s},i}\right)$ for the neutral tungsten, as determined by Molière's method of the Thomas–Fermi model [32], by the DHFS method from [32] and by DFT using the *GAUSSIAN* code as the density of [12]. All methods use three exponentials.

Method	Molière (Thomas–Fermi)	DHFS (3 exp.)	DFT (3 exp.)
$\overline{\lambda}_{W,1}$	28.4633	28.6330	40.7776
$\overline{\lambda}_{W,2}$	5.6926	4.2426	4.7464
$\overline{\lambda}_{W,3}$	1.4231	1.2340	1.2612
$\overline{A}_{W,1}$	0.1	0.15	0.0964
$\overline{A}_{W,2}$	0.55	0.6871	0.7058
$\overline{A}_{W,3}$	0.35	0.1629	0.1978

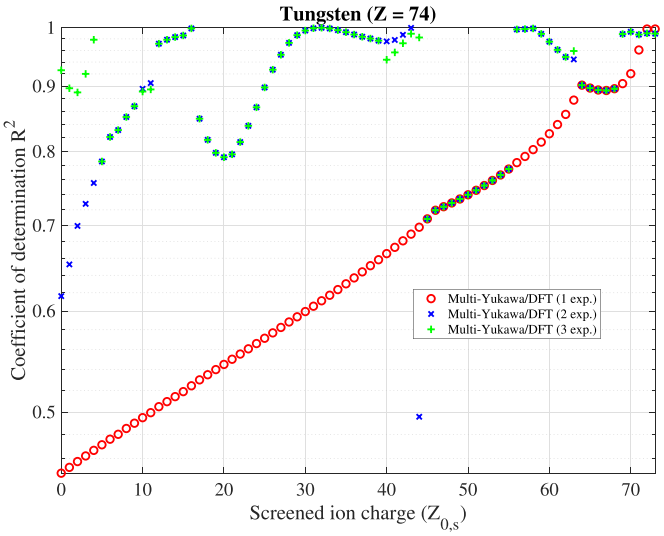

Figure 12. Coefficient of determination R^2 as a function of all screened ion charges $Z_{0,s}$ for tungsten to illustrate how well MY reproduces the results of DFT calculated by the *GAUSSIAN* code [12]: red circles (single exponential), blue crosses (two exponentials) and green x-marks (three exponentials). When points exactly overlap in the figure, this means that despite the method seeking three exponentials, only solutions with two or one exponentials are found.

as shown in figure 13, the approximate MY linear densities remain fairly close to the values obtained by DFT, even if not all the oscillations can be well reproduced. The differences between the coefficients result from their large sensitivity due to small changes, illustrating the ill-conditioned nature of the problem here addressed. This justifies *a posteriori* the chosen method, compared to a standard least-squares fit procedure that cannot converge when multiple close solutions exist [43]. In figure 12, the usual coefficient of determination R^2 is displayed for all the ionization states of tungsten to illustrate how well the MY reproduces the results of DFT for the atomic density[11]. The fact that $R^2 > 0.44$ regardless of the number of exponentials indicates that the MY is an appropriate simplified

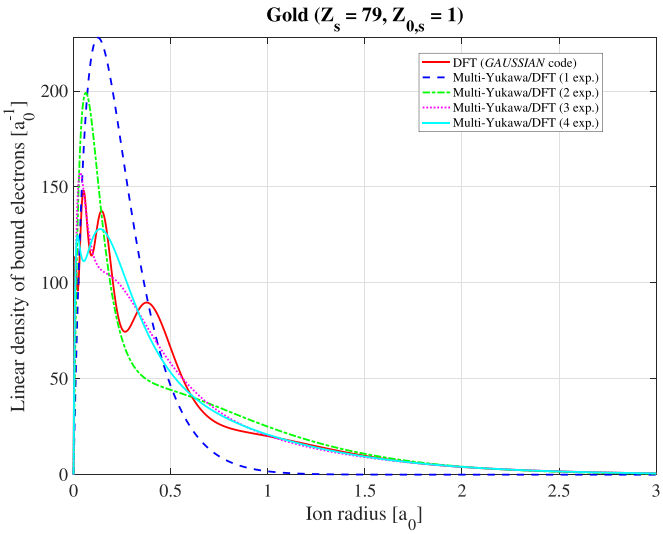

Figure 13. Linear density (lower plot) $4\pi\bar{r}^2\overline{\rho}_{Z_{0,s}}(\bar{r})$ for gold ion, $Z_{0,s} = 1$, calculated from DFT (red full line) using the *GAUSSIAN* code [12] and approximated using the method of moments with the use of atomic linear density $4\pi\bar{r}^2\overline{\rho}_{Z_{0,s}}(\bar{r})$ for charged gold element, $Z_{0,s} = 1$, calculated from DFT (red full line) using the *GAUSSIAN* code [12] and approximated using the method of moments with a single exponential (blue dashed line), two exponentials (green dotted dashed line), three exponentials (pink dashed line) and four exponentials (cyan full line).

atomic model for describing quantum code outputs. As expected, with a single exponential, R^2 gradually increases up to unity for the hydrogen-like atom, indicating that the standard Yukawa model is more appropriate for highly ionized atoms. This also illustrates the limits of this model for very weakly ionized atoms, which justifies the need for the MY description. Conversely, for up to three exponentials, R^2 always remains higher than 0.8, and often close to unity even for neutral or weakly ionized atoms. Between $Z_{0,s} = 45$ and $Z_{0,s} = 55$, as well as in the interval $Z_{0,s} = 64 - 68$, the method of moments is not able to identify a set of two or three exponentials because the density $\overline{\rho}_{Z_{0,s}}(\bar{r})$ fall-off with the distance from the nucleus has a nearly single exponential dependence. In this case, the R^2 coefficient is lower, as shown in figure 12, and the density of bound electrons is therefore less accurately described compared to other ionization states. Nevertheless, detailed calculations have shown that the impact on the atomic form factor still remains moderate. The fact that $R^2 \geqslant 0.7$ indicates that the MY model remains well consistent with the results of DFT and the MCDHF codes, even for these more difficult cases.

In order to illustrate the capability of the method to identify a best fit with more than three exponentials, the case of the weakly ionized gold atom Au^{1+} is shown in figure 13. Some differences can be seen in the inner part of the bound electron density between three and four exponentials, especially when

[11] The coefficient of determination is calculated according to the standard formula $R^2 = 1 - SS_{\rm res}/SS_{\rm tot}$ where $SS_{\rm res} = \sum_j (\overline{\rho}^{\rm num}_{Z_{0,s}}(\bar{r}_j) - \overline{\rho}_{Z_{0,s}}(\bar{r}_j))^2$ is the residual sum of squares and $SS_{\rm tot} = \sum_j (\overline{\rho}^{\rm num}_{Z_{0,s}}(\bar{r}_j) - \langle\overline{\rho}^{\rm num}_{Z_{0,s}}\rangle)^2$ is the total sum of squares. The sum is performed on all radial locations $\bar{r}_j$. Here, $\langle\overline{\rho}^{\rm num}_{Z_{0,s}}\rangle = (1/N_{\rm gridpoint})\sum_j \overline{\rho}^{\rm num}_{Z_{0,s}}(\bar{r}_j)$ is the mean of the calculated bound electron density. With this definition, $0 \leqslant R^2 \leqslant 1$ if the model is consistent with numerical data. Zero indicates a very poor agreement, and if $R^2 = 1$, the agreement is perfect.

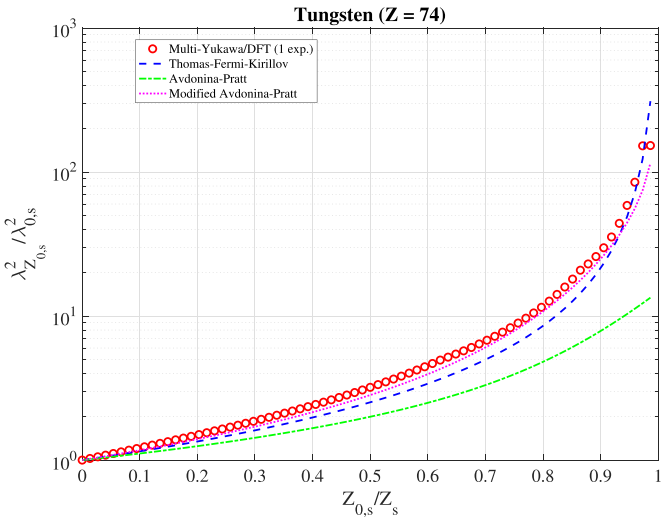

Figure 14. Relative evolution of the square of the inverse normalized screening length as a function of the normalized ion charge. Red circles: numerical value from the MY description of the atomic potential with a single exponential; blue dashed line: approximate Thomas–Fermi model from Kirillov *et al* [22]; green dotted dashed line: $\varphi_s(x) = (1-x^{n_s+1})/(1-x)$ from a fit of the Hartree–Fock–Slater potential [26, 28]; magenta dotted line: modified formulation $\varphi_s(x) = (1-x^{n_s+1})/(1-x)^{3/2}$ of the fit of the Hartree–Fock–Slater (HFS) atomic potential.

$\bar{r} < 0.5$, but they have no impact on the atomic form factor. The coefficient of determination increases from $R^2 = 0.4223$ for a single exponential to $R^2 = 0.6597$ for two exponentials, $R^2 = 0.8546$ for three and finally to $R^2 = 0.9646$ for four exponentials, indicating that the MY solution with the highest possible number of exponentials gives a better agreement with DFT and MCDHF calculations.

Although the Yukawa model fails to provide an accurate description of quantum relativistic calculations, except for rather highly stripped atoms, it is interesting to evaluate, with the procedure here detailed, the ratio $\lambda^2_{Z_{0,s}}/\lambda^2_{0,s} = \varphi_s(x)$ describing the relative change of the screening length with the normalized ionization state, i.e. $x = Z_{0,s}/Z_s$. For the approximate Thomas–Fermi model derived by Kirillov *et al* [22], $\varphi_s(x) = (1-x)^{-4/3}$, while from a fit of DHFS calculations, a heuristic dependency of the form $\varphi_s(x) = \left(1-x^{n_s+1}\right)/(1-x)$ was guessed with $n_s = Z_s\,(1/3 - 0.0020 \times Z_s)$ [26, 28]. As shown in figure 14, $\lambda^2_{Z_{0,s}}/\lambda^2_{0,s}$ is an increasing function of $Z_{0,s}/Z_s$ whose order of magnitude is reasonably well reproduced by the approximate Thomas–Fermi model. If the heuristic dependence in [26, 28] is far from the numerical calculations based on DFT, it is found that a modified formulation $\varphi_s(x) = (1-x^{n_s+1})/(1-x)^{3/2}$ gives a much better agreement. This improvement is valid for all elements, whatever Z_s is, in particular for light elements. Nevertheless, it should not hide the fact that the Yukawa model with a single exponential is not appropriate for describing the density of bound electrons for weakly ionized elements, even if the variation of the relative quantity $\lambda^2_{Z_{0,s}}/\lambda^2_{0,s}$ with $Z_{0,s}/Z_s$ can be reasonably well reproduced.

3. Generalized electron–ion collision operator

3.1. Elastic scattering

In kinetic calculations, the Coulomb collision operator may be expressed formally as $\mathrm{d}f_\mathrm{e}/\mathrm{d}t|_\mathrm{coll} \equiv \sum_s \sum_{Z_{0,s}} \mathbf{C}_{e,Z_{0,s}}\left(f_\mathrm{e}, f_{Z_{0,s}}\right) + \mathbf{C}_{e,e}\left(f_\mathrm{e}, f_\mathrm{e}\right)$ where $\mathbf{C}_{e,Z_{0,s}}\left(f_\mathrm{e}, f_{Z_{0,s}}\right)$ describes the interactions between the momentum distribution function $f_\mathrm{e}(t,\mathbf{x},\mathbf{p})$ of test electrons and the momentum distribution function $f_{Z_{0,s}}(t,\mathbf{x},\mathbf{p}_s)$ of atoms of species s with an ionization state $Z_{0,s}$, while $\mathbf{C}_{e,e}\left(f_\mathrm{e}, f_\mathrm{e}\right)$ is the linearized electron–electron collision operator[12] [10]. Here, all ionization states present in the plasma must be considered, with $Z_{0,s}$ ranging from zero for the neutral atom to Z_s for the fully stripped one. The density $n_{Z_{0,s}}(t,\mathbf{x}) = \int f_{Z_{0,s}}(t,\mathbf{x},\mathbf{p}_s)\,\mathrm{d}^3\mathbf{p}_s$ of ions with a net charge $Z_{0,s}$ at the spatial location $\mathbf{x}$ results from the local balance between ionization and recombination processes, assuming in general that $f_{Z_{0,s}}$ is a Maxwellian distribution. The relative fraction of partially ionized atoms is given by the ratio $n_{Z_{0,s}}(t,\mathbf{x})/n_s(t,\mathbf{x})$, where $n_s(t,\mathbf{x}) = \sum_{Z_{0,s}} n_{Z_{0,s}}(t,\mathbf{x})$ may be obtained by considering a local collisional-radiative equilibrium, as for the *OPEN-ADAS* database in the *LUKE* code [5, 10].

The incorporation of the partial screening effects for elastic scattering in kinetic calculations requires that we re-express the friction vector and diffusion tensor $\mathbf{A}_{Z_{0,s}}$ and $\mathbb{D}_{Z_{0,s}}$ of the Fokker–Planck formulation of the collision operator, assuming that small angle scattering still predominates for Coulomb collisions, which remains a good assumption even in the presence of high-Z impurities [7],

$$\mathbf{C}_{e,Z_{0,s}}\left(f_\mathrm{e}, f_{Z_{0,s}}\right) \simeq -\nabla_p\left(\mathbf{A}_{Z_{0,s}} f_\mathrm{e}(t,\mathbf{x},\mathbf{p})\right) + \nabla_p\nabla_p\left(\mathbb{D}_{Z_{0,s}} f_\mathrm{e}(t,\mathbf{x},\mathbf{p})\right), \tag{15}$$

with

$$\mathbf{A}_{Z_{0,s}} = \frac{1}{\Delta t}\int \mathrm{d}\triangle\mathbf{p}\,\mathcal{P}^{Z_{0,s}}_{\Delta t}(\mathbf{x},\triangle\mathbf{p},\mathbf{p})\,\triangle\mathbf{p}, \tag{16}$$

and

$$\mathbb{D}_{Z_{0,s}} = \frac{1}{2}\frac{1}{\Delta t}\int \mathrm{d}\triangle\mathbf{p}\,\mathcal{P}^{Z_{0,s}}_{\Delta t}(\mathbf{x},\triangle\mathbf{p},\mathbf{p})\,\triangle\mathbf{p}\triangle\mathbf{p}^\mathrm{T}, \tag{17}$$

[12] The Fokker–Planck collision operator used here describes electron dynamics in plasmas whose temperatures range from a few eV to several keV. Test electrons may be classical or relativistic when the Belaiev–Budker $e-e$ collision operator is considered. When the distortion of the distribution function from a Maxwellian represents a small fraction of the electron population, it is possible to linearize the electron−electron collision operator and by construction the Maxwellian is an eigenfunction of it. To account for self-collisions between fast electrons and the thermal bulk is particularly important for an accurate quantitative estimate of the rf-driven or Ohmic current source [44, 45]. It is an integral term usually determined to conserve particles and momentum, but not energy. Therefore, the electron temperature of the plasma must be a given parameter (by transport code for example), which is assumed to change slowly at the scale of the collision time. The full self-consistency between the bulk electron temperature and the fast electron energy losses may be obtained, but always requires the use of an external transport code. Therefore, the possible radiative cooling of the bulk electrons must be a part of the transport code, but not of the Fokker–Planck calculations themselves, due to the linearization. If the time scales of radiative cooling of the bulk electrons and collisions are similar, the time ordering will fail, and the whole approach should be revisited.

where $\mathcal{P}_{\Delta t}^{Z_{0,s}}$ is the transition probability describing the fact that an electron is at phase space point $(\mathbf{x},\mathbf{p})$ and time t, given that it was at point $(\mathbf{x}-\triangle\mathbf{x},\mathbf{p}-\triangle\mathbf{p})$ at time $t-\Delta t$, due to a collision with a partially ionized atom. By definition, $\int \mathrm{d}\triangle\mathbf{p}\mathcal{P}_{\Delta t}^{Z_{0,s}}(\mathbf{x},\triangle\mathbf{p},\mathbf{p})=1$, which states that all electrons are taken into account, irrespective of the initial phase space location $(\mathbf{x}-\triangle\mathbf{x},\mathbf{p}-\triangle\mathbf{p})$. Here, $\triangle\mathbf{p}^{\mathrm{T}}$ is the transposed vector of $\triangle\mathbf{p}$, with $\triangle\mathbf{p}=\mathbf{p}-\mathbf{p}_s$, for all $\mathbf{p}_s$ values and all scattering directions with respect to $\mathbf{p}$ directions, where $\mathbf{p}_s$ is the momentum of the ion of net charge $Z_{0,s}$. Since the transition probability is proportional to the product of the elementary cross-section $\mathrm{d}\sigma_{e,Z_{0,s}}(\mathbf{p})$ with the density of targets per unit surface $u_s\Delta t f_{Z_{0,s}}(t,\mathbf{x},\mathbf{p}_s)$, where u_s is the relative velocity before the scattering process between the test electron and the atoms of species s with a net ionization state $Z_{0,s}$, the friction vector is,

$$\mathbf{A}_{Z_{0,s}}=\int \mathrm{d}^3\mathbf{p}_s f_{Z_{0,s}}(t,\mathbf{x},\mathbf{p}_s)\int \mathrm{d}\Omega\frac{\mathrm{d}\sigma_{e,Z_{0,s}}}{\mathrm{d}\Omega}u_s\triangle\mathbf{p}, \tag{18}$$

while the diffusion tensor is,

$$\mathbb{D}_{Z_{0,s}}=\frac{1}{2}\int \mathrm{d}^3\mathbf{p}_s f_{Z_{0,s}}(t,\mathbf{x},\mathbf{p}_s)\int \mathrm{d}\Omega\frac{\mathrm{d}\sigma_{e,Z_{0,s}}}{\mathrm{d}\Omega}u_s\triangle\mathbf{p}\triangle\mathbf{p}^{\mathrm{T}}. \tag{19}$$

Here, the Møller relative velocity $\overline{u}_s$ normalized to the speed of light c is given by the relation,

$$\overline{u}_s=|\overline{\mathbf{u}}_s|=\frac{\sqrt{(\overline{\mathbf{v}}-\overline{\mathbf{v}}_s)^2-(\overline{\mathbf{v}}\times\overline{\mathbf{v}}_s)^2}}{1-\overline{\mathbf{v}}\cdot\overline{\mathbf{v}}_s}, \tag{20}$$

where $\overline{\mathbf{v}}=\overline{\mathbf{p}}/\gamma_{\mathrm{e}}$ is the electron (or test particle) velocity[13] and $\overline{\mathbf{v}}_s=\overline{\mathbf{p}}_s m_{\mathrm{e}}/m_{Z_{0,s}}$ is the ion velocity of mass $m_{s,Z_{0,s}}\simeq m_s$ since m_{e} is much less than the ion nucleus mass m_s. Here, $\overline{\mathbf{p}}_s=\mathbf{p}_s/(m_{\mathrm{e}}c)$ and $\overline{\mathbf{p}}=\mathbf{p}/(m_{\mathrm{e}}c)$. However, since $|\overline{\mathbf{v}}_s|\ll|\overline{\mathbf{v}}|$, because of the large difference in mass between m_{e} and m_s, the relative velocity may be simplified and $\overline{u}_s\simeq|\overline{\mathbf{v}}-\overline{\mathbf{v}}_s|$, even for run-away electrons. Indeed, in tokamak plasmas, for an ion temperature of 5.11 keV, $\overline{v}_s^{\mathrm{th}}\simeq 2\times10^{-3}$ for hydrogen and ten times less for tungsten. Møller corrections to $\overline{u}_s$ are therefore always negligible since the energy of these electrons cannot exceed 30 MeV, because of synchrotron radiation losses [47].

The fully screened relativistic Mott cross-section of collision between an electron and an ion of charge $Z_{s,0}^2$ is,

$$\frac{\mathrm{d}\sigma_{e,Z_{0,s}}}{\mathrm{d}\Omega}=Z_{0,s}^2\frac{r_{\mathrm{e}}^2}{4}\frac{(1-x^2)\overline{p}^2+1}{\overline{p}^4x^4}, \tag{21}$$

where $x=\sin(\theta/2)$, with θ being the usual deflection angle of the electron and r_{e} the classical electron radius. Spin and relativistic corrections are negligible in the non-relativistic limit, and when $\overline{p}^2\ll1$, the Mott cross-section merges with the usual Rutherford expression [48, 49]. Since $\overline{p}=\gamma\beta$, where $\beta=\overline{v}=\sqrt{1-1/\gamma^2}$ and γ is the Lorentz factor, for 200 keV slide-away electrons, $\overline{p}^2\simeq0.93$, while for 20 MeV run-away electrons, $\overline{p}^2\simeq1610$.

Knowing that $|\triangle\mathbf{p}|=2|\mathbf{p}|\sin(\theta/2)$ and that the angular integral is taken over $\int\mathrm{d}\Omega=\int_{x_{\min}}^{x_{\max}}\sin\theta\mathrm{d}\theta\int_0^{2\pi}\mathrm{d}\phi$, where ϕ is the azimuthal angle in the center of the mass frame, the fully screened friction vector $\mathbf{A}_{Z_{0,s}}$ and diffusion tensor $\mathbb{D}_{Z_{0,s}}$ are,

$$\mathbf{A}_{Z_{0,s}}=-\Upsilon\int \mathrm{d}^3\overline{\mathbf{v}}_s f_{Z_s}(t,\mathbf{x},\overline{\mathbf{v}}_s)\frac{\hat{\mathbf{u}}_s}{\overline{u}_s^2}\int_{x_{\min}}^{x_{\max}}\mathrm{d}x\frac{(1-x^2)\overline{p}^2+1}{x}Z_{0,s}^2, \tag{22}$$

and

$$\mathbb{D}_{Z_{0,s}}=\frac{1}{2}\Upsilon\int \mathrm{d}^3\overline{\mathbf{v}}_s f_{Z_{0,s}}(t,\mathbf{x},\overline{\mathbf{v}}_s)\frac{1}{\overline{u}_s}(\mathbb{I}-\hat{\mathbf{u}}_s\hat{\mathbf{u}}_s)\times\int_{x_{\min}}^{x_{\max}}\mathrm{d}x\frac{(1-x^2)\overline{p}^2+1}{x}(1-x^2)Z_{0,s}^2, \tag{23}$$

where $\Upsilon=4\pi r_{\mathrm{e}}^2c$, while $x_{[\min]\max}=(1+\overline{b}_{[\max]\min}^2)^{-1/2}$, with $\overline{b}=b/b_{90}$ being the normalized impact parameter of the Coulomb collision, with respect to the perpendicular deflection impact parameter $b_{90}=r_{\mathrm{e}}Z_{0,s}^2\beta^{-2}$. Here, the electron velocity normalized to the speed of light is linked to the Lorentz factor by the relation $\gamma=(1-\beta^2)^{-1/2}$. The values of $\overline{b}_{[\max]\min}$ are discussed in appendix C. In equation (23), the term $(\mathbb{I}-\hat{\mathbf{u}}_s\hat{\mathbf{u}}_s)$ is the usual perpendicular collision operator.

Since both definite integrals $\int_{x_{\min}}^{x_{\max}}\ldots\mathrm{d}x/x$ in equations (22) and (23) give the same value, one obtains,

$$\int_{x_{\min}}^{x_{\max}}\ldots\frac{\mathrm{d}x}{x}\simeq\gamma^2\int_{x_{\min}}^{x_{\max}}\frac{\mathrm{d}x}{x}=(\overline{p}^2+1)\ln\frac{\overline{b}_{\max}}{\sqrt{1+\overline{b}_{\min}^2}}, \tag{24}$$

where $\ln\Lambda_{e,Z_{s,0}}=\ln(\overline{b}_{\max}/\sqrt{1+\overline{b}_{\min}^2})$ is the Coulomb logarithm. Therefore, taking $x_{\min}=1/\Lambda_{e,Z_{0,s}}$ and $x_{\max}=1$, equations (22) and (23) may be approximated by,

$$\mathbf{A}_{Z_{0,s}}\simeq-\Upsilon\int \mathrm{d}^3\overline{\mathbf{v}}_s f_{Z_{0,s}}(t,\mathbf{x},\overline{\mathbf{v}}_s)\frac{\hat{\mathbf{u}}_s}{\overline{u}_s^2}(\overline{p}^2+1)\int_{1/\Lambda_{e,Z_{0,s}}}^{1}Z_{0,s}^2\frac{\mathrm{d}x}{x}, \tag{25}$$

and

$$\mathbb{D}_{Z_{0,s}}\simeq\frac{1}{2}\Upsilon\int \mathrm{d}^3\overline{\mathbf{v}}_s f_{Z_{0,s}}(t,\mathbf{x},\overline{\mathbf{v}}_s)\frac{1}{\overline{u}_s}(\mathbb{I}-\hat{\mathbf{u}}_s\hat{\mathbf{u}}_s)(\overline{p}^2+1)\times\int_{1/\Lambda_{e,Z_{0,s}}}^{1}Z_{0,s}^2\frac{\mathrm{d}x}{x}. \tag{26}$$

The calculation of the Coulomb logarithm $\ln\Lambda_{e,Z_{0,s}}$ is discussed in appendix C.

The partial screening is taken into account by replacing $Z_{0,s}^2\to|Z_s-F_{Z_{0,s}}(\overline{q})|^2$ in equations (25) and (26), where $\overline{q}=2\overline{p}\sin(\theta/2)=2\overline{p}x$, and following the definition in [7], the Fokker–Planck screening function $g_{Z_{0,s}}(\overline{p})$ is defined as,

$$\int_{1/\Lambda_{e,Z_{0,s}}}^{1}|Z_s-F_{Z_{0,s}}(\overline{q})|^2\frac{\mathrm{d}x}{x}\equiv Z_{0,s}^2\ln\Lambda_{e,Z_{0,s}}+g_{Z_{0,s}}(\overline{p}), \tag{27}$$

[13] The Møller relative velocity, which is the numerator term in equation (20), must be corrected by $(1-\overline{\mathbf{v}}\cdot\overline{\mathbf{v}}_s)^{-1}$ in order to guarantee that the interaction rate is unchanged by a Galilean transformation [46].

or

$$g_{Z_{0,s}}(\bar{p}) = \int_{1/\Lambda_{e,Z_{0,s}}}^{1} \left(\left| Z_s - F_{Z_{0,s}}(\bar{q}) \right|^2 - Z_{0,s}^2 \right) \frac{\mathrm{d}x}{x}, \tag{28}$$

since

$$Z_{0,s}^2 \int_{1/\Lambda_{e,Z_{0,s}}}^{1} \frac{\mathrm{d}x}{x} = Z_{0,s}^2 \ln \Lambda_{e,Z_{0,s}}. \tag{29}$$

The formulation (28) guarantees that $\int_{1/\Lambda_{e,Z_{0,s}}}^{1} |Z_s - F_{Z_{0,s}}(\bar{q})|^2 \mathrm{d}x/x = Z_{0,s}^2 \ln \Lambda_{e,Z_{0,s}}$ for weakly energetic electrons, while conversely, for very energetic ones, it is $Z_s^2 \ln \Lambda_{e,Z_s}$. However, as pointed out in [7], partial screening cannot be described in a strict Fokker–Planck sense other than in the complete and no screening limits. In order to maintain dominant screening terms and avoid unphysical behavior for partial screening, only terms to the lowest order in x must be considered, which allows $\bar{q}$ to be significant for large electron energies, and consequently take the full form of $F_{Z_{0,s}}(\bar{q})$. The corresponding Fokker–Planck operator is then equivalent to the first Legendre mode of the Boltzmann operator at non-relativistic energies, and differs by a factor of order $1/\ln \Lambda_{e,Z_{0,s}}$ in the ultra-relativistic limit.

In the limit of an almost zero ion temperature, as in the post-disruptive regime in tokamaks, $f_{Z_{0,s}}(t,\mathbf{x},\bar{\mathbf{v}}_s) \simeq n_{Z_{0,s}}(t,\mathbf{x})\,\delta(\bar{v}_s)/\left(4\pi\bar{v}_s^2\right)$ where $\delta(\bar{v}_s)$ is the Dirac function, thus assuming that ions are at rest. In this case, the integration over $\mathbf{v}_s$ may be performed analytically, and expressions in [7] may be retrieved. However, the implementation of the screening effects in kinetic codes for studying standard regimes like in the *LUKE* code is slightly different, because of the finite ion temperature, which requires that $\mathbf{A}_{Z_{0,s}}$ and $\mathbb{D}_{Z_{0,s}}$ be expressed in terms of Rosenbluth potentials, allowing a convenient conservative formulation of the collision operator. Knowing that $\nabla_{\bar{\mathbf{v}}}(1/\bar{u}_s) = \partial(1/\bar{u}_s)/\partial\bar{\mathbf{v}} = -\hat{\mathbf{u}}_s/\bar{u}_s^2$, $\nabla_{\bar{\mathbf{v}}}\bar{u}_s = \hat{\mathbf{u}}_s$ and $\nabla_{\bar{\mathbf{v}}}\nabla_{\bar{\mathbf{v}}}u = (\mathbb{I} - \hat{\mathbf{u}}_s\hat{\mathbf{u}}_s)/\bar{u}_s$, the integral $\int \mathrm{d}^3\bar{\mathbf{v}}_s$ may be permuted with the derivatives $\partial/\partial\bar{\mathbf{v}}$, and the term $\left(\bar{p}^2+1\right)\left[\int_{1/\Lambda_{e,Z_{0,s}}}^{1} \left|Z_s - F_{Z_{0,s}}(\bar{q})\right|^2 \mathrm{d}x/x\right]$ itself, which is independent of $\bar{\mathbf{u}}_s$, so,

$$\mathbf{A}_{Z_{0,s}} \simeq -\Upsilon\left(\bar{p}^2+1\right)\left[\int_{1/\Lambda_{e,Z_{0,s}}}^{1} \left|Z_s - F_{Z_{0,s}}(\bar{q})\right|^2 \frac{\mathrm{d}x}{x}\right] \times \frac{\partial}{\partial\bar{\mathbf{v}}} H_{Z_{0,s}}(t,\mathbf{x},\bar{\mathbf{v}}), \tag{30}$$

where

$$H_{Z_{0,s}}(t,\mathbf{x},\bar{\mathbf{v}}) = \int \mathrm{d}^3\bar{\mathbf{v}}_s f_{Z_{0,s}}(t,\mathbf{x},\bar{\mathbf{v}}_s)\frac{1}{\bar{u}_s}, \tag{31}$$

while

$$\mathbb{D}_{Z_{0,s}} \simeq \frac{1}{2}\Upsilon\left(\bar{p}^2+1\right)\left[\int_{1/\Lambda_{e,Z_{0,s}}}^{1} \left|Z_s - F_{Z_{0,s}}(\bar{q})\right|^2 \frac{\mathrm{d}x}{x}\right] \times \frac{\partial}{\partial\bar{\mathbf{v}}}\frac{\partial}{\partial\bar{\mathbf{v}}} G_{Z_{0,s}}(t,\mathbf{x},\bar{\mathbf{v}}), \tag{32}$$

with

$$G_{Z_{0,s}}(t,\mathbf{x},\bar{\mathbf{v}}) = \int \mathrm{d}^3\bar{\mathbf{v}}_s f_{Z_{0,s}}(t,\mathbf{x},\bar{\mathbf{v}}_s)\,\bar{u}_s. \tag{33}$$

In the coordinate system (p,ξ,φ) used by the *LUKE* Fokker–Planck solver in momentum space [50], where ξ is the cosine of the pitch-angle, the expression of the collision operator in terms of the divergence of the electron flux in momentum space $\nabla_{\mathbf{p}}\cdot\mathbf{S}_{\mathbf{p}}^{\mathrm{coll}}(f_\mathrm{e})$ is,

$$S_p^{\mathrm{coll}} = -D_{pp}^{\mathrm{coll}}\frac{\partial f_\mathrm{e}}{\partial p} + \frac{\sqrt{1-\xi^2}}{p}D_{p\xi}^{\mathrm{coll}}\frac{\partial f_\mathrm{e}}{\partial\xi} + F_p^{\mathrm{coll}} f_\mathrm{e}, \tag{34}$$

$$S_\xi^{\mathrm{coll}} = -D_{\xi p}^{\mathrm{coll}}\frac{\partial f_\mathrm{e}}{\partial p} + \frac{\sqrt{1-\xi^2}}{p}D_{\xi\xi}^{\mathrm{coll}}\frac{\partial f_\mathrm{e}}{\partial\xi} + F_\xi^{\mathrm{coll}} f_\mathrm{e}, \tag{35}$$

assuming a local axisymmetric plasma. By symmetry, $D_{p\xi}^{\mathrm{coll}} = D_{\xi p}^{\mathrm{coll}} = F_\xi^{\mathrm{coll}} = 0$. The contribution of elastic electron–ion collisions to the non-zero diffusion and friction terms D_{pp}^{coll} and F_p^{coll}, which describes momentum exchange between particles, is always very small compared to the one of the electron–electron collisions, because of the very large difference in mass between electrons and ions, and may therefore be neglected. The single large non-zero term arising from electron–ion collision is $D_{\xi\xi}^{\mathrm{coll}}$, which is proportional to $Z_{0,s}^2 \ln \Lambda_{e,Z_{0,s}}$. Consequently, introducing the partial screening in kinetic calculations requires simply to make the transformation $Z_{0,s}^2 \ln \Lambda_{e,Z_{0,s}} \to Z_{0,s}^2 \ln \Lambda_{e,Z_{0,s}} + g_{Z_{0,s}}(\bar{p})$ for the pitch-angle diffusion $D_{\xi\xi}^{\mathrm{coll}}$, with a careful account for the Coulomb logarithm $\ln \Lambda_{e,Z_{s,0}}$ with $Z_{0,s}$, as discussed in appendix C. Here, $D_{\xi\xi}^{\mathrm{coll}}$ incorporates the contribution of all ion species present in the plasma and their respective ionization states.

3.2. Inelastic scattering

In the presence of partially ionized high-Z atoms in the plasma, energetic electrons may lose a part of their kinetic energy by interacting with the bound electrons of a partially ionized atom whichconsequently jumps into a transient excited state. The slowing-down process, which is taken into account by Fokker–Planck calculations, is therefore the sum of multiple terms, the usual one from $e-e$ collisions, described in the LUKE kinetic code by the relativistic Belaiev–Budker collision operator [10, 51], the Abraham–Lorentz–Dirac reaction force for very energetic electrons arising from synchrotron radiation losses [47] and the new one from $e-i$ excitation. The latter can be deduced from Bethe's stopping-power formula describing the losses of energy $\mathrm{d}E$ per unit length $\mathrm{d}x$ [35, 52]:

$$-\left.\frac{\mathrm{d}E}{\mathrm{d}x}\right|_{Z_{0,s}} = 4\pi r_\mathrm{e}^2 n_{Z_{0,s}}(Z_s - Z_{0,s})\frac{m_\mathrm{e}c^2}{\beta^2}\left[\ln B_{Z_{0,s}} - \beta^2\right], \tag{36}$$

with

$$B_{Z_{0,s}} = \frac{\sqrt{2}\gamma\beta\sqrt{\gamma-1}}{\left\langle\hbar\omega_{Z_{0,s}}\right\rangle/m_\mathrm{e}c^2}, \tag{37}$$

where $\langle \hbar\omega_{Z_{0,s}} \rangle$ is the mean excitation energy for the ion of net charge $Z_{0,s}$. Since the energy loss over a distance $\triangle x$ is equivalent to the work of an effective drag force $F_p^{\text{excitation}}(p)$ over that distance, its expression in Fokker–Planck calculations in simply,

$$F_p^{\text{excitation}}(p) = -\sum_s \sum_{Z_{0,s}} \left.\frac{\mathrm{d}E}{\mathrm{d}x}\right|_{Z_{0,s}}. \tag{38}$$

The validity of the Bethe slowing down formula holds principally for fast electrons, whose kinetic energy E is much larger than the mean excitation energy $\langle \hbar\omega_{Z_{0,s}} \rangle$. In this case, the logarithm term always predominates over the small spin corrections given by the $-\beta^2$ term or possible very small additional terms. For electrons whose kinetic energy becomes low compared to the mean excitation energy, the Bethe formula indicates that the stopping power tends to decrease. Within this limit, the dominant inelastic term comes from $e-e$ collisions, as the Bethe formula goes to zero. Unfortunately, the Bethe formula may reverse sign, a non-physical effect that is an intrinsic limitation of the Bethe approach. This problem was identified in [7] and bypassed by performing an interpolation. In this case, $\ln B_{Z_{0,s}}$ in equation (36) is replaced by $\ln(1+B_{Z_{0,s}}^{n_B})/n_B$, with n_B an integer that is chosen heuristically to be 5. When $B_{Z_{0,s}} \gg 1$, $\ln(1+B_{Z_{0,s}}^{n_B})/n_B \simeq \ln B_{Z_{0,s}}$, and the Bethe formula is well retrieved. The Bethe-like expression guarantees that in the limit $\overline{p} = \gamma\beta \to 0$, $\ln(1+B_{Z_{0,s}}^{n_B})/n_B - \beta^2$ is always positive and smoothly becomes very small. The exact value of $\ln(1+B_{Z_{0,s}}^{n_B})/n_B - \beta^2$ is not critical since the dominant inelastic term is from $e-e$ collisions. Another approach, is also to enforce inelastic collisions from the excitation of high-Z elements to zero, when $\ln B_{Z_{0,s}} - \beta^2$ becomes negative[14]. Both methods are equivalent numerically.

Regarding the formulation of the Fokker–Planck solver in the *LUKE* code, as shown in equations (34) and (35) in [10, 47, 50], the drag force $F_p^{\text{excitation}}(p)$, as given by equation (38), may be readily incorporated in F_p^{coll}.

4. Fokker–Planck screening function

From the definition of the Fokker–Planck screening function given by equation (28), and making the change of variable $y = \hat{q}/x = 2\overline{p}/\alpha$, where $\overline{p} = p/(m_e c)$, $g_{Z_{0,s}}(\overline{p})$ may be expressed as the sum of two terms $g_{Z_{0,s},1}(\overline{p})$ and $g_{Z_{0,s},2}(\overline{p})$ where,

$$g_{Z_{0,s},1}(\overline{p}) = 2Z_s \int_{y/\Lambda}^{y} \left(N_s - F_{Z_{0,s}}(\hat{q})\right) \frac{\mathrm{d}\hat{q}}{\hat{q}}, \tag{39}$$

and

$$g_{Z_{0,s},2}(\overline{p}) = \int_{y/\Lambda}^{y} \left(F_{Z_{0,s}}^2(\hat{q}) - N_s^2\right) \frac{\mathrm{d}\hat{q}}{\hat{q}}. \tag{40}$$

Here, $\Lambda \equiv \Lambda_{Z_{0,s}}$, in order to simplify notations.

[14] For low-energy electrons, $\gamma \simeq 1+\beta^2/2$, so that $\sqrt{\gamma-1} \simeq \beta/\sqrt{2}$. Within this limit, $B_{Z_{0,s}} \simeq 2E/\langle \hbar\omega_{Z_{0,s}} \rangle$. The term $\ln B_{Z_{0,s}} - \beta^2$ becomes negative if $\ln B_{Z_{0,s}} < \beta^2$, which leads to a transcendental equation in E for determining this threshold.

The form factor given by equation (3) may be recast in the simple form,

$$F_{Z_{0,s}}(\hat{q}) = N_s \sum_i \frac{\overline{A}_{0,s,i}}{1+\left(\hat{q}a_{Z_{0,s,i}}\right)^2}, \tag{41}$$

since $a_{Z_{0,s,i}} = \alpha \bar{a}_{Z_{0,s,i}}/2$ and $\alpha\hat{q} = \bar{q}$. Therefore,

$$g_{Z_{0,s},1}(\overline{p}) = 2Z_s \int_{y/\Lambda}^{y} \left(N_s - N_s \sum_i \frac{\overline{A}_{0,s,i}}{1+\left(\hat{q}a_{Z_{0,s,i}}\right)^2}\right) \frac{\mathrm{d}\hat{q}}{\hat{q}}, \tag{42}$$

or

$$g_{Z_{0,s},1}(\overline{p}) = Z_s\left(Z_s - Z_{0,s}\right) \sum_i \overline{A}_{0,s,i} \ln\left(1+\left(\overline{p}\bar{a}_{Z_{0,s,i}}\right)^2\right), \tag{43}$$

assuming that the condition $2\overline{p}a_{Z_{0,s,i}}/(\alpha\Lambda) = \overline{p}a_{Z_{0,s,i}}/\Lambda \ll 1$ holds. This is always valid in tokamak plasmas since the Debye sphere has numerous particles.

In much the same way,

$$\begin{aligned} g_{Z_{0,s},2}(\overline{p}) = &+N_s^2 \sum_i \overline{A}_{0,s,i}^2 \widetilde{g}_{Z_{0,s},2,i}(\overline{p}) \\ &+N_s^2 \sum_i \sum_{j\neq i} \overline{A}_{0,s,i}\overline{A}_{0,s,j} \widetilde{g}_{Z_{0,s},2,i,j}(\overline{p}), \end{aligned} \tag{44}$$

where

$$\widetilde{g}_{Z_{0,s},2,i}(\overline{p}) = \int_{y/\Lambda}^{y} \frac{1-\left(1+\left(\hat{q}a_{Z_{0,s,i}}\right)^2\right)^2}{\left(1+\left(\hat{q}a_{Z_{0,s,i}}\right)^2\right)^2} \frac{\mathrm{d}\hat{q}}{\hat{q}}, \tag{45}$$

and

$$\widetilde{g}_{Z_{0,s},2,i,j}(\overline{p}) = \int_{y/\Lambda}^{y} \frac{1-\left(1+\left(\hat{q}a_{Z_{0,s,i}}\right)^2\right)\left(1+\left(\hat{q}a_{Z_{0,s,j}}\right)^2\right)}{\left(1+\left(\hat{q}a_{Z_{0,s,i}}\right)^2\right)\left(1+\left(\hat{q}a_{Z_{0,s,j}}\right)^2\right)} \frac{\mathrm{d}\hat{q}}{\hat{q}}, \tag{46}$$

which can be integrated analytically so that,

$$\widetilde{g}_{Z_{0,s},2,i}(\overline{p}) = -\frac{1}{2}\frac{\left(\overline{p}\bar{a}_{Z_{0,s,i}}\right)^2}{1+\left(\overline{p}\bar{a}_{Z_{0,s,i}}\right)^2} - \frac{1}{2}\ln\left(1+\left(\overline{p}\bar{a}_{Z_{0,s,i}}\right)^2\right), \tag{47}$$

while

$$\begin{aligned} &\widetilde{g}_{Z_{0,s},2,i,j,2}(\overline{p}) \\ &= -\frac{1}{4}\ln\left|1+\overline{p}^2\left(\bar{a}_{Z_{0,s,i}}^2+\bar{a}_{Z_{0,s,j}}^2\right)+\overline{p}^4\bar{a}_{Z_{0,s,i}}^2\bar{a}_{Z_{0,s,j}}^2\right| \\ &\quad + \frac{\bar{a}_{Z_{0,s,i}}^2+\bar{a}_{Z_{0,s,j}}^2}{2\sqrt{\overline{\Delta}}}\left[\ln\left|\frac{4\bar{a}_{Z_{0,s,i}}^2\bar{a}_{Z_{0,s,j}}^2\overline{p}^2+2\left(\bar{a}_{Z_{0,s,i}}^2+\bar{a}_{Z_{0,s,j}}^2\right)-\sqrt{\overline{\Delta}}}{4\bar{a}_{Z_{0,s,i}}^2\bar{a}_{Z_{0,s,j}}^2\overline{p}^2+2\left(\bar{a}_{Z_{0,s,i}}^2+\bar{a}_{Z_{0,s,j}}^2\right)+\sqrt{\overline{\Delta}}}\right|\right. \\ &\quad \left. - \ln\left|\frac{2\left(\bar{a}_{Z_{0,s,i}}^2+\bar{a}_{Z_{0,s,j}}^2\right)-\sqrt{\overline{\Delta}}}{2\left(\bar{a}_{Z_{0,s,i}}^2+\bar{a}_{Z_{0,s,j}}^2\right)+\sqrt{\overline{\Delta}}}\right|\right], \end{aligned} \tag{48}$$

with

$$\sqrt{\overline{\Delta}} = 2\left|\bar{a}^2_{Z_{0,s,i}} - \bar{a}^2_{Z_{0,s,j}}\right|. \tag{49}$$

Gathering all terms,

$$\begin{aligned} g_{Z_{0,s}}(\bar{p}) = {} & Z_s\left(Z_s - Z_{0,s}\right)\sum_i \overline{A}_{0,s,i}\ln\left(1+\left(\bar{p}\bar{a}_{Z_{0,s,i}}\right)^2\right) - \frac{\left(Z_s - Z_{0,s}\right)^2}{2} \\ & \times \sum_i \overline{A}^2_{0,s,i}\left(\frac{\left(\bar{p}\bar{a}_{Z_{0,s,i}}\right)^2}{1+\left(\bar{p}\bar{a}_{Z_{0,s,i}}\right)^2} + \ln\left(1+\left(\bar{p}\bar{a}_{Z_{0,s,i}}\right)^2\right)\right) \\ & + 2\left(Z_s - Z_{0,s}\right)^2 \sum_i \sum_{j>i} \overline{A}_{0,s,i}\overline{A}_{0,s,j}\widetilde{g}_{Z_{0,s},2,i,j}(\bar{p}), \end{aligned} \tag{50}$$

with

$$\begin{aligned} & \widetilde{g}_{Z_{0,s},2,i,j}(\bar{p}) \\ & = -\frac{1}{2}\frac{a^2_{Z_{0,s,i}} + a^2_{Z_{0,s,j}}}{a^2_{Z_{0,s,j}} - a^2_{Z_{0,s,i}}}\ln\left|\frac{1+\bar{p}^2\bar{a}^2_{Z_{0,s,j}}}{1+\bar{p}^2\bar{a}^2_{Z_{0,s,i}}}\right| \\ & \quad - \frac{1}{4}\ln\left|1+\bar{p}^2\left(\bar{a}^2_{Z_{0,s,i}} + \bar{a}^2_{Z_{0,s,j}}\right) + \bar{p}^4\bar{a}^2_{Z_{0,s,i}}\bar{a}^2_{Z_{0,s,j}}\right| \\ & \quad + \frac{\bar{a}^2_{Z_{0,s,i}} + \bar{a}^2_{Z_{0,s,j}}}{4\left|\bar{a}^2_{Z_{0,s,i}} - \bar{a}^2_{Z_{0,s,j}}\right|} \\ & \quad \times \left[\ln\left|\frac{2\bar{a}^2_{Z_{0,s,i}}\bar{a}^2_{Z_{0,s,j}}\bar{p}^2 + \left(\bar{a}^2_{Z_{0,s,i}} + \bar{a}^2_{Z_{0,s,j}}\right) - \left|\bar{a}^2_{Z_{0,s,i}} - \bar{a}^2_{Z_{0,s,j}}\right|}{2\bar{a}^2_{Z_{0,s,i}}\bar{a}^2_{Z_{0,s,j}}\bar{p}^2 + \left(\bar{a}^2_{Z_{0,s,i}} + \bar{a}^2_{Z_{0,s,j}}\right) + \left|\bar{a}^2_{Z_{0,s,i}} - \bar{a}^2_{Z_{0,s,j}}\right|}\right| \right. \\ & \quad \left. - \ln\left|\frac{\left(\bar{a}^2_{Z_{0,s,i}} + \bar{a}^2_{Z_{0,s,j}}\right) - \left|\bar{a}^2_{Z_{0,s,i}} - \bar{a}^2_{Z_{0,s,j}}\right|}{\left(\bar{a}^2_{Z_{0,s,i}} + \bar{a}^2_{Z_{0,s,j}}\right) + \left|\bar{a}^2_{Z_{0,s,i}} - \bar{a}^2_{Z_{0,s,j}}\right|}\right|\right], \end{aligned} \tag{51}$$

and, as expected, $\lim_{\bar{p}\to 0} g_{Z_{0,s}}(\bar{p}) = 0$ is verified regardless of the element and its ionization state $Z_{0,s,}$.

In the case of a single exponential corresponding to the standard Yukawa atomic potential, equation (50) simplifies to the usual form:

$$\begin{aligned} g_{Z_{0,s}} = \frac{1}{n}\left[\left(Z_s^2 - Z_{0,s}^2\right)\ln\left(1+\left(\bar{p}\bar{a}_{Z_{0,s,1}}\right)^n\right)\right. \\ \left. - \left(Z_s - Z_{0,s}\right)^2\frac{\left(\bar{p}\bar{a}_{Z_{0,s,1}}\right)^n}{1+\left(\bar{p}\bar{a}_{Z_{0,s,1}}\right)^n}\right], \end{aligned} \tag{52}$$

where $n = 2$, since $\overline{A}_{0,s,1} = 1$, while $\widetilde{g}_{Z_{0,s},2,i,j}(\bar{p}) = 0$ by definition. Using the Thomas–Fermi–Kirillov model [22], $n = 3/2$, and equation (6) in [6] is well retrieved. The difference is generally small for tungsten, a few percent, between the MY and Thomas–Fermi–Kirillov models.

The analytical expression of $g_{Z_{0,s}}(\bar{p})$ may be easily implemented in Fokker–Planck solvers, allowing fast and accurate kinetic calculations, whatever $\bar{p}$ and the type of elements and their level of ionization. As shown in figure 15, $g_{Z_{0,s}}(\bar{p})$ from equation (50) for neutral tungsten with the use of three exponentials is very close to the numerical estimate $g^{\mathrm{num}}_{Z_{0,s}}(\bar{p})$ directly obtained in the limit $\bar{p} \gg 1$, from DFT calculations using results of the *GAUSSIAN* code. The formula is,

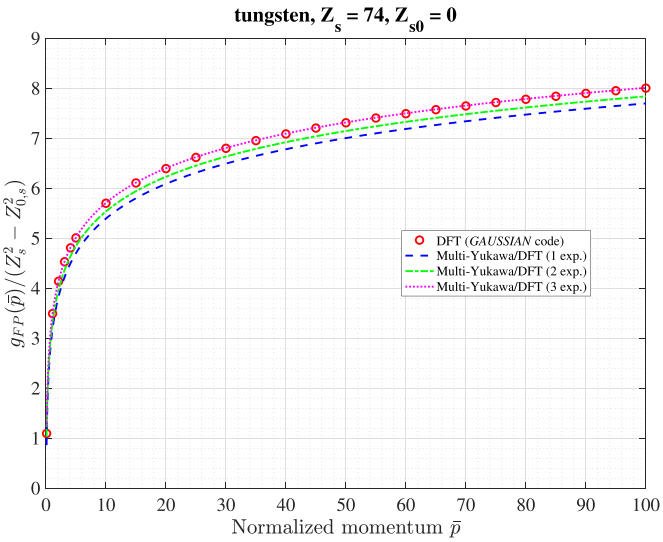

Figure 15. Normalized Fokker–Planck screening function for the neutral tungsten element, $Z_{0,s} = 0$, as a function of the normalized momentum $\bar{p} = p/(m_e c)$, calculated from DFT results (red circles) using the *GAUSSIAN* code [12] for $\bar{\rho}^{\mathrm{num}}_{Z_{0,s}}$ and equation (53) and approximated using the method of moments (multi-Yukawa) given by equation (50) with a single exponential (blue dashed line), two exponentials (green dotted dashed line) and three exponentials (pink dashed line).

$$\begin{aligned} g^{\mathrm{num}}_{Z_{0,s}}(\bar{p}) = {} & \left(Z_s^2 - Z_{0,s}^2\right)\left(\ln\left(2\bar{p}/\alpha\right) + \gamma_{\mathrm{EM}} - 1\right) + 2Z_s N_s \hat{I}_{1,Z_{0,s}} \\ & + N_s^2\left(\frac{1}{2} - \hat{I}_{2,Z_{0,s}}\right), \end{aligned} \tag{53}$$

where

$$\hat{I}_{1,Z_{0,s}} \equiv \frac{4\pi}{N_s}\int_0^\infty \bar{\rho}^{\mathrm{num}}_{Z_{0,s}}(\bar{r}_1)\,\bar{r}_1^2\ln\bar{r}_1\mathrm{d}\bar{r}_1, \tag{54}$$

with

$$\hat{I}_{2,Z_{0,s}} = \frac{4\pi^2}{N_s^2}\int_0^\infty \bar{\rho}^{\mathrm{num}}_{Z_{0,s}}(\bar{r}_1)\,\hat{J}_{2,Z_{0,s}}(\bar{r}_1)\,\bar{r}_1\mathrm{d}\bar{r}_1, \tag{55}$$

and

$$\begin{aligned} \hat{J}_{2,Z_{0,s}}(\bar{r}_1) = \int_0^\infty \bar{\rho}^{\mathrm{num}}_{Z_{0,s}}(\bar{r}_2)\,\bar{r}_2\mathrm{d}\bar{r}_2\left(\left(\bar{r}_1+\bar{r}_2\right)^2\ln\left(\bar{r}_1+\bar{r}_2\right)\right. \\ \left. - \left(\bar{r}_1-\bar{r}_2\right)^2\ln\left|\bar{r}_1-\bar{r}_2\right|\right), \end{aligned} \tag{56}$$

from [7], γ_{EM} being the Euler–Mascheroni constant [53].

Since equation (53) is derived in the limit $\bar{p} \gg 1$, it is consequently not valid at low $\bar{p}$, and $g^{\mathrm{num}}_{Z_{0,s}}(\bar{p})$ does not converge towards zero when $\bar{p} \leqslant 0.5$, as shown in figure 16 for the neutral atom of tungsten. When the number of exponentials is reduced, $g_{Z_{0,s}}(\bar{p})$ is always lower than $g^N_{Z_{0,s}}(\bar{p})$. The relative error is about 13% at $\bar{p} = 1$ for a single exponential. This tendency is similar for an ionized atom, as shown for W^{42+} in figure 17. In this case, only two exponentials are necessary to accurately reproduce the atomic potential. For ionization states ranging between W^{45+} and W^{55+}, where only a single exponential can be found by the MY procedure described

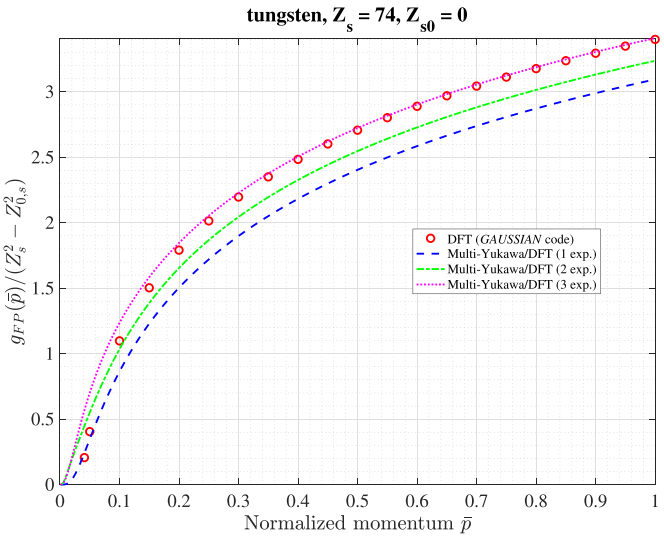

Figure 16. Normalized Fokker–Planck screening function for the neutral tungsten element, $Z_{0,s} = 0$, as a function of the normalized momentum $\bar{p} = p/(m_e c)$ between $\bar{p} = [0, 1]$ calculated from DFT results (red circles) using the *GAUSSIAN* code [12] for $\bar{\rho}^{\mathrm{num}}_{Z_{0,s}}$ and equation (53) and approximated using the method of moments (multi-Yukawa) given by equation (50) with a single exponential (blue dashed line), two exponentials (green dotted dashed line) and three exponentials (pink dashed line). When $\bar{p} < 0.4$, the numerical value of the normalized Fokker–Planck screening function falls off more rapidly than the MY expression with the use of three exponentials, and does not converge towards zero for $\bar{p} \approx 0$, as expected from theory.

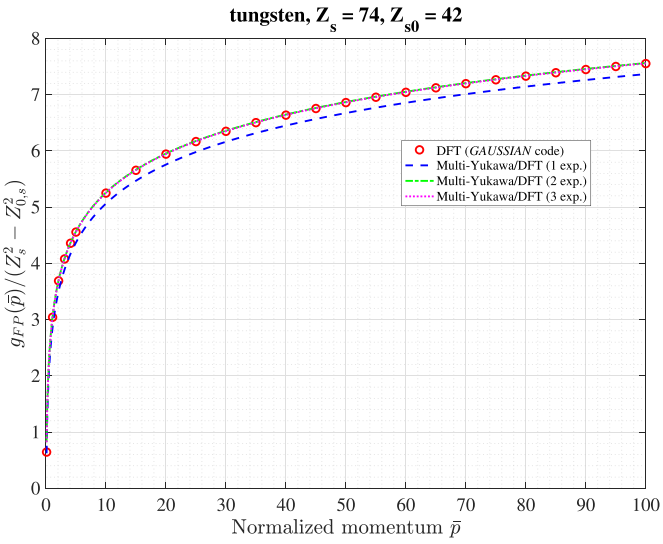

Figure 17. Normalized Fokker–Planck screening function for the charged tungsten element, $Z_{0,s} = 42$, as a function of the normalized momentum $\bar{p} = p/(m_e c)$, calculated from DFT results (red circles) using the *GAUSSIAN* code [12] for $\bar{\rho}^{\mathrm{num}}_{Z_{0,s}}$ and equation (53) and approximated using the method of moments (multi-Yukawa) given by equation (50) with a single exponential (blue dashed line), two exponentials (green dotted dashed line) and three exponentials (pink dashed line).

in section 2, the relative deviation of $g_{Z_{0,s}}(\bar{p})$ from $g^{\mathrm{num}}_{Z_{0,s}}(\bar{p})$ remains small whatever the $\bar{p}$ value, in the order of a few percent, even if the coefficient of determination R^2, shown in figure 12, is lower. This results from the fact that $g_{Z_{0,s}}(\bar{p})$ is itself an integral, which smooths out possible errors.

5. Mean excitation energy

The mean excitation energy $\langle \hbar\omega_{Z_{0,s}} \rangle$ is the key parameter to describe enhanced slowing down of the electrons by transferring energy to partially ionized high-Z elements in a hot plasma. It is formally defined as $\langle \hbar\omega_{Z_{0,s}} \rangle = (1/Z_{0,s}) \sum_{ik} f_{ik} \ln(\hbar\omega_{ik})$, where f_{ik} is the dipole oscillator strength of the transition ω_{ik} for the atomic system between quantum states $|i\rangle$ and $|k\rangle$, according to Bethe's theory [34, 54]. Its determination from first principles calculations is a considerable challenge, so except for elements that do not require relativistic corrections, $\langle \hbar\omega_{Z_{0,s}} \rangle$ is generally obtained from empirical laws constrained by measurements for neutral atoms only [55–58]. Recent advanced calculations carried out by a non-relativistic multi-configurational self-consistent field (MCSCF) code have allowed us to estimate $\langle \hbar\omega_{Z_{0,s}} \rangle$ for all ionization states of the elements lighter than argon $Z_s \leqslant 18$ [14, 15, 59]. Although this result represents considerable progress, the accurate determination of $\langle \hbar\omega_{Z_{0,s}} \rangle$ for many higher-Z elements, such as tungsten, is still missing, which makes it difficult to study the impact of inelastic processes by electron–ion interaction in a hot plasma. In this context, several simple models have been introduced to compare their impact on kinetic calculations.

In general, MCSCF calculations show that $\langle \hbar\omega_{Z_{0,s}} \rangle$ has an exponential-like dependence with $Z_{0,s}$, which can be easily determined within the two limits, i.e. for the neutral atom and for the hydrogen-like atom characterized by a single valence electron. For low-Z neutral elements, $\langle \hbar\omega_{Z_{0,s}} \rangle$ has a rather complex structure, while it becomes almost proportional to Z_s for $Z_s > 18$, i.e. $\hbar \langle \omega_{Z_{0,s}} \rangle \simeq 10 Z_s$ eV, this being known as the Bloch relation [55]. For $Z_s < 18$, $\langle \hbar\omega_{Z_{0,s}} \rangle$ oscillates with Z_s and tends to increase up to approximately 50% as its value decreases. The Z_s dependence of $\langle \hbar\omega_{Z_{0,s}} \rangle$ for neutral atoms can be well described by a statistical approach to the energy loss process, known as the LPA [37, 55]. In the other limit corresponding to a single bound electron, $\langle \hbar\omega_{Z_{0,s}} \rangle = Z_s^2 I_H$ eV, where $I_H = 14.9916$ eV is obtained from non-relativistic quantum calculations [14, 60]. Consequently, $\langle \hbar\omega_{Z_{0,s}} \rangle$ may be approximated by the simple heuristic relation,

$$\ln \langle \hbar\omega_{Z_{0,s}} \rangle \simeq \ln\left(\frac{I_H}{10} Z_s\right) \frac{Z_{0,s}}{Z_s - 1} + \ln(10 Z_s), \qquad (57)$$

where $Z_{0,s}$ is the charge of the fully screened ion, and $\hbar\omega_{Z_{0,s}}$ is expressed in eV units. This relation can be considered as an upper bound of $\langle \hbar\omega_{Z_{0,s}} \rangle$, since electron–electron correlations tend to reduce the mean excitation energy [14]. This method has been used to quantify the impact of tungsten on the toroidal plasma current driven by RF waves at the lower hybrid frequency in tokamaks [4].

It is shown that for argon, in figure 18, the exponential interpolation given by equation (57) is in good agreement for both weakly and highly ionized states compared

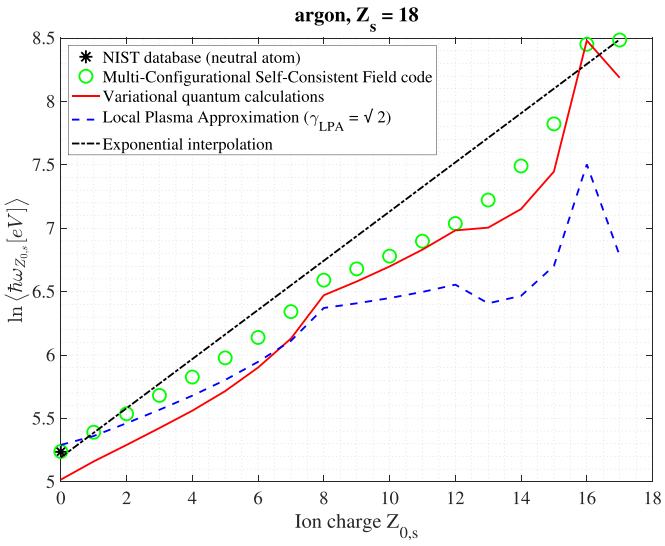

Figure 18. Variation of the logarithm of the mean excitation energy in eV units for argon, as a function of the level of ionization. Black dotted dashed line: exponential interpolation determined from neutral atom and hydrogen-like ion according to equation (57); green circles: numerical results from the MCSCF quantum code [14]; blue dashed line: LPA model from equation (59) with $\gamma_{\mathrm{LPA}} = \sqrt{2}$ using the MY atomic model with the use of three exponentials calibrated against DFT calculations (*GAUSSIAN* code) [37]; red full line: variational quantum model from equation (62) using the MY atomic model with the use of three exponentials calibrated against DFT calculations (*GAUSSIAN* code) [36]; black star: mean excitation energy for the neutral atom from the NIST database [62].

to MCSCF calculations [14]. In between, results obtained with the MCSCF code are lower, especially in the interval $Z_{0,s} = [10-15]$. However, the difference never exceeds a factor two.

More refined approaches may be considered, taking into account the density of bound charges calculated in the ground-state. Indeed, since excited states are transient with a characteristic time that is generally much smaller than the mean collision time, elements in the plasma are principally in a ground-state from which atom transitions must be considered to evaluate $\langle \hbar\omega_{Z_{0,s}} \rangle$. Two models are interesting for this purpose, the LPA approach [37], dedicated principally to very weakly ionized atoms and a variational quantum description [36]. Although restricted to non-relativistic elements, the latter may be an interesting alternative even for high-Z elements, as it is expected to be valid within a larger range of $Z_{0,s}$ values. For both approaches, the MY description of the density of bound electrons may be used, allowing a unified description of the atomic physics in kinetic calculations, not only for elastic Coulomb collisions but also for inelastic processes.

5.1. LPA

The LPA has been widely used to calculate the mean excitation energies of neutral atoms [55]. The LPA formula can be extended to any ionization state, according to the relation,

$$\ln\left\langle \hbar\omega_{Z_{0,s}} \right\rangle = \frac{4\pi}{N_s}\int_0^\infty \bar{r}^2 \bar{\rho}_{Z_{0,s}}(\bar{r}) \ln\left(\gamma_{\mathrm{LPA}}\sqrt{4\pi}\alpha^2 m_e c^2 \sqrt{\bar{\rho}_{Z_{0,s}}(\bar{r})}\right) \mathrm{d}\bar{r}. \tag{58}$$

The LPA formula gives generally poor results when the ionization state is high and a fewer number of electrons remain bound, because of the basic difficulties encountered when one tries to derive this scheme from first principles, i.e. starting with the standard definition of the oscillator strength in terms of dipole matrix elements and carrying out a systematic deduction [61]. In particular, the choice of γ_{LPA} is rather arbitrary, and its value, from heuristic arguments, is generally set at $\sqrt{2}$. Incorporating equation (2) into equation (58) with $\gamma_{\mathrm{LPA}} = \sqrt{2}$,

$$\begin{aligned}\ln\left\langle \hbar\omega_{Z_{0,s}} \right\rangle &= \sum_i \bar{\lambda}^2_{Z_{0,s,i}} \bar{A}_{Z_{0,s,i}} \int_0^\infty \bar{r}\exp\left(-\bar{\lambda}_{Z_{0,s,i}}\bar{r}\right) \\ &\times \ln\left(\sqrt{2}\alpha^2 m_e c^2 \sqrt{\frac{Z_s - Z_{0,s}}{\bar{r}} \sum_j \bar{\lambda}^2_{Z_{0,s,j}} \bar{A}_{Z_{0,s,i}} \exp\left(-\bar{\lambda}_{Z_{0,s,j}}\bar{r}\right)}\right) \mathrm{d}\bar{r}.\end{aligned} \tag{59}$$

As shown for argon in figure 18, which is the highest-Z element for which advanced numerical quantum calculations are available [14], a good quantitative agreement is found between LPA calculations using equation (59) and MCSCF ones for the neutral atom. The value from the NIST database is also consistent with the LPA level [62]. As the ion charge $Z_{0,s}$ is increasing, the departure from the results of the numerical quantum calculations is more and more pronounced, and with the LPA, the limit for the hydrogen-like ion is never recovered, indicating that the model fails completely in this regime. For the case of tungsten, the lack of quantum calculations prevents an accurate comparison as for argon. Nevertheless, the departure from the hydrogen-like limit is also very large, while for the neutral atom, the agreement between the value given by the NIST database and the estimate from the Bloch relation is very good, as shown in figure 19.

5.2. Variational quantum description

A non-relativistic variational quantum model to calculate the mean excitation energy, initially derived for inertial fusion experiments, is an interesting approach to obtain a more accurate estimate $\langle \hbar\omega_{Z_{0,s}} \rangle$ as a function of $Z_{0,s}$. According to [36], the mean excitation energy of the ground state is given by the relation $\ln\langle \hbar\omega_{Z_{0,s}} \rangle = \frac{1}{2}\ln S(1)/S(-1)$ where $S(-1) = 2m_e a_0^2 \langle \bar{r}^2 \rangle / (3\hbar^2)$ and $S(1) = 4K_0/3$. The functions S are moments of the strength distribution of oscillators [54], which may be expressed as a function of K_0, the averaged kinetic energy of the cloud of bound electrons, and $\langle \bar{r}^2 \rangle = (4\pi/N_s)\int_0^\infty \bar{r}^4 \bar{\rho}_{Z_{0,s}}(\bar{r})\,\mathrm{d}\bar{r}$ or $\langle \bar{r}^2 \rangle = 6\mathcal{R}_2$ from equation (6). Therefore,

$$\left\langle \hbar\omega_{Z_{0,s}} \right\rangle^2 = 2\frac{K_0}{\langle \bar{r}^2 \rangle}\alpha^2 m_e c^2, \tag{60}$$

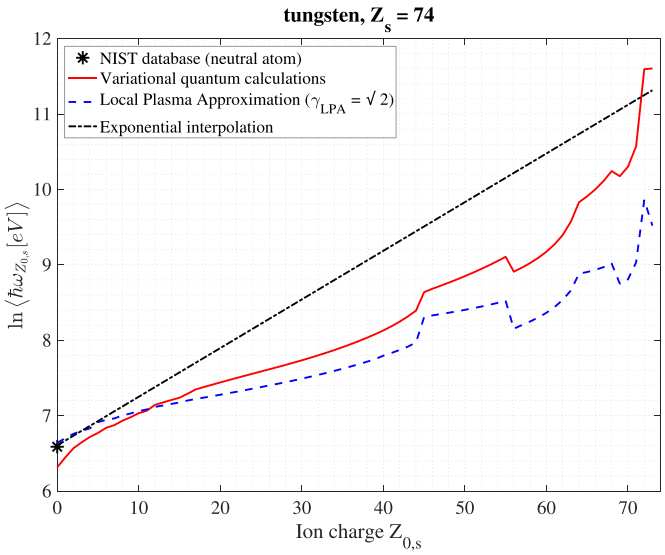

Figure 19. Variation of the logarithm of the mean excitation energy in eV units for tungsten, as a function of the level of ionization. Black dotted dashed line: exponential interpolation determined from neutral atom and hydrogen-like ion according to equation (57); blue dashed line: LPA model from equation (59) with $\gamma_{\mathrm{LPA}} = \sqrt{2}$ using the MY atomic model with the use of three exponentials calibrated against DFT calculations (*GAUSSIAN* code) [37]; red full line: variational quantum model from equation (62) using the MY atomic model with the use of three exponentials calibrated against DFT calculations (*GAUSSIAN* code) [36]; black star: mean excitation energy for the neutral atom from the NIST database [62].

where $\alpha^2 m_e c^2 \simeq 27.21\,\mathrm{eV}$, which is about twice the Rydberg unit of energy. The calculation of K_0 is performed using the virial theorem, $2K_0 \simeq -\langle U_{Z_{0,s}} \rangle$, where $U_{Z_{0,s}}$ is the atomic potential related to the density of bound charge $\rho_{Z_{0,s}}$ by the Poisson's equation, as given by equation (1), using the MY description. Therefore, since,

$$\begin{aligned}\langle U_{Z_{0,s}} \rangle = &-\frac{Z_s - N_s}{4\pi\epsilon_0 a_0} \sum_i \overline{\lambda}_{Z_{0,s,i}} \overline{A}_{Z_{0,s,i}} \\ &- \frac{N_s}{4\pi\epsilon_0 a_0} \left(\frac{1}{2} \sum_i \overline{A}^2_{Z_{0,s,i}} \overline{\lambda}_{Z_{0,s,i}} \right. \\ &\left. + \sum_i \sum_{j \neq i} \overline{A}_{Z_{0,s,i}} \overline{A}_{Z_{0,s,j}} \frac{\overline{\lambda}^2_{Z_{0,s,i}}}{\overline{\lambda}_{Z_{0,s,i}} + \overline{\lambda}_{Z_{0,s,j}}} \right), \end{aligned} \tag{61}$$

one obtains,

$$\begin{aligned}\langle \hbar\omega_{Z_{0,s}} \rangle = &\frac{\alpha^2 m_e c^2}{\sqrt{6 \sum_i \overline{\lambda}^{-2}_{Z_{0,s,i}} \overline{A}_{Z_{0,s,i}}}} \\ &\times \left[(Z_s - N_s) \sum_i \overline{\lambda}_{Z_{0,s,i}} \overline{A}_{Z_{0,s,i}} + N_s \left(\sum_i \overline{A}^2_{Z_{0,s,i}} \frac{\overline{\lambda}_{Z_{0,s,i}}}{2} \right. \right. \\ &\left. \left. + \sum_i \sum_{j \neq i} \overline{A}_{Z_{0,s,i}} \overline{A}_{Z_{0,s,j}} \frac{\overline{\lambda}^2_{Z_{0,s,i}}}{\overline{\lambda}_{Z_{0,s,i}} + \overline{\lambda}_{Z_{0,s,j}}} \right) \right]^{1/2}, \end{aligned} \tag{62}$$

by reporting equation (61) in the expression equation (60). In equation (62), parameters $(\overline{A}_{0,s,i}, \overline{\lambda}_{Z_{0,s,i}})$ are those obtained from the method of moments discussed in section 2.3.

For a single exponential, equation (62) simplifies to $\langle \hbar\omega_{Z_{0,s}} \rangle = \alpha^2 m_e c^2 \sqrt{\overline{\lambda}^3_{Z_{0,s,1}} N_s / 12}$, and for neutral atoms, i.e. when $N_s = Z_s$, $\langle \hbar\omega_{Z_{0,s}} \rangle = 9.44 Z_s\,\mathrm{eV}$, considering the Thomas–Fermi model for which $\overline{\lambda}_{Z_{0,s,1}} = 1.13 Z_s^{1/3}$, as defined in section 2.2. Using a similar approach based on an approximate description of the Thomas–Fermi model [21], the same value is found, as shown in [36]. Both relations are very close to the heuristic Bloch relation, which can also be well reproduced by the LPA model [55]. Another approximate description of the Thomas–Fermi model given in [22] gives $\langle \hbar\omega_{Z_{0,s}} \rangle \simeq 12.10 Z_s\,\mathrm{eV}$, about 12% larger than the value given by the exact Thomas–Fermi model, but still close to the Bloch relation [55].

As shown for argon in figure 18, the quantitative agreement between the non-relativistic variational quantum model and the results of the MCSCF code is good, especially above $Z_{0,s} = 8$. The analytical model has the correct dependency up to the hydrogen-like atom, which is an important assessment of the method. With the MY description of the atomic potential, small departures are observed at low $Z_{0,s}$, even if it never exceeds 20% approximately for the neutral atom. This discrepancy arises from the large sensitivity of $\langle \hbar\omega_{Z_{0,s}} \rangle$ to the atomic model in this limit. Indeed, when $\langle \hbar\omega_{Z_{0,s}} \rangle$ is calculated using the approximate Thomas–Fermi atomic models instead of the MY one, the agreement with the Bloch relation for neutral atoms is much better, within 5%.

When applied to the case of tungsten, as displayed in figure 19, $\langle \hbar\omega_{Z_{0,s}} \rangle$ exhibits globally a consistent agreement with the expected limits for a neutral atom and an almost fully stripped one. For argon, the agreement is less accurate near $Z_{0,s} = 0$, with a similar relative error. Conversely, the LPA model, $\langle \hbar\omega_{Z_{0,s}} \rangle$ has a correct variation with $Z_{0,s}$ when its value is close to Z_s, making the variational quantum description more appropriate, even if relativistic effects are not considered.

From estimates of $\langle \hbar\omega_{Z_{0,s}} \rangle$ using the LPA and the variational quantum descriptions, both using the MY atomic model for the ground-state, there is a trade-off for an accurate estimate of $\langle \hbar\omega_{Z_{0,s}} \rangle$ whatever $Z_{0,s}$ would be to consider the largest of the values given by both models. This approach would allow us to accurately describe atomic physics in kinetic calculations, either for a cold plasma such as after a major disruption or for a standard hot magnetized plasma expected during regular tokamak operation. This option is considered in the 3D linearized relativistic bounce-averaged Fokker–Planck code *LUKE* to study both the physics of post-disruptive runaway and slide-away RF-driven electrons [10, 47].

6. Conclusion

The incorporation of atomic physics in kinetic calculations is becoming mandatory in order to study the impact of high-Z elements in fusion plasmas. The MY approach for describing the atomic potential, regardless of the ionization state, is

particularly convenient to obtain consistent analytical solutions for both elastic and inelastic scattering processes that occur in a plasma. This allows fast and accurate kinetic calculations while the full atomic physics can be incorporated, over a very wide range of plasma regimes and electron kinetic energies. With this approximate and accurate atomic model, the dynamics of electrons in a plasma can be studied from the runaway energy range (a few tens of MeV) in very cold post-disruptive plasmas to slide-away electrons in hot plasmas without changing the atomic model depending upon the studied physics.

The great advantages of the method proposed here are its robustness and flexibility. Indeed, the calibration procedure against advanced numerical atomic codes is rigorous and the parameters defining the MY atomic potential are unique, as their identification does not rely on a non-linear least-squares fit procedure, which is inappropriate for the non-linear problem here addressed. The method, initially restricted to neutral atoms, has been extended here to any ionization state of any type of element, making it universal. While it was initially developed for up to three exponentials, it has been extended to an arbitrary number of them. However, for all the elements with an atomic number less than 74 (tungsten), the method does not find more than three exponentials, regardless of their ionization states. This method is also flexible since the impact of most advanced atomic simulations can be investigated without changing the structure of the kinetic code, but just by modifying the coefficients of the MY potential. Although simple, the method allows for having a more realistic description of atomic physics compared to simplified atomic models, such as the well-known Thomas–Fermi model and all its approximate representations.

The study presented here has been restricted to microscopic collision processes for kinetic calculations. However, it can be extended to other physical quantities, in particular, those that are derived in the first Born approximation, as already shown for the bremsstrahlung of fast electrons on neutral atoms, where partial screening effects may also be important. It is likely that this method can be extended to many more processes, such as ionization and knock-on collisions by energetic electrons (beyond Fokker–Planck approximation), opening the possibility of a unified and rigorous description of most of the atomic physics in kinetic descriptions of plasmas.

Acknowledgments

This study has been partially funded by the National Science Centre, Poland (NCN) Grant HARMONIA 10 No. 2018/30/M/ST2/00799. We gratefully acknowledge Poland's high-performance computing infrastructure PLGrid (HPC Centers: ACK Cyfronet AGH) for providing computer facilities and support within computational Grant No. PLG/2022/015994. This study has been published within the framework of the international project co-financed by the Polish Ministry of Education and Science, as program 'PMW' . This study has been carried out within the framework of the EUROfusion Consortium, funded by the European Union via the Euratom Research and Training Programme (Grant Agreement No. 101052200—EUROfusion). Views and opinions expressed are however those of the authors only and do not necessarily reflect those of the European Union or the European Commission. Neither the European Union nor the European Commission can be held responsible for them.

Appendix A. Moliere's model

From Moliere's description of the Thomas–Fermi model [32], the atomic charge density may be expressed as $\rho^M_{Z_{0,s}}(\hat{r}) = (Z_s - Z_{0,s})\sum \beta_i^2 B_i \exp(-\beta_i \hat{r}) / \left(4\pi \hat{r} b_s^3\right)$ with β_i and B_i independent of the atomic number Z_s, where the distance r to the nucleus is normalized to the Thomas–Fermi atomic characteristic length b_s, i.e. $\check{r} = r/b_s$. The conversion to atomic units may easily be obtained, i.e. $\beta_i \check{r} \rightarrow \beta_i (r/a_0)(a_0/b_s) \equiv \bar{\lambda}^M_{Z_{0,s,i}} \bar{r}$ so that $\bar{\lambda}^M_{Z_{0,s,i}} = \beta_i a_0/b_s = \beta_i/\bar{b}_s = \beta_i Z_s^{1/3}/\alpha^{\mathrm{TF}}$ or $\beta_i = \bar{b}_s \bar{\lambda}^M_{Z_{0,s,i}}$ where $\bar{b}_s = \alpha^{\mathrm{TF}} Z_s^{-1/3}$ and $\alpha^{\mathrm{TF}} = \left[9\pi^2/2\right]^{1/3}/4 \simeq 0.885$. In much the same way, $\beta_i^2 B_i/(\check{r} b_s^3) = (\bar{\lambda}^M_{Z_{0,s,i}})^2 B_i/(\bar{r} a_0^3)$ and $A^M_{Z_{0,s,i}} = B_i$.

Therefore, for tungsten $(Z = 74)$, since $Z_s^{1/3} = 4.1983$ while $B_1 = 0.1$, $B_2 = 0.55$, $B_3 = 0.35$, and $\beta_1 = 6.0$, $\beta_2 = 1.20$, $\beta_3 = 0.30$ from [32], coefficients which are used in plots for figures 6, 13 and 8 are $\left(\lambda_1^{W-M}, A_1^{W-M}\right) = (28.4633, 0.1)$, $\left(\lambda_2^{W-M}, A_2^{W-M}\right) = (5.6926, 0.55)$ and $\left(\lambda_3^{W-M}, A_3^{W-M}\right) = (1.4231, 0.35)$. Comparisons with values for a three exponentials representation of the atomic density obtained with DHFS and DFT models are given in table 2.

Appendix B. Quantum simulations

B.1. GAUSSIAN code

DFT is a computational quantum mechanics modelling method used in physics, chemistry and materials science to investigate the electronic structure, principally the ground state, of many-body systems, in particular atoms. Using this theory, the properties of a many-electron system can be determined by using functionals, i.e. functions of another function, which is the spatially dependent electron density in this case.

DFT is the method of reference in order to calculate the number density of bound electrons averaged over a solid angle as a function of the radius for all ionization states of any atom. There are many tools dedicated to DFT calculations, and among them, the commercial code *GAUSSIAN* is one of [12]. Version *g*09 has been used for the calculations described in the present paper. Regarding the simplicity of the atomic configuration in a tokamak plasma, i.e. field-free atoms, results obtained with this tool are likely independent of the code version. The excellent agreement with the results obtained with the latest version of the *GRASP* code described in appendix B.2 validates this assumption.

The settings of the DFT calculations can be summarized as follows: the atomic model PBE1PBE describing the hybrid-exchange correlation functional is chosen. The basis set on which the solution is determined may be internal to

the *GAUSSIAN* code (6-311G, cc-pVDZ or AUG-cc-pVDZ, AUG- standing for augmented), as for most atoms that do not require relativistic quantum calculations (up to Krypton approximately). It may also be external to the *GAUSSIAN* code, like the natural orbital-relativistic correlation consistent basis set ANO-RCC, when quantum relativistic calculations must be performed (accessible from the www.basissetexchange.org website) [63]. In the latter, the calculations are performed by solving the Douglas–Kroll–Hess second-order scalar relativistic Hamiltonian for the Dirac equation, instead of solving the usual Schrödinger equation. More advanced details may be obtained from the online *GAUSSIAN* code documentation accessible from the https://gaussian.com website.

In the calculations, the spin multiplicity requires special care. It may be obtained from Hund's rules for low-Z elements, but is usually obtained from the NIST database (https://physics.nist.gov/asd) [62]. It is important to note that for six ionization states of tungsten ranging from W^{49+} to W^{50+}, no spin multiplicity is given likely because of the energy closeness of the different shells due to strong spin–orbit coupling. Therefore, these ions require a specific treatment to perform *GAUSSIAN* calculations.

Once *GAUSSIAN* calculations are carried out, results are post-processed using the *Multiwfn* program that can be downloaded from the https://sobereva.com/multiwfn website [64].

B.2. GRASP code

MCDHF calculations have been done with the General Relativistic Atomic Structure Package (*GRASP*), version 2018 [13, 65]. The FORTRAN 95 code can be downloaded from the website https://github.com/compas/grasp and easily compiled. Specific scripts have been written from the documentation, using predefined ion configurations [1]: He (1s(2) = 2 electrons; [2]: Ne ([He] + 2s(2)2p(6) = 10 electrons; [3]: Ar ([Ne] + 3s(2)3p(6) = 18 electrons; [4]: Kr ([Ar] + 3d(10)4s(2)4p(6) = 36 electrons; [5]: Xe ([Kr] + 4d(10)5s(2)5p(6) = 54 electrons; [6]: Rn ([Xe] + 4f(14)5d(10)6s(2)6p(6) = 86 electrons, in order to minimize duration and memory requirements for the calculations. This is especially important for weakly ionized high-Z elements, such as tungsten. Once the radial wavefunctions have been calculated, the atomic density of bound electrons is determined using the dedicated module *RDENSITY,* which can be downloaded from the CPC Library and compiled like all other modules of the *GRASP* code [66].

Appendix C. Coulomb logarithm

The Coulomb logarithm $\ln\Lambda_{e,Z_{s,0}} = \ln(\bar{b}_{\max}/\sqrt{1+\bar{b}_{\min}^2})$ from equation (24) may be explicitly evaluated, taking into account the plasma conditions, the type of element and its net charge. Since the Coulomb potential is screened at a distance larger than the Debye length λ_D, the upper limit is $\bar{b}_{\max} = \lambda_D/b_{90}$. For multispecies plasmas, $\lambda_D \to \lambda_D^{e-i} \simeq \lambda_D^e\left(1+Z_{\rm eff}T_{\rm e}/T_i\right)^{-1/2}$, where λ_D^e is the usual electron Debye length, and $Z_{\rm eff} = \sum_s\sum_{Z_{0,s}} n_{Z_{0,s}} Z_{0,s}^2/n_{\rm e}$ is the effective charge, knowing that $\sum_s\sum_{Z_{0,s}} n_{Z_{0,s}}(t,\mathbf{x})\,Z_{0,s} = n_{\rm e}$ from electroneutrality. In most kinetic calculations it is usually assumed that all ion species have the same temperature T_i whatever their net charge.

The value of $\bar{b}_{\min}$ depends of the ratio b_q/b_{90} where b_q is deduced from the uncertainty principle. If $b_q/b_{90} \gg 1$, quantum effects predominate and $\ln\Lambda^q_{e,Z_{0,s}} \simeq \ln(\lambda_D/b_q)$, otherwise the classical limit corresponding to $\bar{b}_{\min} = 0$ can be taken, and $\ln\Lambda^c_{e,Z_{s,0}} \simeq \ln(\lambda_D/b_{90})$ [67, 68]. Consequently, $\ln\Lambda^q_{e,Z_{0,s}}$ is less than $\ln\Lambda^c_{e,Z_{0,s}}$. The quantum limit may be determined from the uncertainty principle $\triangle p\triangle x > \hbar/2$ where the momentum increment is approximated by $\triangle p = \mu_s u_s$, $\mu_s = m_{\rm e}m_s/(m_{\rm e}+m_s)$ being the reduced mass between colliding particles. Therefore, assuming $\triangle x \simeq b_q$, the impact parameter is $b_q \approx \hbar/(2\mu_s u_s)$ or $b_q \approx (\lambda_C/4\pi)(m_{\rm e}/\mu_s)/\bar{u}_s$, where λ_C is the Compton length. The ratio $\bar{b}_{\min} = b_q/b_{90} = \bar{u}_s/(2Z_{0,s}\alpha)$ since $b_{90} = r_{\rm e}\left(Z_{0,s}/\bar{u}_s^2\right)(m_{\rm e}/\mu_s)$ for Coulomb collisions and $\lambda_C/r_{\rm e} = 2\pi/\alpha$. A rough estimate of the smooth transition between classical and quantum limits may be obtained by averaging $\bar{u}_s$ over the electron and ion distribution functions. In this case, the square root of the mean square velocity is $\langle\langle\bar{u}_s\rangle\rangle \simeq \sqrt{3\overline{T}_{\rm e}}$ where $\overline{T}_{\rm e} = T_{\rm e}/\left(m_{\rm e}c^2\right)$ and the normalized plasma temperature threshold above which quantum effects are significant is $\overline{T}^q_{e,Z_{0,s}} = 4Z_{s,0}\alpha^2/3$. For $Z_{0,s} = 1$, $T^q_{e,Z_{0,s}} = 36\,eV$, so that the quantum limit must always be taken under standard tokamak plasma conditions with isotopes of hydrogen. For $Z_{0,s} = 42$, corresponding to the net ionization of tungsten at $T_{\rm e} = 3\,keV$, then $T^q_{e,Z_{0,s}}$ is much larger, $T^q_{e,Z_{0,s}} = 64\,keV$, and the classical limit is conversely always valid in tokamak plasmas. Since $m_{\rm e} \ll m_s$, $\mu_s \simeq m_{\rm e}$, and $\ln\Lambda^c_{e,Z_{0,s}} \simeq \ln\lambda_D/r_{\rm e} + 2\ln\bar{u}_s - \ln Z_{0,s}$, while $\ln\Lambda^q_{e,Z_{0,s}} \simeq \ln\lambda_D/r_{\rm e} + \ln\bar{u}_s + \ln(2\alpha)$. If $\ln\Lambda^q_{e,Z_{0,s}}$ and $\ln\Lambda^c_{e,Z_{0,s}}$ are both heavily weighted by the ratio $\lambda_D/r_{\rm e}$, the regime dominated by quantum effects concerns principally fast electrons for partially ionized high-Z elements whose kinetic energy is greater than $\overline{T}^q_{e,Z_{0,s}}$. In the quantum limit, $\Lambda^a_{e,Z_{0,s}}$ is independent of the ion net charge $Z_{0,s}$.

In standard MKSA units, with $\lambda_D = \lambda_D^e$, $\ln\Lambda^q_{e,Z_{s,0}} = 0.5\ln T_{\rm e}\,[keV] - 0.5\ln n_{\rm e}\left[10^{20}\,m^{-3}\right] + \ln\bar{u}_s + 18.61$ and the thermal value is $\ln\Lambda^{q-{\rm th}}_{e,Z_{0,s}} \simeq \ln T_{\rm e}\,[keV] - 0.5\ln n_{\rm e}\left[10^{20}\,m^{-3}\right] + 16.04$. Using λ_D^{e-i}, the Coulomb logarithm must be reduced by the term $-0.5\ln(1+Z_{\rm eff}T_{\rm e}/T_i)$, and for a pure hydrogen plasma with $T_{\rm e} = T_i$, $\ln\Lambda^{q-{\rm th}}_{e,Z_{0,s}} \simeq \ln T_{\rm e}\,[keV] - 0.5\ln n_{\rm e}\left[10^{20}\,m^{-3}\right] + 15.7$, a value very close to those found in the literature [67, 69]. Additional small differences may arise from the choice of the averaged velocity. For relativistic electrons, $\bar{u}_s \simeq \bar{v}$, since ions may be considered at rest, $\ln\Lambda^{q-{\rm rel}}_{e,Z_{0,s}} \simeq \ln\Lambda^{q-{\rm th}}_{e,Z_{0,s}} + \ln\bar{p} - 0.5\ln\overline{T}_{\rm e} - 0.5\ln 3$, as far as $\bar{p} > \sqrt{3\overline{T}_{\rm e}}$ or $\overline{E}_c \gg 3\overline{T}_{\rm e}/2$, where $\overline{E}_c$ is the kinetic energy normalized to the electron rest mass energy. Following [7], $\ln\Lambda^q_{e,Z_{0,s}}$ may be approximated by $\ln\Lambda^q_{e,Z_{0,s}} \simeq \ln\Lambda^{q-{\rm th}}_{e,Z_{0,s}} + \ln(1+(\bar{p}/(\sqrt{3\overline{T}_{\rm e}}))^k)/k$ with $k = 5$, in order to have a smooth transition from the thermal limit of the Coulomb logarithm.

Conversely to the quantum limit, $\ln\Lambda^c_{e,Z_{0,s}}$ in the classical limit is weakly dependent on the ion charge $Z_{0,s}$ and is more sensitive to $T_{\rm e}$, since $\ln(\Lambda^c_{e,Z_{0,s}}/\Lambda^q_{e,Z_{0,s}}) = \ln(\bar{u}_s/(2\alpha Z_{0,s}))$. In MKSA units, $\ln\Lambda^{c-{\rm th}}_{e,Z_{0,s}} = 1.5\ln T_{\rm e}\,[keV] - 0.5\ln n_{\rm e}\left[10^{20}\,m^{-3}\right] - \ln Z_{s,0} + 17.69$ and $\ln\Lambda^{c-{\rm rel}}_{e,Z_{0,s}} = \ln\Lambda^{c-{\rm th}}_{e,Z_{0,s}} + 2\ln\bar{p} - \ln\overline{T}_{\rm e} - \ln 3$. It

can be also approximated by the expression $\ln\Lambda^{c}_{e,Z_{0,s}} \simeq \ln\Lambda^{c-\mathrm{th}}_{e,Z_{0,s}} + \ln(1+\left(\overline{p}^2/\left(3\overline{T}_\mathrm{e}\right)\right)^k)/k$. The choice of the electron–ion Coulomb logarithm, $\ln\Lambda_{e,Z_{0,s}}\left(\overline{p},\overline{T}_\mathrm{e}\right)$, therefore depends on the type of element s, its local ionization state $Z_{0,s}$ and the temperatures T_e and T_i at the same location in the plasma.

ORCID iDs

Y. Savoye-Peysson https://orcid.org/0000-0001-8594-9474
D. Mazon https://orcid.org/0000-0001-5560-2277
J. Bielecki https://orcid.org/0000-0002-3460-8677
D. Dworak https://orcid.org/0000-0002-0768-1748
K. Król https://orcid.org/0000-0002-7178-2607
A. Jardin https://orcid.org/0000-0003-4910-1470
M. Scholz https://orcid.org/0000-0002-7330-1782
J. Walkowiak https://orcid.org/0000-0002-9787-1691
J. Decker https://orcid.org/0000-0003-0220-2653

References

[1] Bourdelle C. *et al* 2015 *Nucl. Fusion* **55** 063017
[2] Garofalo A.M. *et al* 2017 *Nucl. Fusion* **57** 076037
[3] Gribov Y. 2006 Plasma of ITER (scenarios 2 and 4), ASTRA-PET simulations (available at: http://ftp.jp.iter.org/)
[4] Peysson Y. *et al* 2021 Effect of partially ionized high-Z atoms on fast electron dynamics in tokamak plasmas *IAEA FEC 2020—The 28th IAEA Fusion Energy Conf. (10–15 May 2021)* (available at: https://nucleus.iaea.org/sites/fusionportal/Shared%20Documents/FEC%202020/fec2020-preprints/preprint1097.pdf)
[5] Summers H.P. 2004 *The ADAS User Manual, Version 2.6* (available at: www.adas.ac.uk)
[6] Hesslow L., Embréus O., Stahl A., DuBois T., Papp G., Newton S. and Fülöp T. 2017 *Phys. Rev. Lett.* **118** 255001
[7] Hesslow L., Embréus O., Hoppe M., DuBois T., Papp G., Rahm M. and Fülöp T. 2018 *J. Plasma Phys.* **84** 905840605
[8] Hesslow L., Embréus O., Wilkie G.J., Papp G. and Fülöp T. 2018 *Plasma Phys. Control. Fusion* **60** 074010
[9] Stahl A., Embréus O., Papp G., Landreman M. and Fülöp T. 2016 *Nucl. Fusion* **56** 112009
[10] Peysson Y. and Decker J. 2014 *Fusion Sci. Technol.* **65** 22
[11] Ostuni V. *et al* 2022 *Nucl. Fusion* **62** 106034
[12] Frisch M.J. *et al* 2016 Gaussian 09, revision e.01 *Technical Report* (Gaussian, Inc.)
[13] Fischer C.F. *et al* 2019 *Comput. Phys. Commun.* **237** 184
[14] Sauer S.P.A. 2015 *Advances in Quantum Chemistry: The Mean Excitation Energy of Atomic Ion* vol 71 (Elsevier Inc.) p 29
[15] Sauer S.P.A. *et al* 2020 *Mol. Phys.* **119** 1–14
[16] Belkhiri M., Fontes C.J. and Poirier M. 2015 *Phys. Rev.* A **92** 032501
[17] Gu M.F. 2008 *Can. J. Phys.* **86** 675
[18] Koch H.W. and Motz J.W. 1959 *Rev. Mod. Phys.* **31** 920
[19] Peysson Y. and Decker J. 2008 *Phys. Plasmas* **15** 092509
[20] Amore P. *et al* 2014 *Appl. Math. Comput.* **232** 929
[21] Green A.E.S., Sellin D.L. and Zachor A.S. 1969 *Phys. Rev.* **184** 1
[22] Kirillov V.D. *et al* 1975 *Fiz. Plazmy* **1** 218
[23] Edwards J.P. *et al* 2017 *Prog. Theor. Exp. Phys.* **2017** 083A01
[24] Pratt R.H. and Tseng H.K. 1972 *Phys. Rev.* A **5** 1063
[25] Pratt R.H., Tseng H.K., Lee C.M., Kissel L., MacCallum C. and Riley M. 1977 *At. Data Nucl. Data Tables* **20** 175
[26] Avdonina N.B. and Pratt R.H. 1993 *J. Quant. Spectrosc. Radiat. Transfer* **50** 349
[27] Pratt R.H. *et al* 1995 *Nucl. Instrum. Methods Phys. Res.* B **99** 156
[28] Lamoureux M. and Avdonina N. 1997 *Phys. Rev.* E **55** 912
[29] Salvat F., Martnez J.D., Mayol R. and Parellada J. 1987 *Phys. Rev.* A **36** 467
[30] Fronsdal C. and Uberall H. 1958 *Phys. Rev.* **111** 580
[31] Haug E. 2008 *Radiat. Phys. Chem.* **207** 207
[32] Moliere G. 1947 *Z. Naturforsch.* A **2** 133
[33] Nilsson E., Decker J., Peysson Y., Granetz R.S., Saint-Laurent F. and Vlainic M. 2015 *Plasma Phys. Control. Fusion* **57** 095006
[34] Bethe H. 1930 *Ann. Phys., Lpz.* **397** 325
[35] Jackson J. 1998 *Classical Electrodynamic* (Wiley)
[36] Garbet X., Deutsch C. and Maynard G. 1987 *J. Appl. Phys.* **61** 907
[37] Linhard J. and Scharff M. 1953 *Dan. Mat. Fys. Medd.* **27** 1–31
[38] Botto D.J., McEnnan J. and Pratt R.H. 1978 *Phys. Rev.* A **18** 580
[39] Sauer S.P.A. 2011 *Molecular Electromagnetism. A Computational Chemistry Approach* (Oxford University Press)
[40] Kohn C. and Ebert U. 2014 *Atmos. Res.* **135–136** 432
[41] Byatt W.J. 1956 *Phys. Rev.* **104** 1298
[42] Bunaciu D., Florescu V., Pratt R.H. and Soon Kim Y. 1980 *Nucl. Phys.* A **339** 329
[43] Walkowiak J., Jardin A., Bielecki J., Peysson Y., Mazon D., Dworak D., Król K. and Scholz M. 2022 *Phys. Plasmas* **29** 022501
[44] Karney C.F.F. 1986 *Comput. Phys. Rep.* **4** 183
[45] Shoucri M. and Shkarofsky I. 1994 *Comput. Phys. Commun.* **82** 287
[46] Cannoni M. 2017 *Int. J. Mod. Phys.* A **32** 1730002
[47] Decker J., Hirvijoki E., Embreus O., Peysson Y., Stahl A., Pusztai I. and Fülöp T. 2016 *Plasma Phys. Control. Fusion* **58** 025016
[48] Heitler W. 1957 *The Quantum Theory of Radiations* 3rd edn (Clarendon)
[49] Solodov A.A. and Betti R. 2008 *Phys. Plasmas* **15** 042707
[50] Decker J. and Peysson Y. 2004 DKE: a fast numerical solver for the 3D drift kinetic equation *Report* EUR-CEA-FC-1736 (Euratom-CEA)
[51] Beliaev S.T. and Budker G.I. 1956 *Sov. Phys. Dokl.* **1** 218
[52] Bethe H. and Heitler W. 1934 *Proc. R. Soc.* A **146** 83
[53] Abramowitz M. and Stegun I.A. 1970 *Handbook of Mathematical Functions* 9th edn (Dover Publication)
[54] Fano U. and Cooper J.W. 1968 *Rev. Mod. Phys.* **40** 441
[55] Chu W.K. and Powers D. 1972 *Phys. Lett.* A **40** 23
[56] Inokuti M. and Turner J.E. 1978 Physics of elementary particles and fields (A3200) *Report No.* CONF-780534–2 (Argonne National Lab.)
[57] Wyckoff H.O. 1984 *Technical Report* 37 (International Commission on Radiation Units and Measurements (ICRU))
[58] Kamakura S., Sakamoto N., Ogawa H., Tsuchida H. and Inokuti M. 2006 *J. Appl. Phys.* **100** 064905
[59] Sauer S.P.A., Sabin J.R. and Oddershede J. 2018 *J. Chem. Phys.* **148** 174307
[60] Rosendorff S. and Schlaile H.G. 1989 *Phys. Rev.* A **40** 6892
[61] Dehmer J.L., Inokuti M. and Saxon R.P. 1975 *Phys. Rev.* A **12** 102
[62] Kramida A. *et al* 2022 *Nist Atomic Spectra Database (Ver. 5.10)* (National Institute of Standards and Technology)
[63] Pritchard B.P., Altarawy D., Didier B., Gibson T.D. and Windus T.L. 2019 *J. Chem. Inf. Model.* **59** 4814

[64] Lu T. and Chen F. 2012 *J. Comput. Chem.* **33** 580
[65] Jonsson P. *et al* 2023 *Atoms* **11** 7
[66] Schiffmann S., Li J.G., Ekman J., Gaigalas G., Godefroid M., Jönsson P. and Bieroń J. 2022 *Comput. Phys. Commun.* **278** 108403
[67] Wesson J. 2004 *Tokamaks* (*The International Series of Monographs on Physics*) (Clarendon)
[68] Mulser P., Alber G. and Murakami M. 2014 *Phys. Plasmas* **21** 042103
[69] Sauter O., Angioni C. and Lin-Liu Y.R. 1999 *Phys. Plasmas* **6** 2834